Smart Materials for Cartilage and Bone Tissue Engineering

Jiabin Zhang

This thesis is submitted for the degree of Doctor of Philosophy

in

School of Chemical Engineering and Advanced Materials

Faculty of Engineering, Computer, and Mathematical Sciences

at

The University of Adelaide

August 2019

Table of contents

List of publications

This doctoral thesis is prepared in "Publication" format under the guideline of "Specifications for Thesis 2019" of University of Adelaide. The following publications are included in the main body of this thesis. They are either published, submitted for publication, or prepared in publication format.

1. **Zhang, J.**; Yun, S.; Bi, J.; Dai, S.; Du, Y.; Zannettino, A. C. W.; Zhang, H., Enhanced multi-lineage differentiation of human mesenchymal stem/stromal cells within poly(*N*-isopropylacrylamide-acrylic acid) microgel-formed three-dimensional constructs. Journal of Materials Chemistry B **2018,** 6 (12), 1799-1814. (Published)

2. **Zhang, J.**; Zhang, M.; Lin, R.; Yun, S.; Du, Y.; Wang, L.; Yao, Q.; Zannettino, A.; Zhang, H., Allogeneic Primary Mesenchymal Stem/Stromal Cell Aggregates within Poly(*N*-Isopropylacrylamide-co-Acrylic Acid) Hydrogel for Osteochondral Regeneration. Applied Materials Today **2019**, 100487. (Published)

3. **Zhang, J.**; Yun, S.; Du, Y.; Zannettino, A. C. W.; Zhang, H., Fabrication of a neo-cartilage patch by fusing cell aggregates generated in a thermosensitive hydrogel onto electrospun film. (Prepared in publication format)

4. **Zhang, J.**; Yun, S.; Karami, A.; Du, Y.; Zannettino, A. C. W.; Zhang, H., Enhanced Chondrogenesis and Osteogenesis by Embedding Human Mesenchymal Stem/Stromal Cells within A Magnetic-Field Responsive "Dancing" Ball. Biotechnology and Bioengineering. (Prepared in publication format)

The following book chapter was published during the period of the PhD study but don't contribute to the main body of this thsis. It is reproduced in the appendices by permission of The Royal Society of Chemistry (DOI: 10.1039/9781788010542-00473).

Zhang, J.; Zhang, H.; Xu, X., CHAPTER 17 Smart Materials to Regulate the Fate of Stem Cells. Smart Materials for Tissue Engineering: Applications, The Royal Society of Chemistry: **2017**, 473-504. (Published)

Abstract

Osteoarthritis (OA) is a chronic disease normally caused by trauma or pathological disorder. Its symptom normally starts from the degeneration of cartilage, resulting in an irregular tough surface, and might progressively extend to subchondral bone, leading to the abnormal joint function and disability. Due to the avascular and condensed structure of cartilage, and the limited number of progenitor cells, it is challenging for regeneration of cartilage defects. Furthermore, because of the distinct structure of cartilage and subchondral bone, stem cell-alone or biomaterial-alone based strategy might not be able to simultaneously fulfil the requirement for regeneration of cartilage and subchondral bone. Hence, in this thesis, a variety of smart materials, such as thermosensitive poly (*N*-isopropylacrylamide-acrylic acid) hydrogel and magnetic field-responsive scaffold, were fabricated, characterized, and utilized for three-dimensional (3D) culture of mesenchymal stem/stromal cells (MSCs) *in vitro*. It was found that MSCs showed quite good cell viability and these smart materials promoted the capacity of multi-lineage differentiation due to either functional enhancement of cell aggregates in the thermosensitive hydrogels or synergy of a dynamic magnetic field, mechanical stimulation, structural topography, dynamic culture, extracellular matrix (ECM)-mimicking materials, and inductive biomolecules in the magnetic field-responsive scaffolds. When allogeneic MSC aggregates were delivered *in vivo* by the thermosensitive hydrogel, osteochondral defects were fully regenerated, which demonstrated that the thermosensitive hydrogel might be a promised vehicle for the delivery of stem cells and facilitate the osteochondral regeneration. Moreover, those autologous chondrogenesis-induced MSCs either in the thermosensitive hydrogel or in the magnetic field-responsive scaffolds were also able to be engineered into a neo-cartilage patch or tissue, respectively, which might also have potential application in cartilage and bone regeneration. In conclusion, the fabricated smart materials including a thermosensitive hydrogel and a magnetic field-responsive scaffold, may assist in stem cell therapy for promising efficacy of OA treatment.

Declaration of a thesis that contains publications

I certify that this work contains no material which has been accepted for the award of any other degree or diploma in my name, in any university or other tertiary institution and, to the best of my knowledge and belief, contains no material previously published or written by another person, except where due reference has been made in the text. In addition, I certify that no part of this work will, in the future, be used in a submission in my name, for any other degree or diploma in any university or other tertiary institution without the prior approval of the University of Adelaide and where applicable, any partner institution responsible for the joint-award of this degree.

I acknowledge that copyright of published works contained within this thesis resides with the copyright holder(s) of those works.

I also give permission for the digital version of my thesis to be made available on the web, via the University's digital research repository, the Library Search and also through web search engines, unless permission has been granted by the University to restrict access for a period of time.

Name: Jiabin Zhang

Signature: _____. Date: 01/08/2019 .

Acknowledgement

I would like to first thank my principal supervisor, Prof. Hu Zhang, for his consistent supervision and inspired advice. I would also like to thank my co-supervisors, Prof. Andrew Zannettino and Prof. Yuguang Du, for their kind encouragement and helpful suggestion on experiment design and manuscript correction.

I appreciate the endless support of my mother, Yamei Li, and my father, Guohe Zhang. Without their encouragement and love, I won't have a passion for science research. I also want to thank my elder brother, Binbin Zhang, for his understanding and support. My great acknowledgement gives to my fiancée, Jiali Cheng. Whenever I feel stressed or depressed, she always encourages me and regards me as the best in her mind. Even though we are far from each other in distance, our hearts are tightly connected. Her lovely smile always accompanies me throughout the hard journey. Her promise of following me wherever I go gives me courage to pursue my dream.

Thank you to my colleagues, Xiaolin Cui, Seonho Yun, Afshin Karami, Bingyang Zhang, Yechuan Zhang, Ming Zhang, Rongcai Lin, Cheng Luo, Jiahua Duan, Lan Li, Guangzhen Yang, Xin Zhang, Huikang Zhang, Lingze Liu, Wenjun Guo, Dongdong Liu, Bolin Jing, Limeng Zhu, Xubing Yuan, Yuzhe Sun, Yalu Yan, Ruilian Li, Chenlu Zhu, and Hua Xu, for their kind help and assistance in the experiments. I would also thank Sharon Paton, Vicki Wilczek, Stephen Fitter, Makoto Kamei, Ashley Slattery, Lisa Anne O'Donovan, Qiuhong Hu, Sarah Chaplin, Randall Grose, Siming Jiao, and Rui Mao, for their patient research training. Many thanks to Jingxiu Bi, Sheng Dai, Xiaojuan Hao, Qingqiang Yao, Liming Wang, Yan Xu, Cheng Tang, Jianjun Li, Zhuo Wang, Chen Zhang, Lishi Ren, Yuchen Zhang, and Cui Feng, for their support and help. I would also thank my buddies, Enze Liu, Li Chen, Yang Liu, and Tianyuan Huang, for the encouragement and friendship.

Lastly, I would like to acknowledge the financial support from Beacon of Enlightenment PhD Scholarship (in partnership with the Institute of Process Engineering, Chinese Academy of

Sciences), Research Travel Scholarship 2018, and Global Learning Travel Grant. I also thank School of Chemical Engineering and Advanced Materials for the daily support.

CHAPTER I

INTRODUCTION

1.1 Background

Osteoarthritis (OA) as a chronic joint disease often causes cartilage degeneration, which may even deteriorate remodeling of subchondral bone under serious situations, resulting in pain or even disability. [1] A normal cartilage structure consists of a typical three-layer architecture: a superficial layer contains horizontally orientated flat chondrocytes, while middle layer and deep layer are occupied with round chondrocytes with a random distribution and condensed chondrons orientated in a vertical direction, respectively. The components and organization of its extracellular matrices (ECMs), such as type 2 collagen, proteoglycans, and hyaluronan, allow cartilage to absorb shocks and bearing loads, one of its physiological functions. [2] In contrast to the avascular structure of cartilage, subchondral bone is rich in blood vessels, which are responsible for transportation of nutrients, wastes, and gases. Besides, the majority of components in bone is type 1 collagen and inorganic minerals, hydroxyapatite. Upon maturation, especially for patients with OA, the hypertrophic chondrocytes will initiate cell apoptosis and be calcified for endochondral ossification. [3] Without the layers of cartilage, patients suffer pain because of lack of a buffering structure to absorb shocks and bearing loads. OA is one of the ten most disabling diseases in developed countries and affects approximately 9.6% of men and 18.0% of women over 60 years old in the world. [1] In 2013, OA composed 4.3% of the combined costs, approximately 16.5 billion US dollars, for all hospitalization in US, which was the second most costly disease. [4]

Unfortunately, such a distinct difference of the structure between cartilage and subchondral bone makes it challenging for restoration of osteochondral tissues using a single therapeutic strategy. [1] Mesenchymal stem/stromal cells (MSCs) as one type of multipotent adult stem cells have shown promising clinical results for treatment of OA-induced cartilage degeneration. [5] However, both intravenous and intra-joint injection of MSCs requires substantial cells to overcome the issues of poor cell survival and retention at the defect sites without compromising the therapeutic efficacy. [6] Therefore, various scaffolds/hydrogels are fabricated to facilitate

implantation of MSCs. Theses engineered scaffolds/hydrogels are not only designed to mimic the structure of cartilage ECMs, but also functionalized to regulate the fate of MSCs. [7] In contrast to conventional geometrical cues for regulation of MSCs, interaction of smart materials with MSCs through changes in external stimuli guides MSCs to differentiate into specific lineages for enhanced therapeutic efficacies. [8]

This thesis mainly focuses on fabrication of different smart materials and how they are used to regulate the fate of stem cells for cartilage and bone tissue engineering. Although a variety of thermo-responsive hydrogels have been previously studied for tissue engineering, this thesis firstly reports enhanced multi-lineage cell differentiation *in vitro* and osteochondral regeneration *in vivo* by formation of cell aggregates *in situ* using an ultra-soft thermo-responsive 3D hydrogel. Cell migration in the hydrogel is first evidenced and a hypothesis of the underlying mechanism is evaluated. A neo-cartilage patch is then fabricated for treatment of degenerated cartilage with irregular superficial defects. Furthermore, this thesis also reports successful fabrication of another one smart material, a magnetic field-responsive scaffold, and first shows enhanced chondrogenesis and osteogenesis of MSCs *in vitro* due to synergic effects of a series of external stimuli, which may be a novel strategy for cartilage and bone tissue engineering.

1.2 Aims and Objectives

OA-induced cartilage degeneration and subchondral bone remodeling are challenging to be completely restored using only one therapeutic strategy, therefore, the aim of the thesis is to fabricate two novel smart materials, a thermo-responsive hydrogel and a magnetic field-responsive scaffold, and explore their regulatory effects on the fate of stem cells and potential applications in cartilage and bone tissue engineering. The overall objectives are listed as below.

Objective 1: Fabrication of MSCs aggregates in a thermo-responsive hydrogel as an *in-vitro* 3D platform for enhancing differentiation of MSCs.

Objective 2: Development of a novel therapeutic strategy for osteochondral regeneration *in vivo* by formation and delivery of MSC aggregates by an injectable thermos-sensitive hydrogel.

Objective 3: Bioengineering an *in vitro* neo-cartilage patch by cell aggregation and fusion within a thermo-sensitive hydrogel for regeneration of a cartilage with irregular superficial defects.

Objective 4: Development of an *in-vitro* platform for implementing multiple stimuli on MSCs to induce their chondrogenesis and osteogenesis in the magnetic field-responsive scaffolds.

1.3 Chapter outline

In this thesis, two smart materials, a thermo-responsive hydrogel and a magnetic field-responsive scaffold, were fabricated and explored for regulation of MSCs *in vitro* and *in vivo* with potential applications in cartilage and bone tissue engineering. The general outline of this thesis is described as below.

Chapter 1: Introduction of the thesis regarding gaps, aims and objectives, and chapter outline.

Chapter 2: literature review of recent research strategies for treatment of OA with an emphasis on cell-based therapy illustrating mechanisms and applications of hydrogel-mediated fabrication of cell aggregates and scaffold-based therapy using thermo-responsive and magnetic field-responsive materials for regulation of stem cell fates.

Chapter 3: Formation of uniform cell aggregates in a thermo-responsive hydrogel, which impeded cell proliferation but enhanced multi-lineage differentiation of MSCs *in vitro*.

Chapter 4: Osteochondral regeneration *in vivo* due to enhanced paracrine effects of MSC aggregates, which promoted homing of endogenous stem/progenitor cells, angiogenesis, immuno-modulation and cell chondrogenesis.

Chapter 5: Interaction between MSCs and the soft thermo-responsive hydrogel facilitated micro-tissue formation by cell migration-mediated cell aggregation and the resultant MSC-derived chondrocytes were harvested and forced to fusion into a neo-cartilage patch *in vitro* for potential application in superficial cartilage regeneration.

Chapter 6: Fabrication of an *in-vitro* platform consisting of magnetic field-responsive scaffolds and a rotating magnet device to study the synergic effect of a dynamic magnetic field, mechanical stimulation, ECM-mimicking materials, dynamic culture, structural topography on chondrogenesis and osteogenesis of MSCs *in vitro*.

Chapter 7: Conclusions and future directions of this thesis.

1.4 Reference

[1] Li MH, Xiao R, Li JB, Zhu Q. Regenerative approaches for cartilage repair in the treatment of osteoarthritis. Osteoarthritis and Cartilage 2017;25:1577-87.

[2] Armiento AR, Stoddart MJ, Alini M, Eglin D. Biomaterials for articular cartilage tissue engineering: Learning from biology. Acta Biomaterialia 2018;65:1-20.

[3] Camarero-Espinosa S, Rothen-Rutishauser B, Foster EJ, Weder C. Articular cartilage: from formation to tissue engineering. Biomaterials Science 2016;4:734-67.

[4] Torio C. Moore B (Truven Health Analytics). National Inpatient Hospital Costs: The Most Expensive Conditions by Payer, 2013 HCUP Statistical Brief 2016;204.

[5] Goldberg A, Mitchell K, Soans J, Kim L, Zaidi R. The use of mesenchymal stem cells for cartilage repair and regeneration: a systematic review. Journal of orthopaedic surgery and research 2017;12:39.

[6] Sart S, Tsai AC, Li Y, Ma T. Three-dimensional aggregates of mesenchymal stem cells: cellular mechanisms, biological properties, and applications. Tissue Engineering Part B: Reviews 2014;20:365-80.

[7] Jayasuriya CT, Chen Y, Liu W, Chen Q. The influence of tissue microenvironment on stem cell-based cartilage repair. Annals of The New York Academy of Sciences 2016;1383:21-33.

[8] Chan A, Orme RP, Fricker RA, Roach P. Remote and local control of stimuli responsive materials for therapeutic applications. Advanced Drug Delivery Reviews 2013;65:497-514.

CHAPTER II

LITERATURE REVIEW

2.1 Osteochondral structure

Hyaline cartilage, or articular cartilage, exists widely in joints, such as shoulder, hip and knee. Developmentally, hyaline cartilage is formed by the condensation of mesenchymal stem/stromal cells (MSCs) at the early stage of skeletogenesis. [1] Condensation of MSCs is mediated by interactions of cell-substrate and cell-cell, and is believed to play an important role in chondrogenesis by initiating a series of critical fate-determining signaling pathways. [2, 3] Upon maturation, cartilage forms a typical three-layer structure, allowing efficient bearing of, and transferring of loads, enabling the smooth movement of a joint. The superficial layer of hyaline cartilage consists of compact flat chondrocytes guided by the horizontal orientation of collagen fibrils, mainly type 2 collagen; the round chondrocytes randomly distribute in the middle layer; the chondrocytes in the deep layer are surrounded by rich type 6 collagen and are organised as vertically orientated chondrons. Hypertrophic chondrocytes in the deep layers express abundant type 10 collagen and ultimately calcify for endochondral ossification. [4] Among all components, extracellular matrices (ECMs) account for approximately 95% to 99% of the total cartilage volume, while the entrapped chondrocytes represent only 1% to 5%. Although chondrocytes have a limited proliferative capacity, they actively synthesise and remodel the extracellular matrix (ECM) proteins that comprise the cartilage, including collagen, proteoglycan, and hyaluronan, endowing cartilage with mechanical strength for normal physiological functions. In contrast to the avascular structure of a cartilage, subchondral bone is rich in blood supply and composed of substrates mainly including type 1 collagen and hydroxyapatite. [5]

2.2 Osteoarthritis and therapeutic strategies

Osteoarthritis (OA) is a chronic joint disease that results in the gradual degeneration of cartilage. Even though the underlying mechanism of OA remains unclear, it is believed that injury, aging, gender, and inflammation are contributing factors. In cases of severe OA, degeneration of cartilage can cause abnormal remodeling of the subchondral bone, resulting in joint pain and

even disability. [6] OA is one of the ten most disabling diseases in developed countries and affects approximately 9.6% of males and 18.0% of females over the 60 years old. [7] Recent therapeutic strategies designed to treat OA include injection of bio-/chemo- therapeutics for prevention of matrix degeneration and/or inflammation, and implantation of cells and/or scaffolds designed to stimulate tissue regeneration. However, due to the distinct organization of cartilage and subchondral bone, it is challenging to restore normal functions of the whole osteochondral tissue simply using a single strategy for treatment of OA. [8]

2.2.1 Bio- and chemo- therapeutics for treatment of OA

Currently, the strategies used to treat OA involves inhibiting matrix-degrading enzymes, such as matrix metalloproteinases (MMPs) [9], and/or pro-inflammatory factors, such as interleukin-1 (IL-1) [10] and tumour necrosis factor alpha (TNF-α) [11], by direct injection of chemical or biological inhibitors that inhibit relevant pathological signaling pathways. Moreover, recruitment of endogenous stem/progenitor cells with chemo- or cytokine- attractants, such as TGF-β [12] or stromal cell-derived factor-1 (SDF-1) [13], or co-delivery of multiple growth factors, such as insulin-like growth factor-1 (IGF-1), basic fibroblast growth factor (FGF-2), transforming growth factor beta (TGF-β), and bone morphogenetic proteins (BMPs), to stimulate cartilage and bone regeneration, may be also a potential treatment option for OA. [14, 15] However, the involved signaling pathways for activation of ECM degradation and/or pro-inflammation are complex, therefore, combination therapy involving the targeting/inhibition may be necessary for optimal treatment of OA. Moreover, the potential side effect of such inhibitors may also need to be assessed since signaling pathways may be required for normal physiological activities. The physiological differences between cartilage and subchondral bone also requires delivery of more than one growth factor in a sustainable and controlled manner for osteochondral regeneration, which may demand assistance from scaffolds/hydrogels.

2.2.2 Cell-based therapy for treatment of OA

Studies show that implantation of cells, such as autologous chondrocyte implantation (ACI), enabled successful cartilage restoration. [16, 17] However, the limited proliferative capacity of chondrocytes and dedifferentiation of chondrocytes when culturing and expanding *in vitro* limit this treatment to only small defects and require the retrieval of non-load-bearing cartilages, usually involving painful invasive surgery. [18] Alternatively, implantation of mesenchymal stem/stromal cells (MSCs), either derived from autologous or allogeneic sources, has been shown to provide comparative efficacy to ACI. [19, 20] MSCs display regenerative and differentiation capacity (i.e. into chondrocytes and osteocytes), immunomodulatory capacity (i.e. anti-inflammation and immunosuppression) and the capacity to recruit endogenous stem/progenitor cells to home to the defect sites by secreting chemoattractant molecules that may collectively act to limit OA-induced cartilage degeneration. [18] Despite these features, studies show that following intravenous injection, the majority of the MSCs accumulated in the lung, while only a small number of cells reached the degenerative defect site. [21] Even though an intraarticular injection of MSCs might avoid such an issue, new challenges arise, such as low cell retention and survival *in situ*, which in turn requires a large number of cells delivered by multiple injections to demonstrate efficacy. [22]

It was reported that formation of cell aggregates *in vitro* might be an effective method to retain cells *in situ* at a high cell viability. [23, 24] Moreover, in comparison with individual cells, cell aggregates have been shown to be capable of enhanced multi-lineage differentiation [25], produce extensive ECMs [26], and secrete growth factors for anti-inflammation and immunosuppression [27-30] and angiogenesis [31]. Although there are various methods to fabricate cell aggregates including spontaneous aggregation, substrate-mediated aggregation, and technology-assisted aggregation, formation of cell aggregates relies mainly on cell aggregation and/or cell proliferation with the influence of various factors in different combination including cell binding sites, stiffness, molecular hydration, anti-adsorption of

proteins, spatial confinement, and forces, such as gravity, centripetal force, centrifugal force, magnetic force, electrical force, and shear force. (Figure 2.1)

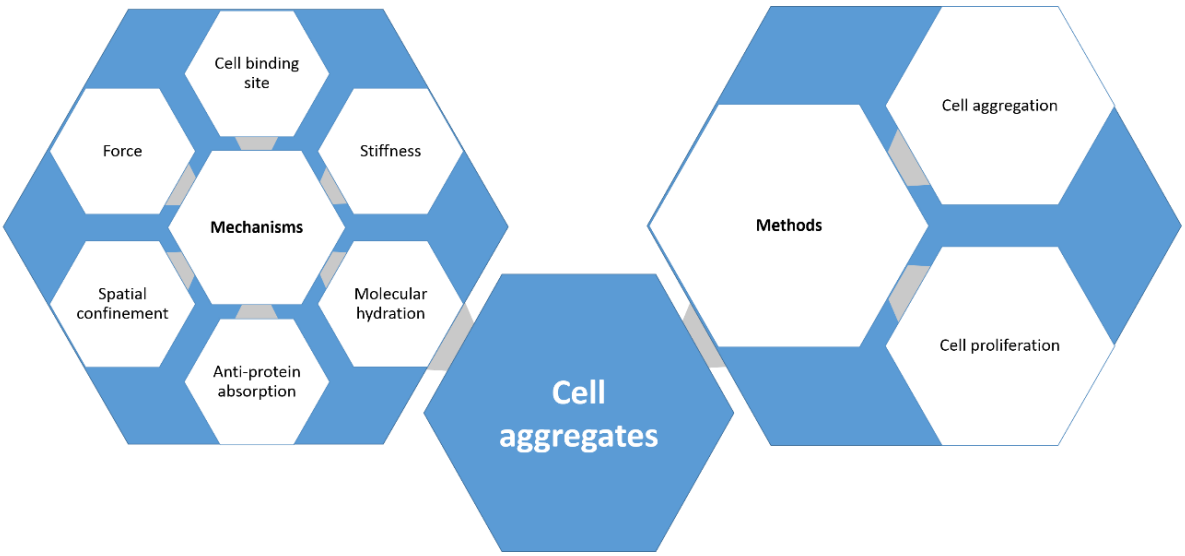

Figure 2.1 Underlying main mechanisms and methods for fabrication of cell aggregates.

2.2.2.1 Spontaneous aggregation-mediated fabrication of cell aggregates

When cell suspensions are added on a non-treated tissue culture plate in the absence of RGD cell binding peptides, individual cells settle down by intrinsic gravity facilitating cell-cell contact and interaction. To minimize surface free energy [32, 33], the individual cells tend to spontaneously aggregate together through surface proteins including cadherins [34], N-cadherin and 11-cadherin for bone marrow-derived MSCs (BMSCs) [35], and E-cadherin for umbilical cord-derived MSCs (UCMSCs) [36]. Such spontaneous aggregation is more evident in embryonic stem cells (ESCs) and induced pluripotent stem cells (iPSCs), which normally form embryoid bodies during morphogenesis. [37-39] Due to differences in cadherin and integrin expression on individual cells, cells with a higher density of cadherin, but a lower levels of integrin, may relocate to the centre of a cell aggregate, while cells with a lower levels of cadherin, but higher density of integrin expression relocate to the periphery. [40] Moreover, the production and accumulation of ECMs is also initiated by cell-cell contact, which may further stabilize the cell aggregates by regulating cell morphology: central with round cells but periphery with spindle-like cells. [41] In addition, the ECMs in the cell aggregates may also play an important role in transduction of biomechanical signals between the extracellular

surrounding environment and intracellular cytoskeletons for an optimal force balance. [42] However, since cell aggregation on the non-adherent plate is initiated by random amoeboid-like movement of the individual cells [33], size distribution of formed cell aggregates can be broad [43]. Previous reports suggest that the size of a cell aggregate is critical for its biological function, such as anti-inflammation [27], osteogenesis [43] and viability [43]. Therefore, spatial confinement, together with the non-adherent surface, is utilized for fabrication of uniform cell aggregation, such as hanging drops and v-96 well plates, in which a certain number of cells are restricted in a limited space and spontaneously aggregate into a single cell aggregate with a controllable size depending on the initial cell seeding density and the geometrical space configuration. [43] Moreover, mechanical force can also be introduced to accelerate cell-cell contacts and not rely on random amoeboid-like movement of cells, such as pellet culture in a polypropylene tube by centrifugal force [44] and agitating culture in a rotating bioreactor by shear force [45]. (Figure 2.2)

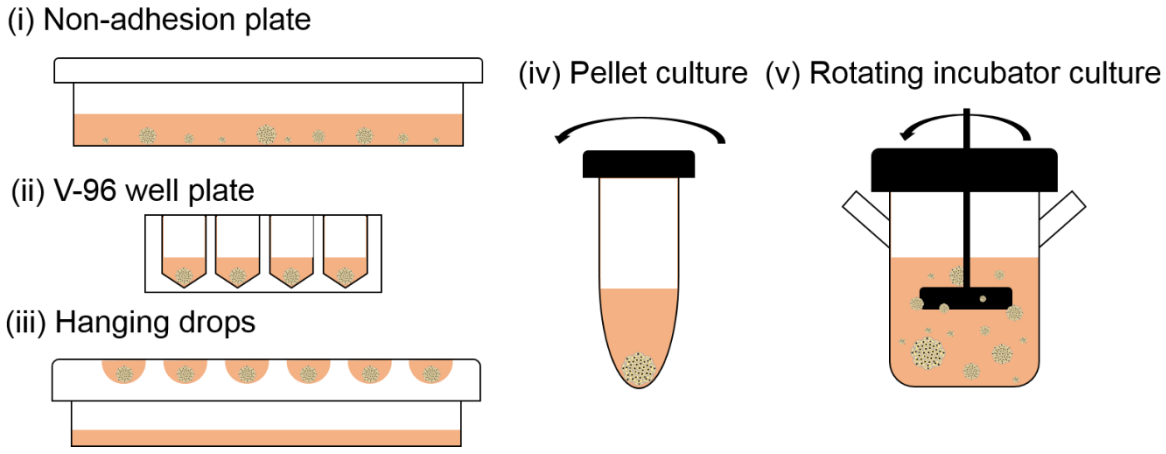

Figure 2.2 Spontaneous cell aggregation-mediated fabrication of cell aggregates by culturing cells (i) on a non-adhesion plate, or (ii) in a v-96 well plate, or (iii) hanging drops on the lid of a tissue culture plate, or (iv) as a pellet in a polypropylene tube, or (v) in a rotating incubator.

2.2.2.2 Substrate-mediated fabrication of cell aggregates

Cell aggregates can also be formed with the assistance of substrates in a two-dimensional (2D) or three-dimensional (3D) manner [46]. These substrates include chitosan-based membranes [47-49], hydrophilic polymer-coated surfaces which form hydrogen bonds to prevent adhesion of cells and adsorption of proteins [24, 49, 50], or thermo-sensitive polymer-coated surfaces

which thermally lift the attached cells, functionalizing as a brush to prevent the detached cells re-binding to the underlying RGD peptides [51, 52]. (Figure 2.3) Although there are already some published reviews summarizing substrate-mediated fabrication of cell aggregates and their mechanism [41, 46, 53, 54], none of publications comprehensively examine the impact of hydrogels on formation of cell aggregates. Therefore, the following review is a systematic examination of current published data which focuses on 2D and 3D hydrogel-mediated fabrication of cell aggregates including their mechanism and potential applications.

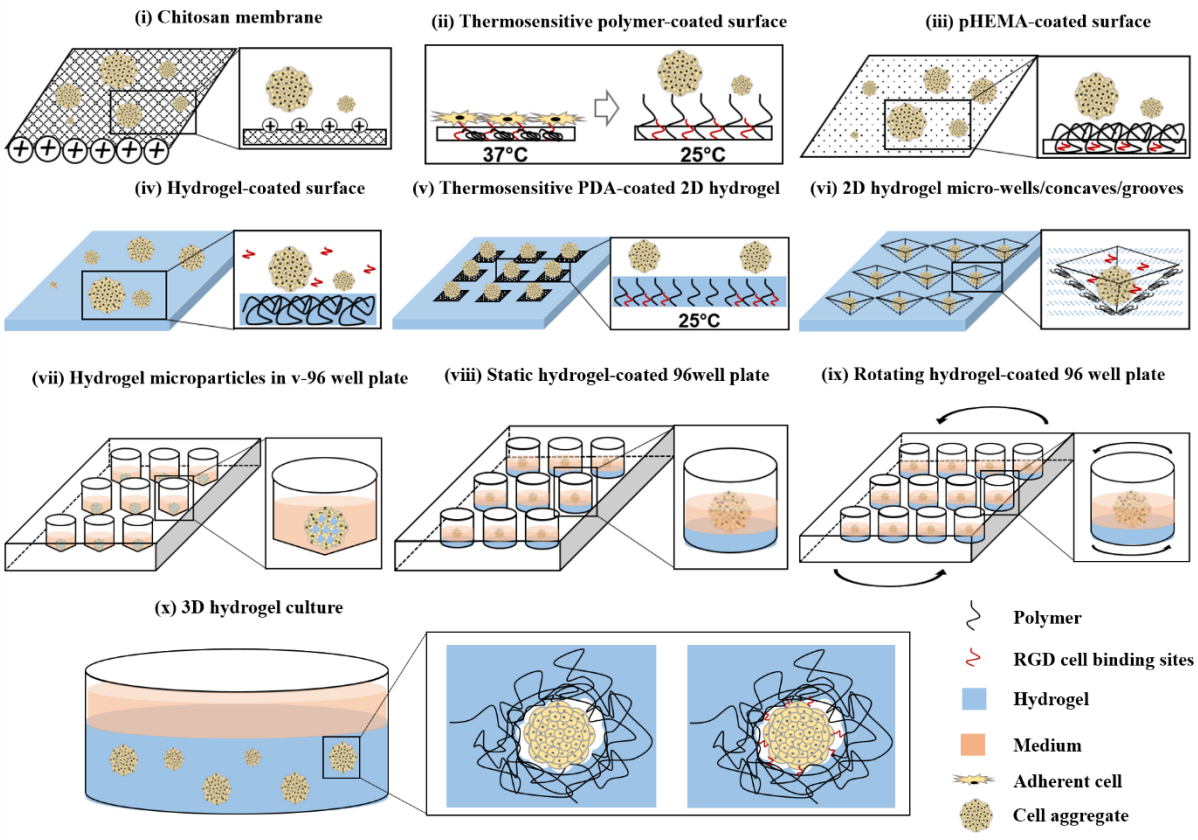

Figure 2.3 Substrate-mediated fabrication of cell aggregates by culturing cells (i) on the chitosan membrane, or (ii) on a thermo-sensitive polymer-coated surface and thermo-lifting for cell harvest, or (iii) on a Poly(2-hydroxyethyl methacrylate) (pHEMA)-coated surface, or (iv) on a hydrogel-coated surface, or (v) on thermo-sensitive 2D hydrogels with micro-patterned coating of polydopamine (PDA), or (vi) on 2D hydrogels micro-wells or concaves or grooves, or (vii) on hydrogel micro-particles in a v-96 well plate, or (viii) in a static hydrogel-coated 96 well plate, or (ix) in a rotating hydrogel-coated 96 well plate, or (x) in 3D hydrogels without (left) or with RGD cell binding sites (right).

2D hydrogel-mediated fabrication of cell aggregates

Hydrogels, rich in water, are widely utilized for cell culture and show promising results for fabrication of cell aggregates. When using as a 2D surface, the mechanism of cell aggregation

on the 2D hydrogels mainly depends on the absence of cell binding sites and inhibition of protein adsorption by molecular hydration (derivatives of alginate/ cellulose/ PEG) [55-64], or shielding of cell binding sites (aggregation of bone marrow homing peptide 1-bis linear self-assembling peptides (BMP1-bis$(LDLK)_3$) [65] or thermal expansion of Tetronic hydrogel [66]). Compared to single-cell-to-spheroids (STS) on non-adherent plates, micro-patterned cell-layer-to-spheroids (CLTS) constructed on a thermo-sensitive hydrogel, not only retain the produced ECMs but also preserve the integrin-mediated cell-ECMs interaction, which is essential for the formation and stabilization of cell aggregates. Different fabrication methods enable cell aggregates capable of distinct biological properties. [66] Besides, stiffness of 2D hydrogels can also play a role on the cell aggregation since both soft [65] and tough [55] hydrogels were previously reported to facilitate generation of cell aggregates, although the effect still needs to be further confirmed using the same hydrogel at various degrees of stiffness. Even though cells are bound to RGD peptides by initial cell-substrate interaction, cell aggregates could still be formed by subsequent cell-cell interaction caused by spatial confinement-mediated cell-cell contacts and substrate-mediated enhancement of cell proliferation. [67, 68] Introduction of spatial confinement [56-59, 69-71] and mechanical force [60, 61] can facilitate fabrication of uniform cell aggregates at an appropriate size with enhanced biological properties in the absence of a necrotic centre. (Figure 2.3) Details of 2D hydrogel-mediated fabrication of cell aggregates can be found in Table 2.1.

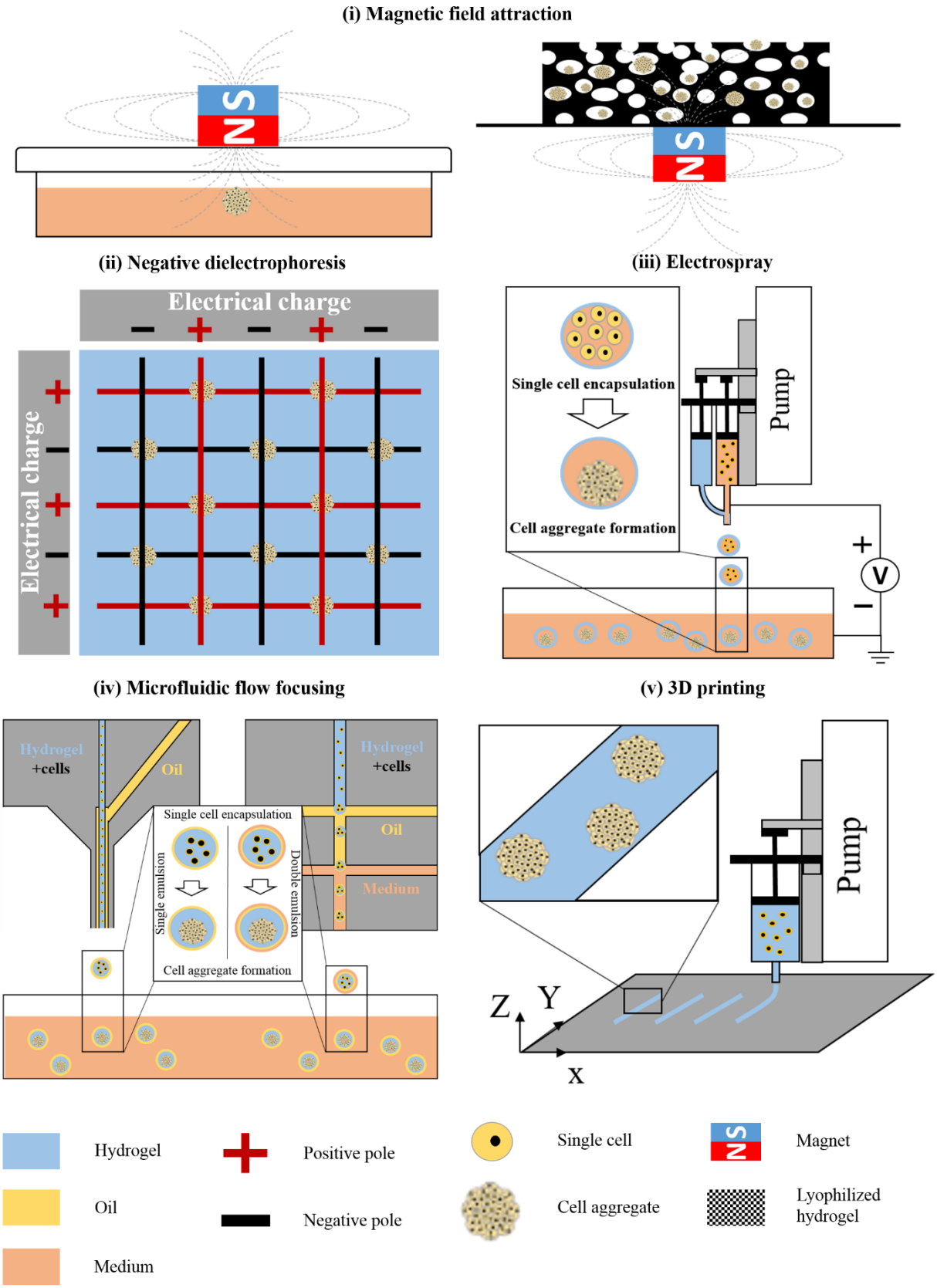

Figure 2.4 Technology-assisted fabrication of cell aggregates by (i) magnetic field attraction of cells at an air-liquid-interface (left) or in a porous scaffold (right), or (ii) negative dielectrophoresis of cells at a lower electric field in a photo-responsive hydrogel, (iii) encapsulating cells in hollow microgels using electrospray, or (iv) encapsulating cells in microgels with a core-shell structure using microfluidic flow-focusing single emulsion (left) or double emulsion (right), or (v) 3D printing cells in hydrogels.

Table 2.1 2D hydrogel-mediated fabrication of cell aggregates.

Material	Fabrication method	Special property	Type of cell	Size of cell aggregate	Result	Mechanism	Application	Ref.
Bone marrow homing peptide 1-bis linear self-assembling peptides (BMP1-bis$(LDLK)_3$)	Solid-phase Fmoc-based chemistry	Self-assembly	Human neural stem cells (hNSCs)	~100 μm in diameter	Compromised cell proliferation and poor neural differentiation markers (βIII tubulin for neuron, GFAP for astrocytes, GALC/O4 for oligodendrocytes)	Very short fragments or aggregation of nanofibers, and the soft mechanical strength induce cell aggregates	Not suitable for neural regeneration	[65]
Tetronic-tyramine	12 (w/v)% tetronic-tyramine hydrogel with an embossed surface (HES) was prepared and chemically crosslinked by 0.1 (v/v)% H_2O_2 and 0.0025 mg/m HRP on PDMS master molds with different surface roughness	N/A	hASCs	50-200 μm in diameter depending on cell seeding densities and surface roughness	Maintenance of cell stemness and multi-lineage differentiation capacity; enhanced of VEGF secretion compared to that in cell aggregates fabricated on commercial low attachment plates	Absence of cell binding sites and inhibition of protein adsorption by molecular hydration and spatial restriction of concaves on HES	Cell therapy and *in-vitro* tissue reconstructi on	[71]
Tetronic-tyramine and polydopamine	Conventional micro-contact printing (μCP) of polydopamine	Thermo-sensitive	Human turbinate mesenchyme stem cells (hTMSCs)	~100 μm in diameter	Higher expression of extracellular matrix (ECM) proteins	Expansion of thermo-sensitive hydrogels	3D cell culture and therapeutic cell delivery	[66]

	onto *in situ* gelation of end group-functional Tetronic hydrogel				(fibronectin and laminin) and stemness markers compared to that of spheroids generated by the low attachment surface; enhanced tri-lineage cell differentiation (osteogenesis, chondrogenesis, and adipogenesis).	when cooling leading to detachment of micro-patterned cell layers and simultaneous cell spheroid formation.	in regenerative medicine	
Gelatin	Water-in-oil method and sieve for fabrication and classification of gelatin micro-particles (GMPs)	N/A	Adipose-derived stem cells (ASCs)	Size increased as the number of incorporated GMPs increased and restricted by the size of the low-attachment concave well (< 200 µm in diameter)	Enhanced cell proliferation by increasing the surface of incorporated GMPs in the cell aggregates	Cell attached on the GMPs and aggregated on low-attachment concave wells	Development of cell spheroids for stem cell therapy and organoid production	[67]
Cellulose	Casting into films with cellulose solution (4 wt% in	N/A	Human adipose-derived stem cells (hASCs)	Size increased as an increase	Enhanced osteogenesis	Absence of cell binding sites and	Tissue engineering	[64]

	LiOH/urea aqueous solution)			in the cell seeding density and culture time		inhibition of protein adsorption by molecular hydration		
Agarose	Casting into micro-wells with a diameter of 200 μm and a depth of 220 μm	Thermo-sensitive	Human umbilical vein endothelial cells (HUVECs), human foreskin fibroblast (HFF), and adipose-derived mesenchymal stem cells (ASCs)	< 200 μm in diameter	Stable cell aggregates and enhanced angiogenesis for HUVECs/HFF/ASCs in a 1/9 cell ratio	Absence of cell binding sites and inhibition of protein adsorption by molecular hydration and spatial restriction of micro-wells	Used as pre-vascularized aggregate building blocks for engineering of large vascularized tissue by 3D printing	[69]
Amikagel	Ring-opening polymerization between amine groups of amikacin hydrates and epoxide groups of poly(ethylene glycol) diglycidyl ether (PEGDE)	N/A	human embryonic stem cell-derived pancreatic progenitor cells (hESC-PP) and HUVECs	Size increased as an increase in the cell seeding density (100-500 μm in diameter)	Enhanced pancreatic islet-specific gene and protein expression; increased the percentage of committed population; induced mature beta-like cells with increased specific gene and protein expression and functional insulin production; mature islet-specific gene	Absence of cell binding sites and inhibition of protein adsorption by molecular hydration and high stiffness	A platform for islet organoid engineering	[55]

					and protein expression when co-aggregating with endothelial cells			
Methacrylated alginate (OMA)/ multi-arm PEG	Schiff base reaction between OMA and 8-arm PEG for the first cross-linking; UV-initiated photopolymerization of OMA with photomasks for the second cross-linking	Photo-sensitive	hASCs	Defined sizes (such as 200 μm in diameter for osteogenesis)	Define cell spheroid sizes, maintain uniform size distribution, and enhanced osteogenesis	Absence of cell binding sites and inhibition of protein adsorption by molecular hydration and spatial restriction of micro-wells	*In-vitro* platform with defined signals for regulation of tissue formation	[56]
Methylcellulose (MC)	12 (wt/v)% solution MC was coated on the micro-well plate	N/A	Human cardiac progenitor cells (hCPCs)	Cell seeding density-dependent (~100 μm in diameter for 5000 cells seeding in 24 h)	Enhanced stemness and growth factor secretion; enhanced cell engraftment and retention	Absence of cell binding sites and inhibition of protein adsorption by molecular hydration and spatial restriction of micro-wells	Cell therapy for myocardium injury	[70]
PEGDA	A concave structure fabricated by dynamic optical projection	Photo-sensitive	hiPSCs	155 μm in diameter with a seeding density of	Maintenance of pluripotency on day 3 while spontaneous	Absence of cell binding sites and inhibition of protein	*In-vitro* embryogenesis and patient-derived	[57]

	stereolithography and UV-initiated polymerization			100 k cells/mL in 3 days	differentiation in 10 days	adsorption by molecular hydration and spatial restriction of concaves	disease modelling with iPSC EBs	
PEG-methacrylated gelatin (GelMA)-HA	UV-initiated photopolymerization of precursor solution (20 (wt/v)% PEGDMA, 10 (wt/v)%GelMA, and 0.1 (wt/v)% thiol-modified HA) with the assistance of a nanopatterned polyurethane acrylate (PUA) mold (ridge × groove × height: 800×800×500 nm)	Photo-sensitive	Dental pulp stem cells (DPSCs)	~100 μm in diameter	Enhanced cell chondrogenesis	Possibly due to RGD-mediated initial cell-scaffold contact and subsequent cell-cell contact in addition to spatial restriction of grooves	Cartilage tissue engineering	[68]
PEG	Micro-well (600 μm in diameter) fabrication by soft lithography (UV-initiated polymerization)	Photo-sensitive	ADSCs	~291 μm in diameter on day 5	Enhanced cell chondrogenesis	Absence of cell binding sites and inhibition of protein adsorption by molecular hydration and spatial	Cartilage tissue engineering	[58]

						restriction of micro-wells		
PEG	Micro-well (150 and 450 µm in diameter) fabrication by soft lithography (UV-initiated polymerization)	Photo-sensitive	mESCs	Micro-well-dependent, and size increased in the PEG hydrogel but stable in the RGD-modified PEG hydrogel	Enhanced cardiogenesis and endothelial lineage differentiation in the PEG hydrogel and enhanced endothelial lineage differentiation in the RGD-modified PEG hydrogel	Absence of cell binding sites and inhibition of protein adsorption by molecular hydration and spatial restriction of micro-wells	Tissue engineering	[59]
Methylcellulose (MC) hydrogel	N/A	Thermo-sensitive	Human umbilical vein endothelial cells (HUVECs) and cord-blood mesenchymal stem cells (cbMSCs)	100-300 µm in diameter dependent on the cell seeding density and rotary speed	Enhanced angiogenic gene expression	Absence of cell binding sites and inhibition of protein adsorption by molecular hydration; increased cell-cell contact caused by rotating-induced centripetal force. A too higher rotary speed constricted	Vascularization	[60, 61]

						cell aggregation		
Methylcellulose (MC)	12 (wt/v)% MC in hot phosphate buffered saline	Thermo-sensitive	mBMSCs	~200 µm in diameter in 24 h	Improved cell retention and integration *in vivo*	Absence of cell binding sites and inhibition of protein adsorption by molecular hydration	Cell therapy	[62]
HA	Micro-well (40-200 µm in diameter, 50 µm in depth) fabrication by soft lithography (UV-initiated polymerization)	Photo-sensitive	mESCs	Dependent on cave size and initial cell seeding density; double in size in one week	High cell viability	Absence of cell binding sites and inhibition of protein adsorption by molecular hydration	*In-vitro* cell study	[63]

3D hydrogel-mediated fabrication of cell aggregates

Generation of cell aggregates in a 2D manner is mainly used for cell study *in vitro*, as additional harvest processes may be required for application *in vivo*. Ho et al. recently reported robust bone formation using a two-step process of fabricating bone marrow-derived mesenchymal stem/stromal cell (BMSC) aggregates with hanging drops and embedding in RGD-modified alginate hydrogels for subcutaneous implantation *in vivo*. [72] Similarly, Oltolina et al. fabricated cardiac progenitor cell aggregates on methylcellulose (MC) hydrogel-coated micro-wells *in vitro* and subsequently implanted the cell aggregates into injured myocardium *in vivo*, and showed enhanced cell engraftment and retention. [70] Huang et al. also reported restoration of blood fusion and rescuing tissues from degeneration when human umbilical vein endothelial cells (HUVEC)-MSC hybrid cell aggregates were fabricated on MC coated micro-wells and implanted to ischemic hindlimbs *in vivo*. [60, 61] Hence, *in-situ* formation of cell aggregates in 3D hydrogels may represent an "easy-to-use method" for *in-vitro* and *in-vivo* applications. (Figure 2.3) When entrapping cells in 3D hydrogels that lack cell binding sites, cell aggregation is induced by a molecular hydration process that serves to prohibit adsorption of proteins and spatial restriction of internal pores. [25, 73-81] In softer hydrogels, with a relatively higher interconnectivity, cells have a high likelihood of encountering each other, thereby forming cell-cell contacts by amoeboid movement. [82, 83] It was also reported that the size of cell aggregates increased in 3D hydrogels of decreasing mechanical strength. [84, 85] When RGD peptides or other ECMs were incorporated by either physical blending or chemical bonding, the entrapped cells were able to attach to hydrogels and migrate in a more efficient manner, mesenchymal migration. [85-89] Initial cell-substrate interactions, together with spatial confinement, could also lead to an increase of cell-cell contacts and cell aggregation. [84, 86-88, 90-92] Enhancement of cell proliferation, by innate properties of hydrogels, might predominate or coordinate cell aggregation during formation of cell aggregates. [39, 81, 86, 87, 93, 94] Organization of an internal structure [78] and hydrolysis of hydrogels [88] have also

been found to contribute to the formation of cell aggregates. It is notable that most of 3D hydrogels used for fabrication of cell aggregates belong to smart materials which can respond to external stimuli, such as thermo-sensitive hydrogels that are able to reversibly respond to a change in the external temperature [25, 39, 73, 78, 79, 86, 90, 92] or photo-sensitive hydrogels that are responsive to light radiation [76, 84, 94, 95]. Such properties enable wide applications of 3D hydrogels for fabrication of cell aggregates both *in vitro* and *in vivo*. While fusion of cell aggregates might be not desirable for an *in-vitro* cell study [43], such as drug screening [96], it is normally necessary for both *in-vitro* and *in-vivo* tissue engineering or regenerative medicine purposes [46, 97], especially scaffold-free tissue engineering [98-100]. Previous reports suggest that cell aggregates can enhance ECMs production. [26, 31, 101] The accumulation and preservation of these ECMs bridge cell aggregates in the 3D hydrogels and assist in the fusion of cell aggregates. [25, 46, 84] Lin et al. recently reported that the fusion ratio of differentiated cell aggregates tended to be lower than that of cell aggregates without induction, indicating the importance of the sequencing of both the multi-aggregation and cell differentiation steps during engineered tissue preparation. [79] By varying the properties of 3D hydrogels, such as stiffness, the fusion process can be well controlled for *in-vivo* applications and may be applicable for long-term cell aggregate culture *in vitro*. [41, 84, 85] For *in-vitro* applications, 3D hydrogels can mimic the *in-vivo* tumour microenvironment and serve as a platform for studies of the impact of individual factors on tumorigenesis, as demonstrated in pancreatic cancer cells [102, 103], prostate cancer stem cells [104, 105], and breast cancer cells [106]. Details of 3D hydrogel-mediated fabrication of cell aggregates are presented in Table 2.2.

2.2.2.3 Technology-assisted fabrication of cell aggregates

However, depending on the stiffness and interconnectivity of hydrogels, it can take more time to fabricate cell aggregates in the 3D hydrogels compared to 2D substrates. To overcome the limitation, some technologies have been developed to increase cell-cell contact by magnetic force [107, 108], electrical force [95], spatial confinement, such as microfluidic flow focusing

[81, 109, 110], electrospray [104], and 3D printing [39, 86, 111]. (Figure 2.4) Details of technology-assisted fabrication of cell aggregates for 2D and 3D hydrogels are described in Table 2.1 and 2.2.

Table 2.2 3D hydrogel-mediated fabrication of cell aggregates.

Material	Fabrication method	Special property	Culture method	Type of cell	Size of cell aggregate	Result	Mechanism	Application	Ref.
Poly (*N*-isopropylacrylamide-co-acrylic acid)	Free radical polymerization	Thermo-sensitive	3D casting culture	Human bone-derived mesenchymal stem/stromal cells (MSCs) and cell line	~100 μm in diameter	Quiescence of cell proliferation but up-regulation of cell chondrogenesis, osteogenesis, and adipogenesis *in vitro*	Spatial restriction and amoeboid cell migration and absence of cell binding sites led to initial cell aggregation, while ECMs accumulation and low mechanical strength of hydrogels facilitated fusion of cell aggregates by ECMs-mediated mesenchymal migration	A platform for studying cell differentiation *in vitro* or implantation of the pre-differentiated cells for tissue regeneration	[25]
Icariin-hyaluronic acid-collagen type I	Free radical polymerization	Thermo-sensitive	3D casting culture	Rabbit bone marrow-derived MSCs	N/A	Enhanced cell chondrogenesis and osteogenesis *in vitro* and osteochondral regeneration *in vivo*	Initial cell-substrate interaction induced subsequent N-cadherin-mediated cell-cell interaction	Osteochondral regeneration	[90]
Hydroxypropyl chitin (HPCH) and Matrigel	Etherification of hydroxyl groups of chitin with propylene oxide in aqueous	Thermo-sensitive	3D printing culture	Human induced pluripotent stem cells (hiPSCs)	Size increased as the concentration of HPCH or Matrigel increased (100-600	Higher concentration of Matrigel leading to cell proliferation competitive to static suspension culture; a higher	A higher concentration of HPCH and a lower concentration of Matrigel impeded cell migration and induced cell proliferation-predominated formation of cell aggregates; A	Scalable expansion of hiPSCs	[86]

	NaOH/urea solution			reprogrammed from human peripheral blood mononuclear cells (hPBMCs)	µm in diameter)	concentration of HPCH but a lower concentration of Matrigel leading to more uniform size distribution of cell aggregates; formation of cell aggregates inducing spontaneous cell differentiation	lower concentration of HPCH and a higher concentration of Matrigel led to the formation of cell aggregates because of a synergy of cell proliferation and cell aggregation.		
Poly(ethylene glycol)-poly(propylene glycol)-poly(ethylene glycol)-pyridine-1,5-dicarboxylate (PEG-PPG-PEG-PDC)	Coupling reaction between PEG-PPG-PEG and PDC	Thermo-sensitive	3D casting culture	Human tonsil-derived mesenchyme stem cells (TMSCs)	200 µm in diameter	Higher expression of stemness, angiogenic, and anti-inflammatory biomarkers; enhanced multi-lineage differentiation	Spatial restriction and low mechanical strength of the hydrogel and absence of cell binding sites	Injectable 3D cell scaffolds for stem cell therapy	[73]
Poly (L-glutamic acid) (PLGA)	Activation with 1-ethyl-3-(3-dimethylaminopropyl) carbodiimide	N/A	3D casting culture	hASCs	Size increased as an increase of the cell seeding density (<	Enhanced angiogenesis and adipogenesis	Spatial restriction and absence of cell binding sites; swollen effect of PLGA hydrogel outweighed the charge	Vascularized adipose tissue engineering	[74]

	hydrochloride (EDC) and crosslinking with adipic dihydrazide (ADH)				200 μm in diameter)		effect on adsorption of adhesive protein		
Bisphosphonate-grafted hyaluronic acid (HA-BP), acrylated bisphosphonate (Ac-BP), magnesium chloride ($MgCl_2$)	Self-assembled nanocomposite hydrogel formation in 20 min with 2 (w/v)% HA-BP, 0.25 M Ac-BP (conjugated with 0.002 M RGD peptide (GCGYGRGDSPG)), and 0.25 M $MgCl_2$	Thixotropic	3D casting culture	hMSCs	~100 μm in diameter	Enhanced cell proliferation and osteogenesis	Spatial restriction and low mechanical strength of the hydrogel and absence of cell binding sites	Application of cell spheroids: N/A; hydrogel application: 3D matrix on cell behaviour and biological process	[75]
Methacrylated hyaluronic acid (Me-HA)	Photopolymerization of hyaluronic acid and methacrylic anhydride	Photo-sensitive	3D casting culture	hiPSCs-derived neural progenitor cells (hiPSC-NPCs)	A larger size in soft hydrogels than stiff hydrogels (mainly distributed at a range of ~100 μm^2 in area)	Enhanced neural differentiation and robust neurite outgrowth in soft hydrogels	Spatial restriction and low mechanical strength of the hydrogel and absence of cell binding sites	3D model for central nervous system (CNS) disease study	[76]

PLGA	PLGA solution dissolved in dimethyl sulfoxide (DMSO) crosslinked with oligo(ethylene glycol)s (OEGs) and lyophilized at -20 °C, -80 °C, or -196 °C	N/A	3D casting culture	hASCs	Size increased as an increase in the culture time (< 200 μm in diameter)	Enhanced angiogenesis	OEGs increased the hydration of PLGA hydrogels and impeded protein adsorption on the polymer material leading to low cell attachment	Bone and fat tissue engineering	[77]
Methoxypolyethylene glycol-poly(alanine) (mPEG-PA)	Ring-opening polymerization of N-carboxyanhydride (NCA) form of L-alanine using amine-terminated mPEG	Thermo-sensitive	3D casting culture	Rabbit chondrocytes	Size increased as an increase in the culture time	Enhanced chondrogenesis	Absence of cell binding sites in the hydrogel; low wettability of β-sheet packed fibers; a narrow space increasing cell-cell interaction; hydration preventing protein adsorption	Cartilage tissue engineering	[78]
RGD peptide ((glycine)4–arginine–glycine–aspartic acid–serine–proline)-	RGD-modified alginate was crosslinked with calcium sulfate solution	N/A	3D casting culture	Mouse chondrocyte cell line (ATDC5)	<50 μm in diameter	Enhanced chondrogenesis	RGD peptides-mediated cell-substrate interaction induced subsequent N-cadherin-mediated cell-cell interaction	Cartilage tissue engineering	[91]

modified alginate									
PNIPAAm-PEG	N/A	Thermo-sensitive	3D casting culture	hiPSCs and hESCs	~100 μm in diameter	Enhanced differentiation of cortical and midbrain dopaminergic neurons	Spatial restriction and low mechanical strength of the hydrogel and absence of cell binding sites	Bio-fabrication of neural tissues	[79]
Poly(ethylene glycol)-poly(L-alanine)-poly(L-aspartate) (PEG−PA−PD), kartogenin (KGN), and arginylglycylaspartic acid (RGD) coated layered double hydroxides (LDHs)	Ring-opening polymerization of N-carboxyanhydride (NCA) form of L-alanine (NCA-A) and 4-benzyl-L-aspartate (NCA-Dz) using amine-terminated mPEG	Thermo-sensitive	3D casting culture	TMSCs	< 100 μm in diameter	Enhanced chondrogenesis	RGD peptides-mediated cell-substrate interaction induced subsequent N-cadherin-mediated cell-cell interaction	Injectable system for stem cell-based tissue engineering and therapy	[92]
PLGA/chitosan (CS) for the top layer, and PLGA-graft-	Surface-initiated ring-open polymerization for PLGA-graft-	N/A	3D casting culture	Rabbit ASCs	80-100 μm in diameter	Enhanced chondrogenesis	Swollen effect of PLGA hydrogels outweighed the charge effect on adsorption of adhesive protein	Osteochondral regeneration	[80]

hydroxyapatite/CS/PLGA for the bottom layer	hydroxyapatite synthesis; ion crosslinking between PLGA-graft-hydroxyapatite, CS, and PLGA; chemical bonding between PLGA and CS by EDC and N-hydroxysuccinimide (NHS); lyophilization at -80 °C								
Heparin-PEG with FGF-2 and Nodal	Michael-type addition reaction by microfluidic flow focusing with gelation	N/A	3D encapsulation culture	mESCs	~200 μm in diameter	Enhanced endodermal differentiation with the affinity of growth factors to the heparin microgel	Spatial restriction and cell proliferation and absence of cell binding sites	Scalable platform for general embryoid body (EB)-based differentiation or development of tailored cell delivery vehicles	[81]

HA	Initially rapid thiol/acrylate reaction (Michael-type addition reaction) and the subsequently slow sulfhydryl oxidation	N/A	3D casting culture	Human Primary salivary stem/progenitor cells (hS/PCs)	~50 µm in diameter	Formation of an acini structure	Spatial restriction and absence of cell binding sites; slow kinetics of disulfide bond formation and a high degree of gel swelling permitted cell proliferation in the hydrogel for formation of the acini structure	Engineering of a functional implantable salivary gland	[93]
Collagen I-HA-RGD	Michael-type addition for functionalization of 8-arm-PEG with RGD, collagen I, or HA; UV-initiated photo-polymerization for the second binding of the remaining double-bond groups in 8-arm-PEG	Photo-sensitive	3D casting culture	Chondroprogenitor cells ATDC5	Size increased during culture (< 50 µm in diameter after 24 h; ~100 µm in diameter in 14 days)	Enhanced chondrogenesis	Initial cell-substrate interaction induced subsequent N-cadherin-mediated cell-cell interaction; low mechanical strength of hydrogels	*in-vitro* platform for study the influence of matrix physiological properties on limb-bud condensation and chondrogenesis	[84]
Gelatin/alginate	15 (wt/v)% gelatin and 4 (wt/v)% alginate in 0.5 (wt/v)% sodium	Thermo-sensitive	3D printing culture	mESCs	Size increased during cell culture (50 µm and 110 µm in	Enhanced cell proliferation and maintenance of pluripotency	Cell proliferation-mediated formation of cell spheroids instead of cell aggregation	High-throughput ESC expansion and size-controllable	[39]

	chloride solution; gel formation when cooling the gelatin solution and structure maintenance after calcium ionic crosslinking				diameter on day 3 and 7, respectively); reduction in the uniformity of EBs but little influence on the average EB size with an increase in the cell seeding density			EB production	
HA	UV-initiated photopolymerization and leaching of gelatin microspheres (0.35 g/mL, 150-200 µm in diameter)	Photo-sensitive	3D casting culture	Porcine chondrocytes	150-200 µm in diameter	Enhanced cell proliferation and chondrogenesis	Cell proliferation and spatial restriction and absence of RGD binding sites	Tissue engineering application	[94]
RGD peptide ((glycine)4-arginine-glycine-aspartic acid-serine-	Carbodiimide chemistry for grafting RGD into alginate and crosslinking	N/A	3D casting culture	hMSCs	Size increased with an increase in the cell seeding density	Enhanced collagen deposition and osteogenesis but impeded cell proliferation	Cell migration-mediated cell-cell contact and aggregation instead of cell proliferation in addition to enhanced hydrolysis of hydrogels in	Building blocks for tissue engineering with hMSCs-	[88]

proline)-grafted alginate	with calcium ions						osteogenic induction medium	ECM microtissues	
Nanofibrillar cellulose (NFC) and HA-gelatin-PEGDA (HG)	Michael-type addition reaction	N/A	3D casting culture	HepaRG liver progenitor cells	40 µm in diameter in one week	Enhanced expression of hepatocyte markers, metabolic activity, and formation of bile duct compartment in the core of cell aggregates	N/A	Hepatic cell culture for drug and chemical testing and tissue engineering	[112]
RGD-modified alginate hydrogel	Aqueous carbodiimide chemistry	N/A	3D casting culture	hMSCs	A large cell aggregate	Enhanced cell proliferation and osteogenesis	Stiffness and RGD-mediated cell migration in addition to cell proliferation at the early stage and fibronectin fibril assembly and actin stress fiber formation at the later stage	Tissue engineering	[87]
Gelatin with methacrylic anhydride (GelMA)	Negative-dielectrophoresis (n-DEP) and UV-initiated photopolymerization	Photo-sensitive	3D casting culture	ESCs	50 to 300 µm in diameter in 6 min (size increased by increasing the distance	Enhanced cell differentiation	Cells were driven by electrical force to accumulate *in situ* within the GelMA hydrogel after photopolymerization.	Cell therapy and tissue regeneration	[95]

					of the band electrode)				
Alginate or RGD-modified alginate	Cell encapsulation by water-in-oil-in-water double emulsion (DE) microfluidic flow focusing without gelation step	N/A	3D encapsulation culture	hMSCs	30-80 μm in diameter in 150 min	Enhanced cell osteogenesis	Spatial restriction of the oil shell and the hydrophilic end of the surfactant (Pico-Surf) prevented cell adhesion	Microscale tissue engineering	[109]

2.2.3 Scaffold-based therapy for treatment of OA

To mimic the ECM-cell interactions found *in-vivo*, fabricated scaffolds generally need to be biocompatible with no demonstrable cytotoxicity and porous for efficient mass and gas exchange. [113] When fabricated scaffolds are applied in the context of tissue regeneration *in vivo*, the biodegradability of the scaffold should be addressed. [114] Furthermore, the influence of fabricated scaffolds on proliferation and differentiation of stem cells are also of great interest for cartilage and bone tissue engineering. Studies have revealed that in addition to stiffness, scaffold topography, such as fiber size and orientation, can also regulate the fate of stem cells. [115-119] In addition to simply providing structural support for stem cell proliferation, studies are now focusing on active control of scaffolds/hydrogels for regulation of stem cell behaviour. [120] Smart materials can respond to external stimuli, such as temperature change, light illumination, stress change, or an external dynamic magnetic field, variation in 3D organization or stiffness, or occurrence of mechanical movement, heat, or electricity. [121-123] The responsive behaviour of smart materials can, therefore, be used to regulate the fate of stem cells.

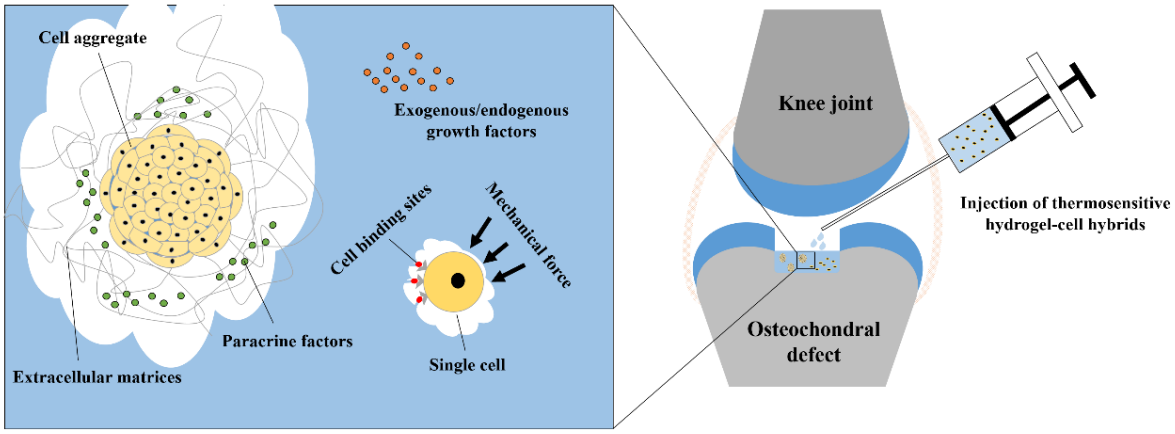

Figure 2.5 Injectable thermo-sensitive hydrogels as a vehicle for delivering cells and/or exogenous growth factors for bone and cartilage tissue engineering. Thermo-sensitive hydrogels form gel in situ after implantation to retain cells at the defect sites. The fate of stem cells can be regulated by physical and biochemical stimuli in vivo. Some thermo-sensitive hydrogels can induce formation of cell aggregates in situ, which advances the healing process.

2.2.3.1 Thermo-responsive materials

Thermo-responsive materials are one category of smart materials that can respond to a temperature change. For example, when the temperature is above the lower critical solution temperature (LCST) or below the upper critical solution temperature (UCST) the hydrogel will form. Moreover, the hydrogel can also be liquefied when temperature is out of the gelation range. As the formation of hydrogels depends mainly on hydrophobic repulsion and/or physically ionic crosslinking, thermo-sensitive behaviour of hydrogels is often reversible. [121] Thermo-responsive hydrogels are widely used as a two-dimensional form for generation of cell spheroids [66] or cell sheets [124-126], which can be easily harvested and utilized as building blocks for tissue engineering or 3D printing *in vitro* [69], or directly implanted for tissue regeneration *in vivo* [62, 127]. Furthermore, thermo-responsive hydrogels have been extensively used as a 3D *in-vitro* platform for stem cell differentiation or a delivery vehicle for *in-vivo* injection of cells and/or bio-reagents into tissue defect sites. Importantly, as tissue defects are often irregular in size and structure, thermo-responsive hydrogels are able to completely fill the defect by *in situ* gelation, which may lead to better tissue regeneration. [128] The retention of implanted stem cells in the context of a thermosensitive hydrogel serves to both enhance their survival and facilitate cell differentiation *in situ.* Furthermore, the hydrogel-cell hybrids allows the cells to be exposed to *in-vivo* mechanical stress and a complex milieu of biomolecules, which promote tissue regeneration adopts normal function. [4, 121, 129-131] (Figure 2.5) The encapsulated stem cells can also be differentiated into specific cell lineages by intrinsic properties of thermo-responsive hydrogels, such as stiffness of poly(*N*-vinylcaprolactam) (PNVCL) hydrogels [132], or conjugation of peptides in poly(ethylene glycol)-b-poly(L-alanine) (PEG-L-PA) hydrogel and RGD peptides-modified poly(organophosphazene) hydrogels [133, 134], or incorporation of biomolecules, such as TGF- β3 in PNIPAAm-co-AAc hydrogels [135]. Thermo-responsive hydrogels, when applied as an injectable vehicle for non-invasive implantation of stem cells *in vivo,* can facilitate self-

assembly of cell aggregates *in situ*. This approach provides the optimal strategy for tissue regeneration owing to the enhanced function of mesenchymal stem/stromal cell aggregates, such as immunomodulation and multi-lineage differentiation. [90] Compared to thermo-responsive hydrogels, thermo-responsive scaffolds are rarely used for application in tissue engineering. [136-138] Maeda et al. recently fabricated a thermo-responsive scaffold by electrospinning poly (*N*-isopropylacrylamide) into nanofibers for cell storage application. [137] Compared to casted thin films, thermo-responsive shrinkage and dissolution of electrospun scaffolds are much quicker and more sensitive. The unique thermo-sensitive property of these electrospun scaffolds could be used for the fabrication of cell aggregates with a controllable size by simply capturing a certain number of cells in the shrunk poly (*N*-isopropylacrylamide) scaffolds at a pre-defined size at 37℃. In these circumstances, the cells are forced into cell aggregates due to absence of cell binding sites in poly (*N*-isopropylacrylamide) scaffolds and confined space- and force- mediated cell-cell interaction. After formation, uniform cell aggregates are able to be released from the thermo-responsive scaffolds at room temperature. The harvested cell aggregates, with a controllable size and uniform distribution, can be used for bone and cartilage tissue engineering. Details of thermo-responsive hydrogels for bone and cartilage tissue engineering can be found in Table 2.3.

Table 2.3 Thermo-responsive hydrogels for cartilage and bone tissue engineering.

Material	Assisted crosslinking method	Biodegradability	Thermo-sensitive behaviour	Dimension	Stem cell type	Differentiation type	Application	Ref.
2.5 wt.% chitosan and 1 wt.% gelatin+Sr	Ionic crosslinking of beta glycerophosphate (β-GP)	Degradable	Sol-gel transition at 36 ℃	3D	Human exfoliated deciduous teeth (SHEDs) MSCs	Osteogenesis	Bone regeneration	[139]
12 mg/mL chitosan and 4 mg/mL hydroxyethyl cellulose (CH-HEC)	Ironic crosslinking of β-GP and covalent crosslinking of glyoxal	Degradable	Sol under 37 ℃ and gel above 37 ℃ for 20 min	3D	Human and rat BMSCs	Chondrogenesis	Cartilage regeneration	[140]
Poly(ethylene glycol)-b-poly(L-alanine) (PEG-L-PA)	/	Degradable	Ion concentration -dependent	3D	ASCs	Chondrogenesis	Cartilage regeneration	[133]
Zinc-doped chitosan/nanohydroxypatite/beta-glycerophosphate (Zn-CS/nHAp/ β-GP)	Ionic crosslinking of β-GP	Degradable	Sol at 4 ℃ and gel at 37 ℃	3D	mMSCs	Osteogenesis	Bone regeneration	[141]
PNIPAAm-co-AAc with TGF- β3	/	No	/	3D	hBMSCs	Chondrogenesis	Cartilage engineering	[135]
Tetronic-tyramine with fibronectin or RGD	/	No	Sol at 4 ℃ and gel at 37 ℃	2D	hMSCs	Osteogenesis and adipogenesis	Cell patch	[124]

Poly(organophosphazene)-RGD	/	Degradable	Sol-gel transition at 37 ℃	3D	Rabbit MSCs	Osteogenesis	Bone tissue engineering	[134]
Poly(*N*-vinylcaprolactam) (PNVCL)	/	No	Molecular weight-dependent (higher molecular weight decreased LCST from 34℃ to 32℃)	3D	hMSCs	Chondrogenesis	Cartilage tissue engineering	[132]
Collagen I and agarose (low gelation temperature)	/	Degradable	Sol-gel transition at 28°C for agarose and 25.9°C after addition of collagen I	3D	hBMSCs	Osteogenesis	3D printing for bone tissue engineering	[142]
3% chitosan and 0.5 M β-GP	Ionic crosslinking of β-GP	Degradable	Gel at 42°C for 10 min	3D	hBMSCs	Nucleus pulposus (NP) cell differentiation;chondrogenesis	Intervertebral disc (IVD) regeneration	[143]
Poly(*N*-isopropylacrylamide-co-acrylic acid) and hydroxyapatite and bone morphogenic protein-2 (BMP-2)	/	No	Sol-gel transition at 37 ℃	3D	Rabbit BMSCs	Osteogenesis	Bone tissue engineering	[144]

2.2.3.2 Magnetic field-responsive materials

Magnetic field-responsive materials are another category of smart materials that can respond to an external magnetic field by either deformation of their initial structures or emission of heat. The magnetic field-responsive behaviour of a scaffold/hydrogel relies on the embedding within, or surface coating of magnetic nanoparticles by either electrospinning, dipping, or layer-by-layer assembly. [145-152]

Influence of magnetic field on fate of MSCs

The cell membrane consists of many ion channels which are responsible for maintenance of the membrane potential. External stimuli are recognised and transferred into intracellular electrical signals by influx or efflux of ions to mediate a change in the membrane potential. It is well known that a magnetic field can remotely influence ionic fluid across the cell membrane and change membrane potential in a non-invasive manner, resulting in an intracellular biological change. [153] Accordingly, the influence of magnetic field on stem cell fate has been extensively studied. For example, a study by Kim et al. showed that proliferation and osteogenic differentiation of human bone marrow-derived mesenchymal stem/stromal cells could be regulated by a magnetic field, with magnetic fields of an intensity of 15 mT showing superior performance in cell proliferation and osteogenesis compared to 3 mT and 50 mT. [154] Moreover, electromagnetic field with a magnetization of 1.6 mT and a frequency of 50 Hz, but not 25 Hz, for 8 h per day over a period of 21 days, was able to stimulate chondrogenesis in the absence of TGF-β1. [155] Furthermore, Parate et al. recently showed that chondrogenesis could be stimulated with a single pulsed electromagnetic field with a frequency of 15 Hz and a magnetization of 2 mT for 10 min. [156] These studies revealed that the influence of a magnetic field on the fate of stem cell differentiation and proliferation depends on several parameters including magnetization and frequency of a pulsed electromagnetic, time and frequency of exposure. Details of the influence of a magnetic field on fate of MSCs can be found in Table 2.4.

Table 2.4 Influence of magnetic field on fate of MSCs.

Type	State	Intensity	Frequency	Cell source	Influence of biological functions	Mechanism	Application	Ref.
Electromagnetic field (EMF)	Pulsed	2 mT	75 Hz	hBMSCs	Impeded cell proliferation but enhanced osteogenesis with mRNA expression and protein secretion of ALP, collagen I, osteocalcin, and osteopontin	A pulsed electromagnetic field interfered with calcium-dependent osteogenic pathways	Bone tissue engineering	[157]
Electromagnetic field	Pulsed	2 mT	15 Hz, 10 min once	hBMSCs	*In vitro* test: enhanced chondrogenesis with mRNA expression of SOX9, Col II, and aggrecan; quantification of collagen II and sulfated GAGs; immunohistochemical staining for collagen II and Safranin O staining for sulfated GAGs	A pulsed electromagnetic field triggered initial influx of calcium, resulting in enhanced cell chondrogenesis	Cartilage tissue engineering	[156]
Electromagnetic field	Pulsed	1 mT	15 Hz, 8 h/day	Rat BMSCs	*In vitro* test: enhanced cell osteogenesis with mRNA and protein expression of RUNX2, BMP-2, and osteocalcin; quantification of ALP activity	An electromagnetic field enhanced cell osteogenesis by extracellular signals which regulated kinase (ERK)1/2 and protein kinase A (PKA) and mitogen-activated protein kinase (MAPK) related signaling pathways	N/A	[158]

Electromagnetic field	Pulsed	1.6 mT	25 Hz and 50 Hz, 8 h/day	Rabbit ASCs	*In vitro* test: biocompatible and enhanced cell chondrogenesis with mRNA expression of Col II (similar impact of 50 Hz to TGF-β1) and SOX9 (synergy of 25 Hz EMF and TGF-β1); Alcian Blue staining for sulfated GAGs	An electromagnetic field regulated cell chondrogenesis through the TGF-dependent pathway	Control and healing of connective tissue defects	[155]
Electromagnetic field	Pulsed	< 40 μT	0.1-0.3 Hz, 24 min/day	hASCs	*In vitro* test: enhanced cell osteogenesis with mRNA expression of RUNX2, osteocalcin, osteopontin, Col I, and ALP; quantification of ALP activity and calcium deposition; Alzarin Red S staining	Synergy of an electromagnetic field and osteogenic induction medium	Bone tissue engineering	[159]
Magnet (15 mm in diameter, 1 mm in thickness)	Static	3, 15, 50 mT	N/A	hBMSCs	*In vitro* test: enhanced cell proliferation and osteogenesis in osteogenic induction medium with mRNA expression of ALP, RUNX2, osteocalcin, osteopontin, osterix, osteonectin; quantification of ALP activity and calcium deposition	A moderate static magnetic field (15 mT) had the superior impact on cell proliferation and osteogenesis	Bone tissue engineering	[154]
Magnet (6 cm in diameter)	Rotative	0.4 T	7.5 Hz, 2 h/day	Human umbilical cord MSCs	*In vitro* test: biocompatible; no influence on cell growth and osteogenesis; inhibited cell adipogenesis with	A dynamic magnetic field regulated the c-Jun N-terminal kinase (JNK)-	Treatment of obesity	[160]

					mRNA expression of FABP4 and PPAR- γ2; protein expression of PPAR- γ2 and immunofluorescent staining	dependent Wnt signaling pathway		
Electromagnetic field	Pulsed	1 mT	50 Hz, 8 days	hBMSCs and mouse ESCs	*In vitro* test: enhanced neural differentiation with quantification and immunofluorescent staining for Tuj1 and NeuroD1 and TH; mRNA expression of ChAT, GAD67, HB9, and Pitx3	A magnetic field enhanced neuron differentiation by the early growth response protein 1 (Egr1)-dependent pathway	Stem cell therapy for neurodegenerative diseases	[161]
Electromagnetic field	Pulsed	1 mT	50 Hz	hBMSCs	*In vitro* test: decreased cell proliferation and mRNA expression of early neuronal marker (Nestin), while enhanced mRNA expression of neuronal differentiation marker (MAP2) and intracellular calcium	An electromagnetic field upregulated expression of ferritin light chain, thioredoxin-dependent peroxide reductase, and tubulin β-6 chain	Stem cell therapy for neurodegenerative diseases	[162]
Electromagnetic field	Pulsed	10 mT	50 Hz, 3 or 6 h	Rat BMSCs	*In vitro* test: enhanced cell proliferation independent of time; increased cells at the G1 phase of a cell cycle and cell proliferation for a longer time of exposure to magnetic field; no influence on cell growth and cycle in 16 h	An electromagnetic field temporally promoted cell growth by increasing cells at the G1 phase of a cell cycle	N/A	[163]

Influence of magnetic nanoparticles on fate of MSCs

Magnetic nanoparticles (MNPs) not only respond to a magnetic field, but also harbour a permanent magnetic moment. [164] Fe_3O_4 and γ-Fe_2O_3 nanoparticles are the most common MNPs used for stem cell labelling and have been applied to cell tracking *in vivo* [165], for accurate targeted delivery [166-168] and for high cell retention [169, 170]. To keep magnetic nanoparticles stable in the solution and enhance their efficiency of up-take, various surface modification methods have been explored. [164, 169, 171] and different coating materials provide distinct effects on the fate of stem cells. [172, 173] However, a study of Wang et al. showed that MNPs as a whole, but not dissolved iron oxide or the coating materials, played a role in promoting cell osteogenesis. [174] Hence, the influence and mechanism of various materials for the surface functionalization of MNPs on biological functions of MSCs require further comprehensive studies. Once taken up by cells, MNPs can trigger a series of intracellular signaling pathways and eventually influence the fate of stem cells with [175, 176] or without [174] the assistance of an external magnetic field. Since cells respond to a mechanical stimuli by the mechano-sensitive channels on the cell membrane, magnetic nanoparticles can be used for studying how stem cells respond to the external mechanical stimulation by binding RGD-functionalized MNPs to integrins on the cell membrane and monitoring the electrophysiological change across the membrane to determine the function of specific ion channels for mechano-sensing. [177] When mounting magnetic nanoparticles to a potassium channel on the cell membrane, TREK1, an external dynamic magnetic field was able to directly induce mechanical stimulation to the stem cells in a remote and controllable manner. This approach led to a change in the membrane potential and triggered intracellular signaling pathways, resulting in enhanced tissue regeneration of load-bearing tissues, such as cartilage and bone. [178] Details of the influence of magnetic nanoparticles on the fate of MSCs can be found in Table 2.5.

Table 2.5 Influence of magnetic nanoparticles on fate of MSCs.

Type	Synthesis method	Surface modification	Size	Magnetization	External magnetic field	Cell source	Influence of biological functions	Mechanism	Application	Ref.
Fe_3O_4	Emulsification of Fe_3O_4 and polymerization of dopamine *in situ*	Polydopamine	56-68 nm in diameter	N/A	No	Rat BMSCs	Non-cytotoxicity and non-apoptosis and no adverse effect on cell growth and differentiation (adipogenesis and osteogenesis) under 50 μg/mL; increased the cell number at the S phase of a cell cycle; enhanced secretion of VEGF and cell migration *in vitro* via the transwell assay and *in vivo* (homing to the inflammable ear after tail vein injection)	Fe_3O_4 enhanced cell adhesion and homing by upregulating expression of C-X-C chemokine receptor 4 and C-C motif receptor 1; enhanced cell migration by increasing migration-related proteins c-Met	Stem cell therapy	[179]
γ-Fe_2O_3	Co-precipitation of	Citrate	64.90 ± 1.53 nm	60.7 emu/g	0.3-0.45 T of magnet	Mouse BMSCs	Reduced cell viability; no adverse influence	Static magnetic field led to	Cell therapy with	[166]

	ferrous and ferric salts solution		in diameter				on cell morphology, proliferation, and differentiation (osteogenesis and adipogenesis); normal secretion of anti-inflammatory factors (hepatocyte growth factor (HGF) and interleukin-1 receptor antagonist (IL-1RN))	temporary loss of cell viability; together with up-taking citrate coated γ-Fe_2O_3 restricted cell proliferation	magnetic targeting	
Fe_3O_4	Co-precipitation of ferrous and ferric salts solution	Carboxylated PEG	40 ± 2 nm in diameter	20 emu/g	0.3 T of magnet (length 8 mm, width 2 mm)	hASCs	*In vivo* test: reduced fibrosis; increased ejection fraction and fractional shortening; more Fe_3O_4 labelled cells accumulated at heart.	Magnet attracted Fe_3O_4 labelled hASCs at the defect heart site after intracardiac injection	Heart tissue regeneration	[167]
Fe_3O_4	N/A	Oleic acid and rhodamine b	5.22 ± 0.9 nm in diameter	N/A	0.32 T of magnet (length 5 mm, width 5 mm,	Mouse BMSCs	*In vitro* test: Minimal cytotoxicity for a concentration less than 15 µg/mL;	Magnet attracted Fe_3O_4 labelled mouse	Tissue regeneration	[168]

					height 5mm)		magnetic attraction enhanced secretion of protein CXCR4; increased reactive oxygen species (ROS); *in vivo* test: enhanced mRNA expression of SDF-1 and immunohistochemical staining for SDF-1; enhanced accumulation of Fe_3O_4 labelled cells at the defect sites one week after nostril injection	BMSCs at the defect heart site		
Fe_3O_4	N/A	Carboxyl and mechano-sensitive ion channel TREK-1 antibody	250 nm in diameter	N/A	Two magnets with a magnetization of 25 mT, dynamic stimulation for 3 h/day	Ovine BMSCs	*In vitro* test: enhanced osteogenesis; *in vivo* test: non-cytotoxicity; initially accelerated repair and preliminarily enhanced bone growth	Dynamic movement of a two-magnet array remotely delivered mechanical stimulation to injected MSCs with	Bone regeneration	[178]

								TREK-1-coated Fe_3O_4 labelling, leading to activation of osteogenesis		
γ-Fe_2O_3	Co-precipitation	Polyglucose sorbitol carboxymethyl-ether (PSC)	8.2 nm in diameter	93 emu/g	No	hBMSCs	*In vitro* test: minimal cytotoxicity; enhanced osteogenesis with mRNA expression of RUNX2, osteocalcin, and osteopontin; ALP quantification and Alizarin red staining	MNPs as a whole upregulated *ZEB2*-dependent long noncoding RNA *INZEB2*	Stem cell therapy	[174]
Fe_3O_4	Co-precipitation	Sodium oleate (SO) and bovine serum albumin (BSA)	190.6 ± 30.9 nm for 3.4% Fe_3O_4 and 208.7 ± 28.9 nm for 13.6%	0.23 emu/g for 3.4% Fe_3O_4 and 0.81 emu/g for 13.6% Fe_3O_4	Static magnetic field with 1 T of magnetization	Rat BMSCs	*In vitro* test: impeded cell proliferation; enhanced cell osteogenesis with mRNA and protein expression of collagen I and osteocalcin; quantification of	MNPs together with a static magnetic field interfered with non-muscle myosin II- and ROCK-	Stem cell therapy	[175]

			Fe_3O_4 in diameter				ALP activity and calcium deposition; double the cell retention rate due to intracellular MNPs with assistance of a static magnetic field	dependent mechano-sensing pathways		
Fe_3O_4	High temperature organic solution phase reaction	Oleic acid and oleylamine and 1,2-distearoyl-sn-glycero-3-phosphoethanolamine-N-[methoxy(polyethylene glycol)-2000] (mPEG-2000 PE) and 1,2-dioleoyl-sn-glycero-3-phosphoethanolamine-N-(Lissamine Rhodamine B Sulfonyl)	N/A	N/A	Electromagnetic field with a magnetization of 1 mT and a frequency of 50 Hz	hBMSCs	*In vitro* test: neural-like morphology change; minimal cytotoxicity and enhanced neural differentiation with mRNA expression of NeuroD1, MAP2, DCX, NF-L, MBP; immunofluorescent staining for NeuroD1 and MBP	MNPs and an electromagnetic field activated the p-CREB-dependent signaling pathway	Neural cell differentiation	[176]

Fe_3O_4	High temperature organic solution phase reaction	Oleic acid and oleylamine and mPEG-2000 PE	N/A	N/A	Electromagnetic field with a magnetization of 1 mT and a frequency of 50 Hz; 8 h/day	hBMSCs	*In vivo* test: enhanced retention of hBMSCs at the spinal injury site; enhanced behavioural recovery including Basso, Beattie, and Bresnahan behavioural test	Enhanced retention of hMSCs facilitated recovery of spinal injury	Spinal regeneration	[170]
Fe_3O_4	N/A	Dextran	182 ± 18 nm in diameter	N/A	Cylindrical magnet	Rabbit BMSCs	*In vitro* test: no influence on cell adipogenesis and osteogenesis and cytokine secretion, while impaired cell chondrogenesis in the absence of a magnetic field; no influence on attachment of Fe_3O_4-labelled hMSCs on fibronectin-coated plates with/without a magnetic field; double cells attached to the	Magnetic force enhanced cell retention at the injury sites	Targeting delivery of stem cells	[169]

							HUVEC layer with a magnetic field; *in vivo* test: 6-fold increase in cell retention and reduced restenosis			
CrO_2 coated polystyrene particle	N/A	Carboxyl and L-arginyl-glycyl-L-aspartic acid (RGD)	4.0–4.5 μm in diameter	N/A	Magnecell magnetic ion channel activation system with a dynamic magnetic field of 0-167 mT at a frequency of 1 Hz for 10 min	hMSCs	*In vitro* test: two particles bound to surface integrins of each cell with an overall 6 pN force when exposed to a dynamic magnetic field; membrane hyperpolarization	A magnetic field remotely exerted a force on the cells by membrane-bounded magnetic particles, resulting in activation of the BK channel and intracellular calcium release	N/A	[177]

Magnetic field-responsive scaffolds/hydrogels for bone and cartilage tissue engineering

The incorporation of magnetic nanoparticles can change the surface properties of scaffolds including roughness, mechanical strength and wettability, which may influence the initial cell-substrate interaction, leading to enhanced cell adhesion and spreading. [145, 152, 180, 181] The coating magnetic nanoparticles on the surface of scaffolds could functionalize as many individual micro-scale magnetic fields, regulating the fate of adjacent stem cells through relevant signaling pathways, such as iron−sulfur cluster assembly protein 1 (ISCA1)-dependent and BMP-2/Smad/Runx2-dependent pathways. [145, 150, 182, 183] (Figure 2.6) Furthermore, the incorporation of superparamagnetic iron oxide nanoparticles and exposure of the scaffold to an alternating magnetic field at a high frequency, can generate heat (hyperthermia effect) within a relatively short time, providing a novel way of treating malignant osteoma. [184-187] Samal et al. recently reported a biocompatible magnetic scaffold fabricated by salt-leaching and dip-coating with MNPs using silk fibroin protein displayed excellent hyperthermic performance, increasing a temperature up to 8 ℃ within 100 s. [148] The same group fabricated another magnetic scaffold with gelatin by casting viscous gelatin and a poly(acrylic acid)-coated MNPs hybrid into multi-layers and crosslinking via carbodimide chemistry. Such a magnetic scaffold was able to increase the surrounding temperature up to 18 ℃ within 70 s when exposing to an alternating magnetic field at a frequency of 293 kHz and a magnetization of 30 mT. [146] Jedlovszky-Hajdu et al. successfully co-electrospun magnetic scaffolds incorporated with poly(succinimide) and oleic acid-coated MNPs, which were capable of hyperthermia with a temperature increase of 7 ℃ within 60 s. [188] Alternatively, iron oxide magnetic nanoparticles can also be used as photothermal conversion agents to kill cancer cells by heating after exposing to near infrared (NIR) light. [182, 189] The photothermal behaviour of iron oxide nanoparticles also allowed a controllable release of bio-reagents from the magnetic scaffolds and these bio-reagents rapidly penetrated into cancer cells for a better treatment of malignant osteoma. [183] Furthermore, magnetic scaffolds/hydrogels can also respond to stimulation of a dynamic

external magnetic field by deformation of their structures, which might function as actuators for mechanical stimulation of stem cells to regulate their differentiation through mechano-related signaling pathways. [151, 190-192] Details of magnetic field-responsive materials for tissue engineering can be found in Table 2.6.

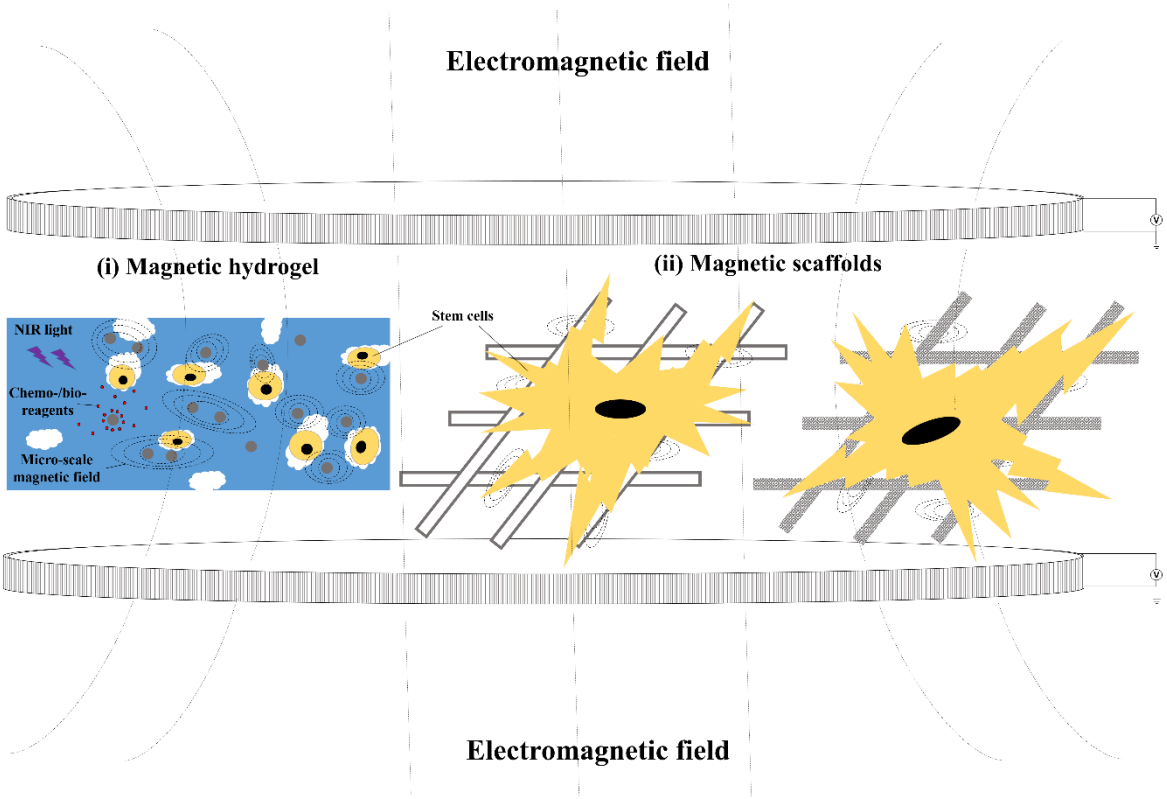

Figure 2.6 Stem cells are cultured (i) in magnetic field-responsive hydrogels with incorporation of chemo-/bio- reagents-loaded magnetic nanoparticles (MNPs), or (ii) on scaffolds with MNPs coated on the surface of nanofibers by dip-coating or layer-by-layer assembly (left) or embedded in nanofibers by co-electrospinning (right).

2.3 Conclusion

In summary, using smart materials for efficient cell delivery and actively regulating the fate of stem cells, may provide a novel approach to treat OA. In this thesis, two smart materials were fabricated and explored for their potential applications in cartilage and bone tissue engineering. A thermo-sensitive poly (*N*-isopropylacrylamide-co-acrylic acid) hydrogel was first evaluated as an *in-vitro* platform for study of MSCs, which showed enhanced multi-lineage differentiation due to formation cell aggregates *in situ*. (Chapter 3) The hydrogel was further used as a delivery vehicle for injection of MSC aggregates into an osteochondral defect *in vivo*, which showed excellent cartilage and bone regeneration due to synergy of enhanced paracrine effects and

multi-potency of MSC aggregates. (Chapter 4) Moreover, the interaction between MSCs and the hydrogel was examined over an extended period and revealed that cell aggregates were formed in response to cell migration-mediated cell aggregation. The resultant MSC-derived chondrocytes were harvested from the thermo-responsive hydrogel and forcing into a neo-cartilage patch *in vitro* for potential application in cartilage regeneration. (Chapter 5) Furthermore, a magnetic field-responsive scaffold was fabricated and utilized as a novel *in-vitro* platform to regulate MSC behaviour and was found to enhance chondrogenesis and osteogenesis of MSCs in the 3D smart scaffold, which may have potential applications in cartilage and bone tissue engineering. (Chapter 6) Results of these studies reveal that the thermo-responsive hydrogel and the magnetic field-responsive scaffold together with MSCs might be novel and promising therapeutic strategies for cartilage and bone regeneration.

Table 2.6 Magnetic field-responsive scaffolds/hydrogels for tissue engineering.

Material	Phase	Fabrication methods	Magnetic intensity	Dimension	Cell	State	External magnetic field	Results	Mechanism	Application	Ref.
Gelatin	Hydrogel	Chemical crosslinking with γ-glycidoxypropyltrimethoxysilane (GPTMS) and physical crosslinking with β-cyclodextrin by host−guest interaction; incorporation with 10 mg/mL F_3O_4 nanoparticles (20-30 nm)	N/A	2D	Rat BMSCs	Static	100 mT of an electromagnetic strength and 40-70 Hz of a frequency for 20 min	*In vitro* test: minimal cytotoxicity; promoted cell growth; enhanced chondrogenesis with mRNA expression of Col II, aggrecan, and SOX9 and Toluidine Blue staining for polysaccharides and immunohistochemical and immunofluorescent staining for collagen II	Pulsed electromagnetic field enhanced chondrogenesis of MSCs grown on a magnetic hydrogel	Cartilage repair	[149]
$CoFe_2O_4$ nanoparticles (CFO)/ Graphen	Scaffold	GO fabricated with a modified Hummers'	38.9 emu/g for GO/CFO and 0.41 emu/g for	2D	hASCs	Dynamic	1 mT of an electromagnetic strength	Biocompatible *in vivo*; impeded cell growth compared to cells cultured on	Pulsed electromagnetic field enhanced cell	Tissue engineering, biosensors and actuators	[151]

e oxide (GO)/ polyvinylidene difluoride (PVDF)		method and decorated with PVP-coated CFO by hydrothermal process (GO/CFO, 5 nm) and homogeneously mixed with PVDF at a concentration of 1% (wt/wt, in respect to PVDF) in dimethylacetamide/acetone (60/40 v/v) for electrospinning	GO/CFO/ PVDF				and 50 Hz of a frequency for 8 h/day	plates in the absence of electromagnetic field; enhanced neural differentiation with mRNA expression of Nestin, B-tubulin III, neuron specific enolase and immunofluorescent staining for nerve growth factor receptor (NGFR) p75	proliferation and neural differentiation		
PLGA and Fe_3O_4 magnetic nanoparticles (MNPs)	Scaffold	Double emulsion fabrication of micro-scaffolds (269.83 ± 10.982 μm) with high	8.105 emu/g	3D	Mouse MSCs	Static	N/A	*In vitro* test: biocompatible; supported cell growth; enhanced cell chondrogenesis with mRNA expression of	N/A	The magnetic property of scaffolds was used for targeting delivery of stem cells	[193]

		porosity and chemical bonding with polyethylenimine (PEI)-coated MNPs by amino bonds						SOX9, aggrecan, and Col II; Alcian Blue staining for sulfated GAGs.		for cartilage tissue engineering by injection and remote guidance	
poly-ε-caprolactone (PCL) and MNPs	Scaffold	Needleless electrospinning with PCL solution and MNPs (50-100 nm)	6.8±0.3 Am^2/kg and 6.1±0.3 Am^2/kg at 10 K and 300 K, respectively	2D	Porcine BMSCs	Static	No	*In vitro* test: enhanced cell proliferation and osteogenesis with quantification of ALP activity in osteogenic induction medium	Incorporation of MNPs enhanced the cell proliferation and osteogenesis	Bone tissue engineering	[152]
PCL and MNPs	Scaffold	Electrospinning PCL solution and MNPs (citric acid surface functionalization, 12 ± 1.34 nm)	1.0–11.2 emu/g (value increased as more MNPs incorporated into electrospun PCL scaffolds)	2D	Rat BMSCs	Static	No	*In vitro* test: enhanced cell adhesion, spreading, and penetration into scaffolds in a dose-dependent manner; enhanced cell osteogenesis with quantification of	Magnetism of MNPs affected the ion channels in cell membrane; incorporation of MNPs in PCL scaffolds changed the	Bone tissue engineering	[150]

								ALP activity and mRNA expression of Col I, osteopontin, and bone sialoprotein; *in vivo* test: biocompatible and biodegradable and bone formation	wettability, mechanical strength and roughness of scaffolds, which promoted cell adhesion, spreading and migration.		
PLGA/PCL/gelatin and γ-Fe_2O_3 magnetic nanoparticles	Scaffold	PLGA, PCL, and gelatin mixed solution was electrospun into scaffolds and positively charged by poly-(diallyldimethylammonium chloride). Scaffolds were dipped	3.56 emu/g	2D	Rat ASCs	Static	No	*In vitro* test: enhanced cell adhesion and spreading; no influence on cell proliferation; enhanced osteogenesis with mRNA expression of ALP, RUNX2, osteocalcin, and Col I; quantification of ALP activity and calcium deposition; no difference of cell osteogenesis	A dense and uniform granular layer of MNPs changed the surface properties of electrospun scaffolds, facilitating cell adhesion and spreading; the magnetism of MNPs	Bone tissue engineering	[145]

		in polyglucose-sorbitol-carboxymethyether (PSC)-coated or citrate-coated MNPs (7-8 nm) solution four times for layer-by-layer assembly.						between PSC-coated MNPs and citrate-coated MNPs	upregulated gene expression of an exogenous magnetoreceptor, ISCA1		

2.4 Reference

[1] Hall BK, Miyake T. All for one and one for all: condensations and the initiation of skeletal development. Bioessays 2000;22:138-47.

[2] DeLise AM, Fischer L, Tuan RS. Cellular interactions and signaling in cartilage development. Osteoarthritis and Cartilage 2000;8:309-34.

[3] Kronenberg HM. Developmental regulation of the growth plate. Nature 2003;423:332-6.

[4] Armiento AR, Stoddart MJ, Alini M, Eglin D. Biomaterials for articular cartilage tissue engineering: Learning from biology. Acta Biomaterialia 2018;65:1-20.

[5] Camarero-Espinosa S, Rothen-Rutishauser B, Foster EJ, Weder C. Articular cartilage: from formation to tissue engineering. Biomaterials Science 2016;4:734-67.

[6] Pap T, Korb-Pap A. Cartilage damage in osteoarthritis and rheumatoid arthritis-two unequal siblings. Nature Reviews Rheumatology 2015;11:606-15.

[7] Li MH, Xiao R, Li JB, Zhu Q. Regenerative approaches for cartilage repair in the treatment of osteoarthritis. Osteoarthritis and Cartilage 2017;25:1577-87.

[8] Huey DJ, Hu JC, Athanasiou KA. Unlike Bone, Cartilage Regeneration Remains Elusive. Science 2012;338:917-21.

[9] Hellingman CA, Davidson ENB, Koevoet W, Vitters EL, van den Berg WB, van Osch GJVM, et al. Smad Signaling Determines Chondrogenic Differentiation of Bone-Marrow-Derived Mesenchymal Stem Cells: Inhibition of Smad1/5/8P Prevents Terminal Differentiation and Calcification. Tissue Engineering Part A 2011;17:1157-67.

[10] Joosten LA, Crisan TO, Azam T, Cleophas MC, Koenders MI, van de Veerdonk FL, et al. Alpha-1-anti-trypsin-Fc fusion protein ameliorates gouty arthritis by reducing release and extracellular processing of IL-1beta and by the induction of endogenous IL-1Ra. Annals of Rheumatic Diseases 2016;75:1219-27.

[11] Fischer JAA, Hueber AJ, Wilson S, Galm M, Baum W, Kitson C, et al. Combined Inhibition of Tumor Necrosis Factor α and Interleukin-17 As a Therapeutic Opportunity in

Rheumatoid Arthritis: Development and Characterization of a Novel Bispecific Antibody. Arthritis & Rheumatology 2015;67:51-62.

[12] Lee CH, Cook JL, Mendelson A, Moioli EK, Yao H, Mao JJ. Regeneration of the articular surface of the rabbit synovial joint by cell homing: a proof of concept study. Lancet 2010;376:440-8.

[13] Zhang F, Leong WY, Su K, Fang Y, Wang DA. A Transduced Living Hyaline Cartilage Graft Releasing Transgenic Stromal Cell-Derived Factor-1 Inducing Endogenous Stem Cell Homing In Vivo. Tissue Engineering Part A 2013;19:1091-9.

[14] Karimi T, Barati D, Karaman O, Moeinzadeh S, Jabbari E. A developmentally inspired combined mechanical and biochemical signaling approach on zonal lineage commitment of mesenchymal stem cells in articular cartilage regeneration. Integrative Biology 2015;7:112-27.

[15] Madry H, Orth P, Kaul G, Zurakowski D, Menger MD, Kohn D, et al. Acceleration of articular cartilage repair by combined gene transfer of human insulin-like growth factor I and fibroblast growth factor-2 in vivo. Archives of Orthopaedic and Trauma Surgery 2010;130:1311-22.

[16] Minas T, Von Keudell A, Bryant T, Gomoll AH. The John Insall Award: A minimum 10-year outcome study of autologous chondrocyte implantation. Clinical Orthopaedics and Related Research 2014;472:41-51.

[17] Peterson L, Vasiliadis HS, Brittberg M, Lindahl A. Autologous chondrocyte implantation: a long-term follow-up. The American Journal of Sports Medicine 2010;38:1117-24.

[18] Makris EA, Gomoll AH, Malizos KN, Hu JC, Athanasiou KA. Repair and tissue engineering techniques for articular cartilage. Nature Reviews Rheumatology 2015;11:21-34.

[19] Zhang J, Huang XW, Wang HJ, Liu XY, Zhang T, Wang YC, et al. The challenges and promises of allogeneic mesenchymal stem cells for use as a cell-based therapy. Stem Cell Research & Therapy 2015;6:234.

[20] Sensebé L, Krampera M, Schrezenmeier H, Bourin P, Giordano R. Mesenchymal stem cells for clinical application. Vox Sanguinis 2010;98:93-107.

[21] Wang C, Cheng L, Xu H, Liu Z. Towards whole-body imaging at the single cell level using ultra-sensitive stem cell labeling with oligo-arginine modified upconversion nanoparticles. Biomaterials 2012;33:4872-81.

[22] Jo CH, Lee YG, Shin WH, Kim H, Chai JW, Jeong EC, et al. Intra-Articular Injection of Mesenchymal Stem Cells for the Treatment of Osteoarthritis of the Knee: A Proof-of-Concept Clinical Trial. Stem cells (Dayton, Ohio) 2014;32:1254-66.

[23] Kelm JM, Fussenegger M. Scaffold-free cell delivery for use in regenerative medicine. Advanced Drug Delivery Reviews 2010;62:753-64.

[24] Cheng NC, Wang S, Young TH. The influence of spheroid formation of human adipose-derived stem cells on chitosan films on stemness and differentiation capabilities. Biomaterials 2012;33:1748-58.

[25] Zhang J, Yun S, Bi J, Dai S, Du Y, Zannettino ACW, et al. Enhanced multi-lineage differentiation of human mesenchymal stem/stromal cells within poly(N-isopropylacrylamide-acrylic acid) microgel-formed three-dimensional constructs. Journal of Materials Chemistry B 2018;6:1799-814.

[26] Amos PJ, Kapur SK, Stapor PC, Shang HL, Bekiranov S, Khurgel M, et al. Human Adipose-Derived Stromal Cells Accelerate Diabetic Wound Healing: Impact of Cell Formulation and Delivery. Tissue Engineering Part A 2010;16:1595-606.

[27] Bartosh TJ, Ylostalo JH, Mohammadipoor A, Bazhanov N, Coble K, Claypool K, et al. Aggregation of human mesenchymal stromal cells (MSCs) into 3D spheroids enhances their antiinflammatory properties. Proceedings of the National Academy of Sciences of the United States of America 2010;107:13724-9.

[28] Ghannam S, Bouffi C, Djouad F, Jorgensen C, Noel D. Immunosuppression by mesenchymal stem cells: mechanisms and clinical applications. Stem Cell Research & Therapy 2010;1:2.

[29] Ren GW, Zhang LY, Zhao X, Xu GW, Zhang YY, Roberts AI, et al. Mesenchymal stem cell-mediated immunosuppression occurs via concerted action of chemokines and nitric oxide. Cell Stem Cell 2008;2:141-50.

[30] Madrigal M, Rao KS, Riordan NH. A review of therapeutic effects of mesenchymal stem cell secretions and induction of secretory modification by different culture methods. Journal of Translational Medicine 2014;12:260.

[31] Bhang SH, Cho SW, La WG, Lee TJ, Yang HS, Sun AY, et al. Angiogenesis in ischemic tissue produced by spheroid grafting of human adipose-derived stromal cells. Biomaterials 2011;32:2734-47.

[32] Steinberg MS. On the Mechanism of Tissue Reconstruction by Dissociated Cells, Iii. Free Energy Relations and the Reorganization of Fused, Heteronomic Tissue Fragments. Proceedings of the National Academy of Sciences of the United States of America 1962;48:1769-76.

[33] Steinberg MS. On the mechanism of tissue reconstruction by dissociated cells. I. Population kinetics, differential adhesiveness. and the absence of directed migration. Proceedings of the National Academy of Sciences of the United States of America 1962;48:1577-82.

[34] Ichinose S, Tagami M, Muneta T, Sekiya I. Morphological examination during in vitro cartilage formation by human mesenchymal stem cells. Cell and Tissue Research 2005;322:217-26.

[35] Wuchter P, Boda-Heggemann J, Straub BK, Grund C, Kuhn C, Krause U, et al. Processus and recessus adhaerentes: giant adherens cell junction systems connect and attract human mesenchymal stem cells. Cell and Tissue Research 2007;328:499-514.

[36] Lee EJ, Park SJ, Kang SK, Kim GH, Kang HJ, Lee SW, et al. Spherical Bullet Formation via E-cadherin Promotes Therapeutic Potency of Mesenchymal Stem Cells Derived From Human Umbilical Cord Blood for Myocardial Infarction. Molecular Therapy 2012;20:1424-33.

[37] Grskovic M, Javaherian A, Strulovici B, Daley GQ. Induced pluripotent stem cells - opportunities for disease modelling and drug discovery. Nature Reviews Drug Discovery 2011;10:915-29.

[38] Murry CE, Keller G. Differentiation of embryonic stem cells to clinically relevant populations: Lessons from embryonic development. Cell 2008;132:661-80.

[39] Ouyang L, Yao R, Mao S, Chen X, Na J, Sun W. Three-dimensional bioprinting of embryonic stem cells directs highly uniform embryoid body formation. Biofabrication 2015;7:044101.

[40] Foty RA, Steinberg MS. The differential adhesion hypothesis: a direct evaluation. Developmental Biology 2005;278:255-63.

[41] Sart S, Tsai AC, Li Y, Ma T. Three-dimensional aggregates of mesenchymal stem cells: cellular mechanisms, biological properties, and applications. Tissue Engineering Part B: Reviews 2014;20:365-80.

[42] Sun YB, Chen CS, Fu JP. Forcing Stem Cells to Behave: A Biophysical Perspective of the Cellular Microenvironment. Annual Review of Biophysics 2012;41:519-42.

[43] Hildebrandt C, Buth H, Thielecke H. A scaffold-free in vitro model for osteogenesis of human mesenchymal stem cells. Tissue Cell 2011;43:91-100.

[44] Baraniak PR, McDevitt TC. Scaffold-free culture of mesenchymal stem cell spheroids in suspension preserves multilineage potential. Cell and Tissue Research 2012;347:701-11.

[45] Frith JE, Thomson B, Genever PG. Dynamic Three-Dimensional Culture Methods Enhance Mesenchymal Stem Cell Properties and Increase Therapeutic Potential. Tissue Engineering Part C: Methods 2010;16:735-49.

[46] Tseng T-C, Wong C-W, Hsieh F-Y, Hsu S-h. Biomaterial Substrate-Mediated Multicellular Spheroid Formation and Their Applications in Tissue Engineering. Biotechnology Journal 2017;12:1700064.

[47] Wong CW, Chen YT, Chien CL, Yu TY, Rwei SP, Hsu SH. A simple and efficient feeder-free culture system to up-scale iPSCs on polymeric material surface for use in 3D bioprinting. Materials Science & Engineering C-Materials for Biological Applications 2018;82:69-79.

[48] Cheng N-C, Wang S, Young T-H. The influence of spheroid formation of human adipose-derived stem cells on chitosan films on stemness and differentiation capabilities. Biomaterials 2012;33:1748-58.

[49] Huang GS, Dai LG, Yen BL, Hsu SH. Spheroid formation of mesenchymal stem cells on chitosan and chitosan-hyaluronan membranes. Biomaterials 2011;32:6929-45.

[50] Worz A, Berchtold B, Moosmann K, Prucker O, Ruhe J. Protein-resistant polymer surfaces. Journal of Materials Chemistry 2012;22:19547-61.

[51] Kim J, Ma T. Endogenous Extracellular Matrices Enhance Human Mesenchymal Stem Cell Aggregate Formation and Survival. Biotechnology Progress 2013;29:441-51.

[52] Yanagihara K, Uchida S, Ohba S, Kataoka K, Itaka K. Treatment of Bone Defects by Transplantation of Genetically Modified Mesenchymal Stem Cell Spheroids. Molecular Therapy-Methods&Clinical Development 2018;9:358-66.

[53] Cui X, Hartanto Y, Zhang H. Advances in multicellular spheroids formation. Journal of the Royal Society Interface 2017;14:20160877.

[54] Lee GH, Lee JS, Wang XH, Lee SH. Bottom-Up Engineering of Well-Defined 3D Microtissues Using Microplatforms and Biomedical Applications. Advanced Healthcare Materials 2016;5:56-74.

[55] Candiello J, Grandhi TSP, Goh SK, Vaidya V, Lemmon-Kishi M, Eliato KR, et al. 3D heterogeneous islet organoid generation from human embryonic stem cells using a novel engineered hydrogel platform. Biomaterials 2018;177:27-39.

[56] Jeon O, Marks R, Wolfson D, Alsberg E. Dual-crosslinked hydrogel microwell system for formation and culture of multicellular human adipose tissue-derived stem cell spheroids. Journal of Materials Chemistry B 2016;4:3526-33.

[57] Hribar KC, Finlay D, Ma X, Qu X, Ondeck MG, Chung PH, et al. Nonlinear 3D projection printing of concave hydrogel microstructures for long-term multicellular spheroid and embryoid body culture. Lab on a Chip 2015;15:2412-8.

[58] Kim B-C, Kim JH, An HJ, Byun W, Park J-H, Kwon IK, et al. Microwell-mediated micro cartilage-like tissue formation of adipose-derived stem cell. Macromolecular Research 2014;22:287-96.

[59] Schukur L, Zorlutuna P, Cha JM, Bae H, Khademhosseini A. Directed Differentiation of Size-Controlled Embryoid Bodies Towards Endothelial and Cardiac Lineages in RGD-Modified Poly(Ethylene Glycol) Hydrogels. Advanced Healthcare Materials 2013;2:195-205.

[60] Huang C-C, Chen D-Y, Wei H-J, Lin K-J, Wu C-T, Lee T-Y, et al. Hypoxia-induced therapeutic neovascularization in a mouse model of an ischemic limb using cell aggregates composed of HUVECs and cbMSCs. Biomaterials 2013;34:9441-50.

[61] Chen D-Y, Wei H-J, Lin K-J, Huang C-C, Wang C-C, Wu C-T, et al. Three-dimensional cell aggregates composed of HUVECs and cbMSCs for therapeutic neovascularization in a mouse model of hindlimb ischemia. Biomaterials 2013;34:1995-2004.

[62] Lee W-Y, Chang Y-H, Yeh Y-C, Chen C-H, Lin KM, Huang C-C, et al. The use of injectable spherically symmetric cell aggregates self-assembled in a thermo-responsive hydrogel for enhanced cell transplantation. Biomaterials 2009;30:5505-13.

[63] Khademhosseini A, Eng G, Yeh J, Fukuda J, Blumling J, III, Langer R, et al. Micromolding of photocrosslinkable hyaluronic acid for cell encapsulation and entrapment. Journal of Biomedical Materials Research Part A 2006;79A:522-32.

[64] Kim HJ, Castaneda R, Kang TH, Kimura S, Wada M, Kim U-J. Cellulose hydrogel film for spheroid formation of human adipose-derived stemcells. Cellulose 2018;25:2589-98.

[65] Pugliese R, Fontana F, Marchini A, Gelain F. Branched peptides integrate into self-assembled nanostructures and enhance biomechanics of peptidic hydrogels. Acta Biomaterialia 2018;66:258-71.

[66] Lee YB, Kim EM, Byun H, Chang H-k, Jeong K, Aman ZM, et al. Engineering spheroids potentiating cell-cell and cell-ECM interactions by self-assembly of stem cell microlayer. Biomaterials 2018;165:105-20.

[67] Kim Y, Baipaywad P, Jeong Y, Park H. Incorporation of gelatin microparticles on the formation of adipose-derived stem cell spheroids. International Journal of Biological Macromolecules 2018;110:472-8.

[68] Nemeth CL, Janebodin K, Yuan AE, Dennis JE, Reyes M, Kim D-H. Enhanced Chondrogenic Differentiation of Dental Pulp Stem Cells Using Nanopatterned PEG-GelMA-HA Hydrogels. Tissue Engineering Part A 2014;20:2817-29.

[69] De Moor L, Merovci I, Baetens S, Verstraeten J, Kowalska P, Krysko DV, et al. High-throughput fabrication of vascularized spheroids for bioprinting. Biofabrication 2018;10:035009.

[70] Oltolina F, Zamperone A, Colangelo D, Gregoletto L, Reano S, Pietronave S, et al. Human Cardiac Progenitor Spheroids Exhibit Enhanced Engraftment Potential. PLOS ONE 2015;10: e0141632.

[71] Kim SJ, Park J, Byun H, Park YW, Major LG, Lee DY, et al. Hydrogels with an embossed surface: An all-in-one platform for mass production and culture of human adipose-derived stem cell spheroids. Biomaterials 2019;188:198-212.

[72] Ho SS, Murphy KC, Binder BYK, Vissers CB, Leach JK. Increased Survival and Function of Mesenchymal Stem Cell Spheroids Entrapped in Instructive Alginate Hydrogels. Stem Cells Translational Medicine 2016;5:773-81.

[73] Ko DY, Patel M, Lee HJ, Jeong B. Coordinating Thermogel for Stem Cell Spheroids and Their Cyto-Effectiveness. Advanced Functional Materials 2018;28:1706286.

[74] Zhang K, Song L, Wang J, Yan S, Li G, Cui L, et al. Strategy for constructing vascularized adipose units in poly(L-glutamic acid) hydrogel porous scaffold through inducing in-situ formation of ASCs spheroids. Acta Biomaterialia 2017;51:246-57.

[75] Zhang K, Feng Q, Xu J, Xu X, Tian F, Yeung KWK, et al. Self-Assembled Injectable Nanocomposite Hydrogels Stabilized by Bisphosphonate-Magnesium (Mg2+) Coordination Regulates the Differentiation of Encapsulated Stem Cells via Dual Crosslinking. Advanced Functional Materials 2017;27:1701642.

[76] Wu S, Xu R, Duan B, Jiang P. Three-dimensional hyaluronic acid hydrogel-based models for in vitro human iPSC-derived NPC culture and differentiation. Journal of Materials Chemistry B 2017;5:3870-8.

[77] Wu J, Zhang K, Yu X, Ding J, Cui L, Yin J. Hydration of hydrogels regulates vascularization in vivo. Biomaterials Science 2017;5:2251-67.

[78] Peng S, Wu C-W, Lin J-Y, Yang C-Y, Cheng M-H, Chu IM. Promoting chondrocyte cell clustering through tuning of a poly(ethylene glycol)-poly(peptide) thermosensitive hydrogel with distinctive microarchitecture. Materials Science & Engineering C-Materials for Biological Applications 2017;76:181-9.

[79] Lin H, Li Q, Lei Y. Three-dimensional tissues using human pluripotent stem cell spheroids as biofabrication building blocks. Biofabrication 2017;9:025007.

[80] Zhang K, He S, Yan S, Li G, Zhang D, Cui L, et al. Regeneration of hyaline-like cartilage and subchondral bone simultaneously by poly(L-glutamic acid) based osteochondral scaffolds with induced autologous adipose derived stem cells. Journal of Materials Chemistry B 2016;4:2628-45.

[81] Siltanen C, Yaghoobi M, Haque A, You J, Lowen J, Soleimani M, et al. Microfluidic fabrication of bioactive microgels for rapid formation and enhanced differentiation of stem cell spheroids. Acta Biomaterialia 2016;34:125-32.

[82] Zhang Q, Lu HX, Kawazoe N, Chen GP. Pore size effect of collagen scaffolds on cartilage regeneration. Acta Biomaterialia 2014;10:2005-13.

[83] Oh SH, Kim TH, Im GI, Lee JH. Investigation of Pore Size Effect on Chondrogenic Differentiation of Adipose Stem Cells Using a Pore Size Gradient Scaffold. Biomacromolecules 2010;11:1948-55.

[84] Carrion B, Souzanchi MF, Wang VT, Tiruchinapally G, Shikanov A, Putnam AJ, et al. The Synergistic Effects of Matrix Stiffness and Composition on the Response of Chondroprogenitor Cells in a 3D Precondensation Microenvironment. Advanced Healthcare Materials 2016;5:1192-202.

[85] Lee BH, Kim MH, Lee JH, Seliktar D, Cho N-J, Tan LP. Modulation of Huh7.5 Spheroid Formation and Functionality Using Modified PEG-Based Hydrogels of Different Stiffness. PLOS ONE 2015;10: e0118123.

[86] Li Y, Jiang X, Li L, Chen Z-N, Gao G, Yao R, et al. 3D printing human induced pluripotent stem cells with novel hydroxypropyl chitin bioink: scalable expansion and uniform aggregation. Biofabrication 2018;10:044101.

[87] Maia FR, Fonseca KB, Rodrigues G, Granja PL, Barrias CC. Matrix-driven formation of mesenchymal stem cell-extracellular matrix microtissues on soft alginate hydrogels. Acta Biomaterialia 2014;10:3197-208.

[88] Raquel Maia F, Lourenco AH, Granja PL, Goncalves RM, Barrias CC. Effect of Cell Density on Mesenchymal Stem Cells Aggregation in RGD-Alginate 3D Matrices under Osteoinductive Conditions. Macromolecular Bioscience 2014;14:759-71.

[89] Liu Y-J, Le Berre M, Lautenschlaeger F, Maiuri P, Callan-Jones A, Heuzé M, et al. Confinement and Low Adhesion Induce Fast Amoeboid Migration of Slow Mesenchymal Cells. Cell 2015;160:659-72.

[90] Yang J, Liu Y, He L, Wang Q, Wang L, Yuan T, et al. Icariin conjugated hyaluronic acid/collagen hydrogel for osteochondral interface restoration. Acta Biomaterialia 2018;74:156-67.

[91] Park H, Kim D, Lee KY. Interaction-tailored cell aggregates in alginate hydrogels for enhanced chondrogenic differentiation. Journal of Biomedical Materials Research Part A 2017;105:42-50.

[92] Lee SS, Choi GE, Lee HJ, Kim Y, Choy J-H, Jeong B. Layered Double Hydroxide and Polypeptide Thermogel Nanocomposite System for Chondrogenic Differentiation of Stem Cells. ACS Applied Materials & Interfaces 2017;9:42668-75.

[93] Ozdemir T, Fowler EW, Liu S, Harrington DA, Witt RL, Farach-Carson MC, et al. Tuning Hydrogel Properties to Promote the Assembly of Salivary Gland Spheroids in 3D. ACS Biomaterials Science & Engineering 2016;2:2217-30.

[94] Fan C, Wang D-A. Effects of Permeability and Living Space on Cell Fate and Neo-Tissue Development in Hydrogel-Based Scaffolds: A Study With Cartilaginous Model. Macromolecular Bioscience 2015;15:535-45.

[95] Ahadian S, Yamada S, Ramon-Azcon J, Ino K, Shiku H, Khademhosseini A, et al. Rapid and high-throughput formation of 3D embryoid bodies in hydrogels using the dielectrophoresis technique. Lab on a Chip 2014;14:3690-4.

[96] Hamilton G, Rath B. Applicability of tumor spheroids for in vitro chemosensitivity assays. Expert Opinion On Drug Metabolism&Toxicology 2019;15:15-23.

[97] Schon BS, Schrobback K, van der Ven M, Stroebel S, Hooper GJ, Woodfield TBF. Validation of a high-throughput microtissue fabrication process for 3D assembly of tissue engineered cartilage constructs. Cell and Tissue Research 2012;347:629-42.

[98] Yu Y, Moncal KK, Li JQ, Peng WJ, Rivero I, Martin JA, et al. Three-dimensional bioprinting using self-assembling scalable scaffold-free "tissue strands" as a new bioink. Scientific Reports 2016;6:28714.

[99] Nycz CJ, Strobel HA, Suqui K, Grosha J, Fischer GS, Rolle M. A Method for High-Throughput Robotic Assembly of 3-Dimensional Vascular Tissue. Tissue Engineering Part A 2019; DOI: 10.1089/ten.TEA.2018.0288.

[100] Bhumiratana S, Eton RE, Oungoulian SR, Wan LQ, Ateshian GA, Vunjak-Novakovic G. Large, stratified, and mechanically functional human cartilage grown in vitro by mesenchymal condensation. Proceedings of the National Academy of Sciences 2014;111:6940-5.

[101] Wang CC, Chen CH, Hwang SM, Lin WW, Huang CH, Lee WY, et al. Spherically Symmetric Mesenchymal Stromal Cell Bodies Inherent with Endogenous Extracellular Matrices for Cellular Cardiomyoplasty. Stem cells (Dayton, Ohio) 2009;27:724-32.

[102] Shih H, Greene T, Korc M, Lin C-C. Modular and Adaptable Tumor Niche Prepared from Visible Light Initiated Thiol-Norbornene Photopolymerization. Biomacromolecules 2016;17:3872-82.

[103] Raza A, Ki CS, Lin C-C. The influence of matrix properties on growth and morphogenesis of human pancreatic ductal epithelial cells in 3D. Biomaterials 2013;34:5117-27.

[104] Rao W, Zhao S, Yu J, Lu X, Zynger DL, He X. Enhanced enrichment of prostate cancer stem-like cells with miniaturized 3D culture in liquid core-hydrogel shell microcapsules. Biomaterials 2014;35:7762-73.

[105] Xu X, Gurski LA, Zhang C, Harrington DA, Farach-Carson MC, Jia X. Recreating the tumor microenvironment in a bilayer, hyaluronic acid hydrogel construct for the growth of prostate cancer spheroids. Biomaterials 2012;33:9049-60.

[106] Yang X, Sarvestani SK, Moeinzadeh S, He X, Jabbari E. Three-Dimensional-Engineered Matrix to Study Cancer Stem Cells and Tumorsphere Formation: Effect of Matrix Modulus. Tissue Engineering Part A 2013;19:669-84.

[107] Souza GR, Molina JR, Raphael RM, Ozawa MG, Stark DJ, Levin CS, et al. Three-dimensional tissue culture based on magnetic cell levitation. Nature Nanotechnology 2010;5:291-6.

[108] Luciani N, Du V, Gazeau F, Richert A, Letourneur D, Le Visage C, et al. Successful chondrogenesis within scaffolds, using magnetic stem cell confinement and bioreactor maturation. Acta Biomaterialia 2016;37:101-10.

[109] Chan HF, Zhang Y, Ho Y-P, Chiu Y-L, Jung Y, Leong KW. Rapid formation of multicellular spheroids in double-emulsion droplets with controllable microenvironment. Scientific Reports 2013;3:3462.

[110] Chan HF, Zhang Y, Leong KW. Efficient One-Step Production of Microencapsulated Hepatocyte Spheroids with Enhanced Functions. Small 2016;12:2720-30.

[111] Williams SK, Touroo JS, Church KH, Hoying JB. Encapsulation of adipose stromal vascular fraction cells in alginate hydrogel spheroids using a direct-write three-dimensional printing system. BioResearch open access 2013;2:448-54.

[112] Malinen MM, Kanninen LK, Corlu A, Isoniemi HM, Lou Y-R, Yliperttula ML, et al. Differentiation of liver progenitor cell line to functional organotypic cultures in 3D nanofibrillar cellulose and hyaluronan-gelatin hydrogels. Biomaterials 2014;35:5110-21.

[113] Pei X, Ma L, Zhang BQ, Sun JX, Sun Y, Fan YJ, et al. Creating hierarchical porosity hydroxyapatite scaffolds with osteoinduction by three-dimensional printing and microwave sintering. Biofabrication 2017;9:045008.

[114] Bryers JD, Giachelli CM, Ratner BD. Engineering biomaterials to integrate and heal: The biocompatibility paradigm shifts. Biotechnology and Bioengineering 2012;109:1898-911.

[115] Yin Z, Chen X, Song HX, Hu JJ, Tang QM, Zhu T, et al. Electrospun scaffolds for multiple tissues regeneration in vivo through topography dependent induction of lineage specific differentiation. Biomaterials 2015;44:173-85.

[116] Chen XN, Fan HY, Deng XW, Wu LN, Yi T, Gu LX, et al. Scaffold Structural Microenvironmental Cues to Guide Tissue Regeneration in Bone Tissue Applications. Nanomaterials 2018;8:960.

[117] Leach JK, Whitehead J. Materials-Directed Differentiation of Mesenchymal Stem Cells for Tissue Engineering and Regeneration. ACS Biomaterials Science & Engineering 2018;4:1115-27.

[118] Das RK, Zouani OF. A review of the effects of the cell environment physicochemical nanoarchitecture on stem cell commitment. Biomaterials 2014;35:5278-93.

[119] Kai D, Jin GR, Prabhakaran MP, Ramakrishna S. Electrospun synthetic and natural nanofibers for regenerative medicine and stem cells. Biotechnology Journal 2013;8:59.

[120] Eslahi N, Abdorahim M, Simchi A. Smart Polymeric Hydrogels for Cartilage Tissue Engineering: A Review on the Chemistry and Biological Functions. Biomacromolecules 2016;17:3441-63.

[121] Zhang J, Zhang H, Xu X. CHAPTER 17 Smart Materials to Regulate the Fate of Stem Cells. Smart Materials for Tissue Engineering: Applications: The Royal Society of Chemistry; 2017. p. 473-504.

[122] Higuchi A, Ling Q-D, Kumar SS, Chang Y, Kao T-C, Munusamy MA, et al. External stimulus-responsive biomaterials designed for the culture and differentiation of ES, iPS, and adult stem cells. Progress in Polymer Science 2014;39:1585-613.

[123] Chan A, Orme RP, Fricker RA, Roach P. Remote and local control of stimuli responsive materials for therapeutic applications. Advanced Drug Delivery Reviews 2013;65:497-514.

[124] Jun I, Lee YB, Choi YS, Engler AJ, Park H, Shin H. Transfer stamping of human mesenchymal stem cell patches using thermally expandable hydrogels with tunable cell-adhesive properties. Biomaterials 2015;54:44-54.

[125] Kaibuchi N, Iwata T, Yamato M, Okano T, Ando T. Multipotent mesenchymal stromal cell sheet therapy for bisphosphonate-related osteonecrosis of the jaw in a rat model. Acta Biomaterialia 2016;42:400-10.

[126] Long T, Zhu ZA, Awad HA, Schwarz EM, Hilton MJ, Dong YF. The effect of mesenchymal stem cell sheets on structural allograft healing of critical sized femoral defects in mice. Biomaterials 2014;35:2752-9.

[127] Kaibuchi N, Iwata T, Onizuka S, Yano K, Tsumanuma Y, Yamato M, et al. Allogeneic multipotent mesenchymal stromal cell sheet transplantation promotes healthy healing of wounds caused by zoledronate and dexamethasone in canine mandibular bones. Regenerative Therapy 2019;10:77-83.

[128] Radhakrishnan J, Subramanian A, Krishnan UM, Sethuraman S. Injectable and 3D Bioprinted Polysaccharide Hydrogels: From Cartilage to Osteochondral Tissue Engineering. Biomacromolecules 2017;18:1-26.

[129] Panadero JA, Lanceros-Mendez S, Ribelles JLG. Differentiation of mesenchymal stem cells for cartilage tissue engineering: Individual and synergetic effects of three-dimensional environment and mechanical loading. Acta Biomaterialia 2016;33:1-12.

[130] Fahy N, Alini M, Stoddart MJ. Mechanical stimulation of mesenchymal stem cells: Implications for cartilage tissue engineering. Journal of Orthopaedic Research 2018;36:52-63.

[131] Choi JR, Yong KW, Choi JY. Effects of mechanical loading on human mesenchymal stem cells for cartilage tissue engineering. Journal of Cellular Physiology 2018;233:1913-28.

[132] Sala RL, Kwon MY, Kim M, Gullbrand SE, Henning EA, Mauck RL, et al. Thermosensitive Poly(N-vinylcaprolactam) Injectable Hydrogels for Cartilage Tissue Engineering. Tissue Engineering Part A 2017;23:935-45.

[133] Yeon B, Park MH, Moon HJ, Kim S-J, Cheon YW, Jeong B. 3D Culture of Adipose-Tissue-Derived Stem Cells Mainly Leads to Chondrogenesis in Poly(ethylene glycol)-Poly(l-alanine) Diblock Copolymer Thermogel. Biomacromolecules 2013;14:3256-66.

[134] Chun C, Lim HJ, Hong KY, Park KH, Song SC. The use of injectable, thermosensitive poly(organophosphazene)-RGD conjugates for the enhancement of mesenchymal stem cell osteogenic differentiation. Biomaterials 2009;30:6295-308.

[135] Park JS, Woo DG, Yang HN, Lim HJ, Park KM, Na K, et al. Chondrogenesis of human mesenchymal stem cells encapsulated in a hydrogel construct: neocartilage formation in animal models as both mice and rabbits. Journal of Biomedical Materials Research. Part A 2010;92:988-96.

[136] Brunelle AR, Horner CB, Low K, Ico G, Nam J. Electrospun thermosensitive hydrogel scaffold for enhanced chondrogenesis of human mesenchymal stem cells. Acta Biomaterialia 2018;66:166-76.

[137] Maeda T, Kim YJ, Aoyagi T, Ebara M. The Design of Temperature-Responsive Nanofiber Meshes for Cell Storage Applications. Fibers 2017;5:13.

[138] Kim YJ, Ebara M, Aoyagi T. A Smart Nanofiber Web That Captures and Releases Cells. Angewandte Chemie International Edition 2012;51:10537-41.

[139] Su W-T, Chou W-L, Chou C-M. Osteoblastic differentiation of stem cells from human exfoliated deciduous teeth induced by thermosensitive hydrogels with strontium phosphate. Materials Science and Engineering: C 2015;52:46-53.

[140] Naderi-Meshkin H, Andreas K, Matin MM, Sittinger M, Bidkhori HR, Ahmadiankia N, et al. Chitosan-based injectable hydrogel as a promising in situ forming scaffold for cartilage tissue engineering. Cell Biology International 2014;38:72-84.

[141] Dhivya S, Saravanan S, Sastry TP, Selvamurugan N. Nanohydroxyapatite-reinforced chitosan composite hydrogel for bone tissue repair in vitro and in vivo. Journal of Nanobiotechnology 2015;13:40.

[142] Campos DFD, Blaeser A, Buellesbach K, Sen KS, Xun WW, Tillmann W, et al. Bioprinting Organotypic Hydrogels with Improved Mesenchymal Stem Cell Remodeling and Mineralization Properties for Bone Tissue Engineering. Advanced Healthcare Materials 2016;5:1336-45.

[143] Richardson SM, Hughes N, Hunt JA, Freemont AJ, Hoyland JA. Human mesenchymal stem cell differentiation to NP-like cells in chitosan-glycerophosphate hydrogels. Biomaterials 2008;29:85-93.

[144] Na K, Kim SW, Sun BK, Woo DG, Yang HN, Chung HM, et al. Osteogenic differentiation of rabbit mesenchymal stem cells in thermo-reversible hydrogel constructs containing hydroxyapatite and bone morphogenic protein-2 (BMP-2). Biomaterials 2007;28:2631-7.

[145] Chen H, Sun J, Wang Z, Zhou Y, Lou Z, Chen B, et al. Magnetic Cell–Scaffold Interface Constructed by Superparamagnetic IONP Enhanced Osteogenesis of Adipose-Derived Stem Cells. ACS Applied Materials & Interfaces 2018;10:44279-89.

[146] Samal SK, Goranov V, Dash M, Russo A, Shelyakova T, Graziosi P, et al. Multilayered Magnetic Gelatin Membrane Scaffolds. ACS Applied Materials & Interfaces 2015;7:23098-109.

[147] Zhang NY, Lock J, Sallee A, Liu HN. Magnetic Nanocomposite Hydrogel for Potential Cartilage Tissue Engineering: Synthesis, Characterization, and Cytocompatibility with Bone Marrow Derived Mesenchymal Stem Cells. ACS Applied Materials & Interfaces 2015;7:20987-98.

[148] Samal SK, Dash M, Shelyakova T, Declercq HA, Uhlarz M, Banobre-Lopez M, et al. Biomimetic Magnetic Silk Scaffolds. ACS Applied Materials & Interfaces 2015;7:6282-92.

[149] Huang JH, Lian YJ, Huang ZW, Zhao PC, Liang Q, Li YL, et al. Magnetic Enhancement of Chondrogenic Differentiation of Mesenchymal Stem Cells. ACS Biomaterials Science & Engineering 2019;5:2200-7.

[150] Singh RK, Patel KD, Lee JH, Lee E-J, Kim J-H, Kim T-H, et al. Potential of Magnetic Nanofiber Scaffolds with Mechanical and Biological Properties Applicable for Bone Regeneration. PLOS ONE 2014;9:1-16.

[151] Esmaeili E, Soleimani M, Ghiass MA, Hatamie S, Vakilian S, Zomorrod MS, et al. Magnetoelectric nanocomposite scaffold for high yield differentiation of mesenchymal stem cells to neural-like cells. Journal of Cellular Physiology 2019;234:13617-28.

[152] Daňková J, Buzgo M, Vejpravová J, Kubíčková S, Sovková V, Vysloužilová L, et al. Highly efficient mesenchymal stem cell proliferation on poly-ε-caprolactone nanofibers with embedded magnetic nanoparticles. International Journal of Nanomedicine 2015;10:7307-17.

[153] Ross CL, Siriwardane M, Almeida-Porada G, Porada CD, Brink P, Christ GJ, et al. The effect of low-frequency electromagnetic field on human bone marrow stem/progenitor cell differentiation. Stem Cell Research 2015;15:96-108.

[154] Kim EC, Leesungbok R, Lee SW, Lee HW, Park SH, Mah SJ, et al. Effects of Moderate Intensity Static Magnetic Fields on Human Bone Marrow-Derived Mesenchymal Stem Cells. Bioelectromagnetics 2015;36:267-76.

[155] Kavand H, Haghighipour N, Zeynali B, Seyedjafari E, Abdemami B. Extremely Low Frequency Electromagnetic Field in Mesenchymal Stem Cells Gene Regulation: Chondrogenic Markers Evaluation. Artificial Organs 2016;40:929-37.

[156] Parate D, Franco-Obregón A, Fröhlich J, Beyer C, Abbas AA, Kamarul T, et al. Enhancement of mesenchymal stem cell chondrogenesis with short-term low intensity pulsed electromagnetic fields. Scientific Reports 2017;7:9421.

[157] Bloise N, Petecchia L, Ceccarelli G, Fassina L, Usai C, Bertoglio F, et al. The effect of pulsed electromagnetic field exposure on osteoinduction of human mesenchymal stem cells cultured on nano-TiO2 surfaces. PLOS ONE 2018;13: e0199046.

[158] Yong Y, Ming ZD, Feng L, Chun ZW, Hua W. Electromagnetic fields promote osteogenesis of rat mesenchymal stem cells through the PKA and ERK1/2 pathways. Journal of Tissue Engineering and Regenerative Medicine 2016;10:E537-E45.

[159] Ferroni L, Tocco I, De Pieri A, Menarin M, Fermi E, Piattelli A, et al. Pulsed magnetic therapy increases osteogenic differentiation of mesenchymal stem cells only if they are pre-committed. Life Sciences 2016;152:44-51.

[160] Du LL, Fan HY, Miao HS, Zhao GF, Hou YY. Extremely Low Frequency Magnetic Fields Inhibit Adipogenesis of Human Mesenchymal Stem Cells. Bioelectromagnetics 2014;35:519-30.

[161] Seong Y, Moon J, Kim J. Egr1 mediated the neuronal differentiation induced by extremely low-frequency electromagnetic fields. Life Sciences 2014;102:16-27.

[162] Kim HJ, Jung J, Park JH, Kim JH, Ko KN, Kim CW. Extremely low-frequency electromagnetic fields induce neural differentiation in bone marrow derived mesenchymal stem cells. Experimental Biology and Medicine 2013;238:923-31.

[163] Li XP, Zhang MS, Bai LM, Bai WF, Xu WC, Zhu HX. Effects of 50 Hz pulsed electromagnetic fields on the growth and cell cycle arrest of mesenchymal stem cells: an in vitro study. Electromagnetic Biology and Medicine 2012;31:356-64.

[164] Assa F, Jafarizadeh-Malmiri H, Ajamein H, Anarjan N, Vaghari H, Sayyar Z, et al. A biotechnological perspective on the application of iron oxide nanoparticles. Nano Research 2016;9:2203-25.

[165] Zhou S, Yin T, Zou Q, Zhang K, Gao G, Shapter JG, et al. Labeling adipose derived stem cell sheet by ultrasmall super-paramagnetic Fe(3)O(4) nanoparticles and magnetic resonance tracking in vivo. Scientific Reports 2017;7:42793.

[166] Silva LHA, Silva SM, Lima ECD, Silva RC, Weiss DJ, Morales MM, et al. Effects of static magnetic fields on natural or magnetized mesenchymal stromal cells: Repercussions for magnetic targeting. Nanomedicine-Nanotechnology Biology and Medicine 2018;14:2075-85.

[167] Naseroleslami M, Aboutaleb N, Parivar K. The effects of superparamagnetic iron oxide nanoparticles-labeled mesenchymal stem cells in the presence of a magnetic field on attenuation of injury after heart failure. Drug Delivery and Translational Research 2018;8:1214-25.

[168] Yun WS, Choi JS, Ju HM, Kim MH, Choi SJ, Oh ES, et al. Enhanced Homing Technique of Mesenchymal Stem Cells Using Iron Oxide Nanoparticles by Magnetic Attraction in Olfactory-Injured Mouse Models. International Journal of Molecular Sciences 2018;19:1376.

[169] Riegler J, Liew A, Hynes SO, Ortega D, O'Brien T, Day RM, et al. Superparamagnetic iron oxide nanoparticle targeting of MSCs in vascular injury. Biomaterials 2013;34:1987-94.

[170] Cho H, Choi YK, Lee DH, Park HJ, Seo YK, Jung H, et al. Effects of magnetic nanoparticle-incorporated human bone marrow-derived mesenchymal stem cells exposed to pulsed electromagnetic fields on injured rat spinal cord. Biotechnology and Applied Biochemistry 2013;60:596-602.

[171] Wang YXJ, Quercy-Jouvet T, Wang HH, Li AW, Chak CP, Xuan SH, et al. Efficacy and Durability in Direct Labeling of Mesenchymal Stem Cells Using Ultrasmall Superparamagnetic Iron Oxide Nanoparticles with Organosilica, Dextran, and PEG Coatings. Materials 2011;4:703-15.

[172] Shrestha S, Jiang PF, Sousa MH, Morais PC, Mao ZW, Gao CY. Citrate-capped iron oxide nanoparticles impair the osteogenic differentiation potential of rat mesenchymal stem cells. Journal of Materials Chemistry B 2016;4:245-56.

[173] Chang YK, Liu YP, Ho JH, Hsu SC, Lee OK. Amine-surface-modified superparamagnetic iron oxide nanoparticles interfere with differentiation of human mesenchymal stem cells. Journal of Orthopaedic Research 2012;30:1499-506.

[174] Wang Q, Chen B, Ma F, Lin S, Cao M, Li Y, et al. Magnetic iron oxide nanoparticles accelerate osteogenic differentiation of mesenchymal stem cells via modulation of long noncoding RNA INZEB2. Nano Research 2017;10:626-42.

[175] Jiang PF, Zhang YX, Zhu CN, Zhang WJ, Mao ZW, Gao CY. Fe3O4/BSA particles induce osteogenic differentiation of mesenchymal stem cells under static magnetic field. Acta Biomaterialia 2016;46:141-50.

[176] Choi YK, Lee DH, Seo YK, Jung H, Park JK, Cho H. Stimulation of Neural Differentiation in Human Bone Marrow Mesenchymal Stem Cells by Extremely Low-Frequency Electromagnetic Fields Incorporated with MNPs. Applied Biochemistry and Biotechnology 2014;174:1233-45.

[177] Kirkham GR, Elliot KJ, Keramane A, Salter DM, Dobson JP, El Haj AJ, et al. Hyperpolarization of Human Mesenchymal Stem Cells in Response to Magnetic Force. IEEE Transactions On Nanobioscience 2010;9:71-4.

[178] Markides H, McLaren JS, Telling ND, Alom N, Al-Mutheffer EA, Oreffo ROC, et al. Translation of remote control regenerative technologies for bone repair. Npj Regenerative Medicine 2018;3:9.

[179] Li XY, Wei ZH, Lv HY, Wu LY, Cui YN, Yao H, et al. Iron oxide nanoparticles promote the migration of mesenchymal stem cells to injury sites. International Journal of Nanomedicine 2019;14:573-89.

[180] Gloria A, Russo T, D'Amora U, Zeppetelli S, D'Alessandro T, Sandri M, et al. Magnetic poly(Ɛ-caprolactone)/iron-doped hydroxyapatite nanocomposite substrates for advanced bone tissue engineering. Journal of The Royal Society Interface 2013;10:20120833.

[181] Zhu YF, Shang FJ, Li B, Dong Y, Liu YF, Lohe MR, et al. Magnetic mesoporous bioactive glass scaffolds: preparation, physicochemistry and biological properties. Journal of Materials Chemistry B 2013;1:1279-88.

[182] Lu JW, Yang F, Ke QF, Xie XT, Guo YP. Magnetic nanoparticles modified-porous scaffolds for bone regeneration and photothermal therapy against tumors. Nanomedicine-Nanotechnology Biology and Medicine 2018;14:811-22.

[183] Yang F, Lu J, Ke Q, Peng X, Guo Y, Xie X. Magnetic Mesoporous Calcium Sillicate/Chitosan Porous Scaffolds for Enhanced Bone Regeneration and Photothermal-Chemotherapy of Osteosarcoma. Scientific Reports 2018;8:7345.

[184] Eppink B, Krawczyk PM, Stap J, Kanaar R. Hyperthermia-induced DNA repair deficiency suggests novel therapeutic anti-cancer strategies. International Journal of Hyperthermia 2012;28:509-17.

[185] Zhang YL, Zhai D, Xu MC, Yao QQ, Chang J, Wu CT. 3D-printed bioceramic scaffolds with a Fe3O4/graphene oxide nanocomposite interface for hyperthermia therapy of bone tumor cells. Journal of Materials Chemistry B 2016;4:2874-86.

[186] Farzin A, Fathi M, Emadi R. Multifunctional magnetic nanostructured hardystonite scaffold for hyperthermia, drug delivery and tissue engineering applications. Materials Science & Engineering C-Materials for Biological Applications 2017;70:21-31.

[187] Kamitakahara M, Ohtoshi N, Kawashita M, Ioku K. Spherical porous hydroxyapatite granules containing composites of magnetic and hydroxyapatite nanoparticles for the hyperthermia treatment of bone tumor. Journal of Materials Science-Materials in Medicine 2016;27:93.

[188] Jedlovszky-Hajdu A, Molnar K, Nagy PM, Sinko K, Zrinyi M. Preparation and properties of a magnetic field responsive three-dimensional electrospun polymer scaffold. Colloid Surface A 2016;503:79-87.

[189] Zhang J, Li JC, Chen SW, Kawazoe N, Chen GP. Preparation of gelatin/Fe3O4 composite scaffolds for enhanced and repeatable cancer cell ablation. Journal of Materials Chemistry B 2016;4:5664-72.

[190] Helminger M, Wu BH, Kollmann T, Benke D, Schwahn D, Pipich V, et al. Synthesis and Characterization of Gelatin-Based Magnetic Hydrogels. Advanced Functional Materials 2014;24:3187-96.

[191] Mack JJ, Cox BN, Sudre O, Corrin AA, Lucato SLDE, Ma C, et al. Achieving nutrient pumping and strain stimulus by magnetic actuation of tubular scaffolds. Smart Materials&Structures 2009;18:104025.

[192] Markaki AE, Clyne TW. Magneto-mechanical stimulation of bone growth in a bonded array of ferromagnetic fibres. Biomaterials 2004;25:4805-15.

[193] Go G, Han J, Zhen J, Zheng S, Yoo A, Jeon MJ, et al. A Magnetically Actuated Microscaffold Containing Mesenchymal Stem Cells for Articular Cartilage Repair. Advanced Healthcare Materials 2017;6:1601378.

CHAPTER III

ENHANCED MULTI-LINEAGE DIFFERENTIATION OF HUMAN MESENCHYMAL STEM/STROMAL CELLS WITHIN POLY (*N*-ISOPROPYLACRYLAMIDE-ACRYLIC ACID) MICROGEL-FORMED THREE-DIMENSIONAL CONSTRUCTS

Statement of Authorship

Title of Paper	Enhanced Multi-Lineage Differentiation of Human Mesenchymal Stem/Stromal Cells within Poly (*N*-isopropylacrylamide-Acrylic Acid) Microgel-Formed Three-Dimensional Constructs
Publication Status	☑ Published ☐ Accepted for Publication ☐ Submitted for Publication ☐ Unpublished and Unsubmitted work written in manuscript style
Publication Details	Zhang, J.; Yun, S.; Bi, J.; Dai, S.; Du, Y.; Zannettino, A. C. W.; Zhang, H., Journal of Materials Chemistry B 2018, 6 (12), 1799-1814. doi: 10.1039/c8tb00376a.

Principal Author

Name of Principal Author (Candidate)	Jiabin Zhang		
Contribution to the Paper	Performed experiments, analysed data, writing manuscript.		
Overall percentage (%)	80%		
Certification:	This paper reports on original research I conducted during the period of my Higher Degree by Research candidature and is not subject to any obligations or contractual agreements with a third party that would constrain its inclusion in this thesis. I am the primary author of this paper.		
Signature		Date	26/07/2019

Co-Author Contributions

By signing the Statement of Authorship, each author certifies that:

i. the candidate's stated contribution to the publication is accurate (as detailed above);

ii. permission is granted for the candidate in include the publication in the thesis; and

iii. the sum of all co-author contributions is equal to 100% less the candidate's stated contribution.

Name of Co-Author	Seonho Yun		
Contribution to the Paper	Experiment design and evaluation of data.		
Signature		Date	16/07/2019

Name of Co-Author	Jingxiu Bi		
Contribution to the Paper	Proof read the manuscript and evaluation.		
Signature		Date	16/07/2019

Name of Co-Author	Sheng Dai		
Contribution to the Paper	Proof read the manuscript and evaluation.		
Signature		Date	26/07/2019

Name of Co-Author	Yuguang Du		
Contribution to the Paper	Proof read the manuscript and evaluation.		
Signature		Date	2019.7.15

Name of Co-Author	Andrew Zannettino		
Contribution to the Paper	Proof read the manuscript, experiment design, and evaluation of data.		
Signature		Date	16 July 2019

Name of Co-Author	Hu Zhang		
Contribution to the Paper	Proof read the manuscript, experiment design, and evaluation of data.		
Signature		Date	July 15, 2019

Please cut and paste additional co-author panels here as required.

Enhanced Multi-Lineage Differentiation of Human Mesenchymal Stem/Stromal Cells within Poly (*N*-Isopropylacrylamide-Acrylic Acid) Microgel-Formed Three-Dimensional Constructs

Jiabin Zhang[1], *Seonho Yun*[1], *Jingxiu Bi*[1], *Sheng Dai*[4], *Yuguang Du*[3], *Andrew C.W. Zannettino*[2]*, *Hu Zhang*[1]*

[1]School of Chemical Engineering, The University of Adelaide, Adelaide, SA 5005, Australia

[2]Adelaide Medical School, The University of Adelaide, Adelaide, SA 5001, Australia

[3]Institute of Process Engineering, Chinese Academy of Sciences, Beijing, 100190, China

[4]School of Engineering, Newcastle University, Newcastle, NE1 7RU, United Kingdom

[*]Corresponding author: E-mail: hu.zhang@adelaide.edu.au (H.Z.), E-mail: andrew.zannettino@adelaide.edu.au (A.C.W.Z.)

Published: Journal of Materials Chemistry B 2018, 6 (12), 1799-1814, DOI: 10.1039/c8tb00376a.

3.1 Graphical abstract

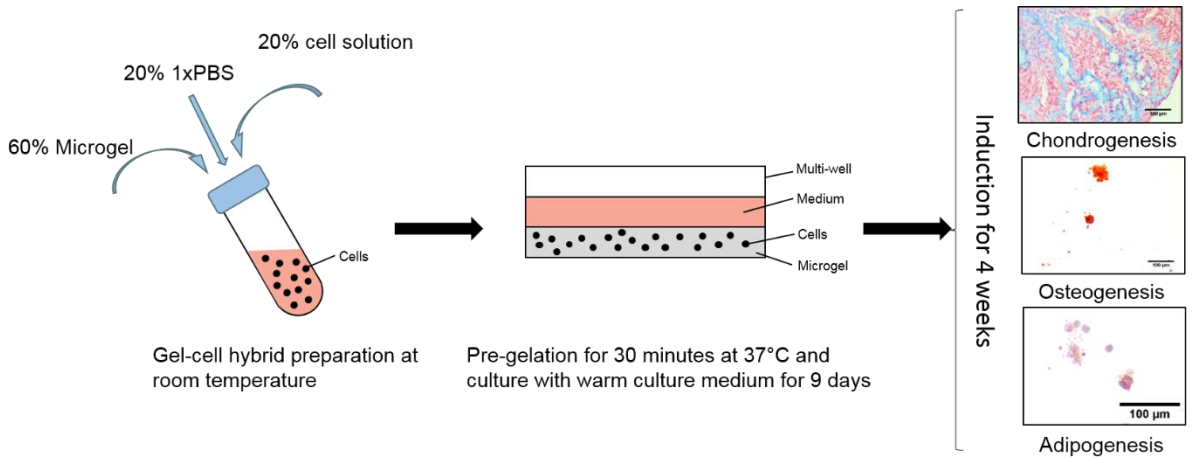

hMSCs derived from normal donors were induced multi-lineage differentiation in the thermosensitive p(NIPAAm-AA) microgel-formed 3D constructs.

3.2 Abstract

Human mesenchymal stem/stromal cells (hMSCs) are a potential cell source of stem cell therapy for many serious diseases and hMSC spheroids have emerged to replace single cell suspensions for cell therapy. Three-dimensional (3D) scaffolds or hydrogels which can mimic properties of the extracellular matrix (ECM) have been widely explored for their application in tissue regeneration. However, there are considerably less studies on inducing differentiation of hMSC spheroids using 3D scaffolds or hydrogels. This study is the first to explore multi-lineage differentiation of a stem cell line and primary stem cells within poly (*N*-isopropylacrylamide) (p(NIPAAm))-based thermosensitive microgel-formed constructs. We first demonstrated that poly (*N*-isopropylacrylamide-co-acrylic acid) (p(NIPAAm-AA)) was not toxic to hMSCs and the microgel-formed constructs facilitated formation of uniform stem cell spheroids. Due to functional enhancement of cell spheroids, hMSCs within the 3D microgel-formed constructs were induced for multi-lineage differentiation as evidenced by significant up-regulation of messenger RNA (mRNA) expression of chondrogenic and osteogenic genes even in the absence of induction media on day 9. When induction media were in-situ supplied on day 9, mRNA expression of chondrogenic, osteogenic and adipogenic genes within the microgel-formed constructs were significantly higher than that in the pellet and 2D cultures, respectively, on day 37. In addition, histological and immunofluorescent images also confirmed successful multi-lineage differentiation of hMSCs within the 3D microgel-formed constructs. Hence, the thermosensitive p(NIPAAm-AA) microgel can be potentially used in an *in-vitro* model for cell differentiation or *in-vivo* transplantation of pre-differentiated human mesenchymal stromal cells into patients for specific lineage differentiation.

KEYWORDS: poly (*N*-isopropylacrylamide); microgel; multi-lineage differentiation; tissue engineering; cell spheroid; human mesenchymal stem/stromal cell

3.3 Introduction

Stem cells, such as human mesenchymal stem/stromal cells (hMSCs), are a potential cellular therapy source to treat serious diseases [1], such as cartilage injury [2-4], spinal injury [5, 6] and cardiac failure [7-9]. They can be differentiated into chondrocytes [10, 11], osteoblasts [12, 13] and adipocytes [14] both *in vitro* and *in vivo*. [15] However, the lack of cell retention within the defective sites following injection as single-cell suspensions limits their clinical application. [16] Hence, stem cell spheroids are emerging as an alternative to single cell suspensions to improve cell retention during implantation. [16, 17] Recent reports also suggest that hMSC spheroids possess enhanced anti-inflammatory and multi-lineage differentiation properties. [16, 18, 19]

However, cellular spheroids have to be carefully prepared for clinical application to mitigate issues, such as necrosis within the center of the spheroid [20]. The size of cellular spheroids is one of important parameters for quality control. It is also essential to have a better understanding of differentiation of cellular spheroids *in vitro* so that the spheroids can be applied to patients.

Three-dimensional (3D) microenvironments are known as native niches that can significantly regulate migration, proliferation, and differentiation of stem cells. [21, 22] The extracellular matrix (ECM) of tissues provides both physical and biochemical cues, such as stiffness and RGD-motifs, respectively, which act in concert to influence cell behavior. [23-25] Water-rich smart hydrogels, allowing mimicking the properties of ECM and customized incorporation of other biochemical stimuli, recently become attractive for stem cell-based tissue engineering. [11, 26-30] Thermosensitive hydrogels are one example of smart hydrogels that can respond to temperature change. They are highly porous and abundant in water, providing 3D mechanical support for cells and facilitating gas and mass exchange between the incorporated cells and the surrounding environment. [31]

Poly (*N*-isopropylacrylamide) (p(NIPAAm)) is a widely used thermosensitive polymer that can reversibly transform from sol to gel status when heated above its lower critical solution temperature (LCST), 32 °C, which is close to the temperature of human body. [32] It can be easily synthesized in a large quantity and even bonded with natural components, such as RGD peptides [33], gelatin [34], hyaluronic acid [14], chitosan [35], to improve its biological properties. When a pNIPAAm hydrogel forms a gel, water is expelled out of the hydrogel and the hydrogel shrinks, via a process of syneresis, making it unsuitable for cell culture. To prevent the syneresis, hydrophilic components, such as acrylic acid (AA), are copolymerized with pNIPAAm. In addition, after further crosslinking, thermosensitive p(NIPAAm-AA) microgels are produced. [32] Once the carboxyl groups of p(NIPAAm-AA) are ionized, the p(NIPAAm-AA) microgel has a negative charge and makes the internal porosity larger, allowing more efficient gas and mass exchange. [32]

Stem cell differentiation into single type of cells in the thermosensitive hydrogels has been reported and the 3D microenvironment offered from the hydrogels is found to have a great impact on cellular differentiation. [35-39] However, there are very few studies comprehensively examining the multi-lineage differentiation of human mesenchymal stromal cell spheroids generated within p(NIPAAm)-based thermosensitive microgel-formed constructs. [15, 16] Therefore, in this study, we successfully synthesized a thermosensitive p(NIPAAm-AA) microgel that not only mimicked 3D ECM properties but also facilitated spheroids harvest because of its thermal reversibility. The microgel showed no toxicity to the hMSCs from both 2D and 3D toxicity assays. After they were cultured within the 3D microgel-formed construct, hMSCs formed uniform cell spheroids of 100 μm in diameter without central necrosis [20], while they proliferated at a much slower rate than the hMSCs grown in 2D conventional culture. Messenger RNA (mRNA) expression of chondrogenic, osteogenic and adipogenic genes were significantly upregulated for both immortalized bone marrow derived human mesenchymal stem/stromal cells (UE7T-13) and primary normal donor derived human

mesenchymal stem/stromal cells (NOD MSCs) in microgel-formed 3D constructs than that in pellet and 2D cultures, respectively. Even in the absence of induction media, UE7T-13 displayed multi-lineage differentiation with a relatively higher mRNA expression of chondrogenic genes (SOX9 and aggrecan) and osteogenic genes (RUNX2 and osterix) due to inductive properties of the matrix and the formation of cell spheroids [16]. Histological images revealed rich glycosaminoglycan (GAGs) distributing within complex chondrogenic micro-tissues, calcification within osteogenic cells, and lipids within adipogenic cells. Immunofluorescent images also showed distinct collagen II A1, osteocalcin and perilipin signals. Hence, we can conclude that the thermosensitive microgel-formed constructs can effectively induce multi-lineage differentiation of human stem cells, which can be potentially used in an *in-vitro* model for cell differentiation and tissue engineering or *in-vivo* transplantation of pre-differentiated human stem cells [40] into patients for specific lineage differentiation.

3.4 Materials and Methods

3.4.1 Microgel synthesis

The poly (*N*-isopropylacrylamide-co-acrylic acid) (p(NIPAAm-AA)) microgel was synthesized by free radical emulsion polymerization as previously described. [32] Briefly, 9.9 mmol of *N*-isopropylacrylamide (NIPAAm, >98%, Tokyo Chemical Industry) (recrystallized in n-hexane and dried overnight), 0.2 mmol of *N*, *N*'-methylenebisacrylamide (MBA, >99%, Sigma-Aldrich), 0.12 mmol of sodium dodecyl sulfate (SDS, >99%, BDH Laboratory Supplies Poole), and 0.1 mmol acrylic acid (AA, 99.5%, Acros Organics) were dissolved in 97 mL of Milli-Q® water. The solution was mechanically stirred and continuously degassed with nitrogen supply at 70 °C for 45 min in a 250 mL of three-necked flask. Subsequently, 3 mL of 1 mM potassium persulfate (KPS, >98%, Chem-Supply) in Milli-Q® water was injected to initiate the polymerization. After synthesis overnight, the microgel was left cool at room temperature and dialyzed with a Spectra/Por® molecular porous membrane tubing (Spectrum Labs, cut-off MW

12-14 kDa) against Milli-Q® water for one week with daily water change. The purified microgel was concentrated by heating at 70 °C, after which 100 μL of microgel was dried and weighted to calculate the final concentration.

3.4.2 Size distribution measurement of p(NIPAAm-AA) microgel

0.5 mg/mL of p(NIPAAm-AA) dissolved in water and 1× Dulbecco's phosphate buffered saline (DPBS, pH ≈ 7.4) were prepared, respectively. Their hydrodynamic diameters were measured by dynamic light scattering (DLS) at 25°C and 37 °C with a Zetasizer (Malvern, Nano-ZS). The detection angle was set at 90° and the intensity autocorrelation function was analyzed by the CONTIN software.

3.4.3 Dynamic moduli measurement

30 mg/mL p(NIPAAm-AA) microgel-formed three-dimensional (3D) constructs were prepared by mixing 50 mg/mL microgel, 0.05 M $MgCl_2$ in 1× Dulbecco's phosphate buffered saline (DPBS, pH ≈ 7.4) and complete growth medium at a volumetric ratio of 3:1:1. The temperature was kept at 37 °C for 60 min prior to measurement by a SR 5 environmental system connected to a water bath (Julabo) and the gap was set to 0.65 mm. The elastic modulus (G') and viscous modulus (G") of the constructs were measured at different stress from 0.1 to 100 Pa under a constant frequency of 0.1 Hz by a SR5 rheometer (Rheometric Scientific) equipped with a 40 mm parallel plate geometry.

3.4.4 Transmittance measurement in the p(NIPAAm-AA) formed 3D constructs

P(NIPAAm-AA) formed 3D constructs were prepared in the same way as described in "Dynamic moduli measurement" section at room temperature. 100 μL of the construct was transferred into each 96-well plate in triplicates and the transmittance was read by a Molecular Devices VersaMax microplate reader. The wavelength of the light was set at 720 nm. The temperature was kept at 37 °C from 0 to 30 min. The transmittance of p(NIPAAm-AA) microgel-formed constructs were recorded every minute during heating at 37 °C. Then the p(NIPAAm-AA) microgel-formed constructs were kept at 37 °C in an incubator. After the

temperature in the microplate reader was set at 25 °C, the p(NIPAAm-AA) microgel-formed constructs were transferred back to the microplate reader. The transmittance of the p(NIPAAm-AA) microgel-formed constructs was measured during cooling at 25 °C and recorded every minute for another 30 min. The transmittance in the blank wells was used as the control. The recorded data were averaged and normalized to the control.

3.4.5 Preparation of cell-gel 3D constructs

Briefly, microgel was sterilized by exposure to UV for 40 min. An immortalised human mesenchymal stromal cell line, UE7T-13 (RIKEN BioResources Center, Ibaraki, Japan, http://en.brc.riken.jp), or bone-derived mesenchymal stromal cells obtained from the iliac crest chips of normal donors (NOD MSCs) with an approval, RAH Protocol No.940911a, from the Royal Adelaide Hospital Ethics Committee as described previously [41, 42] (ND0127 NODs, ND0303 NODs, ND0055 NODs, ND0302 NODs, ND0057 NODs and ND0059 NODs) were cultured on T-75 flask in a humidified, 5% CO_2 and 37°C incubator with a complete growth medium feeding and changing every other day (α-modified Eagle's medium (MEM, Sigma-Aldrich) supplemented with 10% fetal calf serum (FCS, Sigma-Aldrich) and 1× additive's (ADDs) (50 U/mL- 50 μg/mL penicillin-streptomycin (CSL), 2 mM L-glutamine (JRH), 1 mM sodium pyruvate (Sigma-Aldrich), 15 mM HEPES (Life Technologies)). Single-cell suspensions were prepared by washing twice with 1× Dulbecco's phosphate-buffered saline (DPBS, Sigma-Aldrich), trypsin digestion (GIBCO), enzyme quenching with the complete medium, discarding supernatant after centrifuging, and resuspending cells in the complete medium. The cell-gel hybrid was prepared by homogeneously mixing single-cell suspension, filter-sterilized magnesium chloride ($MgCl_2$) solution (dissolving hexahydrate magnesium chloride (Chem-Supply) in 1× DPBS and filtered with 0.22 μm of porosity of syringe filter), and the microgel at a volumetric ratio 1:1:3, resulting in the certain cell density and final concentration of 0.01M $MgCl_2$ and 30 mg/mL microgel, respectively. Passage 45-48 of UE7T-13 and passage 5-6 of NOD MSCs were used in the experiments reported.

3.4.6 Cell proliferation assay

Cell proliferation within the microgel was measured by 4-[3-(4-Iodophenyl)-2-(4-nitrophenyl)-2H-5-tetrazolio]-1,3-benzene disulfonate (WST-1, Sigma-Aldrich) cell proliferation assay. Briefly, 50 μL of coating microgel at a volumetric ratio of 50 mg/mL microgel : 0.05 M $MgCl_2$ in 1× DPBS : complete growth medium of 3:1:1 was coated on the each well of 96-well plate at 37 °C for 30 min. Then 125 μL of UE7T-13 cell-gel hybrid with a density of 1.0×10^6 or 1.0×10^5 cells/mL was gelled on the coated 96-well plate in the humidified incubator containing 5% CO_2 at 37 °C for additional 30 min. Warm complete growth medium (125 μL) was added into each well and regularly changed every other day on a dry block heater (Ratek Instruments) at 37 °C for up to 14 days. After 1, 5, 9 and 14 days, the 96-well was cooled down at room temperature and homogeneously mixed with 20 μL of WST-1 after discarding the 100 μL of complete growth medium above the hydrogel. Continuous incubation of the WST-1 mixture was carried out in a humidified incubator containing 5% CO_2 at 37 °C for 4 hr. The absorbed wavelength of solubilized formazan was measured at 450 nm by an iMark™ microplate reader (BIO-RAD) after liquidation of cell-gel hybrids on the ice. Cells cultured on the two-dimensional (2D) 96-well plate were considered as a control and processed in the same way as for the 3D cultures while using Milli-Q® water to replace the microgel. To eliminate the background absorbance, the same experiment was performed without cells as a reference. The difference in measured values between absorbance and reference were used for temporal profile of cell proliferation. Three different NOD MSCs (ND0302 NODs, ND0127 NODs and ND0059 NODs) with a density of 1.0×10^5 cells/mL were processed in the same way as UE7T-13.

3.4.7 Cell viability assay

The cytotoxicity of the microgel was measured by the MTT assay as described previously. [32] Briefly, 100 μL of UE7T-13 cells in the complete growth medium were seeded onto each well of 96-well plate at a density of 1.0×10^5 cells/mL and cell attachment was achieved by overnight incubation in a humidified incubator containing 5% CO_2 at 37 °C. The media were changed

with a series of different microgel concentration dissolved in the complete growth medium (0.05 mg/mL, 0.1 mg/mL, 0.5 mg/mL, 1 mg/mL, 5 mg/mL, 30 mg/mL) at 100 μL per well and cultured for another 24 hr. Subsequently, the medium containing the microgel was changed with the same volume of fresh complete growth medium and 10 μL of 5 mg/mL 3-(4,5-Dimethylthiazol-2-yl)-2,5-diphenyltetrazolium bromide (MTT, Thermo Fisher Scientific) was added into each well. Following an additional 4 hr incubation, all media were collected and discarded and 100 μL of dimethyl sulfoxide (DMSO, Chem-Supply) was added to each well to dissolve the formed formazan crystals within the cells. Cells fed by the medium without the microgel were used as a control and processed in the same way as the cells exposed to the microgel. The absorbance of the dissolved formazan in DMSO was read by an iMark^{TM} microplate reader (BIO-RAD) at a wavelength of 595 nm. All reading absorbance were normalized to the absorbance value of the control and presented as relative absorbance.

3.4.8 Cell viability staining

UE7T-13 viability within the microgel was measured by fluorescently staining cells with the Live&Dead staining kit (Thermo Fisher Scientific). Briefly, 250 μL of coating microgel was added into each well of 48-well plate and incubated at 37°C for 30 min to initiate gel formation. The warm cell-gel hybrid with a density of 1.0×10^6 cells/mL was gently added into each microgel-coated 48-well plate that was kept at 37 °C using a hotplate. Gel formation was initiated and cells in the gel were continuously incubated in a humidified incubator containing 5% CO_2 at 37 °C with 500 μL of complete medium which was regularly changed every other day up to 9 days. The working solution was prepared as 4 μM calcein AM and 2 μM ethidium homodimer-1 in 1× DPBS. After 1 or 9 days, 500 μL of the feeding medium on each cell-gel hybrid was discarded, while the 48-well plate was cooled down at room temperature. 250 μL of the working solution was added into each well and homogeneously mixed with the cell-gel hybrid. After incubation at room temperature for 20 min, cells were imaged with a fluorescent microscope. Cell-gel hybrids on the 48-well plate without the microgel were also stained and

imaged as described above. In addition, pellets (**Control 1**) were cultured by spinning down the same amount of the cells in a 10 mL polypropylene tube (SARSTEDT Australia). In addition, cells were also cultured on the 1.5% agar coated 48-well plate (**Control 2**). **Control 1** and **Control 2** were both cultured in a humidified incubator containing 5% CO_2 at 37 °C for up to 9 days with medium change every other day. After 1 or 9 days, **Control 1** were stained as cell-gel hybrids and transferred to 48-well plate for fluorescent imaging, while **Control 2** were directly *in-situ* fluorescently imaged after Live&Dead staining with a CKX41 fluorescent microscope (Olympus). Live cells were shown as green, while dead cells were shown as red.

3.4.9 Trypan Blue cell counting and Annexin/7-AAD apoptosis flow cytometry

UE7T-13 cell-gel hybrids were prepared on the microgel-coated 48-well plate as described in the "Cell viability staining" section. After incubation in a humidified atmosphere containing 5% CO_2 at 37 °C for 24 hr, cell-gel hybrids were liquefied at room temperature, transferred into 15 mL of polypropylene tubes and diluted with 10 mL of 1× DPBS. The cells were centrifuged at 383 rcf for 10 min and homogeneously resuspended in 500 μL fresh complete growth medium after discarding the supernatant. 11 μL of cell solution was mixed with the same volume of Trypan Blue (Sigma-Aldrich) and completely mixed before manual cell counting on a BS.748 cell counting chamber plate (Hawksley) under a CX41optical microscope (Olympus). Live cells without blue staining, and blue stained dead cells were counted. Cells cultured on the 2D 48-plate were used as a control and processed similarly as 3D cells. Subsequently, the number of live cells divided by the total cells was presented as cell viability. Relative cell viability was normalized with respect to the cell viability in 2D culture.

After Trypan Blue cell counting, the remaining cell suspensions of 3D and 2D were centrifuged in FACS tubes at 383 rcf for 2 min. The supernatant was discarded, and the cells were washed with 2 mL of cold binding buffer (10 mM HEPES and 5 mM calcium chloride (Scharlau) in 20 mL 1× Hank's balanced salt solution (Sigma-Aldrich)) and centrifuged at 383 rcf for 2 min. After the supernatant was discarded, cells were enzymatically digested in 1 mL of proteinase

(1.5 mg/mL of collagenase (Scimar) and 2 mg/mL of dispase (Invitrogen)) for 10 min and neutralized in 10 mL of complete growth medium. Then cells were centrifuged again and gently resuspended in 50 μL of binding buffer. The fresh UE7T-13 detached by enzymatic digestion from T-75 flask were centrifuged in FACS tubes and cell apoptosis induced by resuspending them in 1 mL of 100% DMSO for 10 min at room temperature (**positive control 1**) or cell necrosis by resuspending in 1 mL of 80% ethanol for 10 min on the ice (**positive control 2**). In addition, the freshly detached cells were also resuspended in 1 mL of complete growth medium (**negative control**). Then 3 mL of complete medium was added into each FACS tube of all controls. The cells were centrifuged at 383 rcf for 2 min, washed once with 2 mL of binding buffer, and resuspended in 50 μL of in-house binding buffer. 5 μL of 2.5 μg/mL PE-AnnexinV (Biolegend) and 20 μL of 7-AAD (Beckman Coulter) were added into each cell suspension of 2D or 3D. **Positive control 1** groups were stained with 5 μL of AnnexinV and 20 μL of in-house binding buffer, while **positive control 2** groups were stained with 5 μL of in-house binding buffer and 20 μL of 7-AAD. **Negative control** groups left unstained and 25 μL of in-house binding buffer was added. FACS tubes were kept in the dark and on ice for 20 min during staining. Cell apoptosis was immediately measured by a flow cytometer (BD, FACSCanto II Analyser) after 200 μL of in-house binding buffer was added into each FACS tube. Only those events which were negative to AnnexinV and 7-AAD were considered as live cells. Eventually, data was presented as relative cell viability by normalizing the percentage of live cells to those cells cultured in 2D.

3.4.10 Scanning electron microscopy (SEM) imaging of cell-gel 3D constructs

The UE7T-13 cell-gel hybrids were prepared as described in "Cell viability staining" section and cultured with the complete growth medium in a humidified atmosphere containing 5% CO_2 at 37 °C. After cultured overnight, the feeding medium on the top of the cell-gel hybrid was removed and cell-gel 3D constructs were immediately frozen in liquid nitrogen. The frozen cell-gel constructs were then dried under vacuum by a Christ Alpha 2-4 LD freeze dryer. The

cross-sections of the cell-gel constructs were then coated with a layer of platinum and imaged with a Philips XL30 FEGSEM at an accelerating voltage of 10 kV.

3.4.11 STRO-1 flow cytometry

UE7T-13 cultured on 2D plates and in cell-gel constructs were prepared, respectively, in triplicate (1 unstained control + 1 STRO-1 negative control+ 1 STRO-1 positive test) as described in "Cell viability staining" section. After overnight, the cells were harvested and suspended in 1mL 1× DPBS. Then the cells were blocked with 1 mL 1× blocking buffer (Hank's balanced salt solution (Sigma-Aldrich) contained 5% heat-inactivated normal human serum, 1% bovine serum albumin (BSA, Sigma-Aldrich), 50 U/mL-50 μg/mL penicillin-streptomycin (CSL) and 5% fetal calf serum (FCS, Sigma-Aldrich)) on ice for 20 min to reduce the non-specific immunofluorescent staining. Then the supernatant was removed after spinning down cells. The cells as the unstained control were resuspended in 100 μL blocking buffer, while the cells as STRO-1 negative control and STRO-1 positive test were incubated in 100 μL 1 A6.12 (isotype matched IgM negative control/ anti-salmonella provided by Dr L Ashman) and 100 μL STRO-1 hybridoma supernatant on ice for 45 min, respectively. All cells were washed in 1 mL of washing buffer (1× Hank's balanced salt solution contained 5% FCS (Sigma-Aldrich)) and centrifuged to remove the supernatant. Then the cells as STRO-1 negative controls and STRO-1 positive tests were incubated in 100 μL 20 μg/mL of a goat-anti-mouse IgM-FITC conjugated second antibody (Southern Biotech), while the cells as unstained controls were resuspended in 100 μL washing buffer. The cells were washed in 1 mL of washing buffer after incubated on ice in the dark for 30 min and fixed in 2% paraformaldehyde (Sigma-Aldrich). The cell suspensions were then measured by a flow cytometer (BD, FACSCanto II Analyser). The representatives of STRO-1 flow cytometry for UE7T-13 cells cultured on 2D plates and in microgel-formed 3D constructs were then presented.

3.4.12 Cell cycle assay

UE7T-13 cell-gel constructs were prepared in triplicate as described in "Cell viability staining" section for fluorescein isothiocyanate (FITC) labelled KI-67 and propidium iodide (PI) double staining. The cells cultured on six independent 2D plates were prepared as the controls (1 unstained control + 1 FITC-KI-67 stained control + 1 PI stained control + 3 FITC-KI-67 and PI double stained controls). After overnight, the cells were harvested by washing and spinning twice in 4 mL washing buffer (1× DPBS contained 1% FCS) at 384 rcf for 5 min. The supernatant was discarded and 2 mL of -20 °C 70% (v/v) ethanol was added in a dropwise manner while vortexing. The fixed cells were centrifuged at 850 rcf for 10 min after incubated at -20 °C for 2 h. Then the ethanol was removed and the cells were washed in 2 mL washing buffer twice at 850 rcf for 10 min. Cells were then suspended in 100 μL washing buffer. The cell suspensions for FITC-KI-67 staining were incubated with 5 μL FITC-labelled KI-67 monoclonal antibody (eBioScience^{TM}, Invitrogen) at room temperature in the dark for 30 min, while the others were only incubated with 5 μL washing buffer. All cells were then washed in 2mL washing buffer twice by centrifuging at 850 rcf for 10 min each. The cells for PI staining were resuspended and incubated in 250 μL PI working solution (1× DPBS contained 100 μg/mL RNase A (Qiagen), 50 μg/mL PI solution (Sigma-Aldrich), and 2 mM $MgCl_2$) at room temperature in the dark for 20 min, while the others were simply incubated in 250 μL washing buffer. After staining, the cell cycle was measured by a flow cytometer (BD, FACSCanto II Analyser).

3.4.13 Cell size distribution assay

Cell-gel hybrids (UE7T-13 and three different NOD MSCs (ND0302 NODs, ND0127 NODs and ND0057 NODs)) were prepared in microgel-coated 48-well plates as described in "Cell viability staining" section and incubated in a humidified atmosphere containing 5% CO_2 at 37 °C. The culture medium was changed every other day for up to 9 days. Cell-gel hybrids were cooled at room temperature and imaged with an optical microscope on day 9. Typically, 5 images were randomly taken with a CKX41 optical microscope (Olympus) for each well and

processed with image J (National Institutes of Health, USA). Subsequently, only cell area larger than 354 μm^2 was measured and number of cells with different area was presented.

3.4.14 The effect of microgels on cell differentiation of UE7T-13 and NOD MSCs with induction media

3D cell-gel hybrids of UE7T-13 and three different NOD MSCs (ND0303 NODs, ND0055 NODs and ND0059 NODs) in the coated 48-well plates were prepared as described in the "Cell viability staining" section. The 48-well plates were incubated in a humidified incubator containing 5% CO_2 at 37°C and the media were regularly changed every other day for up to 9 days. Cell differentiation was induced by replacing the complete medium with (1) chondrogenic inductive medium to stimulate chondrogenesis (high glucose Dulbecco's Modified Eagle's Medium (DMEM-high, Sigma-Aldrich) supplemented with 1× ITS+ Premix (BD Biosciences), 50 U/mL- 50 μg/mL penicillin-streptomycin (CSL), 2 mM L-glutamine, 100 μM L-ascorbate-2-phosphate (WAKO), 0.1 μM DBL^{TM} Dexamethasone sodium phosphate (Hospira Australia), 0.125% bovine serum albumin (BSA, Sigma-Aldrich), 10 ng/mL human transforming growth factor-beta 3 (TGF-β3, Chemicon International); (2) osteogenic inductive medium to stimulate osteogenesis (MEM supplemented with 5% FCS (Sigma-Aldrich), 1× ADDs, 100 μM L-ascorbate-2-phosphate, 0.1 μM Dexamethasone, 2.64 mM potassium dihydrogenphosphate (KH_2PO_4, BDH)); (3) adipogenic inductive medium to stimulate adipogenesis (MEM supplemented with 10% FCS (Sigma-Aldrich), 1× ADDs, 100 μM L-ascorbate-2-phosphate, 0.1 μM Dexamethasone, 60 μM indomethacin (Sigma-Aldrich)). Cells were continuously cultured in the humidified incubator containing 5% CO_2 at 37°C for another 4 weeks with chondrogenic medium change three times weekly, while osteogenic and adipogenic medium change twice weekly. Pellets of cells, centrifuged at 600 rcf for 5 min and cultured in a 10 mL polypropylene tube, were used as the control for 3D chondrogenesis, while cells on the 2D 48-well plate were considered as the control of 3D for osteogenesis and adipogenesis. The controls

were cultured and differentiated in the same way as 3D while the microgel was replaced with Milli-Q® water. The mRNA of cells was extracted and analyzed after 37 days.

3.4.15 The effect of microgels on cell differentiation of UE7T-13 without induction media

3D cell-gel hybrids of UE7T-13 were prepared in microgel-coated 48-well plates as described in "Cell viability staining" section, while cell-gel hybrids were kept in the complete growth medium for up to 37 days. Cells centrifuged at 600 rcf for 5 min and cultured in a polypropylene tube were used as chondrogenic control while cells cultured on a 2D 48-well plate were used as osteogenic and adipogenic controls. The controls were cultured in the same way as cells within 3D microgel-formed constructs. After 9 days or 37 days, the mRNA of cells was extracted and analyzed.

3.4.16 RNA extraction

At pre-determined time points, cell-gel hybrids were harvested and centrifuged as described in the "Trypan Blue cell counting and AnnexinV/7-AAD apoptosis flow cytometry" section. The cells were subsequently lysed by homogeneously mixing with 1 mL of ambion® TRIzol (Life Technologies) for 5 min at room temperature. The separated top layer was retained after addition of 200 μL chloroform and spinning at 12000 rcf for 15 min at 4 °C. Then mRNA was precipitated by addition of 1.5 μL glycogen (Roche Diagnostics) and incubating on ice for 1 hr after gently mixing with 500 μL of isopropanol. The precipitated mRNA was centrifuged at 12000 rcf for 10 min at 4 °C and washed with 75% of cold ethanol at 7500 rcf for 5 min. mRNA was dissolved in 30 μL of RNase free water at 55 °C for 10 min after removal of all ethanol. mRNA concentration was measured by a Nanodrop spectrophotometer (Thermo Fisher Scientific).

3.4.17 Reverse transcription polymerase chain reaction (RT-PCR)

1 μg of extracted mRNA was homogeneously mixed with 1 μL 100 ng/mL of random primers (Geneworks) and 1 μL 10 mM of dNTPs (Adelab Scientific) and nuclease free water (Invitrogen) to a final volume of 14 μL in a PCR tube. The mixture was incubated at 65 °C for

5 min and subsequently placed on ice for 1 min by a Veriti 96 well thermal cycler (Applied Biosystems). Subsequently, the solution was homogeneously mixed with 6 μL of reverse transcriptase pre-mix (1 μL 100 mM of DTT (Thermo Fisher Scientific, Invitrogen) and 1 μL 200 U/μL of SuperScript™ IV reverse transcriptase (Thermo Fisher Scientific, Invitrogen) dissolved in 4 μL of 5x superscript IV reverse transcriptase buffer (Thermo Fisher Scientific, Invitrogen)). RT-PCR was initiated by a Veriti 96 well thermal cycler with the setting of 55 °C for 60 min and 80 °C for 10 min. After RT-PCR, the cDNA was diluted with 80 μL of nuclease free water and stored at -20 °C.

3.4.18 Real-time polymerase chain reaction

2 μL cDNA of each sample was mixed with 7.5 μL of RT² SYBR® GREEN ROX™ qPCR Mastermix (QIAGEN), 0.75 μL forward/reverse primer pair (10 μM each, gene sequence of β-actin, chondrogenic, osteogenic, and adipogenic genes as detailed in Table 3.1), and 4.75 μL of nuclease free water and loaded into a clear thin-walled Hard-Shell® 96-well PCR plate (BIO-RAD). The gene for each sample was prepared in triplicate and run by a CFX Connect™ Real-Time PCR Detection System (BIO-RAD). Meanwhile, nuclease free water was used as a control.

Table 3.1 Specific primers for reverse transcription polymerase chain reaction.

Primers	**Sequence (5'➔3')**
β-actin	Forward: GATCATTGCTCCTCCTGAGC
	Reverse: GTCATAGTCCGCCTAGAAGCAT
SOX9	Forward: AGGTGCTCAAAGGCTACGAC
	Reverse: GCTTCTCGCTCTCGTTCAGA
Aggrecan	Forward: CTGCTTCCGAGGCATTTC
	Reverse: GCTCGGTGGTGAACTCTAGC
Collagen II	Forward: ATCACAGGCTTCCATTGACC
	Reverse: CTCCACAGCATCGATGTCAC
RUNX2	Forward: GTGGACGAGGCAAGAGTTTCA
	Reverse: CATCAAGCTTCTGTCTGTGCC

Osteocalcin	Forward: ATGAGAGCCCTCACACTCCTCG
	Reverse: GTCAGCCAACTCGTCACAGTCC
Osterix	Forward: CTGCGGGACTCAACAACTCT
	Reverse: GAGCCATAGGGGTGTGTCAT
Adipsin	Forward: GACACCATCGACCACGAC
	Reverse: CCACGTCGCAGAGAGTTC
C-ebpα	Forward: GGGCAAGGCCAAGAAGTC
	Reverse: TTGTCACTGGTCAGCTCCAG
Adiponectin	Forward: GCTGGGAGCTGTTCTACTGC
	Reverse: CGATGTCTCCCTTAGGACCA

3.4.19 Frozen tissue section preparation

Cell-gel hybrids of UE7T-13 or ND0303 NODs were prepared as described in "Cell viability staining" section and induced cell differentiation on day 9. Cells were cultured in chondrogenic, osteogenic, and adipogenic media for another 4 weeks, while cells cultured within the microgel with complete growth medium (without the addition of inductive media) were used as controls. After 37 days, the cells were harvested by diluting the cell-gel hybrids within cool 1×DPBS and spinning at 383 rcf for 5 min. The harvested cells were resuspended in 0.5 mL of 4% cold paraformaldehyde (PFA, Sigma-Aldrich) overnight for fixation. The cells were washed three times in 1 mL of 1×DPBS by centrifuging at 383 rcf for 10 min and immersed in 0.5 mL of 30% sucrose (Chem-Supply) overnight. The cell solution within sucrose was then transferred to the surface of a GF/C glass microfiber circle paper (Whatman, diameter of 2.1 cm) with filter papers and Kimwipes® absorbing water from the bottom. The side of the glass microfiber circle paper that contained cells were covered with one droplet of OCT compound (Tissue-Tek) and left on the working bench for 10 min. A standard pre-labeled Cryomold® (Tissue-Tek, 25mm x 20mm x 5mm) was upside down and allowed its bottom to loosely contact with the side of glass microfiber paper containing OCT. The OCT compound was topped-up on the other side of the glass microfiber paper after the Cryomold® was turned over. The Cryomold® with cells

was placed on the dry ice for freezing, after which the frozen Cryomold® was covered by aluminum foil in a sealed bag and stored at -80 °C.

Prior to sectioning, the frozen OCT-embedded cells were equilibrated to -20 °C for 20 min. Cells were then sectioned onto gelatin-coated slides (dipping microscope glass slides (Livingstone) 3-5 times (5 sec each) in 0.5 % (wt/v) of gelatin (Sigma-Aldrich) and 0.05 % (wt/v) chromium potassium sulfate dodecahydrate ($CrK(SO_4)_2 \bullet 12H_2O$, Sigma-Aldrich) solution and dry at room temperature for 24 hr) at 8 μm of thickness by a Cryostat Shandon Cryotome E (Thermo Fisher Scientific). The frozen tissue sections were kept in a sealed slide box at -80 °C.

3.4.20 Histological staining

3.4.20.1 Oil Red O staining

Frozen tissue slides were brought to room temperature for 1 hr and rinsed by 60% of isopropanol three times. The sectioned tissues were subsequently stained with Oil Red O working solution for 15 min, which was prepared by diluting 0.5% (wt/v) of isopropanol dissolved Oil Red O (ICN Biomedicals) stock solution in Milli-Q® water with the volumetric ratio of 3:2. Three washes in 60% of isopropanol were applied to wash out the unbound dye. The sectioned tissues were lightly stained in Mayer's hematoxylin (Fronine) by dipping the sections 5 times. The cells were "blued" by washing the sections in distilled water for 1 min. The sectioned slides were mounted with Aquatex® aqueous mountant (Merck) and covered with coverslips (Corning, 24mm x 50mm). Finally, the stained tissues were imaged with a CKX41 microscope.

3.4.20.2 Alizarin Red S staining

The frozen tissue sections were brought to room temperature for 1 hr and stained with 2% of Alizarin Red S solution (Sigma-Aldrich, pH 4.3 in Milli-Q® water) for 5 min. The sectioned tissues were, in turn, dehydrated with acetone, acetone:xylene (volumetric ratio 1:1), and xylene

(three times each). The sectioned slides were mounted in the CV mountant (Leica) and covered with coverslips. Finally, the stained tissues were imaged with a CKX41 microscope.

3.4.20.3 Alcian Blue staining

The frozen tissue sections were brought to room temperature for 1 hour and stained in 1% of Alcian Blue solution (Sigma-Aldrich, pH 2.5 in 3% of acetic acid) for 30 min. The sectioned tissues were counterstained with 0.1% of nuclear fast red solution (Sigma-Aldrich) for 5 min. After staining, sectioned slides were rinsed with distilled water to remove the dyes. 70% of ethanol, 100% of ethanol, and xylene were in turn used to dehydrate the tissues. After drying in air, the sectioned slides were mounted in the CV mountant and covered with coverslips. Finally, the stained tissues were imaged with a CKX41 microscope.

3.4.21 Immunofluorescent staining

The frozen tissue sections were brought to room temperature for 1 hr and covered with 200 μL of 5% normal serum from the same species as secondary antibody (normal goat serum (Thermo Fisher Scientific) for chondrogenic and adipogenic sections, while normal rabbit serum (Thermo Fisher Scientific) for osteogenic sections, diluting in 0.3% of Triton x-100/1×DPBS (Sigmar-Aldrich)) per section in a humidified box at room temperature for 60 min. After the blocking solution was removed, 250 μL of collagen II A1 primary antibody from rabbit (Santa Cruz) with 1:250 dilution in 0.3 % of Triton x-100/1×DPBS was added onto each chondrogenic tissue sectioned slide, 250 μL of perilipin primary antibody from rabbit (Cell signaling) with 1:250 dilution in 0.3% of Triton x-100/1×DPBS was added onto each adipogenic tissue sectioned slide, 250 μL of osteocalcin primary antibody from goat (Santa Cruz) with 1:250 dilution in 0.3% of Triton x-100/1×DPBS was added to each osteogenic tissue sectioned slides, respectively. The tissue sections were kept in a humidified box at 4 °C overnight. Then the sections were washed 3 times in 1×DPBS after flicking away the primary antibodies. 250 μL of the secondary antibodies (fluorescein (FITC) labeled goat-anti-rabbit secondary antibody (SouthernBiotech) with 1:250 dilution in 0.3% of Triton x-100/1×DPBS for chondrogenic and

adipogenic tissue sections, while FITC labeled rabbit-anti-goat secondary antibody (SouthernBiotech) with 1:250 dilution in 0.3% of Triton x-100/1×DPBS for osteogenic tissue sections) were added onto each slide and incubated at room temperature for 2 hr in a humidified box in the dark. In addition, the tissue sections were counterstained in 300 nM of DAPI (Sigma-Aldrich) for 15 min and rinsed three times in 1×DPBS for 5 min at room temperature. Finally, the tissue sections were imaged with an IX53 fluorescent microscope (Olympus) immediately after being mounted in the ProLong Gold Antifade reagent (Invitrogen) and covered with coverslips. After imaging, the tissue section slides were stored flat at 4 °C in the dark.

3.4.22 Statistical Analysis

All experiments were performed in triplicates. Data are presented as mean ± standard error (SE). Comparison between means was processed by one-tailed student t-test. Differences were considered as significant when $p < 0.05$, or the most significant when $p < 0.001$.

3.5 Results

3.5.1 Thermosensitive property of p(NIPAAm-AA).

Because of shrinkage after gelation [43], other investigators have copolymerized pNIPAAm with hydrophilic monomers to reduce the effect of syneresis.[32, 44, 45] In this study, p(NIPAAm-AA) microgel was successfully synthesized as preciously described[32]. The thermosensitive behavior, i.e. sol status at room temperature, while gelation at 37 °C (Figure S3.1), was confirmed by mixing 50 mg/mL of microgel with 0.05 M $MgCl_2$ dissolved in 1×DPBS and medium with a volumetric ratio of 3:1:1. Successful copolymerization of acrylic acid with *N*-isopropylacrylamide was confirmed with the evidence of microgel size increase in water compared to that in 1× DPBS at 25 °C (Figure S3.2 a). More carboxyl groups ionized in water than in 1× DPBS, which counteracted the hydrophobic effect of the backbone and increased the microgel size. However, external temperature became the dominant factor influencing the microgel size at 37 °C. Hence, no significant difference between the microgel size in water and 1× DPBS was seen. To study the reversibility of the thermosensitive behavior,

the time-dependent gelation process of p(NIPAAm-AA) microgel-formed 3D constructs was also investigated by measuring the transmittance at 37 °C and 25 °C. When the constructs were transferred from room temperature to 37 °C, the transmittance gradually decreased within 5 min, while sharply dropped down from 5 min to 10 min (Figure S3.2 b). After 15 min, the transmittance was kept at around 0%. The p(NIPAAm-AA) microgel-formed 3D constructs formed gel completely after incubation at 37 °C for 30 min. When the temperature was changed to 25 °C, transmittance of p(NIPAAm-AA) microgel-formed constructs sharply increased within 5 min and then kept at 100%, where the p(NIPAAm-AA) microgel-formed constructs were completely liquefied. In addition, the dynamic moduli of p(NIPAAm-AA) microgel-formed 3D constructs were measured by varying external stress at a frequency of 0.1 Hz at 37 °C (Figure S3.2 c). When the external stress increased above 0.12 Pa, the viscous modulus (G") became larger than the elastic modulus (G'), which was considered as the liquefied stress that transformed the gel status of the p(NIPAAm-AA) microgel-formed 3D constructs to the sol status.

3.5.2 No cytotoxicity of p(NIPAAm-AA) microgels to UE7T-13.

To study the cytotoxicity of the microgel to hMSCs cultured on a flat surface, different concentrations of the microgel dissolved in 1×DPBS were added to UE7T-13 pre-seeded 96 wells. The cells showed relatively high viability at a concentration ranging from 0.05 mg/mL to 5 mg/mL, while viability was reduced to 60% when the microgel was used at a concentration of 30 mg/mL (Figure S3.3 a). To further study the cytotoxicity of p(NIPAAm-AA) microgels to hMSCs at the concentration of 30 mg/mL, UE7T-13 were incorporated within the microgel-formed 3D constructs and cultured with complete growth medium for 24 hr. The relative cell viability was approximately 100%, irrespective of the methods for evaluating the cell viability (Trypan Blue staining and flow cytometry following PE-AnnexinV/7-AAD staining) (Figure S3.3 b). In addition, the majority of the cells cultured within the microgel-formed 3D constructs

(Figure S3.4) remained viable after cultured in the complete growth medium for 9 days (Figure S3.5 a ii).

3.5.3 Proliferation within 3D microgel-formed constructs compared with that on 2D surfaces.

To study the cell proliferation of hMSCs within the microgel-formed constructs, UE7T-13 and primary human mesenchymal stromal cells from three different normal donors (NOD MSCs) were cultured in the 3D microgel-formed constructs with the complete growth medium for up to 14 days. Since the reduction of WST-1 to soluble formazan is linearly proportional to cell number within a certain range, cell proliferation can be determined simply from the absorbance of the soluble formazan. UE7T-13 proliferated more slowly within 3D microgel-formed constructs than on the 2D plate (Figure 3.1 a). This difference was the most significant when 1×10^5 cells/mL were seeded from day 1 to day 9 while relatively significant from day 9 to day 14 (Figure 3.1 a). At a higher cell seeding density, 1×10^6 cells/mL, cell proliferation within the 3D microgel-formed constructs was still significantly lower than that on 2D plate throughout the 14-day culture (Figure 3.1 a). The results were consistent with the cell proliferation of three different NOD MSCs, which also showed a lower cell proliferation rate within the 3D microgel-formed constructs compared to the 2D plate when a seeding density of 1×10^5 cells/mL was used (Figure 3.1 b). Notably, this difference for NOD MSCs proliferation between 3D microgel-formed constructs and 2D culture was significant at all time points examined (Figure 3.1 b). After UE7T-13 cells from 2D plates and 3D microgel-formed constructs were harvested on day 1, cell surface stemness marker STRO-1 [42] was detected by flow cytometry. It was found that over 90% of cells from 2D plates and 3D microgel-formed constructs still kept STRO-1 antigen expression. There was no significant difference between both cell culture systems (Figure S3.6 a). To determine the reason for the low cell proliferation, cell cycle of UE7T-13 cells cultured on 2D plates and in 3D microgel-formed constructs was measured by FITC-KI-67 antibody and propidium iodide (PI) double staining flow cytometry. The result indicated that more UE7T-13

cells cultured within 3D microgel-formed constructs remained at the G0 phase of a cell cycle than those on 2D plates (Figure S3.6 b), while less UE7T-13 cells cultured within 3D microgel-formed constructs stayed at the S and G2/M phase of a cell cycle (Figure S3.6 b).

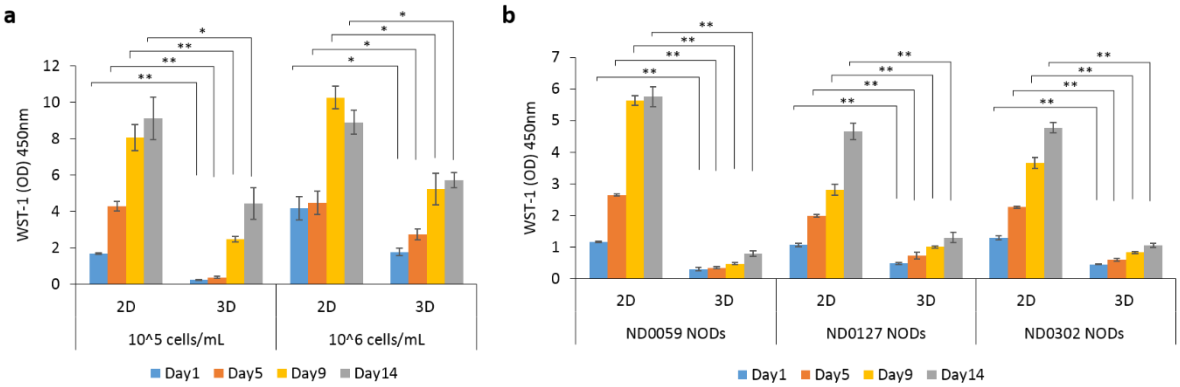

Figure 3.1 Proliferation of (a) UE7T-13 and (b) three NOD MSCs for 14 days. (2D: cells cultured on the multi-well plate, 3D: cells cultured within the thermosensitive p(NIPAAm-AA) microgel-formed constructs. Data were presented as the mean ± standard error (n = 3). *p < 0.05, **p < 0.001.

3.5.4 Multi-lineage cell differentiation of UE7T-13 within 3D microgel-formed constructs in the absence of induction media.

Even though the microgel was not toxic to the hMSCs, the cell proliferation rate of UE7T-13 and NOD MSCs within 3D microgel-formed constructs was significantly lower than that observed in 2D culture (Figure 3.1). To determine if this reduction in cell proliferation was accompanied by an increased propensity for hMSC differentiation within 3D microgel-formed constructs, mRNA expression of UE7T-13 for a range of osteogenic, adipogenic and chondrogenic genes was measured by quantitative real time PCR after 9 days and 37 days of culture in the complete growth media. On day 9, UE7T-13 cultured in 3D microgel-formed constructs showed higher mRNA expression of chondrogenic, osteogenic and adipogenic genes than the controls (Figure 3.2). Particularly SOX9, aggrecan, RUNX2 and osterix exhibited significant difference between 3D and the controls. However, on day 37 only mRNA expression of aggrecan within 3D microgel-formed constructs was significantly higher than that of cell pellets cultured within polypropylene tubes (Figure 3.3). Notably, the mRNA expression of

SOX9, collagen II, RUNX2, osteocalcin and adiponectin within 3D microgel-formed constructs on day 37 was significantly lower than that observed on day 9 (Figure 3.3).

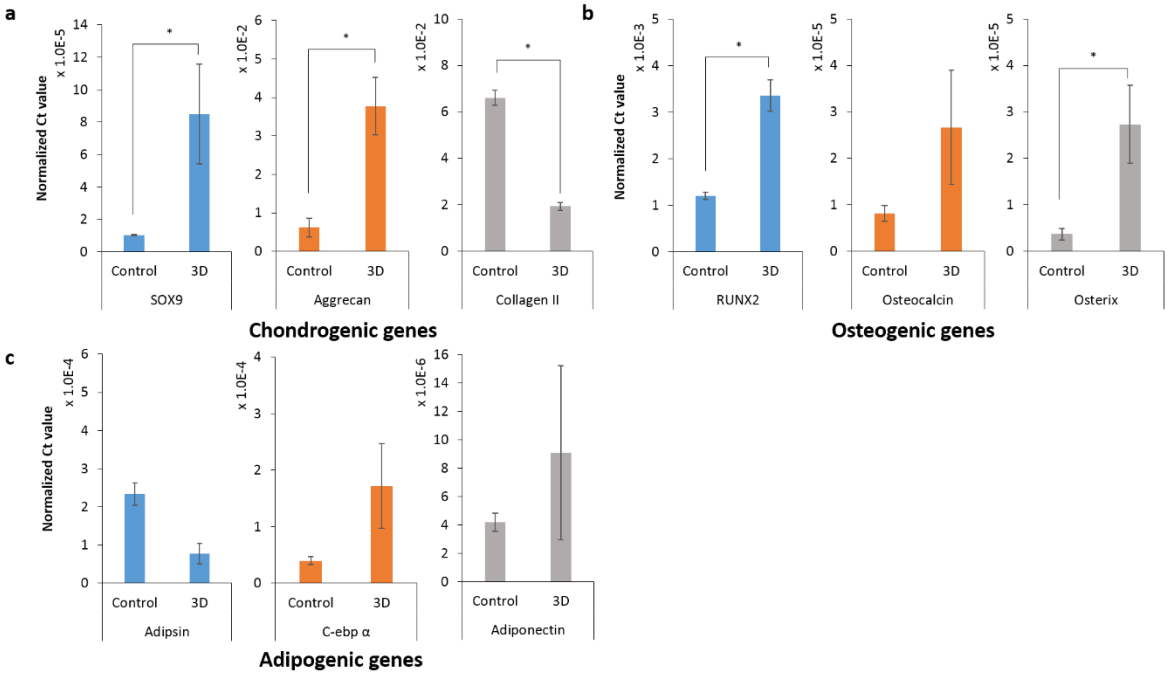

Figure 3.2 Cell differentiation of UE7T-13 without induction media. (a) Chondrogenic gene expression (control: cell pellets cultured in the polypropylene tube by centrifuge, 3D: cells cultured within the thermosensitive p(NIPAAm-AA) microgel-formed constructs); (b) osteogenic gene expression (control: cells cultured on the multi-well plate, 3D: cells cultured within thermosensitive p(NIPAAm-AA) microgel-formed constructs); and (c) adipogenic gene expression (control: cells cultured on the multi-well plate, 3D: cells cultured within thermosensitive p(NIPAAm-AA) microgel-formed constructs); of UE7T-13 without induction media on day 9. mRNA expression of genes were analysed by qRT-PCR and normalized to β-Actin. Data were presented as the mean ± standard error (n = 3). *p < 0.05.

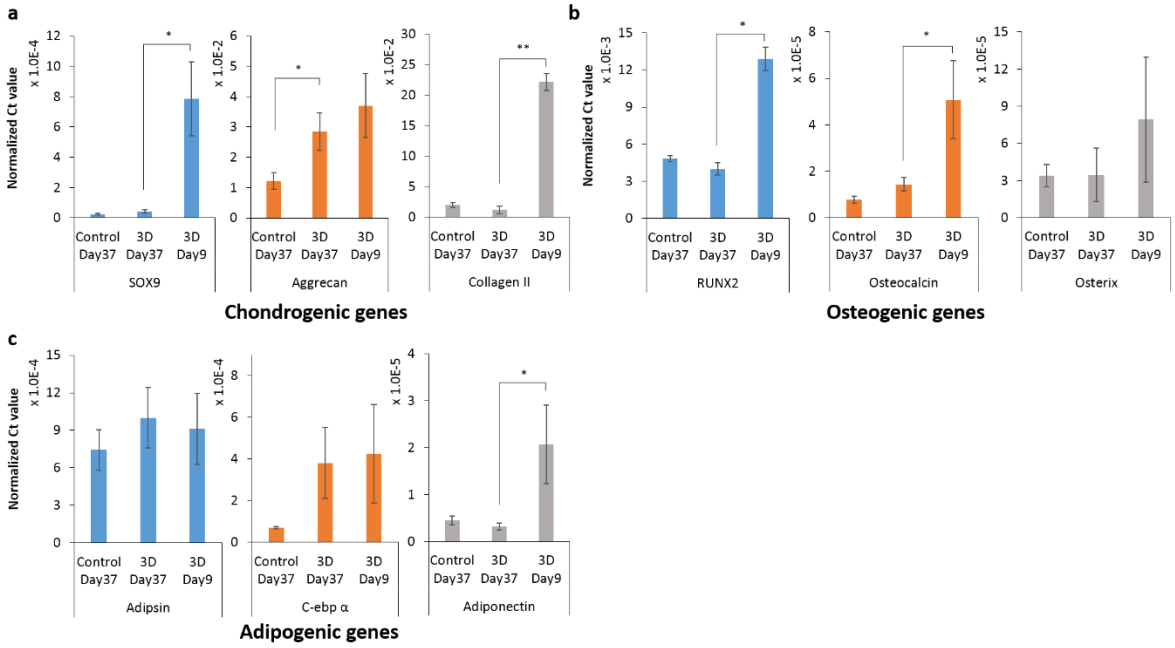

Figure 3.3 Cell differentiation of UE7T-13 without induction media. (a) Chondrogenic gene expression (control: cell pellets cultured in the polypropylene tube by centrifuge, 3D: cells cultured within the thermosensitive p(NIPAAm-AA) microgel-formed constructs); (b) osteogenic gene expression (control: cells cultured on the multi-well plate, 3D: cells cultured within thermosensitive p(NIPAAm-AA) microgel-formed constructs); and (c) adipogenic gene expression (control: cells cultured on the multi-well plate, 3D: cells cultured within thermosensitive p(NIPAAm-AA) microgel-formed constructs); of UE7T-13 without induction media on day 9 and day 37. mRNA expression of genes were analysed by qRT-PCR and normalized to β-Actin. Data were presented as the mean ± standard error (n = 3). *p < 0.05, **p < 0.001.

3.5.5 Multi-lineage differentiation of hMSCs in 3D microgel-formed constructs in specific induction medium.

From the studies described in Figure 3.1, it was evident that the maximal proliferative activity reached on day 9 of culture, after which cell proliferation decreased. Notably, on day 9, UE7T-13 appeared to form uniform cell spheroids within the 3D microgel-formed constructs with the help of microgel pre-coating on the culture plate on day 9 (Figure 3.4 a i, Figure 3.4 b and Figure S3.5 a, b).

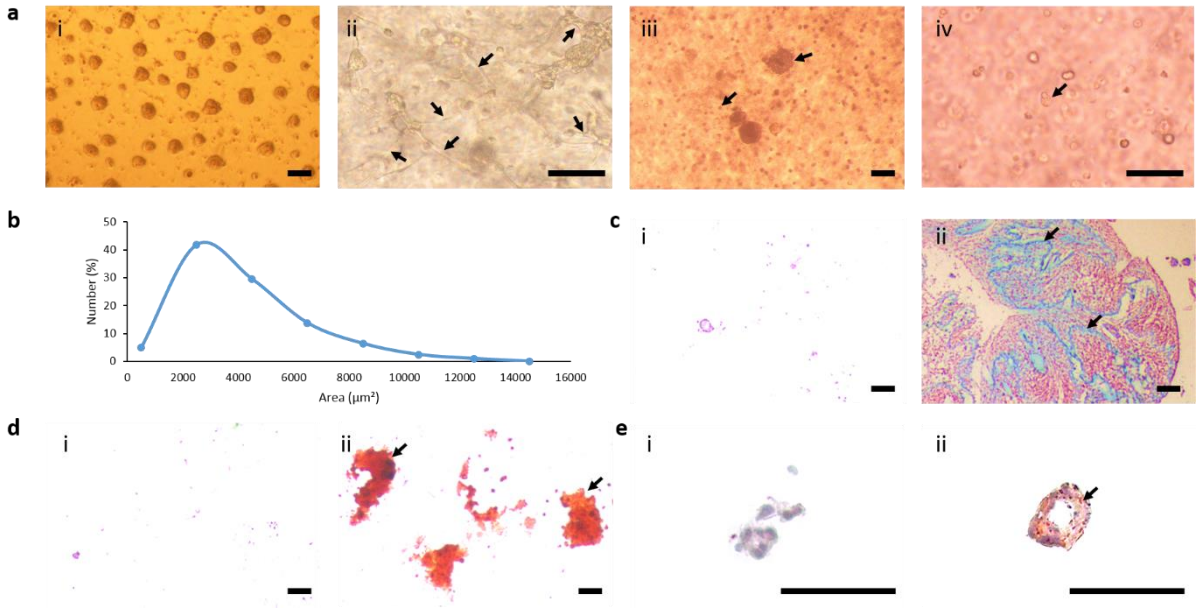

Figure 3.4 Differentiation of UE7T-13 cell spheroids within the thermosensitive p(NIPAAm-AA) microgel-formed constructs. (a) Optical images showed (i) generation of cell spheroids on day 9 without induction. (ii) Early connection of cell spheroids on day 37 within chondrogenic medium (Arrows point to the inter-spheroid connection sites). (iii) Mineralization of cell spheroids on day 37 within osteogenic medium (Arrows point to the mineralized cell spheroids). (iv) Lipids formation on day 37 within adipogenic medium (Arrow points to the lipids). (b) Size distribution of cell spheroids on day 9 without induction (n = 3, where five optical imaged were randomly taken for each and measured by image J). (c) Histological images of (i) no-induction and (ii) induction in chondrogenic medium by Alcian Blue staining on day 37 (Red-nuclei; Blue-glycosaminoglycans (GAGs); Arrows point to the GAGs sites). (d) Histological images of (i) no-induction and (ii) induction in osteogenic medium by Alizarin red S staining on day 37 (Red-calcium deposition; Arrows point to the deposited calcium sites). (e) Histological images of (i) no-induction and (ii) induction in adipogenic medium by Oil red O staining on day 37 (Blue-nuclei; Red-lipids; Arrow points to the lipid within the cells). Scale bar: 100 µm.

UE7T-13 cells were cultured for 9 days and the cell differentiation was induced within chondrogenic, osteogenic or adipogenic induction media. After further 4 weeks of culture, the cells were harvested and lysed for the study of mRNA expression. Chondrogenic genes (SOX9, aggrecan and collagen II) and osteogenic genes (RUNX2 and osteocalcin) and adipogenic genes (adipsin, c-ebp α and adiponectin) within 3D microgel-formed constructs all showed significantly higher mRNA expression than the controls (Figure 3.5), confirming that the 3D microgel promoted hMSC differentiation.

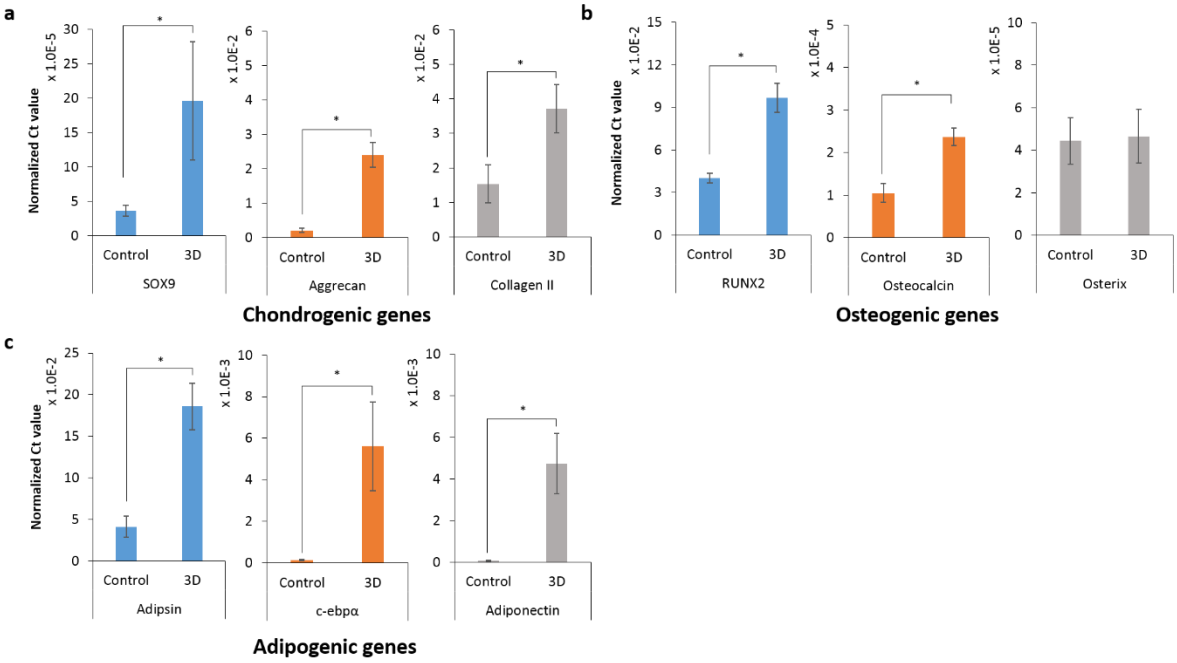

Figure 3.5 Cell differentiation of UE7T-13 with induction media. (a) Chondrogenic gene expression (control: cell pellets cultured in the polypropylene tube by centrifuge, 3D: cells cultured within the thermosensitive p(NIPAAm-AA) microgel-formed constructs); (b) osteogenic gene expression (control: cells cultured on the multi-well plate, 3D: cells cultured within thermosensitive p(NIPAAm-AA) microgel-formed constructs); and (c) adipogenic gene expression (control: cells cultured on the multi-well plate, 3D: cells cultured within thermosensitive p(NIPAAm-AA) microgel-formed constructs); of UE7T-13 with induction media on day 37 by adding specific induction media on day 9. mRNA expression of genes were analysed by qRT-PCR and normalized to β-Actin. Data were presented as the mean ± standard error (n = 3). *p < 0.05.

Human patient-derived hMSC from three different normal donors (NOD MSCs) were cultured within the 3D microgel-formed constructs. Cell spheroids of NOD MSCs were successfully formed after one day of culture (Figure 3.6 a i), which continued to increase after 9-day culture with the complete growth medium (data not shown). The size of NOD MSC spheroids from three different normal donors on day 1 were uniformly distributed and were similar to that of UE7T-13 on day 9 (Figure 3.6 b).

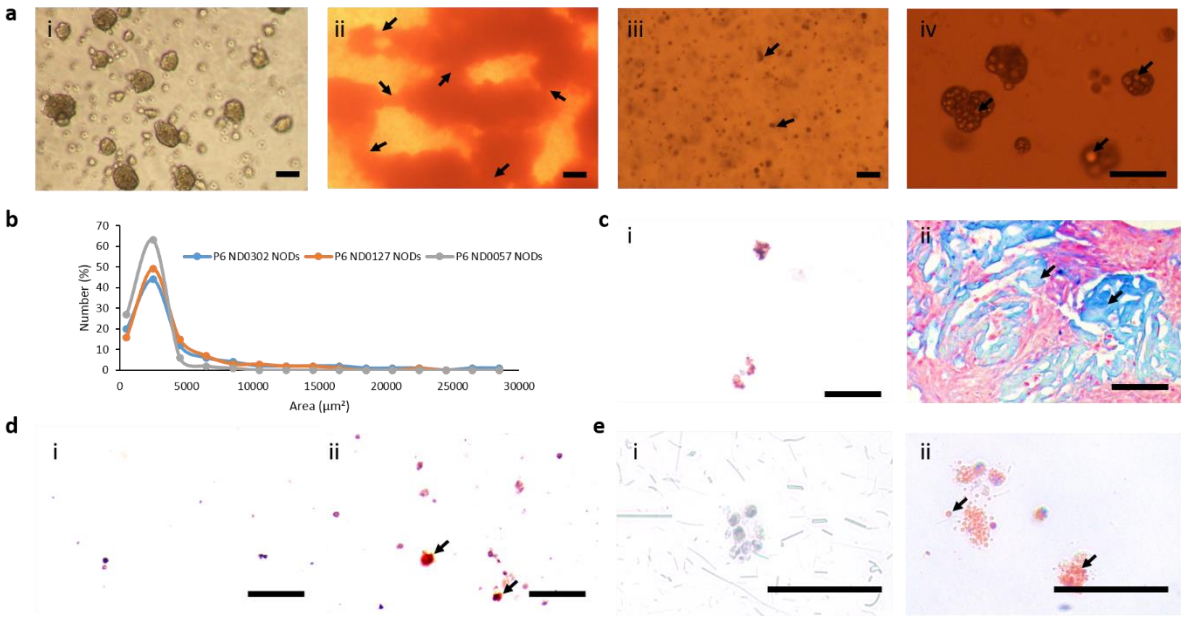

Figure 3.6 Differentiation of NOD MSC spheroids within the thermosensitive p(NIPAAm-AA) microgel-formed constructs. (a) Optical images showed (i) generation of cell spheroids on day 1 without induction. (ii) Inter-spheroid connection of cell spheroids on day 37 within chondrogenic medium (Arrows point to the connection sites). (iii) Mineralization of cell spheroids on day 37 within osteogenic medium (Arrows point to the mineralized cell spheroids) (iv) Lipids formation on day 37 within adipogenic medium (Arrows point to the lipids). (b) Size distribution of cell spheroids on day 1 without induction (n = 3, where five optical imaged were randomly taken for each and measured by image J). (c) Histological images of (i) no-induction and (ii) induction in chondrogenic medium by Alcian Blue staining on day 37 (Red-nuclei; Blue-glycosaminoglycans (GAGs); Arrows point to the GAGs sites). (d) Histological images of (i) no-induction and (ii) induction in osteogenic medium by Alizarin red S staining on day 37 (Red-calcium deposition; Arrows point to the deposited calcium sites). (e) Histological images of (i) no-induction and (ii) induction in adipogenic medium by Oil red O staining on day 37 (Blue-nuclei; Red-lipids; Arrows point to the lipid within the cells). Scale bar: 100 µm.

NOD MSCs were subsequently cultured in the induction media on day 9 for up to 37 days. After induction for 4 weeks, quantitative PCR was performed to measure the mRNA expression of specific genes within NOD MSCs. mRNA expression of SOX9, aggrecan, RUNX2, osterix and c-ebp α from three different normal donors was significantly higher within 3D microgel-formed constructs than the 2D controls. Similar differences were observed for mRNA expression of adipsin and adiponectin within 3D microgel-formed constructs (Figure 3.7). However, due to normal donor cell variation, only NOD MSCs from two different normal donors (ND0303 NODs and ND0059 NODs) displayed significant difference between 3D and the 2D controls (Figure 3.7).

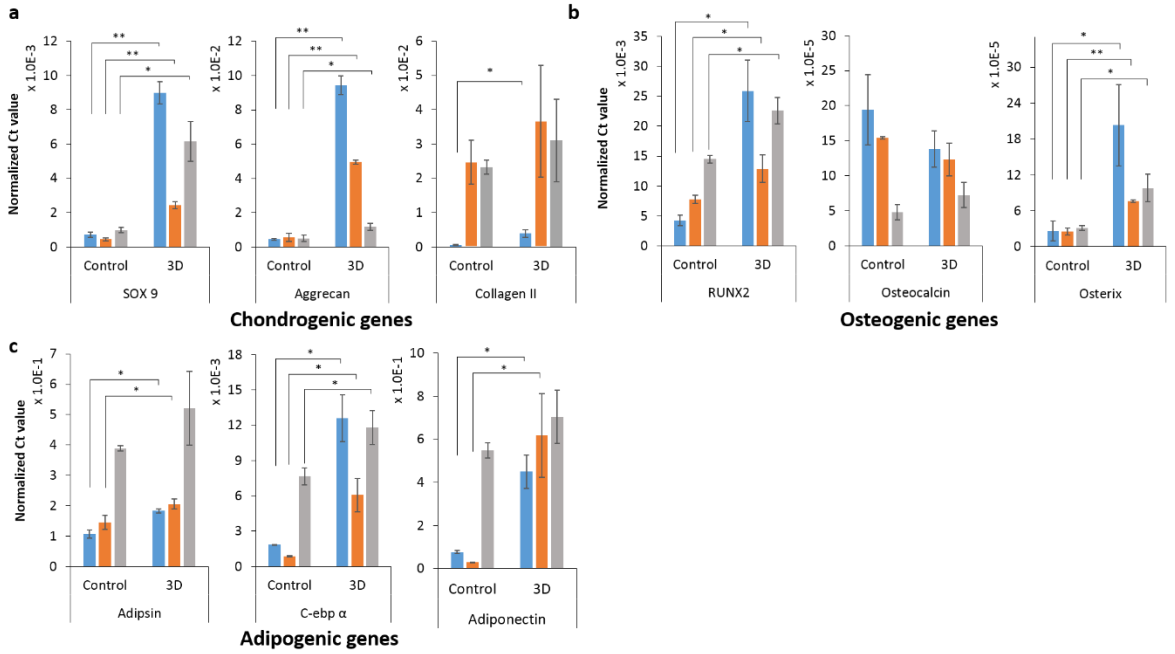

Figure 3.7 (a) Chondrogenic gene (control: cell pellets cultured in the polypropylene tube by centrifuge, 3D: cells cultured within the thermosensitive p(NIPAAm-AA) microgel-formed constructs); (b) osteogenic gene (control: cells cultured on the multi-well plate, 3D: cells cultured within thermosensitive p(NIPAAm-AA) microgel-formed constructs); and (c) adipogenic gene expression (control: cells cultured on the multi-well plate, 3D: cells cultured within thermosensitive p(NIPAAm-AA) microgel-formed constructs) of three NOD MSCs on day 37 by adding specific induction media on day 9. Blue: ND0303 NODs; orange: ND0059 NODs; grey: ND0055 NODs. mRNA expression of genes was analysed by qRT-PCR and normalized to β-Actin. Data were presented as the mean ± standard error (n = 3). *p < 0.05, ** p < 0.001.

3.5.6 Evident staining of differentiated hMSCs within 3D microgel-formed constructs.

To further confirm the multi-lineage differentiation of human stem cells within 3D microgel-formed constructs, both histological and immunofluorescent staining were performed for UE7T-13 and NOD MSCs. Mineralization within osteogenic groups (Figure 3.4 a iii and Figure 3.6 a iii), and lipids within adipogenic groups (Figure 3.4 a iv and Figure 3.6 a iv) were evident by a optical microscope prior to any staining. Chondrogenic differentiation, as marked Alcian Blue staining of glycosaminoglycan (GAG) expression, a significant component of cartilage, was evident in hMSCs cultured in the 3D microgel-formed constructs (Figure 3.4 c and Figure 3.6 c). UE7T-13 and NOD MSCs, cultured within the 3D microgel-formed constructs for 37 days without induction medium, formed small cell spheroids and showed no visible blue staining (Figure 3.4 c i and Figure 3.6 c i), while cells cultured within the 3D microgel-formed

constructs in chondrogenically inductive media for 4 weeks formed a more complex micro-tissue and showed rich blue-staining GAGs among the micro-tissue section (Figure 3.4 c ii and Figure 3.6 c ii). Moreover, UE7T-13 and NOD MSCs cultured within 3D microgel-formed constructs in osteogenic-induction media for 4 weeks showed distinct red by Alizarin Red S staining as evidence of calcification (Figure 3.4 d ii and Figure 3.6 d ii). On contrary, cells cultured within 3D microgel-formed constructs with the complete growth medium for up to 37 days were not stained red by Alizarin Red S (Figure 3.4 d i and Figure 3.6 d i). Furthermore, lipids were only found for cells cultured with adipogenic-induction medium for up to 37 days (Figure 3.4 e and Figure 3.6 e) by Oil Red O staining.

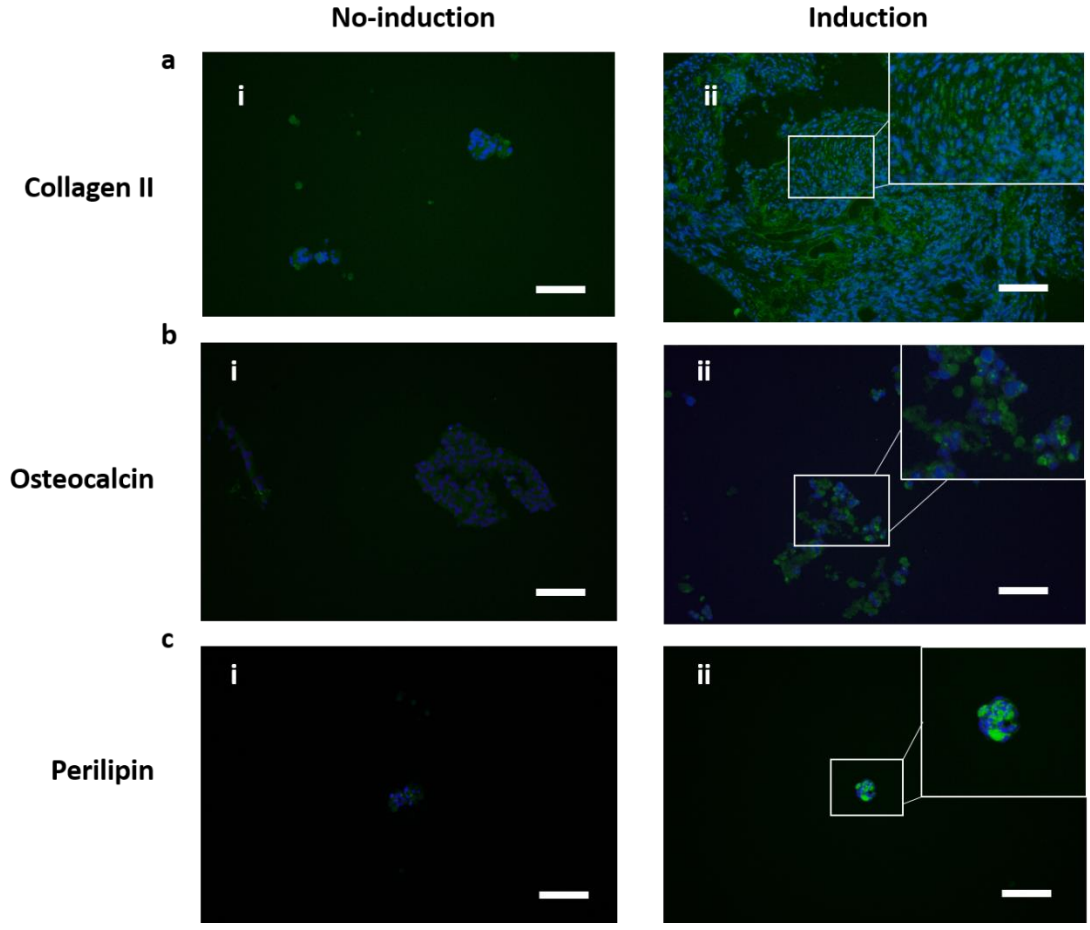

Figure 3.8 Immunofluorescent images of UE7T-13 within the thermosensitive p(NIPAAm-AA) microgel-formed constructs on day 37. (a) Collagen II A1 expression of (i) no-induction and (ii) induction in chondrogenic medium (Blue-DAPI; Green-collagen II A1). (b) Osteocalcin expression of (i) no-induction and (ii) induction in osteogenic medium (Blue-DAPI; Green-osteocalcin). (c) Perilipin expression of (i) no-induction and (ii) induction in adipogenic medium (Blue-DAPI; Green-perilipin). Scale bar: 100 µm.

Immunofluorescent staining of collagen II A1, osteocalcin, and perilipin was also performed to confirm the multi-lineage differentiation of hMSCs in 3D microgel-formed constructs. The green FITC-labeled collagen II A1 was well distributed within the chondrogenesis-induced microtissue and much more distinct than cells within 3D microgel-formed constructs without induction (Figure 3.8 a and Figure 3.9 a). In addition, distinguishable osteocalcin (Figure 3.8 b and Figure 3.9 b) and perilipin (Figure 3.8 c and Figure 3.9 c) expression was observed for UE7T-13 and NOD MSCs with induction media on day 37 as evidenced by the green staining, indicative of osteogenic and adipogenic differentiation, respectively. However, neither FITC-osteocalcin signal nor FITC-perilipin signal was detected for UE7T-13 and NOD MSCs cultured in the p(NIPAAm-AA) microgel-formed 3D constructs with only complete growth medium on day 37.

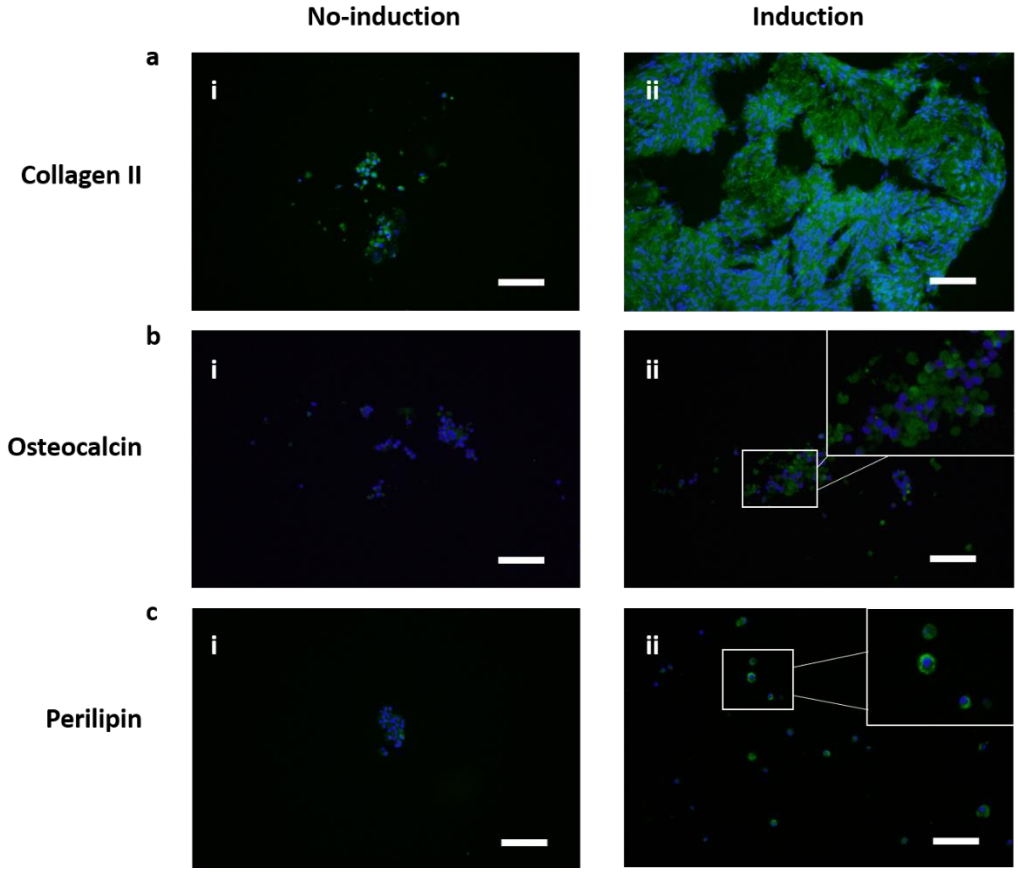

Figure 3.9 Immunofluorescent images of NOD MSCs within the thermosensitive p(NIPAAm-AA) microgel-formed constructs on day 37. (a) Collagen II A1 expression of (i) no-induction and (ii) induction in chondrogenic medium (Blue-DAPI; Green-collagen II A1). (b) Osteocalcin expression of (i) no-induction and (ii) induction in osteogenic medium (Blue-DAPI; Green-osteocalcin). (c) Perilipin expression of (i) no-induction and (ii) induction in adipogenic medium (Blue-DAPI; Green-perilipin). Scale bar: 100 μm.

3.6 Discussion

The thermosensitive property of the p(NIPAAm-AA) microgel was mainly maintained by the hydrophobic interaction and physical ionic crosslinking. [44] Hence, the reversibility of sol and gel transformation, on the one hand, could be controlled by the external temperature change, which influenced the hydrophobicity of p(NIPAAm-AA). When the temperature was increased to 37 °C, the hydrophobic interaction between the p(NIPAAm-AA) was enhanced leading to the shrinkage of microgels. Then water was expelled from the center of the microgels, which made the constructs cloudy, while the forming Mg^{2+}/COO^{-} physical ionic bonding promoted the gel formation and further decreased the transmittance of the constructs (Figure S3.2 b). The liquefied process of p(NIPAAm-AA) microgel-formed 3D constructs was contrary to the gelation process. On the other hand, the external stress can also induce the p(NIPAAm-AA) transform from gel status, where elastic modulus (G') was higher than the viscous modulus (G") (G'>G"), to sol status, where elastic modulus was lower than viscous modulus (G'<G"), by breaking down the physical ionic crosslinking (Figure S3.2 c). When the external force was absent, physical ionic crosslinking could be easily formed, making the p(NIPAAm-AA) gelate again at 37 °C.

While p(NIPAAm-AA) thermosensitive 3D microgels have been previously demonstrated to support 3D culture of murine embryonic mesenchymal progenitor cells (C3H/10T1/2) and the cell proliferation within 3D microgel-formed constructs was higher than 2D plate [32], human MSCs have not been previously examined. Hence, in this study, UE7T-13 and NOD MSCs were used to assess the biological performance of p(NIPAAm-AA) microgels. From the surface toxicity assay, no toxicity of the microgel for the UE7T-13 was observed at concentrations ranging from 0.05 mg/mL to 5 mg/mL (Figure S3.3 a), with greater than 90% of cells remaining viable after 24 hr of culture. However, the cell viability decreased to approximately 60% with an increase in microgel concentration to 30 mg/mL. To eliminate influence of pH change caused by the ionization of carboxyl group within p(NIPAAm-AA), p(NIPAAm-AA) microgel was

dissolved in 1×DPBS and cultured overnight in complete growth medium prior to the addition of cells. We found that the microgel could not gel at 37 °C in the complete growth media. Instead, the viscous microgel was found to cover the adherent UE7T-13 and hinder the gas and mass exchange between the cells and the surrounding medium resulting in a reduced cell viability at the microgel concentration of 30 mg/mL. This assertion was supported by our previous studies which showed that p(NIPAAm) hydrogel at concentrations below 30 mg/mL did not increase apoptosis or necrosis (Figure S3.3 b). [46]

When UE7T-13 and NOD MSCs were incorporated within the 3D microgel-formed constructs and cultured with the complete growth medium for up to 14 days, the cells displayed reduced cell proliferation compared with cells cultured in 2D. This was most evident when NOD MSCs, were cultured in 3D microgel-formed constructs (Figure 3.1). These findings were contrary to our previously published findings [32]. This difference might be related to the fact that cell adhesion and active migration could be limited in soft 3D hydrogels [47, 48], particularly for p(NIPAAm)-based microgels with lack of binding sites [49]. Moreover, previous studies also suggested that human MSCs typically generated less ECM [50], suggesting that cell proliferation and survival were only possible when hMSCs formed cell spheroids within the soft 3D microgel-formed constructs [16, 51]. However, passive mass and gas diffusion within cell spheroids might be limited as the cell condensation and an increase in the cell spheroids size. [52] Furthermore, since the stiffness of p(NIPAAm-AA) microgel-formed constructs was low [32] and the microgel-cell hybrids were free-floating in culture medium, human MSCs became quiescent under such an environment [53] (Figure S3.6 b). Consequently, their proliferation was suppressed in the 3D microgel-formed constructs at a rate of around half of that observed in 2D cultures on day 1 (Figure 3.1). Once cell spheroids were formed, stem cell differentiation was enhanced by the elevated secretion of endogenous growth factors and ECM proteins. [16] Uniform UE7T-13 spheroids within 3D microgel-formed constructs showed significantly higher mRNA expression of chondrogenic genes (SOX9 and aggrecan) and

osteogenic genes (RUNX2 and osterix) on day 9 (Figure 3.2) compared to the controls even without induction media, while the difference was only seen for the mRNA expression of aggrecan on day 37 (Figure 3.3 a). It was reported that size of cell spheroids would decrease after reaching the maximal size [16, 49, 54], which were also confirmed in cell spheroids cultured on low attachment plates (Figure S3.5 c) and in the 15 mL polypropylene tubes (Figure S3.5 d) in this study. When most of UE7T-13 spheroids decreased and broke down into individual cells on day 37 (Figure 3.4 c i and Figure 3.6 c i), the functional enhancement of cell spheroids was lost, leading to a reduction of mRNA expression of chondrogenic genes (SOX9 and collagen II), osteogenic genes (RUNX2 and osteocalcin) and adipogenic genes (adiponectin) compared to those observed on day 9 (Figure 3.3). However, since the progress of cell spheroids formation within 3D microgel-formed constructs was slower than that on a low attachment plate and from the force-spinning (Figure S3.5), cell spheroids continued to increase in size even after cell induction, which maintained functional enhancement of cell spheroids to continuously up-regulate the mRNA expression of chondrogenic, osteogenic and adipogenic genes (Figure 3.5 and Figure 3.7). The benefit of cell spheroids was more distinct for the mRNA expression of collagen II, which showed a significantly higher value for the 3D than the control on day 37 (Figure 3.5 a), while the difference was reverse on day 9 (Figure 3.2 a). In addition, the progression of increasing cell spheroid in size also allows more efficient supply of inductive and/or biochemical stimuli to stem cells due to the higher surface area of small cell spheroids than that of large cell pellets. Hence, hMSCs cells within 3D microgel-formed constructs showed a significant increase in chondrogenesis, osteogenesis and adipogenesis compared to the controls.

In addition, cell spheroids within 3D microgel-formed constructs even established inter-spheroid connections to form a network during chondrogenesis (Figure 3.4 a ii and Figure 3.6 a ii). This inter-spheroid connectivity was more evident for NOD MSCs compared with UE7T-13, with evidence of a stronger network seen in chondrogenic NOD MSCs (Figure 3.6 a ii).

This may be related to the fact that the NOD MSCs were freshly isolated from human bones and would be easily adapted to the 3D environment *in vitro*, while UE7T-13 were already modified and adapted to the 2D plate after many passages. [55] We noted that the cell spheroid network started to contract and formed a porous chondrogenic micro-tissue (Figure 3.4 c ii and Figure 3.6 c ii). Since the major components of ECM within cartilage are acidic polysaccharides [56], such as glycosaminoglycans (GAGs) and collagen II, Alcian Blue was used to distinguish and stain GAGs. It was shown that GAGs with distinct blue color were well distributed in the chondrogenic micro-tissue of UE7T-13 and NOD MSCs (Figure 3.4 c and Figure 3.6 c). In addition, abundant collagen II A1 was also labeled with green FITC-secondary antibody within the chondrogenic micro-tissue of UE7T-13 and NOD MSCs (Figure 3.8 a ii and Figure 3.9 a ii). The chondrogenic micro-tissue formed within the 3D microgel-formed constructs was similar to that formed by pellet culture [57], while the chondrogenic progress of hMSCs in the 3D microgel-formed constructs was more consistent with that *in vivo* [58]. Moreover, calcification (Figure 3.4 a iii and Figure 3.6 a iii) and lipids (Figure 3.4 a iv and Figure 3.6 a iv) were seen in the optical images of osteogenic and adipogenic cells and evidenced by Alizarin Red S staining (Figure 3.4 d ii and Figure 3.6 d ii) and Oil Red O staining (Figure 3.4 e ii and Figure 3.6 e ii), respectively. Furthermore, osteocalcin, an osteogenesis-relative protein, and perilipin, a lipid droplet-associated protein, were both clearly labeled by FITC-secondary antibody and distinguished as green in immunofluorescent images within UE7T-13 (Figure 3.8 b ii and Figure 3.8 c ii) and NOD MSCs (Figure 3.9 b ii and Figure 3.9 c ii) after specific induction. Herein, we confirm that multi-lineage differentiation of human mesenchymal stromal cells is successfully induced in 3D microgel-formed constructs with the specific induction media. Moreover, UE7T-13 cultured in the p(NIPAAm-AA) microgel-formed constructs without induction media showed relatively high mRNA expression of aggrecan on day 9 and 37(Figure 3.2 a and Figure 3.3 a), and some chondrogenic staining (FITC-collagen II in Figure 3.8 a i and Figure 3.9 a i) on day 37, which indicated that the p(NIPAAm-AA)

microgel-formed constructs could selectively promote hMSCs chondrogenesis. It was believed that the distinct chondrogenic induction was due to the synergy of cell spheroids, induction medium and environment formed by the p(NIPAAm-AA) microgels. These experimental results support that human mesenchymal stem/stromal cells within the 3D microgel-formed constructs can be efficiently induced for multi-lineage differentiation. Hence, the p(NIPAAm-AA) microgel can be potentially used as an *in-vitro* model for cell differentiation and tissue engineering or transplanted *in-vivo* into patients for specific lineage differentiation.

3.7 Conclusion

In this study, we demonstrated that the p(NIPAAm-AA) thermosensitive microgel was not toxic to human mesenchymal stromal cells and facilitated formation of uniform cell spheroids within the 3D microgel-formed constructs. The spheroid formation within the 3D microgel-formed constructs significantly up-regulated mRNA expression of chondrogenic genes (SOX9 and aggrecan) and osteogenic genes (RUNX2 and osterix) in UE7T-13 even without the induction media, but the free-floating soft microgel-formed constructs and the cell spheroids led to slow cell proliferation. When induction media were supplied *in situ*, the mRNA expression of chondrogenic, osteogenic and adipogenic genes within UE7T-13 and NOD MSCs has been significantly up-regulated. Successful cell differentiation was confirmed as evidenced by Alcian Blue stained GAGs and FITC-secondary antibody labeled collagen II A1 within the chondrogenic micro-tissue, Alizarin Red S stained calcification and FITC-secondary antibody labeled osteocalcin within osteogenic cells, and Oil Red O stained lipids and FITC-secondary antibody labeled perilipin. Hence, we concluded that highly efficient multi-lineage differentiation of human mesenchymal stromal cells can be achieved within the 3D thermosensitive microgel-formed constructs.

SUPPLEMENTARY INFORMATION

For further details of (1) thermosensitive behavior of p(NIPAAm-AA) microgel-formed constructs (Figure S3.1); (2) Size distribution of the microgel, time-dependent gelation process,

and the stress-dependence of dynamic moduli of p(NIPAAm-AA) (Figure S3.2); (3) UE7T-13 viability assay after 24 hr (Figure S3.3); (4) SEM images of cell-gel 3D constructs (Figure S3.4); (5) Live&Dead staining of UE7T-13 in different culture systems (Figure S3.5); and (6) Cell stemness and cell cycle assay (Figure S3.6), please refer to the "Supplementary information".

CONFLICTS OF INTEREST

There are no conflicts to declare.

ACKNOWLEDGEMENTS

HZ would like to acknowledge the financial support from ARC Discovery Project (DP160104632) and The Medical Advancement Without Animal (MAWA) Trust. JBZ thanks the IPE-UoA Scholarship (BES).

3.8 Reference

[1] Arthur A, Zannettino A, Gronthos S. The therapeutic applications of multipotential mesenchymal/stromal stem cells in skeletal tissue repair. Journal of Cellular Physiology 2009;218:237-45.

[2] Frith JE, Cameron AR, Menzies DJ, Ghosh P, Whitehead DL, Gronthos S, et al. An injectable hydrogel incorporating mesenchymal precursor cells and pentosan polysulphate for intervertebral disc regeneration. Biomaterials 2013;34:9430-40.

[3] McCarty RC, Xian CJ, Gronthos S, Zannettino ACW, Foster BK. Application of Autologous Bone Marrow Derived Mesenchymal Stem Cells to an Ovine Model of Growth Plate Cartilage Injury. The Open Orthopaedics Journal 2010;4:204-10.

[4] Frith JE, Menzies DJ, Cameron AR, Ghosh P, Whitehead DL, Gronthos S, et al. Effects of bound versus soluble pentosan polysulphate in PEG/HA-based hydrogels tailored for intervertebral disc regeneration. Biomaterials 2014;35:1150-62.

[5] Tony G, David O, Peter G, Andrew Z, Jeffrey Victor R, Graham J. Current and Future Applications for Stem Cell Therapies in Spine Surgery. Current Stem Cell Research & Therapy 2013;8:381-93.

[6] Freeman BJC, Kuliwaba JS, Jones CF, Shu CC, Colloca CJ, Zarrinkalam MR, et al. Allogeneic Mesenchymal Precursor Cells Promote Healing in Postero-lateral Annular Lesions and Improve Indices of Lumbar Intervertebral Disc Degeneration in an Ovine Model. Spine 2016;41:1331-9.

[7] Richardson JD, Nelson AJ, Zannettino ACW, Gronthos S, Worthley SG, Psaltis PJ. Optimization of the Cardiovascular Therapeutic Properties of Mesenchymal Stromal/Stem Cells–Taking the Next Step. Stem Cell Reviews and Reports 2013;9:281-302.

[8] Psaltis PJ, Zannettino ACW, Worthley SG, Gronthos S. Concise Review: Mesenchymal Stromal Cells: Potential for Cardiovascular Repair. Stem cells (Dayton, Ohio) 2008;26:2201-10.

[9] Psaltis PJ, Carbone A, Nelson AJ, Lau DH, Jantzen T, Manavis J, et al. Reparative Effects of Allogeneic Mesenchymal Precursor Cells Delivered Transendocardially in Experimental Nonischemic Cardiomyopathy. JACC: Cardiovascular Interventions 2010;3:974-83.

[10] Wu K-H, Mei C, Lin C-W, Yang K-C, Yu J. The influence of bubble size on chondrogenic differentiation of adipose-derived stem cells in gelatin microbubble scaffolds. Journal of Materials Chemistry B 2018;6:125-32.

[11] Aisenbrey EA, Bryant SJ. Mechanical loading inhibits hypertrophy in chondrogenically differentiating hMSCs within a biomimetic hydrogel. Journal of materials chemistry B, Materials for biology and medicine 2016;4:3562-74.

[12] Paul A, Manoharan V, Krafft D, Assmann A, Uquillas JA, Shin SR, et al. Nanoengineered biomimetic hydrogels for guiding human stem cell osteogenesis in three dimensional microenvironments. Journal of materials chemistry B, Materials for biology and medicine 2016;4:3544-54.

[13] Hu Y, Gao W, Wu F, Wu H, He B, He J. Low molecular weight gels induced differentiation of mesenchymal stem cells. Journal of Materials Chemistry B 2016;4:3504-8.

[14] Xiao X, Yu L, Dong Z, Mbelek R, Xu K, Lei C, et al. Adipose stem cell-laden injectable thermosensitive hydrogel reconstructing depressed defects in rats: filler and scaffold. Journal of Materials Chemistry B 2015;3:5635-44.

[15] Goldberg A, Mitchell K, Soans J, Kim L, Zaidi R. The use of mesenchymal stem cells for cartilage repair and regeneration: a systematic review. Journal of orthopaedic surgery and research 2017;12:39.

[16] Sart S, Tsai AC, Li Y, Ma T. Three-dimensional aggregates of mesenchymal stem cells: cellular mechanisms, biological properties, and applications. Tissue Engineering Part B: Reviews 2014;20:365-80.

[17] Cui X, Hartanto Y, Zhang H. Advances in multicellular spheroids formation. Journal of the Royal Society Interface 2017;14:20160877.

[18] Bartosh TJ, Ylöstalo JH, Mohammadipoor A, Bazhanov N, Coble K, Claypool K, et al. Aggregation of human mesenchymal stromal cells (MSCs) into 3D spheroids enhances their antiinflammatory properties. Proceedings of the National Academy of Sciences 2010;107:13724-9.

[19] Jeon O, Marks R, Wolfson D, Alsberg E. Dual-crosslinked hydrogel microwell system for formation and culture of multicellular human adipose tissue-derived stem cell spheroids. Journal of Materials Chemistry B 2016;4:3526-33.

[20] Takei T, Kitazono J, Tanaka S, Nishimata H, Yoshida M. Necrotic regions are absent in fiber-shaped cell aggregates, approximately 100 mum in diameter. Artificial Cells, Nanomedicine, and Biotechnology 2016;44:62-5.

[21] Page H, Flood P, Reynaud EG. Three-dimensional tissue cultures: current trends and beyond. Cell&Tissue Research 2013;352:123-31.

[22] Muduli S, Lee HH-C, Yang J-S, Chen T-Y, Higuchi A, Kumar SS, et al. Proliferation and osteogenic differentiation of amniotic fluid-derived stem cells. Journal of Materials Chemistry B 2017;5:5345-54.

[23] Akhmanova M, Osidak E, Domogatsky S, Rodin S, Domogatskaya A. Physical, Spatial, and Molecular Aspects of Extracellular Matrix of In Vivo Niches and Artificial Scaffolds Relevant to Stem Cells Research. Stem Cells International 2015;2015:35.

[24] Hettiaratchi MH, Guldberg RE, McDevitt TC. Biomaterial strategies for controlling stem cell fate via morphogen sequestration. Journal of Materials Chemistry B 2016;4:3464-81.

[25] Higuchi A, Ling Q-D, Kumar SS, Chang Y, Alarfaj AA, Munusamy MA, et al. Physical cues of cell culture materials lead the direction of differentiation lineages of pluripotent stem cells. Journal of Materials Chemistry B 2015;3:8032-58.

[26] Eslahi N, Abdorahim M, Simchi A. Smart Polymeric Hydrogels for Cartilage Tissue Engineering: A Review on the Chemistry and Biological Functions. Biomacromolecules 2016;17:3441-63.

[27] Zhang J, Zhang H, Xu X. CHAPTER 17 Smart Materials to Regulate the Fate of Stem Cells. Smart Materials for Tissue Engineering: Applications: The Royal Society of Chemistry; 2017. p. 473-504.

[28] Sala RL, Kwon MY, Kim M, Gullbrand SE, Henning EA, Mauck RL, et al. Thermosensitive Poly(N-vinylcaprolactam) Injectable Hydrogels for Cartilage Tissue Engineering. Tissue Engineering Part A 2017;23:935-45.

[29] Caliari SR, Burdick JA. A practical guide to hydrogels for cell culture. Nature Methods 2016;13:405.

[30] Wang P-Y, Lee HH-c, Higuchi A, Ling Q-D, Lin H-R, Li H-F, et al. Pluripotency maintenance of amniotic fluid-derived stem cells cultured on biomaterials. Journal of Materials Chemistry B 2015;3:3858-69.

[31] Rai V, Dilisio MF, Dietz NE, Agrawal DK. Recent strategies in cartilage repair: A systemic review of the scaffold development and tissue engineering. Journal of Biomedicial Materials Research Part A 2017;105:2343-54.

[32] Shen Z, Bi J, Shi B, Nguyen D, Xian CJ, Zhang H, et al. Exploring thermal reversible hydrogels for stem cell expansion in three-dimensions. Soft Matter 2012;8:7250-7.

[33] Smith E, Yang J, McGann L, Sebald W, Uludag H. RGD-grafted thermoreversible polymers to facilitate attachment of BMP-2 responsive C2C12 cells. Biomaterials 2005;26:7329-38.

[34] Ren Z, Wang Y, Ma S, Duan S, Yang X, Gao P, et al. Effective Bone Regeneration Using Thermosensitive Poly(N-Isopropylacrylamide) Grafted Gelatin as Injectable Carrier for Bone Mesenchymal Stem Cells. ACS Applied Materials & Interfaces 2015;7:19006-15.

[35] Mellati A, Kiamahalleh MV, Madani SH, Dai S, Bi J, Jin B, et al. Poly(N-isopropylacrylamide) hydrogel/chitosan scaffold hybrid for three-dimensional stem cell culture and cartilage tissue engineering. Journal of Biomedical Materials Research Part A 2016;104:2764-74.

[36] Mellati A, Fan C-M, Tamayol A, Annabi N, Dai S, Bi J, et al. Microengineered 3D cell-laden thermoresponsive hydrogels for mimicking cell morphology and orientation in cartilage tissue engineering. Biotechnology and Bioengineering 2017;114:217-31.

[37] Xu Y, Li Z, Li X, Fan Z, Liu Z, Xie X, et al. Regulating myogenic differentiation of mesenchymal stem cells using thermosensitive hydrogels. Acta Biomaterialia 2015;26:23-33.

[38] Navaei A, Truong D, Heffernan J, Cutts J, Brafman D, Sirianni RW, et al. PNIPAAm-based biohybrid injectable hydrogel for cardiac tissue engineering. Acta Biomaterialia 2016;32:10-23.

[39] Dai Z, Shu Y, Wan C, Wu C. Effects of pH and thermally sensitive hybrid gels on osteogenic differentiation of mesenchymal stem cells. Journal of biomaterials applications 2015;29:1272-83.

[40] Zscharnack M, Hepp P, Richter R, Aigner T, Schulz R, Somerson J, et al. Repair of Chronic Osteochondral Defects Using Predifferentiated Mesenchymal Stem Cells in an Ovine Model. The American Journal of Sports Medicine 2010;38:1857-69.

[41] Atkins GJ, Kostakis P, Pan B, Farrugia A, Gronthos S, Evdokiou A, et al. RANKL expression is related to the differentiation state of human osteoblasts. Journal of bone and mineral research : the official journal of the American Society for Bone and Mineral Research 2003;18:1088-98.

[42] Fitter S, Gronthos S, Ooi SS, Zannettino ACW. The Mesenchymal Precursor Cell Marker Antibody STRO-1 Binds to Cell Surface Heat Shock Cognate 70. Stem cells (Dayton, Ohio) 2017;35:940-51.

[43] Bischofberger I, Trappe V. New aspects in the phase behaviour of poly-N-isopropyl acrylamide: systematic temperature dependent shrinking of PNiPAM assemblies well beyond the LCST. Scientific Reports 2015;5:15520.

[44] Gan T, Guan Y, Zhang Y. Thermogelable PNIPAM microgel dispersion as 3D cell scaffold: effect of syneresis. Journal of Materials Chemistry 2010;20:5937-44.

[45] Pollock JF, Healy KE. Mechanical and swelling characterization of poly(N-isopropyl acrylamide -co- methoxy poly(ethylene glycol) methacrylate) sol-gels. Acta Biomater 2010;6:1307-18.

[46] Mellati A, Valizadeh Kiamahalleh M, Dai S, Bi J, Jin B, Zhang H. Influence of polymer molecular weight on the in vitro cytotoxicity of poly (N-isopropylacrylamide). Materials Science and Engineering: C 2016;59:509-13.

[47] Maia FR, Fonseca KB, Rodrigues G, Granja PL, Barrias CC. Matrix-driven formation of mesenchymal stem cell–extracellular matrix microtissues on soft alginate hydrogels. Acta Biomaterialia 2014;10:3197-208.

[48] Balikov DA, Crowder SW, Boire TC, Lee JB, Gupta MK, Fenix AM, et al. Tunable Surface Repellency Maintains Stemness and Redox Capacity of Human Mesenchymal Stem Cells. ACS Applied Materials & Interfaces 2017;9:22994-3006.

[49] Barnes AL, Genever PG, Rimmer S, Coles MC. Collagen–Poly(N-isopropylacrylamide) Hydrogels with Tunable Properties. Biomacromolecules 2016;17:723-34.

[50] Pek YS, Wan ACA, Ying JY. The effect of matrix stiffness on mesenchymal stem cell differentiation in a 3D thixotropic gel. Biomaterials 2010;31:385-91.

[51] Martino MM, Mochizuki M, Rothenfluh DA, Rempel SA, Hubbell JA, Barker TH. Controlling integrin specificity and stem cell differentiation in 2D and 3D environments through regulation of fibronectin domain stability. Biomaterials 2009;30:1089-97.

[52] Hildebrandt C, Büth H, Thielecke H. A scaffold-free in vitro model for osteogenesis of human mesenchymal stem cells. Tissue and Cell 2011;43:91-100.

[53] Oh S-A, Lee H-Y, Lee JH, Kim T-H, Jang J-H, Kim H-W, et al. Collagen Three-Dimensional Hydrogel Matrix Carrying Basic Fibroblast Growth Factor for the Cultivation of Mesenchymal Stem Cells and Osteogenic Differentiation. Tissue Engineering Part A 2011;18:1087-100.

[54] Occhetta P, Centola M, Tonnarelli B, Redaelli A, Martin I, Rasponi M. High-Throughput Microfluidic Platform for 3D Cultures of Mesenchymal Stem Cells, Towards Engineering Developmental Processes. Scientific Reports 2015;5:10288.

[55] Zhao L, Li G, Chan K-M, Wang Y, Tang P-F. Comparison of Multipotent Differentiation Potentials of Murine Primary Bone Marrow Stromal Cells and Mesenchymal Stem Cell Line C3H10T1/2. Calcified Tissue International 2009;84:56-64.

[56] Theocharis AD, Skandalis SS, Gialeli C, Karamanos NK. Extracellular matrix structure. Advanced Drug Delivery Reviews 2016;97:4-27.

[57] Garcia J, Mennan C, McCarthy HS, Roberts S, Richardson JB, Wright KT. Chondrogenic Potency Analyses of Donor-Matched Chondrocytes and Mesenchymal Stem Cells Derived

from Bone Marrow, Infrapatellar Fat Pad, and Subcutaneous Fat. Stem Cells International 2016;2016:11.

[58] Boeuf S, Richter W. Chondrogenesis of mesenchymal stem cells: role of tissue source and inducing factors. Stem Cell Research & Therapy 2010;1:31.

Supplementary information

Enhanced Multi-Lineage Differentiation of Human Mesenchymal Stem/Stromal Cells within Poly (*N*-Isopropylacrylamide-Acrylic Acid) Microgel-Formed Three-Dimensional Constructs

Jiabin Zhang[1], Seonho Yun[1], Jingxiu Bi[1], Sheng Dai[1], Yuguang Du[3], Andrew C.W. Zannettino[2], Hu Zhang[1]**

[1]School of Chemical Engineering, The University of Adelaide, Adelaide, SA 5005, Australia

[2]Adelaide Medical School, The University of Adelaide, Adelaide, SA 5001, Australia

[3]Institute of Process Engineering, Chinese Academy of Sciences, Beijing, 100190, China

[*]Corresponding author: E-mail: hu.zhang@adelaide.edu.au (H.Z.), E-mail: andrew.zannettino@adelaide.edu.au (A.C.W.Z.)

Published: Journal of Materials Chemistry B 2018, 6 (12), 1799-1814, DOI: 10.1039/c8tb00376a

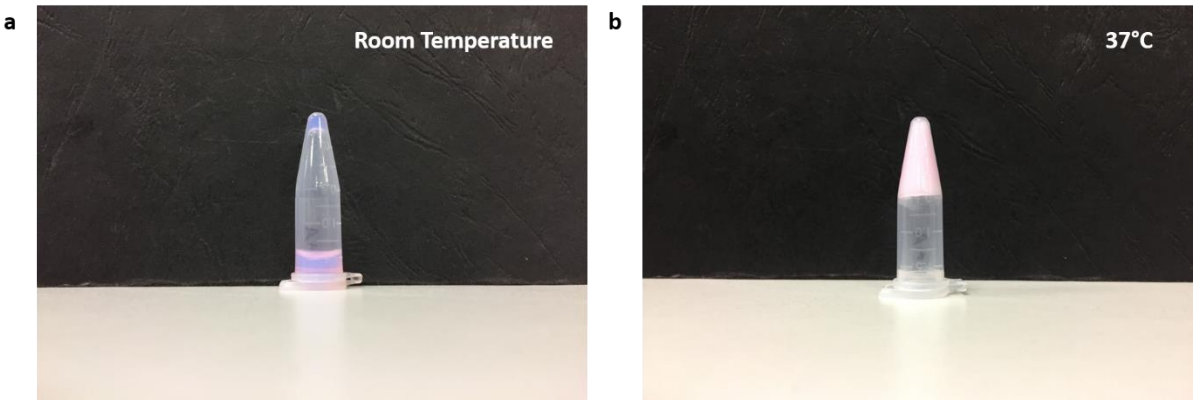

Figure S3.1 Thermosensitive behaviour of p(NIPAAm-AA) microgel-formed 3D constructs. (a) sol status at room temperature and (b) gel status at 37°C.

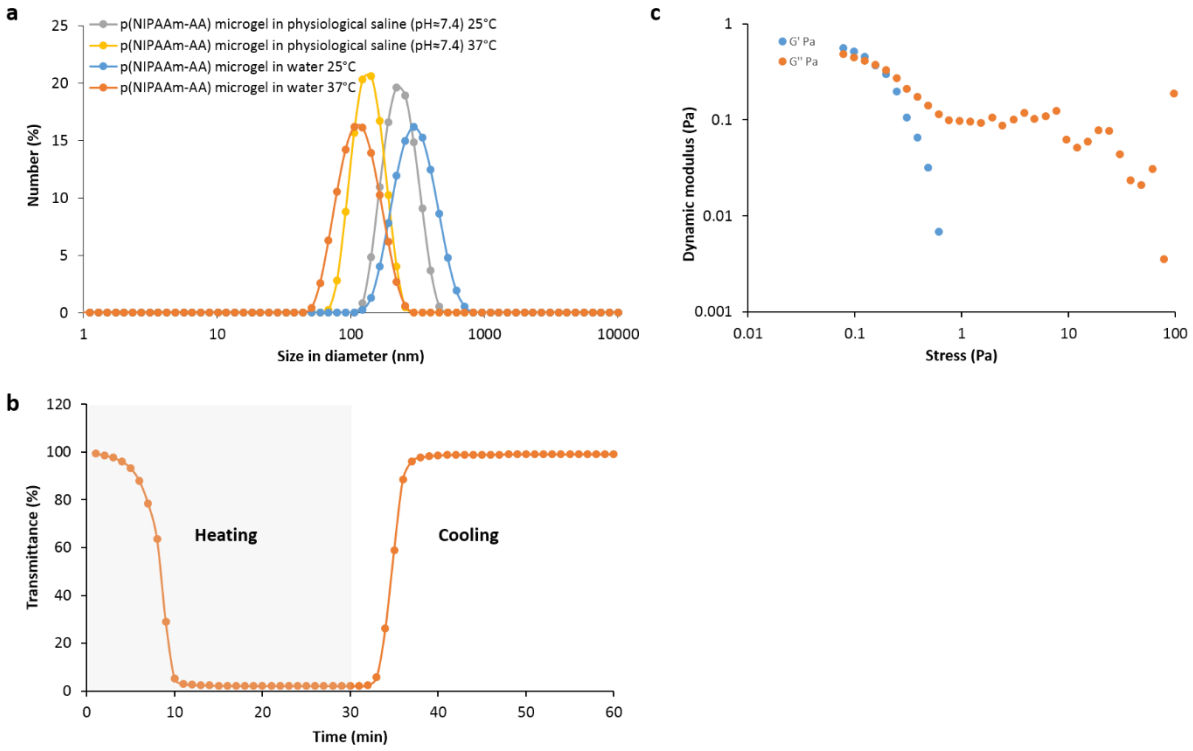

Figure S3.2 (a) Size distribution of 0.5 mg/mL p(NIPAAm-AA) microgels in Milli-Q® water or 1×DPBS (pH ≈ 7.4) at 25°C and 37 °C. (b) Time-dependent gelation process was investigated by measuring the transmittance (%) of the p(NIPAAm-AA) microgel-formed three-dimensional (3D) constructs heating from 0 to 30 min and cooling from 31 to 60 min with a wavelength of 720 nm light. (c) The stress dependence of the dynamic moduli (elastic modulus G' and viscous modulus G'') of 30 mg/mL p(NIPAAm-AA) microgel-formed constructs at 37 °C.

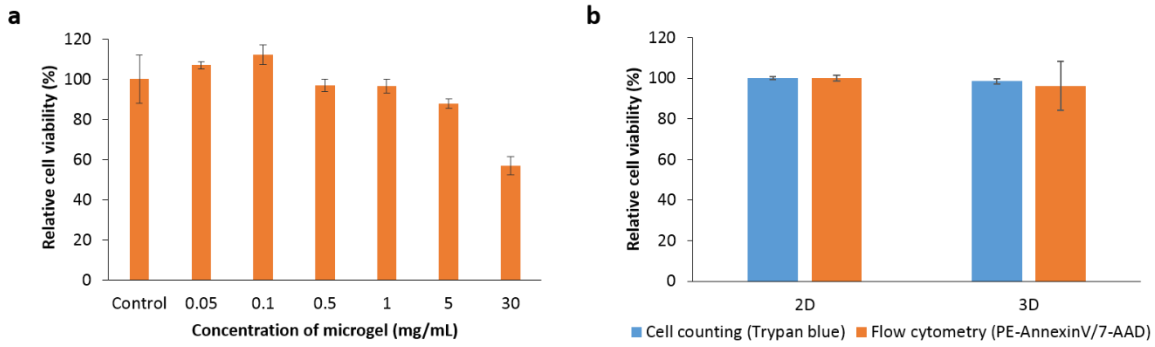

Figure S3.3 UE7T-13 cell viability assay after 24 hours. (a) Surface toxicity assay of various concentration of p(NIPAAm-AA) microgel by MTT. Control: without microgel. The MTT absorbance was normalized to the control and presented as relative cell viability. (b) 3D toxicity assay of microgel at the concentration of 30mg/mL by cell counting with Trypan Blue staining or flow cytometry with PE-AnnexinV and 7-AAD double staining. 2D: cells cultured on the multi-well plate; 3D: cells cultured within the thermosensitive p(NIPAAm-AA) microgel-formed constructs. The cell viability was normalized to 2D and presented as relative cell viability. Results were mean ± standard error (n = 3). No significant difference was found between 2D and 3D.

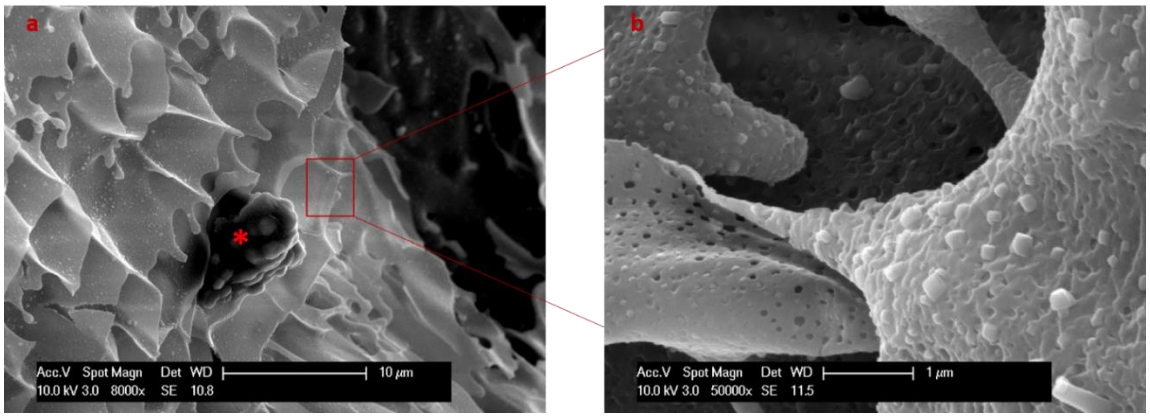

Figure S3.4 SEM images of the cross-sectional p(NIPAAm-AA) microgel-formed 3D construct. The microgel-formed constructs were quickly freezed in liquid nitrogen when at gel status and dried under vacuum. (a) UE7T-13 cells were cultured in the 3D construct on day 1. The asterisk showed an incorporated cell within p(NIPAAm-AA) microgel-formed 3D constructs. (b) Morphology of the 3D construct at higher magnification.

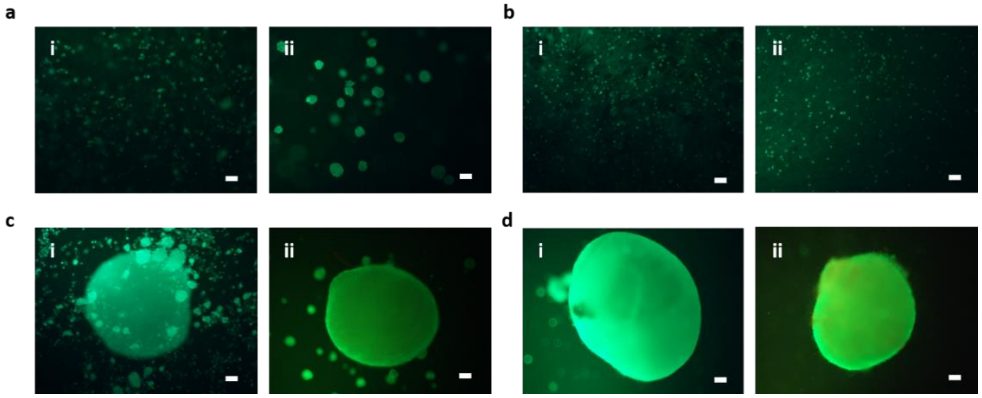

Figure S3.5 Fluorescent images of UE7T-13 cells cultured (a) in the thermosensitive p(NIPAAm-AA) microgel-formed 3D constructs with an additional layer of p(NIPAAm-AA) microgel coating on the bottom; (b) in the thermosensitive p(NIPAAm-AA) microgel-formed 3D constructs without p(NIPAAm-AA) coating; (c) on the low attachment surface; (d) in the polypropylene tube for (i) 1 day and (ii) 9 days by calcein AM and ethidium homodimer-1 double staining. Green: live cells; Red: dead cells. Scale bar: 100 µm.

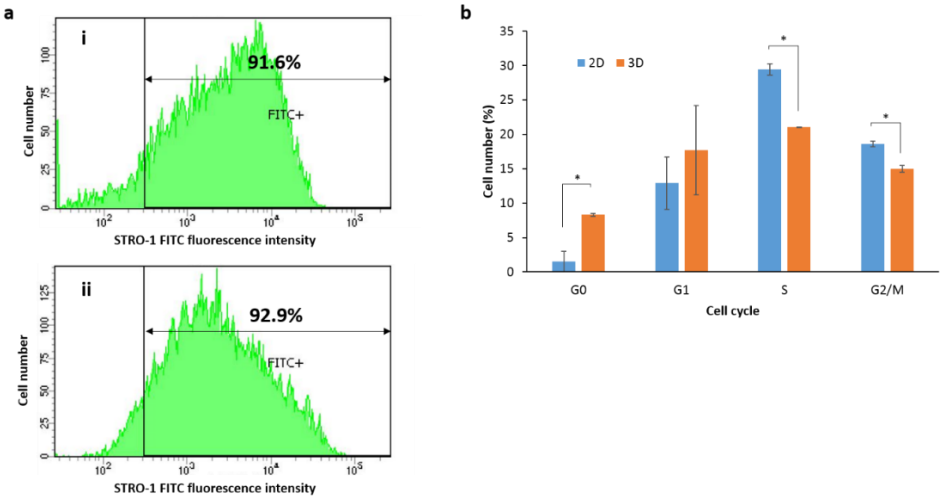

Figure S3.6 (a) Representative STRO-1 flow cytometry of UE7T-13 in (i) 2D and (ii) 3D. The percentage of fluorescein isothiocyanate (FITC)-labelled STRO-1 positive cells for 2D and 3D was 91.6% and 92.9%, respectively. (b) Cell cycle assay of UE7T-13 in 2D and 3D by FITC-labelled KI-67 antibody and propidium iodide (PI) double staining flow cytometry. Data was presented as the mean ± standard error (n = 3). *p < 0.05. 2D: cells were cultured on the two-dimensional plates; 3D: Cells were cultured in the p(NIPAAm-AA) microgel-formed three-dimensional constructs.

CHAPTER IV

ALLOGENEIC PRIMARY MESENCHYMAL STEM/STROMAL CELL AGGREGATES WITHIN POLY(*N*-ISOPROPYLACRYLAMIDE-CO-ACRYLIC ACID) HYDROGEL FOR OSTEOCHONDRAL REGENERATION

Statement of Authorship

Title of Paper	Allogeneic Primary Mesenchymal Stem/Stromal Cell Aggregates within Poly(*N*-Isopropylacrylamide-co-Acrylic Acid) Hydrogel for Osteochondral Regeneration
Publication Status	☑ Published ☐ Accepted for Publication ☐ Submitted for Publication ☐ Unpublished and Unsubmitted work written in manuscript style
Publication Details	Zhang, J.; Zhang, M.; Lin, R.; Yun, S.; Du, Y.; Wang, L.; Yao, Q.; Zannettino, A.; Zhang, H., Appllied Materials Today 2019, 100487. doi: 10.1016/j.apmt.2019.100487.

Principal Author

Name of Principal Author (Candidate)	Jiabin Zhang		
Contribution to the Paper	Performed experiments, analysed data, writing manuscript.		
Overall percentage (%)	80%		
Certification:	This paper reports on original research I conducted during the period of my Higher Degree by Research candidature and is not subject to any obligations or contractual agreements with a third party that would constrain its inclusion in this thesis. I am the primary author of this paper.		
Signature		Date	30/10/2019

Co-Author Contributions

By signing the Statement of Authorship, each author certifies that:

i. the candidate's stated contribution to the publication is accurate (as detailed above);

ii. permission is granted for the candidate in include the publication in the thesis; and

iii. the sum of all co-author contributions is equal to 100% less the candidate's stated contribution.

Name of Co-Author	Ming Zhang		
Contribution to the Paper	Performed partial experiments.		
Signature		Date	2019-07-17

Name of Co-Author	RongcaiLin		
Contribution to the Paper	Performed partial experiments.		
Signature		Date	2019-07-16

Name of Co-Author	Seonho Yun		
Contribution to the Paper	Experiment design and evaluation of data.		
Signature		Date	16/07/2019

Name of Co-Author	Yuguang Du		
Contribution to the Paper	Proof read the manuscript and evaluation.		
Signature		Date	2019.7.15

Name of Co-Author	Liming Wang		
Contribution to the Paper	Proof read the manuscript and evaluation of data.		
Signature		Date	7/18/2019

Name of Co-Author	Qingqiang Yao		
Contribution to the Paper	Proof read the manuscript and evaluation of data.		
Signature		Date	8-15-2019

Name of Co-Author	Andrew Zannettino		
Contribution to the Paper	Proof read the manuscript, experiment design, and evaluation of data.		
Signature		Date	16 July 2019

Name of Co-Author	Hu Zhang		
Contribution to the Paper	Proof read the manuscript, experiment design, and evaluation of data.		
Signature		Date	July 15, 2019

Allogeneic Primary Mesenchymal Stem/Stromal Cell Aggregates within Poly(*N*-Isopropylacrylamide-co-Acrylic Acid) Hydrogel for Osteochondral Regeneration

Jiabin Zhang [a], Ming Zhang [c], Rongcai Lin [c], Seonho Yun [a], Yuguang Du [e], Liming Wang [c], Qingqiang Yao [c,], Andrew Zannettino [b,]*, Hu Zhang [a, d,]**

[a] School of Chemical Engineering, The University of Adelaide, Adelaide, SA 5005, Australia

[b] Adelaide Medical School, The University of Adelaide, Adelaide, SA 5001, Australia

[c] Department of Orthopaedic Surgery, Institute of Digital Medicine, Nanjing First Hospital, Nanjing Medical University, Nanjing, 210006, China

[d] Henry E. Riggs School of Applied Life Sciences, Keck Graduate Institute, California, CA 91711, USA

[e] Institute of Process Engineering, Chinese Academy of Sciences, Beijing, 100190, China

*Corresponding Authors: Dr Q Yao (yaoqingqiang@njmu.edu.cn), Prof. A Zannettino (andrew.zannettino@adelaide.edu.au), and Prof. H Zhang (hu_zhang@kgi.edu)

Published: Applied Materials Today 2019, 100487, DOI: 10.1016/j.apmt.2019.100487.

4.1 Graphical abstract

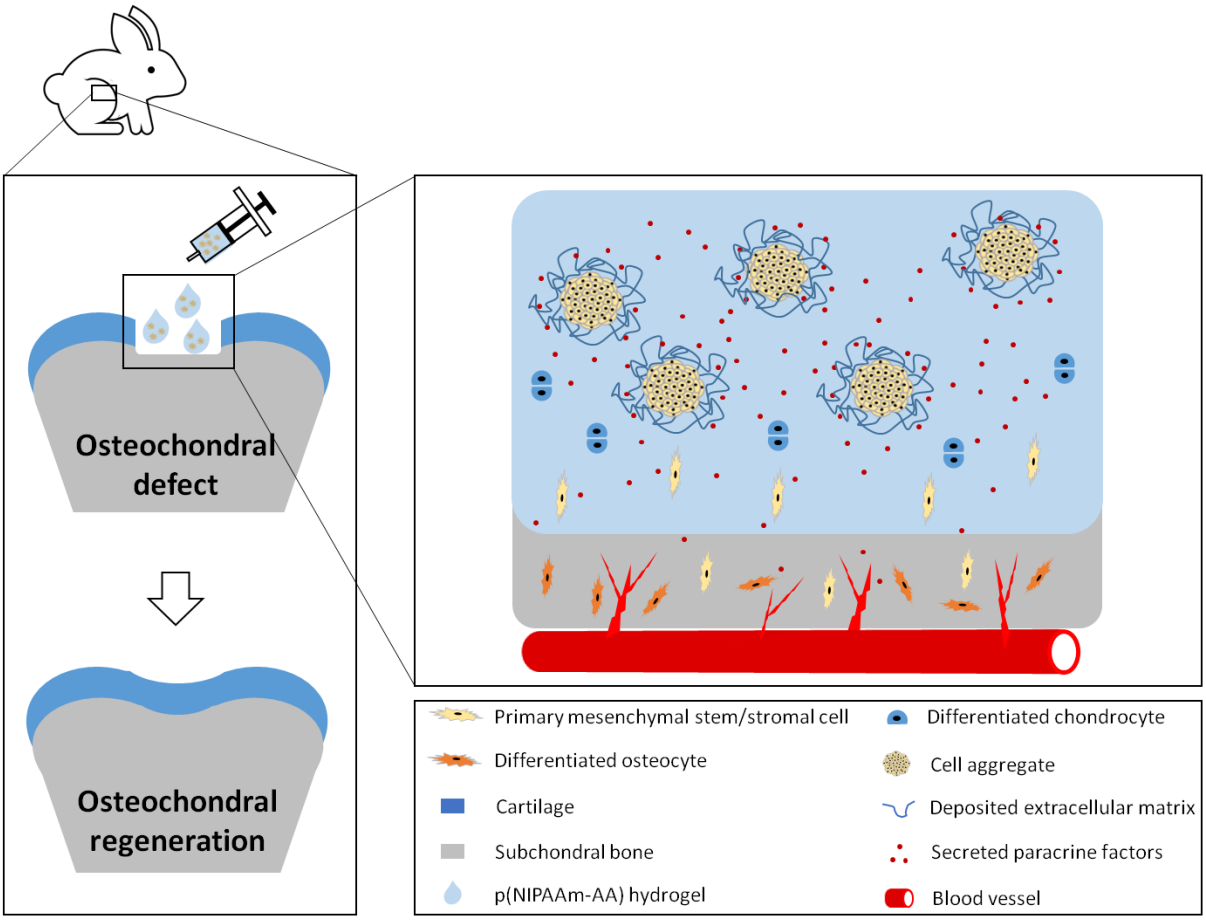

HIGHLIGHTS

- An injectable thermosensitive p(NIPAAm-AA) hydrogel is used for delivery of primary allogeneic mesenchymal stem/stromal cells (MSCs).
- Formation of MSC aggregates in p(NIPAAm-AA) hydrogel.
- Osteochondral regeneration by synergy of paracrine effects and multipotent properties of MSC aggregates.

4.2 Abstract

Osteoarthritis (OA) is an inflammation-related chronic disease that causes progressive degeneration of cartilage, which might even extend to subchondral bones. Due to the unique physiological structural differences between cartilage and subchondral bone, it is challenging to restore the full function of an osteochondral defect. In this study, a thermosensitive poly(*N*-isopropylacrylamide-co-acrylic acid) (p(NIPAAm-AA)) hydrogel was used as a carrier for allogeneic primary mesenchymal stem/stromal cells to determine the therapeutic efficacy of the cell-hydrogel hybrid on osteochondral regeneration. At a similar mechanical strength, p(NIPAAm-AA) hydrogel facilitates formation of cell aggregates of allogeneic primary MSCs *in situ*, while the fibrin hydrogel supports cell binding and the development of a spindle morphology. While the p(NIPAAm-AA) hydrogel did not induce any inflammatory effects, the fibrin hydrogel was found to elicit a pro-inflammatory response. MSC aggregates promotes expression of paracrine signaling-related genes (*TGFB1*, *VEGF*, *CXCL12*, *IGF1*, *BMP2*, *BMP7*, *WNT3A*, *CTNNB1*) as well as expression of chondrogenesis-related genes (*SOX9*, *ACAN*, and *COL2A1*) and generation of extracellular matrices (ECMs) (type 2 collagen and glycosaminoglycans) in chondrogenic induction medium. The functional enhancement of paracrine effects by MSC aggregates (i.e. the immunomodulatory effect and the stimulation of stem/progenitor cells homing) and induced differentiation of MSCs might play a synergistic role in the generation of the neo-cartilage and subchondral bone at an osteochondral defect site *in vivo*. Delivery of primary allogeneic MSCs in the context of a thermosensitive p(NIPAAm-AA) hydrogel to an osteochondral defect site may be a novel and promising strategy for osteochondral regeneration.

KEYWORDS: thermosensitive hydrogel, mesenchymal stem/stromal cells, cell aggregates, osteochondral regeneration

4.3 Introduction

Osteoarthritis (OA) is a chronic joint disease mainly caused by injury or other pathological abnormalities. Serious inflammation often obstructs the normal function of a joint, leading to progressive degeneration of cartilage and remodeling of the subchondral bone. [1] A normal hyaline cartilage is rich in glycosaminoglycans, proteoglycans, and type 2 collagen, and is devoid of blood vessels and type 1 collagen. In contrast, there is an abundant vasculature, type 1 collagen and calcium deposition in the subchondral bone. [2] Such anatomical differences at the subchondral site makes it challenging for functional restoration of the entire osteochondral defect. To address this issue, a variety of strategies have been employed, such as delivery of multiple growth factors [3-8] including transforming growth factor (TGF) for cartilage and bone morphogenetic protein (BMP) for bone in a controlled manner, or implantation of a three-dimensional (3D) scaffold with defined pore sizes and fiber orientation to mimic the specific architecture and topography of cartilage and bone [9, 10]. However, in these studies, the incorporated growth factors was not sustained and non-responsive to the *in-vivo* physiological changes. [6] Moreover, in these studies, the physical cues required for osteochondral regeneration were limited, with the 3D scaffold simply serving to provide the structural support for the homing of endogenous stem/progenitor cells. [11] Alternatively, cell-based therapy by injection of mesenchymal stem/stromal cells (MSCs) *in vivo* had shown promise in the relief of OA-induced pain and knee joint repair [12] due to pluripotency and immunomodulatory effects (i.e. immunosuppression and anti-inflammation) of MSCs [13, 14]. Moreover, because of the low immunogenicity, high immunosuppressive capacity, and easy accessibility allogeneic MSCs can be a reliable and promising alternative cell source for the cell-based therapy in contrast to the limited autologous MSCs. [15] Once implanted, MSCs could either differentiate into a specific cell type, or consistently secrete specific growth factors for immunomodulation and attraction of endogenous stem/progenitor cells from the surrounding normal tissues, all of which were implemented as required according to the *in-vivo* physiological changes. [13, 16]

However, when implanted without the assistance of a three-dimensional (3D) scaffold, MSCs were poorly retained at the defect site and exhibited poor survival, necessitating the use of large numbers of cells to demonstrate an effect. [17, 18] Hence, injectable hydrogels, such as thermosensitive hydrogels, that form a gel in response to the temperature change, have been explored as a potential carrier for the delivery of MSCs. [19-21] Furthermore, cell aggregates were able to enhance cell survival and biological function, including production of extracellular matrices, secretion of growth factors, and multi-lineage differentiation, when compared with single cells. Thus, delivery of cell aggregates has emerged as a novel strategy for stem cell-based therapy. [22, 23] Hence, an injectable hydrogel that could be employed as a carrier and simultaneously promote generation of cell aggregates would be the best candidate for osteochondral regeneration. It was previously reported that a thermosensitive p(NIPAAm-AA) hydrogel enhanced multi-lineage cell differentiation by facilitating formation of cell aggregates *in situ*. [24] In this study, the p(NIPAAm-AA) hydrogel was evaluated for its capacity to support MSC-mediated osteochondral regeneration. Fibrin hydrogel, which has been utilized for osteochondral regeneration, was used at an equivalent mechanical strength to the p(NIPAAm-AA) hydrogel and served as a positive control. Cell viability, proliferation, and differentiation of human and rabbit primary MSCs in the p(NIPAAm-AA) hydrogel and fibrin hydrogel were compared *in vitro*. The inflammatory effect of both hydrogels was assessed prior to animal experiments. The therapeutic benefit of injection of p(NIPAAm-AA) hydrogel with primary allogeneic MSCs into a rabbit model with an osteochondral defect at the knee joint was assessed. Furthermore, the underlying mechanism of this p(NIPAAm-AA) hydrogel/MSCs hybrid graft for enhancing osteochondral regeneration was also examined.

4.4 Experimental Section

4.4.1 P(NIPAAm-AA) hydrogel synthesis

Poly (*N*-isopropylacrylamide-co-acrylic acid) (p(NIPAAm-AA)) was synthesized by free radical emulsion polymerization. [25] Briefly, 9.9 mmol recrystallized *N*-isopropylacrylamide

(NIPAAm, Tokyo Chemical Industry), 0.1 mmol acrylic acid (AA, Acros Organics), 0.2 mmol *N',N'*-methylenebisacrylamide (MBA, Sigma-Aldrich), and 0.12 mmol sodium dodecyl sulfate (SDS, BDH Laboratory Supplies) were homogeneously dissolved in 97 mL of ultra-pure water and degassed with continuous supply of nitrogen gas in a three-necked flask at 50 °C for 45 min. The polymerization was initiated by quickly adding 3 mL of 1.0 mM potassium persulfate (KPS, Chem-Supply) into the precursor solution after the temperature was raised to 70 °C. The reaction was performed overnight under the protection of nitrogen gas. To remove the unreacted monomers, the synthesized polymer solution was dialyzed in a MW 12-14 kDa molecular membrane tubing (Spectrum Labs) and against ultra-pure water for 7 days with daily water change. The polymer solution was then concentrated to a concentration of approximately 130 mg mL^{-1} by stirring and heating at 70 °C. The concentration was calculated by drying and weighting 100 µL of the polymer solution. The p(NIPAAm-AA) hydrogel was sterilized by exposing to UV light for at least 2 h.

4.4.2 Mechanical characterization of hydrogels

The fibrinogen (Sigma-Aldrich) solution at a concentration of 0.5 mg mL^{-1}, 0.75 mg mL^{-1}, or 1 mg mL^{-1} was prepared by dissolving in complete cell medium (α-minimal essential medium (MEM, Sigma-Aldrich) supplemented with 10 % fetal bovine serum (FBS, Sigma-Aldrich) and 50 U mL^{-1}/50 µg mL^{-1} penicillin/streptomycin (P/S, CSL)) with 0.01 M magnesium chloride ($MgCl_2$, Chem-Supply). 1 mL of the above solution was added onto the rheometer stage and homogeneously mixed with 20 µL of 100 U mL^{-1} thrombin (Sigma-Aldrich). The distance between two parallel plates (40 mm in diameter) was set at 0.65 mm and the temperature was kept at 37 °C for 30 min to allow complete formation of fibrin gel. Shear stresses of the fibrin hydrogels were measured by a SR5 rheometer (Rheometric Scientific) at a constant frequency of 1.5915 Hz and a strain varying from 0 to 100 %. Storage modulus (G'), loss modulus (G"), and absolute complex modulus (|G*|) of the fibrin hydrogels were measured at a frequency of 1.5915 Hz and a shear stress varying from 0.1 Pa to 100 Pa. In addition, the p(NIPAAm-AA)

hydrogel was prepared at a concentration of 30 mg mL^{-1} by homogeneously mixing 50 mg mL^{-1} p(NIPAAm-AA) hydrogel, 0.05 M $MgCl_2$ solution, and complete cell medium at a volumetric ratio of 3 : 1 :1. The shear stress was measured at a varying strain and the dynamic moduli at a varying shear stress, a similar procedure for characterization of the fibrin hydrogel.

4.4.3 Scanning electron microscopy (SEM)

0.75 mg mL^{-1} fibrin hydrogel and 30 mg mL^{-1} p(NIPAAm-AA) were prepared and freeze-dried overnight by an Alpha 2-4 LD Freeze dryer (Martin Christ). After coating with a thin layer of platinum, the samples were imaged under a XL30 FEGSEM (Philips) at an accelerating voltage of 10 kV.

4.4.4 Live&Dead staining

The human bone-derived mesenchymal stem/stromal cells (NOD MSCs) used in this study were obtained from normal donors (ND0303, ND0055, ND0059, ND0128, and ND0361) with approval from Adelaide Hospital Ethics Committee (RAH Protocol No.940911a) as described in the previous study. [26, 27] Low passage (i.e. < passage 5) were used in this study and their multi-pluripotency were evaluated as previously described. [24] To avoid the variation between donors, cells derived from three different normal donors were used in each experiment. 30 mg mL^{-1} p(NIPAAm-AA) or 0.75 mg mL^{-1} fibrin hydrogels were coated on the bottom of the 48-well plates (250 µL per well). 1× PBS was replaced with the complete cell medium to dilute the concentrated hydrogels. After gel formation at 37 °C, the same volume of cell-gel hybrids, prepared by dispersing the ND0303 NOD MSC suspension at a density of 5.0×10^6 cells mL^{-1} in the complete cell medium with p(NIPAAm-AA) or fibrin hydrogels, was gently layered on the p(NIPAAm-AA)- or fibrin-coated wells. The cell-gel hybrids were allowed to gel by incubating at 37 °C for 60 min in a humidified incubator including 5 % CO_2, after which the cell-gel hybrids were top-upped with complete cell medium (500 µL per well) and incubated overnight in a humidified incubator including 5 % CO_2. 250 µL of the staining solution (4 µM Calcein AM and 2 µM Ethidium Homodimer-1 (Thermo-Fisher)) was added into each well

containing the cell-gel hybrids and stored in dark for 20 min at 37 °C. The morphology of the cells cultured in the hydrogels was imaged with or without fluorescence by a CKX41 fluorescent microscope (Olympus). Live cells were stained with a green color while dead cells with a red color.

4.4.5 Cell proliferation assay

125 µL cell-gel hybrids were prepared at a final cell density of 1.0×10^5 cells mL^{-1} and casted on each fibrin- or p(NIPAAm-AA)- coated well in a 96-well plate. 125 µL of complete cell medium was top-upped and changed every two days. NOD MSCs from three different normal donors (ND0059, ND0128, and ND0361) were used. After each time point (day 1, 5, 9, and 14), 50 µL of the spent medium was removed from each well. 25 µL of 4-[3-(4-Iodophenyl)-2-(4-nitrophenyl)-2H-5-tetrazolio]-1,3-benzene disulfonate (WST-1, Sigma-Aldrich) was then added into the cell-gel hybrids and incubated at 37 °C for 4 h in a humidified incubator including 5 % CO_2. The absorbance was measured by an iMark microplate reader (BIO-RAD) at a wavelength of 450 nm. NOD MSCs cultured on the two-dimensional (2D) 96-well plate were used as a control.

4.4.6 Chondrogenesis of primary MSCs *in vitro*

To induce chondrogenesis of human NOD MSCs (ND0055, ND0059, and ND0128), 30 mg mL^{-1} p(NIPAAm-AA) or 0.75 mg mL^{-1} fibrin hydrogels were mixed with NOD MSCs at a cell density of 1.0×10^6 cells mL^{-1} in the high glucose chondrogenic induction medium (Dulbecco' Modified Eagle's Medium (DMEM-high, Sigma-Aldrich), 1× ITS pre-mix (BD Biosciences), 50 U mL^{-1}/50 µg mL^{-1} P/S, 2 mM L-glutamine (Sigma-Aldrich), L-ascorbate-2-phosphate (WAKO), 0.1 µM Dexamethasone sodium phosphate (Hospira Australia), 0.125 % bovine serum albumin (BSA, Sigma-Aldrich), and 10 ng mL^{-1} human transforming growth factor (TGF-β3, Lonza)). Cell aggregates were formed overnight and cultured in the induction medium at 37 °C for up to 4 weeks in a humidified incubator including 5 % CO_2 with medium change twice per week. After inducing chondrogenesis for 4 weeks, cells were lysed in TRIzol

(Life Technology) for 5 min at room temperature. Total RNA was extracted for reverse transcription polymerase chain reaction (RT-PCR) to synthesize cDNA as previously described. [24] Chondrogenesis-related genes (SOX-9 (*SOX9*), aggrecan (*ACAN*), collagen 2A1 (*COL2A1*), collagen 10A1 (*COL10A1*)) were then assessed using Real-Time PCR (qPCR) with human primer pairs (Table S4.1) and normalized to the value of actin-beta gene (*ACTB*).

4.4.7 Histology and immunofluorescence staining

After inducing chondrogenesis for 4 weeks, the cells cultured in p(NIPAAm-AA) hydrogel were harvested by diluting and centrifuging in the cold 1× PBS. The cells were then, in turn, fixed in the 4 % paraformaldehyde solution (PFA, Sigma-Aldrich) and cryoprotected in 30 % sucrose solution overnight. Cells cultured in the fibrin hydrogel were directly processed for fixing and cryoprotecting. The cells were embedded in the OCT components (Tissue-Tek) and cryo-sectioned on gelatin-coated glass slides (Sigma-Aldrich) at a thickness of 8 µm by a Cryostat Shandon Cryotome E (Thermo-Fisher).

Prior to staining, the sections were dried in a fume hood for 1 h. To evaluate the production of sulfated glycosaminoglycans (GAGs), the sectioned cells were stained in 1.0 % Alcian Blue solution (Sigma-Aldrich) and 0.1 % nuclear fast red solution. After blocking in the 5 % normal goat serum, the sections were in turn immersed in collagen 2A1 primary antibody from rabbits (Santa Cruz) in a humidified box at 4 °C overnight and FITC-labelled goat-anti-rabbit secondary antibody (SouthernBiotech) for 2 h in a humidified sheltered box at room temperature, and 300 nM DAPI (Sigma-Aldrich) for immunofluorescent staining of type 2 collagen. After mounting, the stained cells were imaged with a IX53 fluorescent microscope (Olympus).

4.4.8 Sulfated glycosaminoglycans quantification

After inducting chondrogenesis for 4 weeks, the cells cultured in hydrogels or cell pellets by spinning cell suspensions in a polypropylene tube at 600 rcf for 5 min were washed with 1× PBS three times and digested in 200 µL digestion solution (62.1 mg of 3.10 U mg^{-1} Papain

(Fluka) + 9.86 mL of 0.05 M sodium phosphate buffer (pH = 6.5, Sigma-Aldrich) + 40 µL of 0.5 M ethylenediaminetetraacetic acid solution (pH = 8, Sigma-Aldrich) + 100 µL of 200 mM N-Acehyl-Cysteine (Sigma-Aldrich)) at 65 °C overnight with gentle vortex at a rotating speed of 700 rpm. 0.25 µg mL^{-1} stock chondroitin-6-sulfate was diluted in the digestion solution to a gradient standard concentration (0.25 µg mL^{-1}, 0.2 µg mL^{-1}, 0.15 µg mL^{-1}, 0.1 µg mL^{-1}, 0.075 µg mL^{-1}, 0.05 µg mL^{-1}, 0.025 µg mL^{-1}, 0 µg mL^{-1}). 150 µL 1,9-Dimethyl Methylene Blue (DMMB) working solution (8 mg DMMB (Sigma-Aldrich) + 2.5 mL ethanol (Chem-Supply) + 1 g sodium formate (Sigma-Aldrich) + 1 mL formic acid (BDH) + 496.5 mL ultrapure water) was either mixed with 50 µL chondroitin-6-sulfate standard solution or digested sample solutions. After gently mixing, the absorbance was read by a Victor3 1420 Multilabel Counter (PerkinElmer) at a wavelength of 525 nm. The concentration of the sulfated GAGs extracted from the cells was calculated according to the standard curve. In addition, the concentration of the DNA extracted from the cells was calculated according to the standard dsDNA curve after measuring the absorbance of 50 µL DNA (extracted sample DNA or standard gradient dsDNA) and 150 µL PicoGreen (1:200 dilution, Thermo-Fisher) mix by a Victor3 1420 Multilabel Counter (PerkinElmer) at the excitation and emission wavelengths of 485 nm and 535 nm, respectively. The production of sulfated GAGs was presented as the relative sulfated GAGs by normalizing the value of sulfated GAGs to that of DNA.

4.4.9 Inflammatory effect of p(NIPAAm-AA) and fibrin hydrogels

A macrophage cell line (Raw264.7, American Type Culture Collection) was used for the inflammatory effect of p(NIPAAm-AA) and fibrin hydrogels. Briefly, 2.5×10^5 Raw264.7 cells were seeded into each well of a 24-well plate and allowed to attach to the bottom for 4 h. 0.75 mg mL^{-1} of fibrin hydrogel or 30 mg mL^{-1} p(NIPAAm-AA) hydrogel was added on the top of the cells at a volume of 500 µL per well. The hydrogels were incubated in a humidified incubator containing 5% CO_2 at 37 °C for 1 h before addition of another 500 µL complete culture medium per well. Raw264.7 cells cultured without hydrogels were used as a negative

control and the cells pre-stimulated with 200 ng mL^{-1} of lipopolysaccharide (LPS, Sigma-Aldrich) for 24 h and cultured without hydrogels were used as a positive control. After incubating for 24 h, the supernatants were collected and used for detection of nitrite production in the medium using Griess reagents as per the manufacturer's protocol. The mRNA expression of pro-inflammation-related genes (interleukin-1 beta (*IL1B)*, interleukin-6 (*IL6*), tumor necrosis factor alpha (*TNFA*), nitric oxide synthase-2 (*NOS2*)) in Raw264.7 cells was also measured by RT-qPCR. All values were normalized to that of *ACTB* gene. The specific mouse primer sequences were shown in Table S4.2.

4.4.10 Cell isolation and characterization for in vivo osteochondral regeneration

The animal experiment was performed by following the approved guidelines of Nanjing Medical University Ethics Committee. Rabbit bone marrow-derived mesenchymal stem/stromal cells (BMSCs) were harvested by aspirating bone marrow from the femurs and tibias of a rabbit (250 g, 2 weeks) and cultured in Dulbecco's Modified Eagle's Medium (DMEM, Sigma-Aldrich) supplemented with 10 % FBS. Rabbit BMSCs at the passage 4 were used for the following experiments. The morphology of the extracted rabbit BMSCs was imaged with an ECLIPSE Ci microscope (Nikon) and the multi-pluripotency of rabbit BMSCs was evaluated by inducing cell differentiation in the chondrogenic induction medium, osteogenic induction medium (DMEM, 15 mM HEPES (Life Technologies), 100 μM L-ascorbic acid 2-phosphate sesquimagnesium salt hydrate (Aladdin), 5 % FBS, 0.1 μM dexamethasone sodium phosphate (Tianxin), 10 mM β-glycerophosphate disodium salt hydrate (Sigma-Aldrich)), or adipogenic induction medium (DMEM, 10 % FBS, 15 mM HEPES, 100 μM L-ascorbic acid 2-phosphate sesquimagnesium salt hydrate, 60 μM indomethacin (Sigma-Aldrich), 0.1 μM dexamethasone sodium phosphate). The cells cultured in the complete culture medium without inductive biomolecules were used as the controls. After inducing chondrogenesis or adipogenesis for 3 weeks, the cells were stained with Alcian Blue/Weigert's Iron Haematoxylin for detecting sulfated GAGs or Oil Red O/Mayer's Haematoxylin for

detecting lipids, while the osteogenesis-induced cells were stained with Alizarin Red S to assess the deposition of calcium after 6 weeks. Furthermore, rabbit BMSCs were also embedded in fibrin and p(NIPAAm-AA) hydrogels and induced chondrogenesis for 4 weeks. Morphology of the induced cells were imaged with an ECLIPSE Ci microscope (Nikon). The mRNA expression of chondrogenesis-related genes (*SOX9*, *ACAN*, and *COL2A1*) was measured by RT-qPCR. All data were normalized to the value of *GADPH* gene. The sequences of the rabbit primer pairs were shown in Table S4.3.

4.4.11 Paracrine effect of cell aggregates

Briefly, rabbit bone marrow-derived mesenchymal stem/stromal cells were cultured in 30 mg mL^{-1} of p(NIPAAm-AA) hydrogel and 0.75 mg mL^{-1} fibrin hydrogel, respectively, at a density of 1.0×10^6 cells mL^{-1}. After culturing overnight, the cell morphology was recorded by an ECLIPSE Ci microscope (Nikon) and the gene expression of the paracrine signaling-related biomolecules (basic fibroblast growth factor (*FGF2*), transforming growth factor beta-1 (*TGFB1*), transforming growth factor beta-3 (*TGFB3*), vascular endothelial growth factor (*VEGF*), stromal cell-derived factor-1 (*SDF-1*), insulin-like growth factor-1 (*IGF-1*), bone morphogenetic protein-2 (*BMP2*), bone morphogenetic protein-7 (*BMP7*), Wnt-3a (*WNT3A*), Wnt-5a (*WNT5A*), catenin beta-1 (*CTNNB1*)) were measured by RT-qPCR. All values were normalized to that of *GAPDH* gene. The sequences of the rabbit primer pairs were shown in Table S4.3.

4.4.12 Defect creation & cell/hydrogel implantation

13 male New Zealand rabbits (~2.5 kg, 3 months) were used in the animal experiment. 1 mL of the anesthetic hybrid (ketamine hydrochloride (Gutian): xylazine Hydrochloride (Huamu) at a volumetric ratio of 10 : 1) was intramuscularly injected into each rabbit for anesthetization. To create the osteochondral defect, a hole with a diameter of 4 mm and a depth of 1.6 mm, approximately 20 μL in volume, was drilled into the lateral hemicondyle of knee joints after trochlear grooves were exposed by medial parapatellar incision and laterally dislocation of the

patella. These rabbits with osteochondral defects were divided into three groups: Group 1 (*n* =5) was injected with 20 µL of the cell-fibrin mixture with 2.5×10^5 cells at the osteochondral defect site on the left legs, while fibrin hydrogels only on the right leg; The osteochondral defect site on the left legs of Group 2 (*n* = 4) was injected with 20 µL of the cell-p(NIPAAm-AA) mixture in which cell aggregates were generated and harvested after culturing 2.5×10^5 cells in p(NIPAAm-AA) hydrogel overnight, while p(NIPAAm-AA) hydrogels only on the right leg; Group 3 (*n* = 4) was injected with 20 µL of 2.5×10^5 cell suspension on the left leg, while 20 µL of cell culture medium without cells on the right leg. Cell density was determined by defect size [28] and kept consistent with the cell density used in "4.4.6 Chondrogenesis of primary MSCs *in vitro*". The incisions were sutured and the defects were kept upwards for at least 30 min. After implantation, each rabbit was intramuscularly injected with 1 mL of 2×10^5 U mL^{-1} penicillin sodium solution (Shiyao) daily up to 3 days.

4.4.13 Characterization of the regenerative osteochondral tissues

After 3 months, the regenerative tissues at the defect site near the distal femurs of the euthanized rabbits were harvested for photographing and micro-computed tomography (µCT) scanning by an Inveon Micro-PET/CT scanner (Siemens) at a voltage of 80 kV, a current of 500 µA, and a spatial resolution of 15 µm. A reconstructed three-dimensional (3D) image of the regenerative tissue was generated by Siemens Inveon Research Workplace (IRW) software to obtain the photographed structure at the regenerative defect. Moreover, the bone regeneration was also evaluated by measuring the values of bone volume/total (tissue) volume (BV/TV), bone surface area/bone volume (BS/BV), trabecular thickness (Tb.Th), and trabecular number (Tb.N) at the defect region with IRW software based on the radiographed µCT images (*n* = 3). The regenerated cartilages (*n* = 3 for each group) were blindly graded based on their macroscopy images by the international cartilage repair society (ICRS) scoring system. [29]

The regenerative tissues were then fixed in the 4 % PFA solution at 4 °C for 1 week with one change by the fresh solution, after which the tissues were decalcified in 14 %

ethylenediaminetetraacetic acid solution (EDTA, pH = 7.1, Macklin) at room temperature under gentle and constant agitation with a change of fresh solution twice per week. When the tissues became soft enough to be easily punctured by a needle, dehydration and paraffin embedding were performed. The tissues were sectioned at a thickness of 5 μm and histologically stained in Haematoxylin & Eosin dye to show the morphology and integration of the regenerative tissues to the surrounding normal tissues, in Safranin O dye to confirm cartilage regeneration, and in Masson's Trichrome dye to evidence generation and accumulation of collagen. Immunofluorescent staining was also performed to display the distribution of collagen type 1 using mouse anti-type 1 collagen primary antibody (Sigma-Aldrich) /Alexa Fluor 488-labelled goat-anti-mouse secondary antibody (Beyotime) and counterstaining with Hoechst 33342 (KeyGEN BioTECH).

4.4.14 Statistics analysis

All experiments except those specifically stated were performed in triplicates. Data were presented as mean ± standard error (SE). The statistic difference was compared using one-tailed student *t* test. *$\rho < 0.05$ and ** $\rho < 0.01$ indicated that the difference was significant and very significant, respectively, while $\rho > 0.05$ for no significant difference (n.s.).

4.5 Results

4.5.1 Characterization of hydrogels

To eliminate the influence of hydrogel stiffness on biological behaviors of primary mesenchymal stem/stromal cells, the dynamic moduli of the fibrin hydrogels at various concentrations were measured by a rheometer to match that of the p(NIPAAm-AA) hydrogel at a concentration of 30 mg mL^{-1} at 37 °C. From the shear stress-strain ramp, the shear stress for 0.75 mg mL^{-1} fibrin hydrogel displayed a linear increase in response to the strain ramp from 0 to 100 %, which was similar to 30 mg mL^{-1} p(NIPAAm-AA) hydrogel. (Figure S4.1a) Notably, fibrin hydrogel at a concentration of 0.75 mg mL^{-1} had a similar absolute complex modulus (|G*|) as that of p(NIPAAm-AA) hydrogel at a concentration of 30 mg mL^{-1}, approximately 1

Pa, when the external shear stress was 0.1 Pa. (Figure S4.1b) The elastic moduli of 0.75 mg mL^{-1} fibrin hydrogel and 30 mg mL^{-1} p(NIPAAm-AA) hydrogel were both over their viscous moduli when the external stress was lower than the critical value, which was the maximal bearing stress of a hydrogel. (Figure 4.1a) When the external shear stress reached 19.06 Pa, the viscous modulus of 0.75 mg mL^{-1} fibrin hydrogel became higher than its elastic modulus, indicating the critical value for 0.75 mg mL^{-1} fibrin hydrogel was around 19 Pa, while the critical value for 30 mg mL^{-1} p(NIPAAm-AA) hydrogel was only 0.2 Pa. (Figure 4.1a)

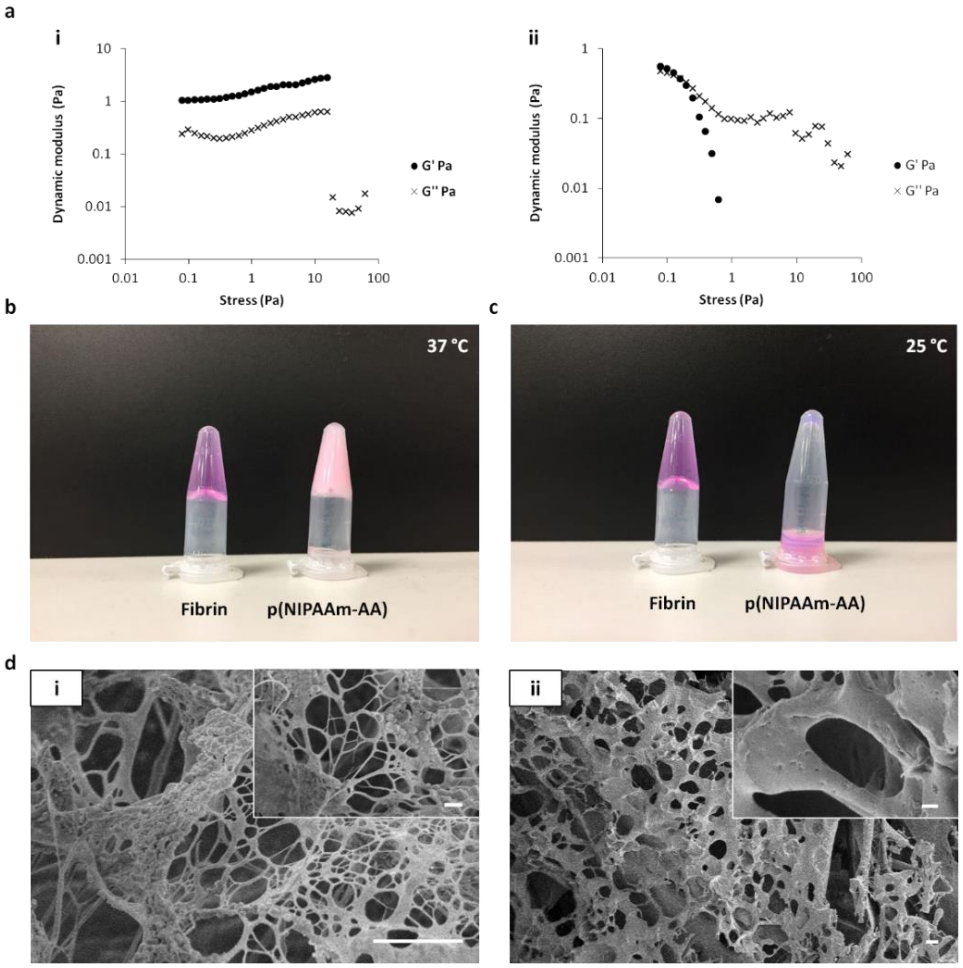

Figure 4.1 (a) Dynamic modulus (storage modulus (G') and loss modulus (G'')) of (i) 0.75 mg mL^{-1} fibrin hydrogel and (ii) 30 mg mL^{-1} p(NIPAAm-AA) hydrogel under different stresses. (b) Optical images of 0.75 mg mL^{-1} fibrin hydrogel (left) and 30 mg mL^{-1} p(NIPAAm-AA) hydrogel (right) at 37 °C. (c) Optical images of 0.75 mg mL^{-1} fibrin hydrogel (left) and 30 mg mL^{-1} p(NIPAAm-AA) hydrogel (right) at 25 °C. (d) SEM images of (i) 0.75 mg mL^{-1} fibrin hydrogel and (ii) 30 mg mL^{-1} p(NIPAAm-AA) hydrogel at a lower magnification (scale bar: 5 μm) and a higher magnification (inset, scale bar: 1 μm).

After the addition of thrombin, the fibrinogen solution was converted into fibrin by forming gel, while the thermosensitive p(NIPAAm-AA) formed a cloudy gel in response to the temperature

at 37 °C. (Figure 4.1b) After cooling the temperature to 25 °C, fibrin hydrogel still presented a gel state, however, p(NIPAAm-AA) hydrogel was liquified into a transparent solution. (Figure 4.1c) Furthermore, SEM images revealed a fibrous structure for the dehydrated fibrin hydrogel, while a porous morphology for the dehydrated p(NIPAAm-AA) hydrogel. (Figure 4.1d)

To study whether the hydrogels induced inflammation, the Raw264.7 macrophage cells were cultured in the complete cell medium containing either 30 mg mL^{-1} of p(NIPAAm-AA) hydrogel or 0.75 mg mL^{-1} of fibrin hydrogel for 24 h. There was no difference in mRNA expression of the pro-inflammatory genes (*IL6*, *TNFA*, *NOS2*) and nitric oxide (NO) production between the cells cultured without hydrogels (M(No-LPS)) and that with p(NIPAAm-AA) hydrogel ((PA(No-LPS)). (Figure S4.2) However, a significant lower mRNA expression of *IL1B* gene ($p < 0.01$) was seen in the cells cultured with p(NIPAAm-AA) hydrogel compared to that cultured without the hydrogel. In contrast, the mRNA expressions of *IL1B*, *IL6*, and *NOS2* genes were all significantly up-regulated ($p < 0.05$ for *IL1B* and *NOS2* genes; $p < 0.001$ for *IL6* gene) for the cells cultured with fibrin hydrogel (F(No-LPS)) compared to that without hydrogels, while they were still lower than those from the cells cultured with lipopolysaccharide (LPS) induction (M(LPs)), used as a positive control. (Figure S4.2) Furthermore, the production of NO also revealed a consistent result with the mRNA expression of these pro-inflammatory genes, producing a significantly higher amount of nitrite ($p < 0.05$) in the supernatant medium of the cells cultured with fibrin hydrogel compared to that without hydrogels, but lower than that of the positive control. (Figure S4.2)

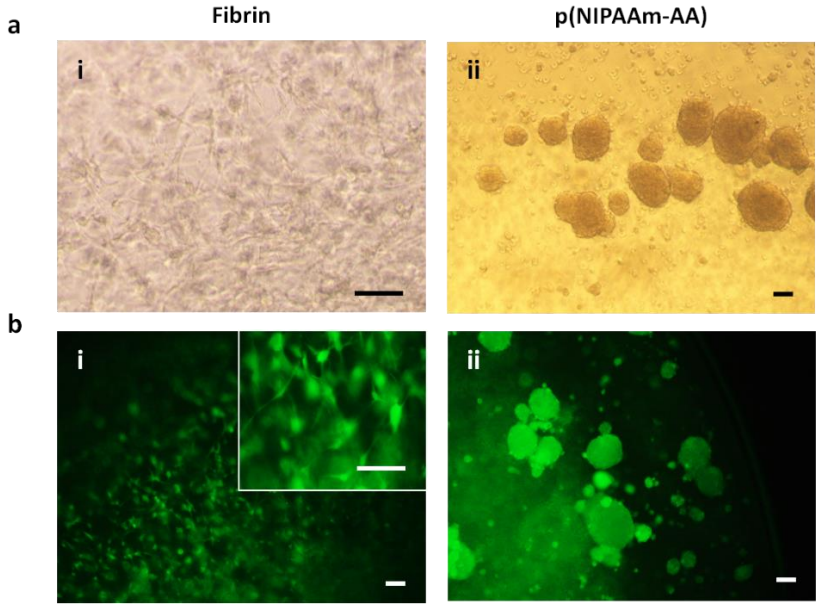

Figure 4.2 (a) Optical microscopy images and (b) Live&Dead staining images of ND0303 NOD MSCs cultured in (i) fibrin hydrogel or (ii) p(NIPAAm-AA) hydrogel with complete medium on day 1. Green: live cells; Red: dead cells. Scale bar: 100 µm.

4.5.2 Cell viability and cell proliferation

The biological properties of p(NIPAAm-AA) and fibrin hydrogels were first studied *in vitro* with human bone-derived mesenchymal stem/stromal cells (NOD MSCs) from normal donors. When seeding inside the hydrogels overnight, primary human NOD MSCs were attached to the fibrils of fibrin hydrogel and exhibited a fibroblast-like morphology, while those cells cultured in the p(NIPAAm-AA) hydrogel formed cell aggregates. (Figure 4.2a) Cell Live&Dead staining revealed good biocompatibility of both fibrin and p(NIPAAm-AA) hydrogels. (Figure 4.2b) Moreover, primary human NOD MSCs were also cultured on two-dimensional (2D) tissue culture plates, and in the fibrin and p(NIPAAm-AA) hydrogels for up to 14 days. The absorbance values indicated the cell number of NOD MSCs derived from three normal donors significantly increased after culturing for 14 days on either 2D plates or in the fibrin hydrogel. However, the cells cultured in the p(NIPAAm-AA) hydrogel did not show any significant increase in the cell number. (Figure 4.3)

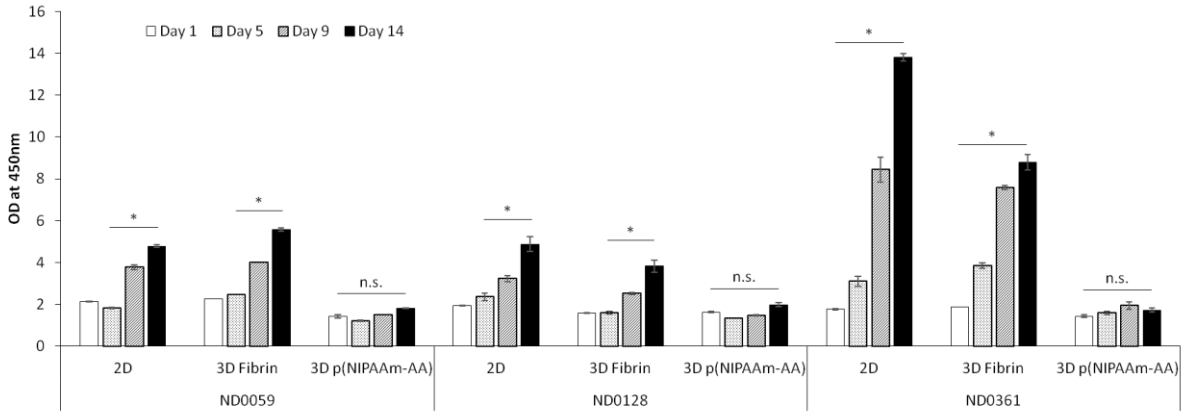

Figure 4.3 Proliferation of NOD MSCs derived from three different normal donors either culturing on a two-dimensional (2D) culture plate, or in the three-dimensional (3D) fibrin hydrogel, or in p(NIPAAm-AA) hydrogel. Data were presented as mean ± standard error (SE), n=3. "*" for $p < 0.05$; "not significant (n.s.)" for $\rho > 0.05$.

4.5.3 Cell differentiation

After inducing chondrogenesis for 4 weeks, the mRNA expression of the chondrogenesis-related genes (*SOX9*, *ACAN*, *COL2A1*, and *COL10A1*) were measured by RT-qPCR. (Figure 4.4) The mRNA expression of *SOX9* and *ACAN* were significantly higher for all NOD MSCs cultured in the p(NIPAAm-AA) hydrogel than NOD MSCs cultured in the fibrin hydrogel. However, due to variation from different donors, significantly increased mRNA expression of *COL2A1* were seen for ND0059 and ND0128 NOD MSCs cultured in the p(NIPAAm-AA) hydrogel compared to those cultured in fibrin hydrogel. In addition, the mRNA expression of *COL10A1* for ND0059 and ND0128 NOD MSCs cultured in the p(NIPAAm-AA) hydrogel was significantly lower than that cultured in the fibrin hydrogel.

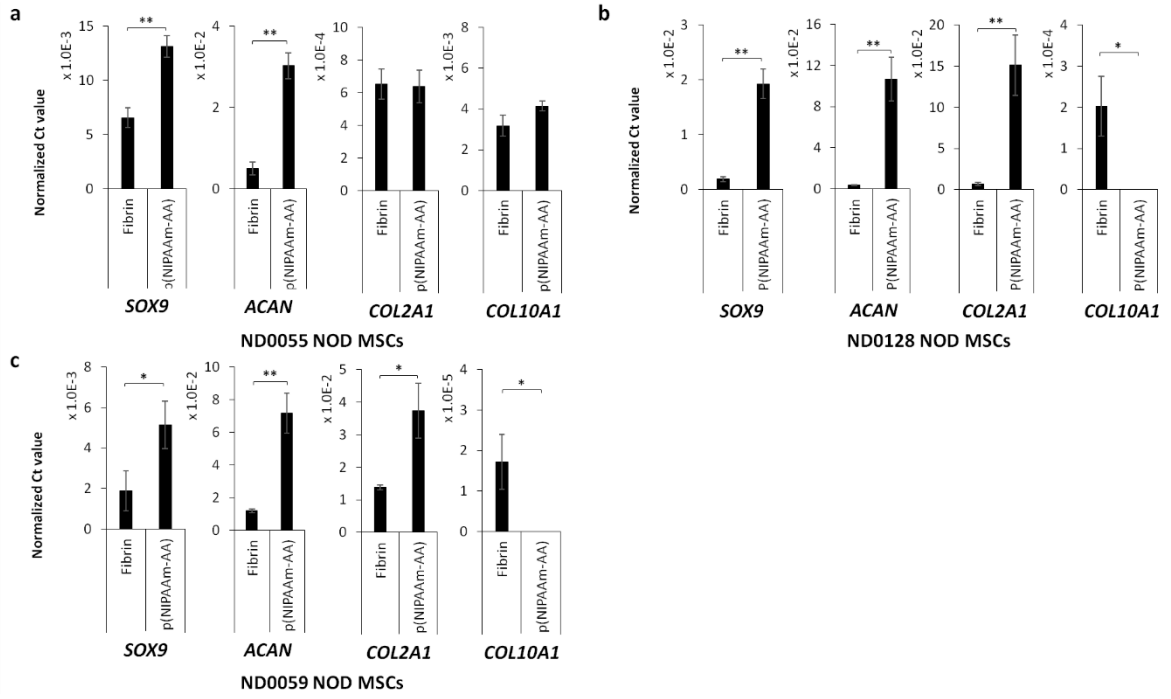

Figure 4.4 mRNA expression of chondrogenesis-related genes (*SOX9*, *ACAN*, *COL 2A1*, *COL 10A1*) for bone-derived mesenchymal stem/stromal cells from three normal donors: (a) ND0055 NOD MSCs, (b) ND0128 NOD MSCs, and (c) ND0059 NOD MSCs cultured in the fibrin or p(NIPAAm-AA) hydrogels on day 29. Data were presented as mean ± standard error (SE), *n*=3. "*" for $\rho < 0.05$; "**" for $\rho < 0.01$.

After culturing in the chondrogenic-induction medium for 4 weeks, the cell-fibrin hybrid shrank to a large pellet that was anchored to the wall of a well (Figure 4.5ai). In contrast, the NOD MSCs cultured in the p(NIPAAm-AA) hydrogel formed aggregated that showed evidence of sprouting which further developed into a cell aggregate network. (Figure 4.5aii) Furthermore, the immunofluorescent images indicated distinct production of collagen 2A1 in both fibrin and p(NIPAAm-AA) hydrogels. (Figure 4.5b) The Alcian Blue staining images also revealed distinct sulfated glycosaminoglycans (GAGs) production (blue color) for cells cultured in the fibrin and p(NIPAAm-AA) hydrogels. (Figure 4.5c) To further quantify the sulfated GAGs production, the sulfated GAGs were extracted and measured by the DMMB assay. The accumulation of sulfated GAGs in p(NIPAAm-AA) was significantly higher than that seen in either the cell pellets or the fibrin hydrogel. On the contrary, there was no significant difference in the production of sulfated GAGs between cell pellets and cells in fibrin hydrogel. (Figure 4.5d)

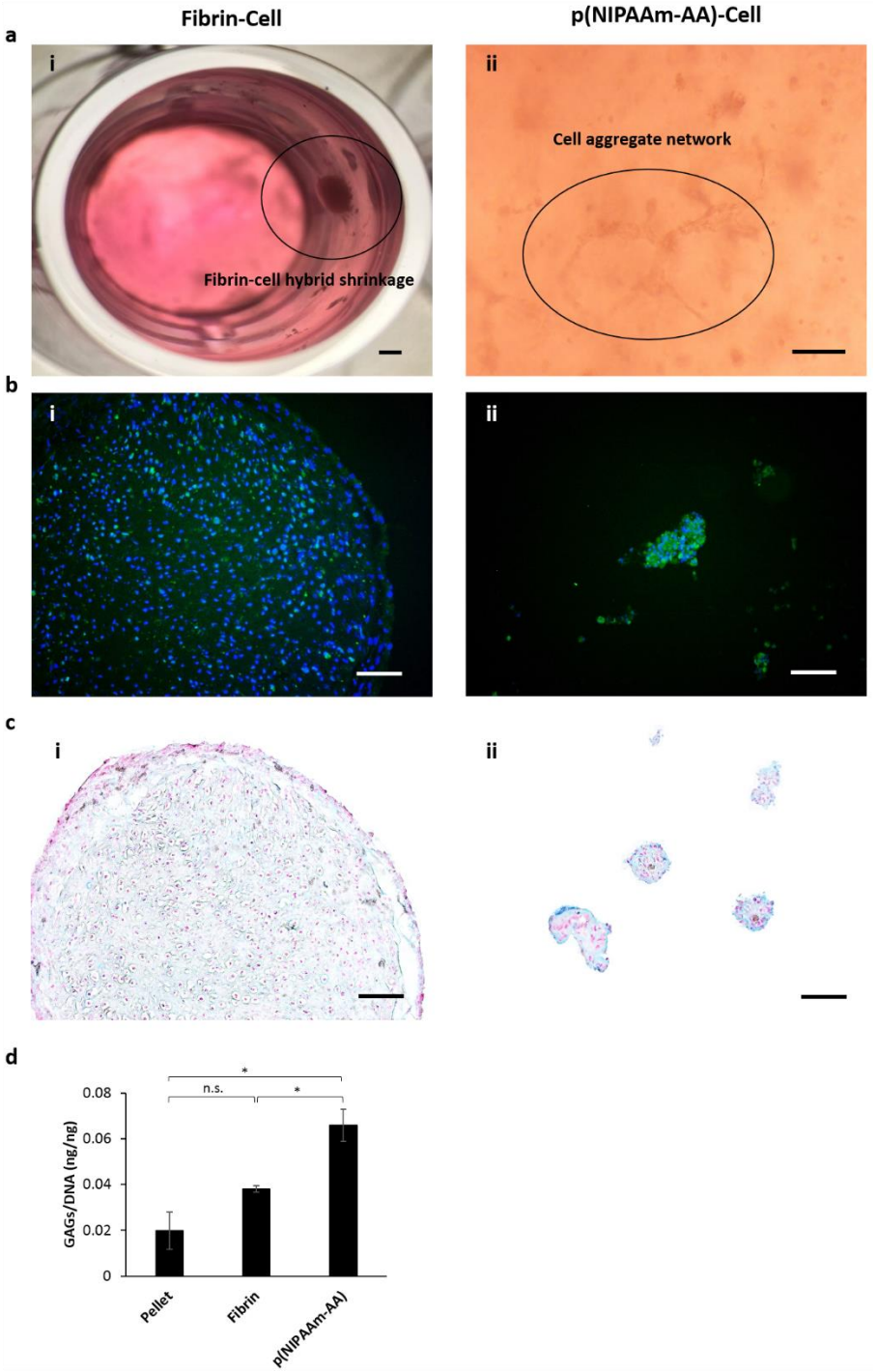

Figure 4.5 (a) Optical images of chondrogenesis-induced NOD MSCs cultured in (i) fibrin hydrogel (scale bar: 1 mm) or (ii) p(NIPAAm-AA) hydrogel (scale bar: 100 μm) for 4 weeks at a lower magnification. (b) Immunofluorescent images of NOD MSCs induced chondrogenesis in (i) fibrin hydrogel or (ii) p(NIPAAm-AA)hydrogel for 4 weeks. Green: collagen 2A1; Blue: cell nuclei. Scale bar: 100 μm. (c) Alcian blue staining images of chondrogenesis-induced NOD MSCs cultured in (i) fibrin hydrogel or (ii) p(NIPAAm-AA) hydrogel for 4 weeks. Blue: sulfated glycosaminoglycans (GAGs); Red: cell nuclei. Scale bar: 100 μm. (d) Relative GAGs production of NOD MSCs induced chondrogenesis in the fibrin hydrogel, the p(NIPAAm-AA) hydrogel, or as pellets in the polypropylene tubes for 4 weeks by normalizing total GAGs to the total cell number. Data were presented as mean ± standard error, n=3. "*" for $\rho < 0.05$; "not significant (n.s.)" for $\rho > 0.05$.

4.5.4 Osteochondral regeneration

4.5.4.1 Characterization of the bone marrow-derived primary mesenchymal stem/stromal cells.

To further assess the efficacy of p(NIPAAm-AA) hydrogel for osteochondral regeneration *in vivo*, rabbit primary bone marrow-derived mesenchymal stem/stromal cells (BMSCs) were used for the following experiments. The multi-potent properties of the rabbit BMSCs was assessed by inducing cell differentiation in induction media (chondrogenic-, osteogenic- and adipogenic-induction media). Compared to rabbit BMSCs cultured in the complete medium without induction biomolecules, more Oil Red O staining for lipids (red color) was seen in the cells cultured in the adipogenic induction medium. Similarly, compared to control media, more Alizarin Red S staining of calcium deposition (red color) from cells cultured in the osteogenic induction medium was observed. (Figure S4.3a-b) However, rabbit BMSCs cultured as cell pellets, by spinning cells in a polypropylene tube either in the complete medium or in the chondrogenic induction medium, produced sulfated GAGs (blue color), but no significant difference was seen between BMSCs pellets in the complete medium or BMSCs in the chondrogenic induction medium. (Figure S4.3c) In addition, the extracted rabbit BMSCs exhibited a typical fibroblast-like morphology. (Figure S4.4a) Prior to implantation into the osteochondral defects, rabbit BMSCs were pre-cultured in fibrin hydrogel or p(NIPAAm-AA) hydrogel to display similar properties of human NOD MSCs (Figure 4.2a). As Figure S4.4b and Figure S4.4c indicated, rabbit BMSCs cultured in the fibrin hydrogel were attached to the fibrils and displayed a fibroblast-like morphology, while cell aggregates were formed in p(NIPAAm-AA) hydrogel after overnight. The chondrogenesis-induced cells in fibrin and p(NIPAAm-AA) hydrogels both produced a significant amount of lipids in the cytoplasm and a rich extracellular matrixces (ECMs) deposition. (Figure S4.4d-e) Furthermore, RT-qPCR results also revealed that the mRNA expression of chondrogenesis-related genes (*SOX9*, *ACAN*,

and *COL2A1*) for rabbit BMSCs cultured in the p(NIPAAm-AA) hydrogel were significantly up-regulated compared to that in the fibrin hydrogel. (Figure S4.4f)

4.5.4.2 Paracrine effect of cell aggregates

The advantages of cell aggregates within p(NIPAAm-AA) hydrogel over individual single cells within fibrin hydrogel were shown by comparing the mRNA expression of paracrine signaling-related genes using RT-qPCR. The mRNA expression of the majority of cytokine genes ($p < 0.05$ for *TGFB1*, *VEGF*, *CXCL12*, *IGF1*, and *BMP7*; $p < 0.01$ for *BMP2*) was significantly enhanced from the cell aggregates cultured in p(NIPAAm-AA) hydrogel compared to that of single cells cultured in fibrin hydrogel. (Figure S4.5) Furthermore, the mRNA expression of *WNT3A* and *CTNNB1* genes, were consistently significantly higher in the cell aggregates compared to the single cells. However, there was no significant difference in the mRNA expression of *FGF2*, *TGFB3*, and *WNT5A* genes between cell aggregates and single cells. (Figure S4.5)

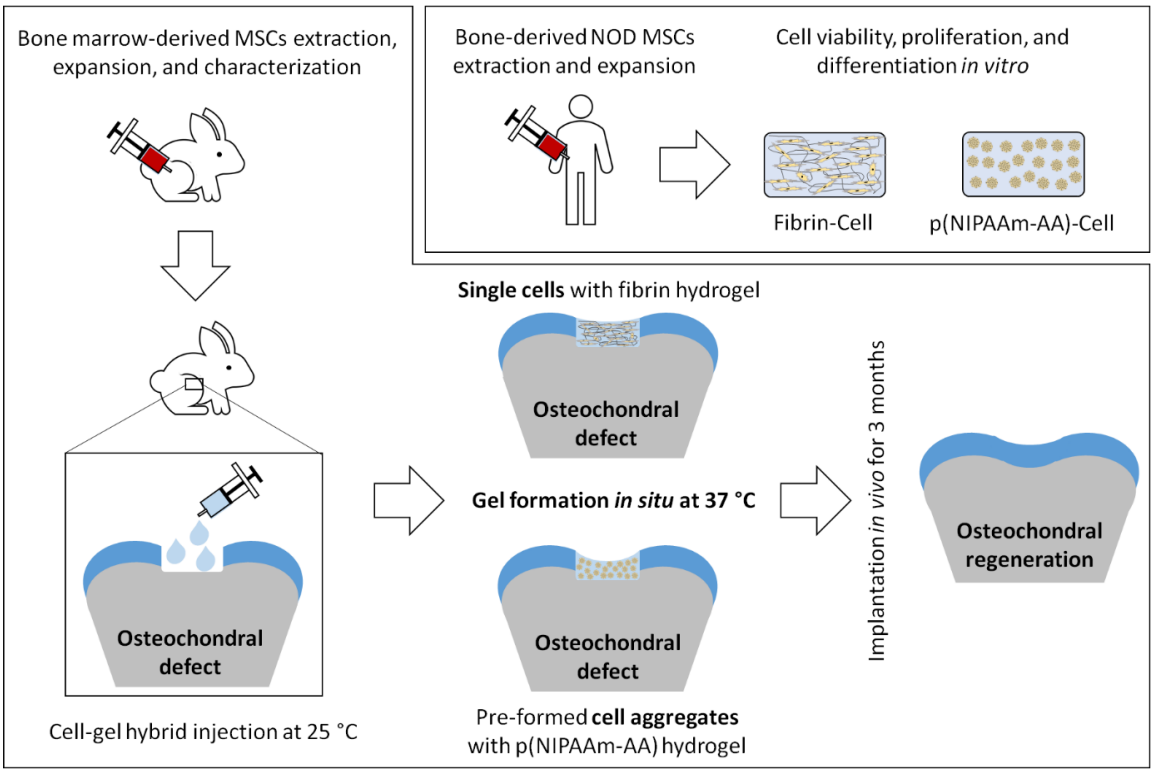

Figure 4.6 Scheme for the study of biological properties of fibrin and p(NIPAAm-AA) hydrogels *in vitro* and their efficacy for osteochondral regeneration *in vivo*.

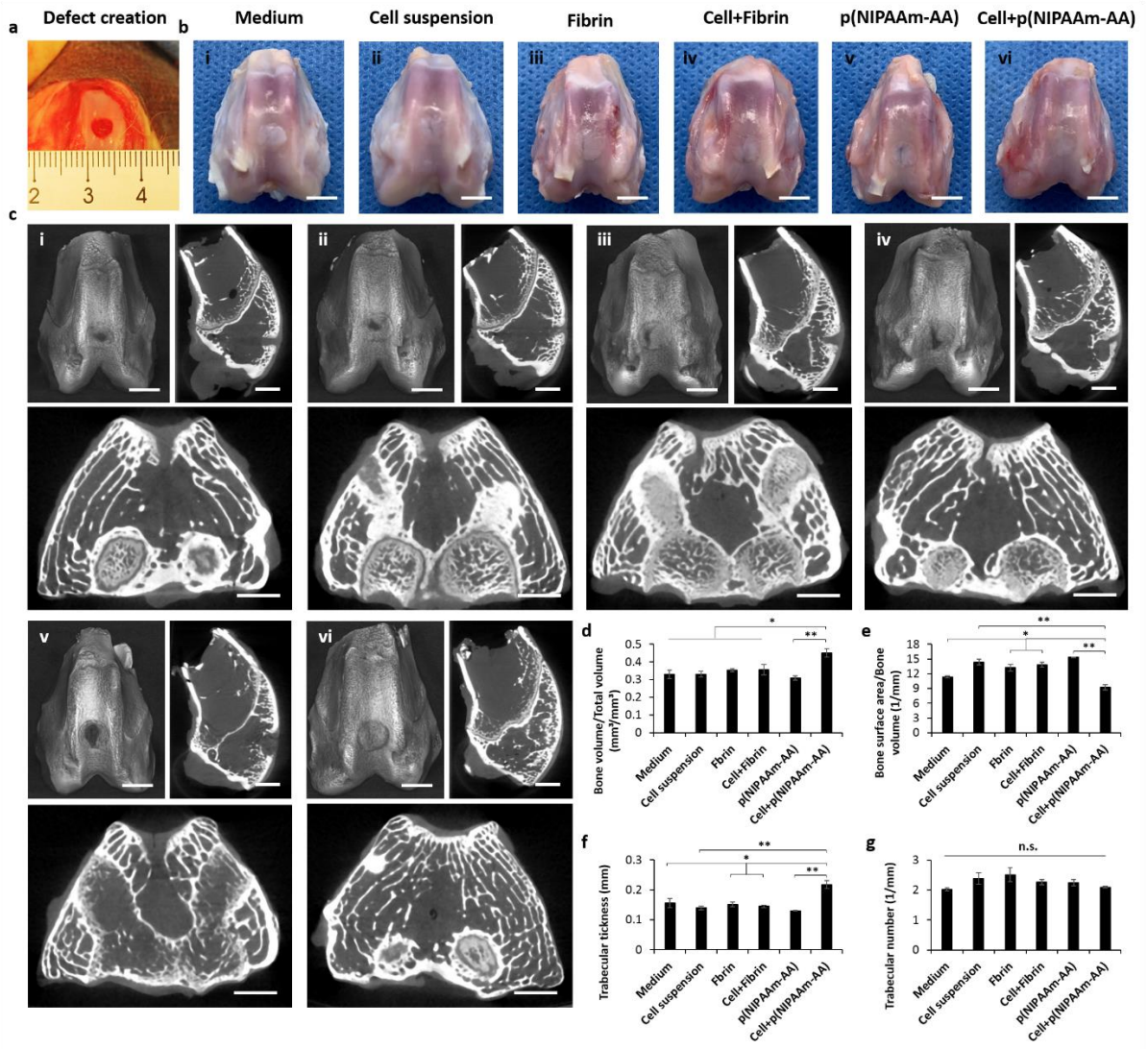

Figure 4.7 (a) A macroscopy image of the generated osteochondral defect with a diameter of 4 mm. (b) Macroscopy images of the regenerative osteochondral tissues three months after the implantation of (i) medium only, (ii) cell suspensions, (iii) fibrin hydrogel, (iv) cell and fibrin hydrogel, (v) p(NIPAAm-AA) hydrogel, (vi) cell and p(NIPAAm-AA) hydrogel. Scale bar: 5 mm. (c) Reconstructed three-dimensional (3D) structure (Top-Left), sagittal section (Top-Right), and transverse section (Bottom) of the regenerative osteochondral defects by micro-computed tomography (µCT) 3 months after the implantation of (i) medium only, (ii) cell suspensions, (iii) fibrin hydrogel, (iv) cell and fibrin hydrogel, (v) p(NIPAAm-AA) hydrogel, (vi) cell and p(NIPAAm-AA) hydrogel. Scale bar: 5 mm. (d-g) Bone volume/total volume, bone surface area/bone volume, trabecular thickness, and trabecular number of the total regenerative osteochondral tissues. Data were measured by Siemens Inveon Research Workplace (IRW) software and presented as mean ± standard error (SE), n=3. "*" for $\rho < 0.05$; "**" for $\rho < 0.01$; "not significant (n.s.)" for $\rho > 0.05$.

In-vivo animal study

Micro-CT

To assess the efficacy of the cell-hydrogel hybrids for cartilage and bone regeneration, pre-formed rabbit BMSC aggregates overnight in the p(NIPAAm-AA) hydrogel were re-embedded

in the p(NIPAAm-AA) hydrogel and injected into an osteochondral defect site, while fibrin hydrogel were injected with rabbit BMSC single-cell suspensions. Following gel formation *in situ* for at least 30 min, the osteochondral defects were treated with different formulations for 3 months. (Figure 4.6) The size of the osteochondral defect created was approximately 4 mm in diameter and 1.6 mm in depth. (Figure 4.7 a) From the macroscopy images, it can be seen that better integration of regenerative cartilage with the surrounding healthy cartilage at the defects was achieved after injection of cell suspensions compared to the hyperplasia of regenerative cartilage with injection of medium only. (Figure 4.7b i-ii) There was no significant difference of regenerative cartilage at the osteochondral defects between the injection of cell-fibrin hybrids and fibrin hydrogel only. (Figure 4.7b iii-iv) The regenerative cartilage was optimal at the osteochondral defect site 3 month post-injection of p(NIPAAm-AA)-cell hybrids (Figure 4.7b vi), which was supported by seamless cartilage integration, a smooth cartilage surface, and absence of central cracks seen in the other groups. (Figure 4.7b ii-v) The superior efficacy of p(NIPAAm-AA)-cell hybrids for cartilage regeneration was further confirmed by the ICRS scores. (Figure S4.6) The ICRS score for the group with the implantation of p(NIPAAm-AA)-cell hybrids was significantly higher than the group with the implantation of fibrin-cell hybrids ($\rho < 0.01$) and the group with implantation of p(NIPAAm-AA) ($\rho < 0.05$). However, there was no significant difference in ICRS score between the groups with implantation of fibrin-cell hybrids and fibrin only, respectively. ($\rho > 0.05$) Moreover, the subchondral bone regeneration was evaluated by micro-computed tomography (μCT), which revealed limited bone regeneration at the osteochondral defects after injection of medium only, cell suspensions, or p(NIPAAm-AA) hydrogel (Figure 4.7c i-ii&v), while evidence of bone regeneration was observed at the osteochondral defects after injection of fibrin-cell hybrids or fibrin hydrogel only (Figure 4.7c iii-iv). Notably, the greatest amount of bone regeneration at the osteochondral defects was observed after injection of p(NIPAAm-AA)-cell hybrids (Figure 4.7c vi). Notably, the results from radiographic processing at the region of osteochondral defects were consistent

with the μCT images. (Figure 4.7d-g) The bone volume/total (tissue) volume (BV/TV) value in the group after injection of p(NIPAAm-AA)-cell hybrids was significantly larger than that in the other groups ($p < 0.01$ for p(NIPAAm-AA); $p < 0.05$ for other groups). (Figure 4.7d) However, the bone surface area/bone volume (BS/BV) value in the group after injection of p(NIPAAm-AA)-cell hybrids was significantly lower than that in other groups ($p < 0.01$ for p(NIPAAm-AA) and cell suspension; $p < 0.05$ for others), the trabecular thickness (Tb.Th) was the highest in the p(NIPAAm-AA)-cell hybrids-treated group ($p < 0.01$ for p(NIPAAm-AA) and cell suspensions; $p < 0.05$ for others). (Figure 4.7e-f) In addition, the trabecular number (Tb.N) in all groups did not show any significant difference. (Figure 4.7g)

Histology staining

Three months after implantation, the regenerative osteochondral tissues were harvested for tissue sectioning and histology staining. The H&E staining revealed that the osteochondral defects after implantation of medium only, cell suspensions, fibrin hydrogel, or p(NIPAAm-AA) hydrogel were partially filled with fibrocartilage containing irregular random collagen fibers and gaps were seen near the central area. (Figure 4.8a-c and Figure 4.8e) The biggest gap was shown in the osteochondral defect region in the presence of p(NIPAAm-AA) hydrogel only. (Figure 4.8e) Moreover, an uneven surface of the regenerative cartilage and poor integration of the regenerative cartilage and subchondral bone to the original surrounding tissues were seen at the osteochondral defects treated with media only, cell suspensions, fibrin hydrogel, or p(NIPAAm-AA) hydrogel in spite of presence of some blood vessels in the deep zone of the fibrocartilages. (Figure 4.8a-c and Figure 4.8e) In contrast, with the implantation of fibrin-cell hybrid or p(NIPAAm-AA)-cell hybrid the osteochondral defects were fully filled with normal osteochondral structures. (Figure 4.8di and Figure 4.8fi) Both regenerated cartilages displayed a smooth surface and collagen fibers of the regenerated cartilages exhibited clear zone-specific orientation, namely horizontal, random, and vertical distribution near the superficial, middle, and deep zone of a cartilage, respectively. (Figure 4.8dii and Figure 4.8fii) Although the

subchondral bones at the defect site with the implantation of either fibrin-cell hybrid or p(NIPAAm-AA)-cell hybrid were well integrated with the surrounding tissues, the integration of regenerative cartilage induced by the fibrin-cell hybrid was limited in comparison to that induced by the p(NIPAAm-AA)-cell hybrid, as a defective structure between the interface of regenerative and original cartilages was seen in the fibrin-cell hybrid treated group. (Figure 4.8diii and Figure 4.8fiii)

The sulfated glycosaminoglycans (GAGs) were detected by staining with Safranin O dye. As Figure 4.9a and Figure 4.9e indicated, no detectable sulfated GAGs were generated at the defect site after treated with medium only or p(NIPAAm-AA) hydrogel only. Only a trace amount of red color was seen near the subchondral area of the regenerative tissue after implantation of cell suspensions. (Figure 4.9b) A similar sulfated GAGs distribution was seen in the regenerative tissue with the implantation of fibrin hydrogel only, while the subchondral area was stained with a much brighter red color compared to that with the implantation of cell suspensions. (Figure 4.9c) Although distinct sulfated GAGs production was seen in the regenerative cartilage after treatment by the fibrin-cell hybrid, the red-stained area was still not large enough to cover the entire defective site. (Figure 4.9d) On the contrary, rich generated sulfated GAGs was distributed throughout the regenerative cartilages after 3 month post-injection of the p(NIPAAm-AA)-cell hybrid and this GAGs distribution was similar to that of the original normal cartilages. (Figure 4.9f) When staining with Masson's Trichrome dye, all regenerative tissues displayed a distinct blue color (Figure S4.7), but similar gaps were observed within the osteochondral defects after implantation of medium only (Figure S4.7a), cell suspensions (Figure S4.7b), fibrin hydrogel (Figure S4.7c), or p(NIPAAm-AA) hydrogel (Figure S4.7e). Besides, orientation and distribution of stained collagen in these groups were different from those of collagen in the surrounding normal tissues, in the absence of a typical three-layer structure in regenerative cartilages and a trabecular morphology in regenerative subchondral bones. (Figure S4.7a-c,e) Moreover, the distinct interface between new and old cartilages

(Figure S4.7i) and a rough surface of the regenerative cartilage (Figure S4.7ii) were also seen at the osteochondral defects with implantation of medium only (Figure S4.7a), cell suspensions (Figure S4.7b), fibrin hydrogel (Figure S4.7c), cell-fibrin hybrid (Figure S4.7d), or p(NIPAAm-AA) hydrogel (Figure S4.7e). In contrast, in the cell-p(NIPAAm-AA) hybrid-treated group, the regenerative tissue consisted of a typical three-layer structure (horizontal at the surficial zone, random at the middle zone, and vertical at the deep zone, respectively) (Figure S4.7fii), and trabecular bone was restored (Figure S4.7fiii), along with a smooth surface and an indistinguishable interface between new and old cartilages (Figure S4.7fi). To confirm the type and distribution of the accumulated collagen, the tissue sections were stained with mouse anti-type 1 collagen primary antibody, Alexa Fluor 488-labelled goat-anti-mouse secondary antibody, and Hoechst 33342. A small amount of collagen type 1 was detected at the regenerative cartilage zone of the osteochondral defects after implantation of fibrin hydrogel or p(NIPAAm-AA) hydrogel, but only trace amounts of collagen type 1 in the regenerative cartilage in other groups. (Figure S4.8) Notably, the collagen type 1 was observed to be present at the bottom of a osteochondral defect in the groups treated by either cell-fibrin hybrid (Figure S4.8d) or cell-p(NIPAAm-AA) hybrid (Figure S4.8f).

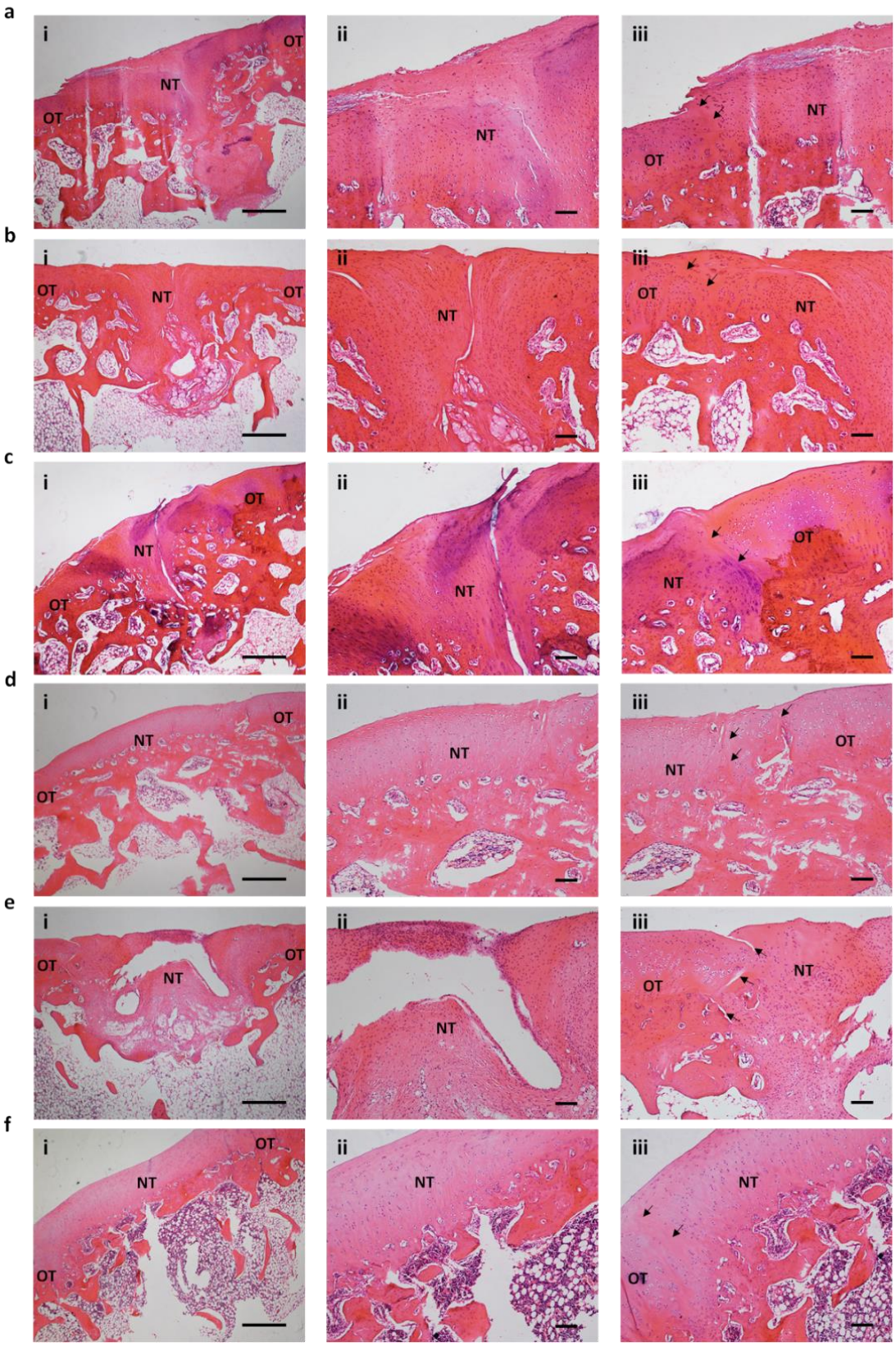

Figure 4.8 Haematoxylin and Eosin staining images of the regenerative osteochondral tissues three months after the implantation of (a) medium only, (b) cell suspensions, (c) fibrin hydrogel, (d) cell and fibrin hydrogel, (e) p(NIPAAm-AA) hydrogel, (f) cell and p(NIPAAm-AA) hydrogel at (i) a lower magnification (Scale bar: 500 μm), (ii) a higher magnification near the centre (Scale bar: 100 μm), (iii) and a higher magnification near the edge (Scale bar: 100 μm). Blue dots: cell nuclei; Pink: collagen; Red: cytoplasm. NT: new tissue; OT: old tissue. Black arrows point to the interface between new tissues and old tissues.

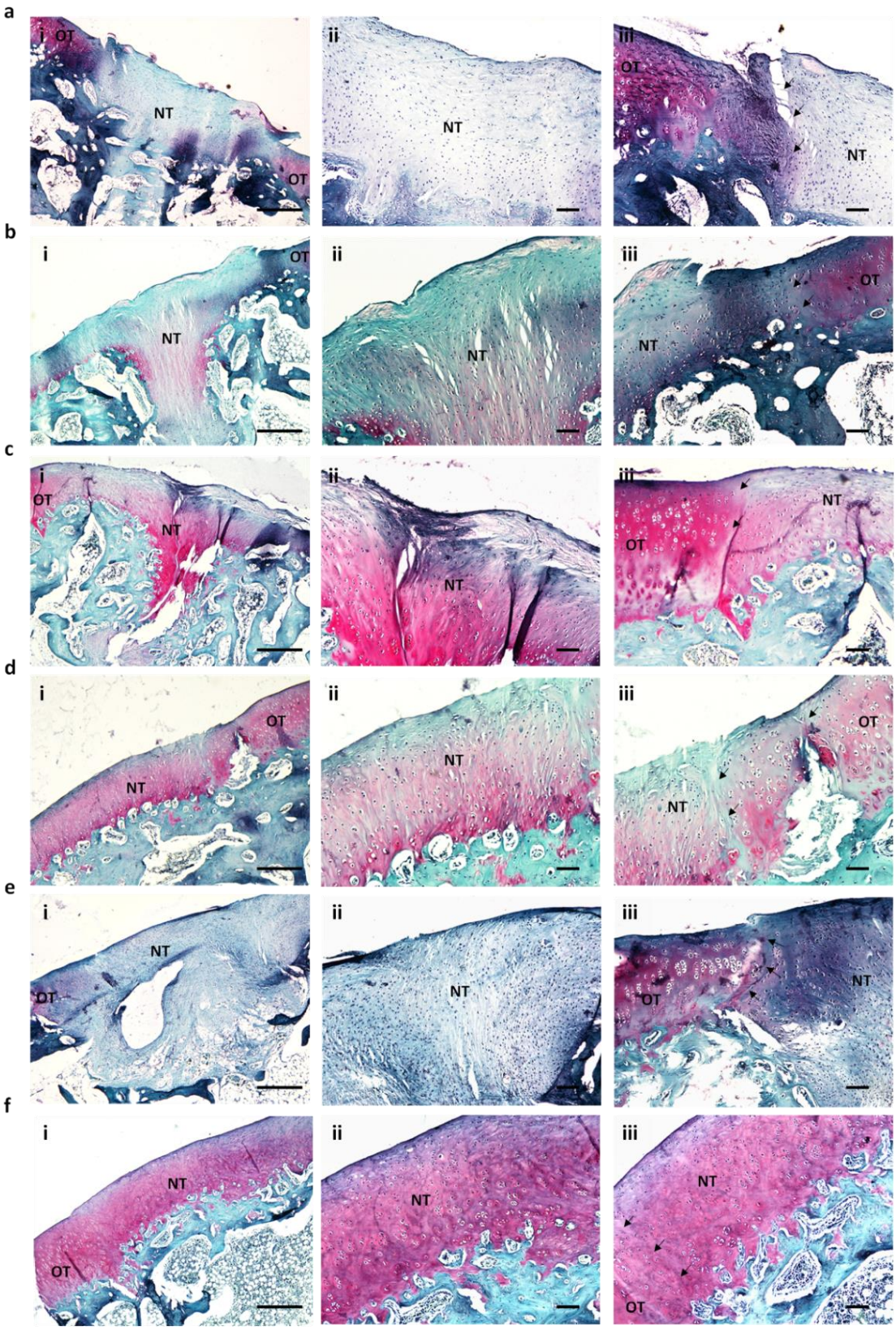

Figure 4.9 Safranin O staining images of the regenerative osteochondral tissues three months after the implantation of (a) medium only, (b) cell suspensions, (c) fibrin hydrogel, (d) cell and fibrin hydrogel, (e) p(NIPAAm-AA) hydrogel, (f) cell and p(NIPAAm-AA) hydrogel at (i) a lower magnification (Scale bar: 500 μm), (ii) a higher magnification near the centre (Scale bar: 100 μm), (iii) and a higher magnification near the edge (Scale bar: 100 μm). Black dots: cell nuclei; Red: sulfated glycosaminoglycans; Green: cytoplasm. NT: new tissue; OT: old tissue. Black arrows point to the interface between new tissues and old tissues.

4.6 Discussion

4.6.1 Characterization of the hydrogels

Fibrin hydrogel, as a natural polymer, has been explored for its potential application in cartilage regeneration. [30, 31] Following cleavage with the enzyme, thrombin, the precursor fibrinogen can be converted into fibrin, which is then polymerized to form a fibrous hydrogel. [32] However, the mechanical strength of the fibrin hydrogel is quite weak, which is similar to the mechanical property of the p(NIPAAm-AA) hydrogel. [33] Hence, in this study fibrin hydrogel was selected as a control to evaluate the feasibility of employing p(NIPAAm-AA) hydrogel for osteochondral regeneration. By varying the concentration of the fibrinogen, fibrin hydrogels with different mechanical strengths were generated at a constant thrombin concentration (2 U mL^{-1}). From the shear stress-strain curves, it could be seen that the slope of the shear stress-strain curve, namely shear modulus, of 0.75 mg mL^{-1} fibrin hydrogel was similar to that of 30 mg mL^{-1} p(NIPAAm-AA) hydrogel, 0.094 Pa and 0.101 Pa, respectively. (Figure S4.1a) In addition, a similar absolute complex modulus value (|G*|), approximately 1 Pa, was obtained for 0.75 mg mL^{-1} fibrin hydrogel and 30 mg mL^{-1} p(NIPAAm-AA) hydrogel when the stress was applied at 0.1 Pa. Therefore, to eliminate the influence of mechanical strength on cell migration, proliferation, or differentiation, fibrin hydrogel at a concentration of 0.75 mg ml^{-1} was used for the following experiments. To maintain a gel status (elastic modulus G' > viscous modulus G"), the applied external stress should be smaller than the critical stress, 19.06 Pa for 0.75 mg ml^{-1} fibrin hydrogel and 0.2 Pa for 30 mg mL^{-1} p(NIPAAm-AA) hydrogel, respectively. (Figure 4.1a) The internal fibrils of fibrin hydrogel were able to bear only small external stresses, and beyond the critical stress values, the fibrils would be broken and irreversibly lose the gel structure. [33] The formation of a gel structure of p(NIPAAm-AA) hydrogel was mainly due to reversible weak ionic crosslinking of Mg^{2+}/COO^{-} and hydrophobic repulsion, thus the p(NIPAAm-AA) hydrogel was liquified at a much smaller external stress. [24] Furthermore, the temperature-dependent hydrophobicity of p(NIPAAm-AA) also allowed its gel status to be

modified in response to the temperature change: a transparent liquid status below the lower critical solution temperature (LCST) while a cloudy gel status above LCST. (Figure 4.1b-c) [25] Even though both hydrogels were porous, the pores in the fibrin hydrogel were created by the fibrils, while the pores in the p(NIPAAm-AA) hydrogel were determined by the size and concentration of the p(NIPAAm-AA) microgels. (Figure 4.1d) [34]

Although fibrin is a natural polymer, it has been reported that it possesses potent pro-inflammatory properties by interaction with various integrins, such as the $\alpha_M\beta_2$ cell surface receptor. [35-37] When fibrinogen is deposited or converted into a fibrin polymer from a soluble monomer, the cryptic binding motif of fibrinogen is exposed to those $\alpha_M\beta_2$-expressing leukocytes, such as macrophage [38], leading to either an acute destructive inflammation [39] or a chronic low-grade inflammation [40]. Therefore, once the stability of fibrin is enhanced in any manner, its inflammatory properties are also correspondingly promoted. [41-43] Besides, it is known that thrombin could also regulate the inflammation through PAR signaling pathways. [38] A similar pro-inflammatory effect was also found for fibrin hydrogel in this study with significant up-regulation of *IL1B*, *IL6*, and *NOS* genes and enhanced nitric oxide production in Raw264.7 macrophage cells. (Figure S4.2) In contrast, since there was no active binding motif in the p(NIPAAm-AA), pro-inflammatory reaction of macrophage cells could not be activated when they were cultured with p(NIPAAm-AA) hydrogel.

4.6.2 Characterization of human NOD MSCs in the hydrogels

Fibrin hydrogel as a protein-rich scaffold supports cell attachment, therefore, mesenchymal stem/stromal cells cultured in the fibrin hydrogel displayed a fibroblast-like morphology. [44] However, due to the absence of cell binding sites, such as RGD peptides, and the spatial restriction of porous p(NIPAAm-AA) hydrogel [34], cells cultured in the p(NIPAAm-AA) hydrogel formed cell aggregates. [22, 45, 46] (Figure 4.2a) Although Live&Dead staining images (Figure 4.2b) revealed excellent biocompatibility for both fibrin hydrogel and p(NIPAAm-AA) hydrogel, quiescent cell propagation was seen in the p(NIPAAm-AA)

hydrogel while consistent cell growth in 2D culture plates and the fibrin hydrogel (Figure 4.3), which was previously evidenced as a result of cell aggregate-induced restriction of a cell cycle at the G0 stage [24]. Enhancement in the secretion of endogenous growth factors and extracellular matrices (ECMs) by cell aggregates [22] might play an important role in facilitating expression of chondrogenesis-related genes (*SOX9*, *COL2A1*, *ACAN*) for cell aggregates from bone-derived mesenchymal stem/stromal cells cultured inside the p(NIPAAm-AA) hydrogel. The expression was significantly higher than that in the fibrin hydrogel in spite of donor-dependent cell source variations. (Figure 4.4) The generation of collagen 2A1 and sulfated glycosaminoglycans (GAGs), which are two main components of a cartilage, further confirmed the benefit of using cell aggregates for promotion of cell chondrogenesis. (Figure 4.5b-c) Even though well distributed cells in the fibrin hydrogel eventually were attracted to form a large cell pellet with a diameter of approximately 1.5 mm (Figure 4.5ai) in the chondrogenic induction medium due to cell-dependent fibrin degradation [30, 47, 48], such a large cell pellet, similar to the cell pellets prepared by spinning cells in a polypropylene tube, may not allow sufficient nutrient delivery into the inner cells and removal of toxic metabolic wastes out of the structure, leading to a necrotic zone in the centre of the pellet, while cells were viable and functional for homogeneous small cell aggregates formed in the p(NIPAAm-AA) hydrogel [24, 49, 50]. Therefore, more sulfated GAGs was produced in the p(NIPAAm-AA) hydrogel than in pellet culture or fibrin hydrogel. (Figure 4.5c) The size difference between cell aggregates and large cell pellet might also lead to the increased expression of *COL10A1*, a terminal chondrogenesis-related marker, for cells cultured in the fibrin hydrogel. [22] (Figure 4.4) In contrast to the conventional viscous hydrogels that restrict migration of cell aggregates within hydrogels [51], as chondrogenesis progressed, the presence of soft p(NIPAAm-AA) hydrogel promoted ECMs accumulation around these cell aggregates, and neighboring cells may migrate inside the p(NIPAAm-AA) hydrogel to bind to the ECMs and eventually cell

aggregate networks were established (Figure 4.5aii), which may be essential for cell communication. [52]

4.6.3 Osteochondral regeneration

It is worth noting that rabbit bone marrow-derived primary mesenchymal stem/stromal cells (BMSCs) cultured as cell pellets in the polypropylene tubes displayed a distinct blue color either in the standard complete culture medium or in the chondrogenic induction medium by Alcian Blue staining (Figure S4.3c), because chondrogenesis of primary BMSCs could be readily induced within the hypoxic cell pellets. [53-55] The similar cell morphology (spindle-like adhesion on the tissue culture plate or in the fibrin hydrogel and cell aggregates in the p(NIPAAm-AA) hydrogel) and the significantly enhanced mRNA expression of chondrogenesis-related genes in p(NIPAAm-AA) hydrogel than fibrin hydrogel were observed from both human NOD MSCs and rabbit BMSCs, which indicated that cell behavior within the hydrogel might be hydrogel-dependent, but species-independent. (Figure S4.4a-c,f) When inducing chondrogenesis, abundant lipids were present within the cells cultured either in the fibrin hydrogel or p(NIPAAm-AA) hydrogel (Figure S4.4d-e), which indirectly confirmed chondrogenic induction of rabbit primary BMSCs to some extent since lipids were reported as the main energy source of chondrocytes. [56, 57] Notably, the deposition of rich ECM around the chondrogenesis-induced rabbit primary BMSCs in the p(NIPAAm-AA) hydrogel (Figure S4.4e) was consistent with the previous studies [58-60], further demonstrating functional enhancement of MSC aggregates in the ECM production. It was reported that the paracrine effect [13, 61] and/or cell differentiation [62, 63] of mesenchymal stem/stromal cells are the key contributing factors for their potential therapeutic application in osteochondral degeneration. Due to functional enhancement by MSC aggregates in the p(NIPAAm-AA) hydrogel, up-regulated mRNA expression of relevant genes may enhance the therapeutic synergy from the paracrine effect and cell differentiation, [1, 13, 14, 64] including transforming growth factor beta 1 (TGF-β1), a cytokine that controls cell proliferation and differentiation

and inhibits immune reaction and inflammation; vascular endothelial growth factor (VEGF), a growth factor that induces angiogenesis; stromal cell-derived factor 1 (SDF-1), a cytokine that regulates angiogenesis and suppresses inflammatory; insulin-like growth factor (IGF-1), a hormone that promotes cell growth and proliferation and prevents cell death; and bone morphogenetic protein 2 and 7 (BMP-2 and BMP-7), the cytokines that mediate cell differentiation and induce bone and cartilage formation. (Figure S4.5) Following the implantation of rabbit primary BMSCs with p(NIPAAm-AA) hydrogel *in vivo*, the cell-p(NIPAAm-AA) hybrid was homogeneously distributed to cover the entire osteochondral defects. Cell aggregates trapped inside the soft gel showed enhanced cell survival and a high retention at the defect site. [65] Furthermore, cell aggregates may reinforce the secretion of the aforementioned paracrine factors in a persistent manner [13], which may attract the migration of autologous MSCs from the surrounding tissues, such as bone marrow and synovium, towards the osteochondral defect sites [66, 67], inhibit the immune reaction and inflammation [14], and facilitate new blood vessel formation [13]. Due to the porous structure and the weak mechanical strength of p(NIPAAm-AA) hydrogel [24], migrated autologous MSCs might penetrate into the p(NIPAAm-AA) hydrogel. Therefore, the defects could be repaired due to deposition and accumulation of cells and extracellular matrices (ECMs). Furthermore, those MSCs which home to the site may then differentiate into chondrocytes to promote cartilage regeneration by a BMP-2/Wnt3a/β-catenin signaling pathway (Figure S4.5). [68, 69] The newly formed blood vessels could facilitate delivery of essential nutrients to the hypertrophic chondrocytes for their endochondral ossification for subchondral bone regeneration. [70-73] The synergy of the paracrine effect and cell differentiation was evidenced in the regenerative tissues at the osteochondral defects with the injection of cell-p(NIPAAm-AA) hybrids compared to that with p(NIPAAm-AA) hydrogel only implantation. It was shown that the regenerative cartilages covered the entire osteochondral defects after implantation of the cell-p(NIPAAm-AA) hybrid, while there were still gaps at the central position of the osteochondral defects with p(NIPAAm-

AA) hydrogel only. (Figure 4.7v-vi and Figure 4.8e-f) Furthermore, biological characterizations and functions of the regenerative tissues at the osteochondral defects after implantation of p(NIPAAm-AA) hydrogel only were also different from those with the implantation of the cell-p(NIPAAm-AA) hybrid. Restoration of endochondral bones with a superior trabecular thickness and a great bone volume (Figure 4.7d,f) and generation of glycosaminoglycan-rich cartilage (Figure 4.9e-f) were achieved by the cell-p(NIPAAm-AA) hybrid. Even though MSCs were embedded in the fibrin hydrogel and delivered into the osteochondral defects, the embedded MSCs would be attracted to form a cell pellet after degradation of fibrils, and the degradation also resulted in lack of supporting scaffolds for the homing of autologous cells. Therefore, the regenerative cartilage and the subchondral bone (Figure 4.7i-iv) were shown to partially cover the osteochondral defects. There was no significant difference in the functional recovery of an endochondral bone with the implantation of medium only, cell suspensions, fibrin hydrogel, or cell-fibrin hybrids (Figure 4.7d-g). Either the fibrous regenerative tissues near the cartilage surface (Figure 4.8c) or poor integration with the surrounding normal cartilages (Figure 4.8d) might hinder functional recovery of a cartilage. It was seen that glycosaminoglycans were only deposited at the middle and deep zones of the regenerative tissues but not at the superficial zone at the osteochondral defect site after injection of fibrin hydrogel or cell-fibrin hybrids. (Figure 4.9c-d) Besides, the cartilage-specific ECM, glycosaminoglycan, was scattering at the osteochondral defect sites with the implantation of medium only or with the implantation of cell suspensions despite of the presence of some neo-fibrous tissues, which were frequently generated after routine microfracture surgery (Figure 4.8a-b and Figure 4.9a-b). [74] Furthermore, the distribution of type 1 collagen, as shown by Masson's Trichome staining (Figure S4.7) and immunofluorescent staining (Figure S4.8), confirmed that the regenerative tissues in the group implanted with the cell-p(NIPAAm-AA) hybrid consisted of functional neocartilage in the absence of type 1 collagen and subchondral bone with abundant type 1 collagen. [2] In contrast to the synergy of the paracrine effect (anti-

inflammation, immunomodulatory, and homing of stem/progenitor cells) and induced differentiation of MSCs in the p(NIPAAm-AA) hydrogel, rapid degradation of the supporting fibril structure (Figure 4.5a) and the pro-inflammation (Figure S4.2) of fibrin hydrogel might have an adverse effect on the therapeutic efficacy of the cell-fibrin hydrogel hybrid at an osteochondral defect.

Compared to conventional strategies that use engineered hydrogels for defined cell differentiation by mimicking the topography, architecture, and mechanical strength of a normal osteochondral tissue [75-77], or for recruitment of stem/progenitor cells by delivery of multiple growth factors [3-5, 78], the MSC aggregates pre-generated and delivered with the p(NIPAAm-AA) thermosensitive hydrogel into the osteochondral defects might simultaneously facilitate both cell differentiation and autogenous stem cell recruitment in a more efficient and persistent manner. Although the mechanical strength of p(NIPAAm-AA) hydrogel might not match that of a health osteochondral tissue, its soft structure promoted the formation of cell aggregates *in situ* and permitted penetration and migration of the recruited cells inside the p(NIPAAm-AA) hydrogel, which was essential for the deposition and the remodelling of ECMs at the osteochondral defect site. In addition, despite p(NIPAAm-AA) is not biodegradable, it was not visible in the regenerative osteochondral tissues with the implantation of cell-p(NIPAAm-AA) hybrid after three months, which might be eventually separated into minor parts during the ECM remodelling and integrated into the osteochondral tissues. Hence, the *in-vivo* terminal destination of p(NIPAAm-AA) still needs to be further tracked and explored before clinical applications. As the *in-vivo* results indicated, the p(NIPAAm-AA) hydrogel might be a potential carrier in the delivery of stem cells for osteochondral regeneration.

4.7 Conclusion

In this study, a thermosensitive p(NIPAAm-AA) hydrogel was used as a delivery vehicle of allogeneic primary MSCs and explored for its potential therapeutic application in osteochondral regeneration. At an equivalent mechanical strength, p(NIPAAm-AA) and fibrin hydrogels both

had excellent biocompatibility, but induced distinct cell morphologies: cell aggregates in p(NIPAAm-AA) hydrogel and spindle single cells in fibrin hydrogel. Unlike the pro-inflammatory properties of the fibrin hydrogel, the p(NIPAAm-AA) hydrogel did not elicit a pro-inflammatory response. Furthermore, gene expression of paracrine signaling-related factors (*TGFB1*, *VEGF*, *CXCL12*, *IGF1*, *BMP2*, *BMP7*, *WNT3A*, and *CTNNB1*) was significantly up-regulated in the cell aggregates. When inducing chondrogenesis *in vitro*, both chondrogenesis-related genes (*SOX9*, *ACAN*, and *COL2A1*) and ECMs (type 2 collagen and glycosaminoglycans) were enhanced for cells cultured in p(NIPAAm-AA) hydrogel. Hence, the synergy of the paracrine effect (anti-inflammation, immunomodulatory, and homing of stem/progenitor cells) and induced differentiation of MSCs have contributed to the functional restoration of an osteochondral defect *in vivo*. This study revealed that the thermosensitive p(NIPAAm-AA) hydrogel together with allogeneic primary MSCs could be applied for osteochondral regeneration.

CONFLICT OF INTEREST

There are no conflicts of interest relating to this work.

SUPPLEMENTARY INFORMATION

Supplementary data can be found in "Supplementary information".

ACKNOWLEDGEMENTS

QQY appreciates the support from National Key Research and Development Program of China (2018YFC1105200-4). HZ would like to acknowledge the financial support from ARC Discovery Project (DP160104632) and The Medical Advancement Without Animal (MAWA) Trust. JBZ thanks the IPE-UoA Scholarship (BES).

DATA AVAILABILITY

The raw data required to reproduce these findings are available to download from https://adelaide.figshare.com/s/ec8eadc9744158e7641f. The processed data required to

reproduce these findings are available to download from https://adelaide.figshare.com/s/58a6b2f221bb9dbf6da8.

4.8 Reference

[1] Li MH, Xiao R, Li JB, Zhu Q. Regenerative approaches for cartilage repair in the treatment of osteoarthritis. Osteoarthritis and Cartilage 2017;25:1577-87.

[2] Camarero-Espinosa S, Rothen-Rutishauser B, Foster EJ, Weder C. Articular cartilage: from formation to tissue engineering. Biomaterials Science 2016;4:734-67.

[3] Reyes R, Delgado A, Sanchez E, Fernandez A, Hernandez A, Evora C. Repair of an osteochondral defect by sustained delivery of BMP-2 or TGF beta(1) from a bilayered alginate-PLGA scaffold. Journal of Tissue Engineering and Regenerative Medicine 2014;8:521-33.

[4] Lu S, Lam J, Trachtenberg JE, Lee EJ, Seyednejad H, van den Beucken JJJP, et al. Dual growth factor delivery from bilayered, biodegradable hydrogel composites for spatially-guided osteochondral tissue repair. Biomaterials 2014;35:8829-39.

[5] Santo VE, Gomes ME, Mano JF, Reis RL. Controlled Release Strategies for Bone, Cartilage, and Osteochondral Engineering-Part II: Challenges on the Evolution from Single to Multiple Bioactive Factor Delivery. Tissue Engineering Part B-Review 2013;19:327-52.

[6] Lam J, Lu S, Kasper FK, Mikos AG. Strategies for controlled delivery of biologics for cartilage repair. Advanced Drug Delivery Reviews 2015;84:123-34.

[7] Chen R, Wang J, Liu CS. Biomaterials Act as Enhancers of Growth Factors in Bone Regeneration. Advanced Functional Materials 2016;26:8810-23.

[8] Deng CJ, Yang Q, Sun XL, Chen L, Feng C, Chang J, et al. Bioactive scaffolds with Li and Si ions-synergistic effects for osteochondral defects regeneration. Applied Materials Today 2018;10:203-16.

[9] Reboredo JW, Weigel T, Steinert A, Rackwitz L, Rudert M, Walles H. Investigation of Migration and Differentiation of Human Mesenchymal Stem Cells on Five-Layered Collagenous Electrospun Scaffold Mimicking Native Cartilage Structure. Advanced Healthcare Materials 2016;5:2191-8.

[10] Deng CJ, Lin RC, Zhang M, Qin C, Yao QQ, Wang LM, et al. Micro/Nanometer-Structured Scaffolds for Regeneration of Both Cartilage and Subchondral Bone. Advanced Functional Materials 2019;29.

[11] Li L, Li JY, Guo JM, Zhang HK, Zhang X, Yin CY, et al. 3D Molecularly Functionalized Cell-Free Biomimetic Scaffolds for Osteochondral Regeneration. Advanced Functional Materials 2019;29:1807356.

[12] Goldberg A, Mitchell K, Soans J, Kim L, Zaidi R. The use of mesenchymal stem cells for cartilage repair and regeneration: a systematic review. Journal of Orthopaedic Surgery and Research 2017;12:39.

[13] Madrigal M, Rao KS, Riordan NH. A review of therapeutic effects of mesenchymal stem cell secretions and induction of secretory modification by different culture methods. Journal of Translational Medicine 2014;12:260.

[14] Wang Y, Chen XD, Cao W, Shi YF. Plasticity of mesenchymal stem cells in immunomodulation: pathological and therapeutic implications. Nature Immunology 2014;15:1009-16.

[15] Zhang J, Huang XW, Wang HJ, Liu XY, Zhang T, Wang YC, et al. The challenges and promises of allogeneic mesenchymal stem cells for use as a cell-based therapy. Stem Cell Research & Therapy 2015;6.

[16] Wu RX, Xu XY, Wang J, He XT, Sun HH, Chen FM. Biomaterials for endogenous regenerative medicine: Coaxing stem cell homing and beyond. Appllied Materials Today 2018;11:144-65.

[17] Ma DY, Zhong CP, Yao H, Liu YP, Chen FL, Li JX, et al. Engineering Injectable Bone Using Bone Marrow Stromal Cell Aggregates. Stem Cells and Development 2011;20:989-99.

[18] Wang X, Rivera-Bolanos N, Jiang B, Ameer GA. Advanced Functional Biomaterials for Stem Cell Delivery in Regenerative Engineering and Medicine. Advanced Functional Materials 2019;29:1809009.

[19] Rai V, Dilisio MF, Dietz NE, Agrawal DK. Recent strategies in cartilage repair: A systemic review of the scaffold development and tissue engineering. Journal of Biomedical Materials Research Part A 2017;105:2343-54.

[20] Lee SH, Lee Y, Chun YW, Crowder SW, Young PP, Park KD, et al. In Situ Crosslinkable Gelatin Hydrogels for Vasculogenic Induction and Delivery of Mesenchymal Stem Cells. Advanced Functional Materials 2014;24:6771-81.

[21] Wang HY, Zhu DQ, Paul A, Cai L, Enejder A, Yang F, et al. Covalently Adaptable Elastin-Like Protein-Hyaluronic Acid (ELP-HA) Hybrid Hydrogels with Secondary Thermoresponsive Crosslinking for Injectable Stem Cell Delivery. Advanced Functional Materials 2017;27:1605609.

[22] Sart S, Tsai A-C, Li Y, Ma T. Three-Dimensional Aggregates of Mesenchymal Stem Cells: Cellular Mechanisms, Biological Properties, and Applications. Tissue Engineering Part B, Reviews 2014;20:365-80.

[23] Ko DY, Patel M, Lee HJ, Jeong B. Coordinating Thermogel for Stem Cell Spheroids and Their Cyto-Effectiveness. Advanced Functional Materials 2018;28:1706286.

[24] Zhang J, Yun S, Bi J, Dai S, Du Y, Zannettino ACW, et al. Enhanced multi-lineage differentiation of human mesenchymal stem/stromal cells within poly(N-isopropylacrylamide-acrylic acid) microgel-formed three-dimensional constructs. Journal of Materials Chemistry B 2018;6:1799-814.

[25] Shen Z, Bi J, Shi B, Nguyen D, Xian CJ, Zhang H, et al. Exploring thermal reversible hydrogels for stem cell expansion in three-dimensions. Soft Matter 2012;8:7250-7.

[26] Atkins GJ, Kostakis P, Pan B, Farrugia A, Gronthos S, Evdokiou A, et al. RANKL expression is related to the differentiation state of human osteoblasts. Journal of Bone and Mineral Research 2003;18:1088-98.

[27] Fitter S, Gronthos S, Ooi SS, Zannettino ACW. The Mesenchymal Precursor Cell Marker Antibody STRO-1 Binds to Cell Surface Heat Shock Cognate 70. Stem Cells 2017;35:940-51.

[28] Veronesi F, Maglio M, Tschon M, Aldini NN, Fini M. Adipose-derived mesenchymal stem cells for cartilage tissue engineering: State-of-The-Art in in vivo studies. Journal of Biomedical Materials Research Part A 2014;102:2448-66.

[29] Van den Borne MPJ, Raijrnakers NJH, Vanlauwe J, Victor J, de Jong SN, Bellernans J, et al. International Cartilage Repair Society (ICRS) and Oswestry macroscopic cartilage evaluation scores validated for use in Autologous Chondrocyte Implantation (ACI) and microfracture. Osteoarthritis and Cartilage 2007;15:1397-402.

[30] Park JS, Yang HN, Woo DG, Jeon SY, Park KH. Chondrogenesis of human mesenchymal stem cells in fibrin constructs evaluated in vitro and in nude mouse and rabbit defects models. Biomaterials 2011;32:1495-507.

[31] Almeida HV, Eswaramoorthy R, Cunniffe GM, Buckley CT, O'Brien FJ, Kelly D. Fibrin hydrogels functionalized with cartilage extracellular matrix and incorporating freshly isolated stromal cells as an injectable for cartilage regeneration. Acta Biomaterialia 2016;36:55-62.

[32] Balakrishnan B, Banerjee R. Biopolymer-Based Hydrogels for Cartilage Tissue Engineering. Chemical Reviews 2011;111:4453-74.

[33] Litvinov RI, Weisel JW. Fibrin mechanical properties and their structural origins. Matrix Biology 2017;60-61:110-23.

[34] Guan Y, Zhang Y. PNIPAM microgels for biomedical applications: from dispersed particles to 3D assemblies. Soft Matter 2011;7:6375-84.

[35] Wright SD, Weitz JI, Huang AJ, Levin SM, Silverstein SC, Loike JD. Complement receptor type three (CD11b/CD18) of human polymorphonuclear leukocytes recognizes fibrinogen. Proceedings of the National Academy of Sciences of the United States of America 1988;85:7734-8.

[36] Altieri DC, Bader R, Mannucci PM, Edgington TS. Oligospecificity of the Cellular Adhesion Receptor Mac-1 Encompasses an Inducible Recognition Specificity for Fibrinogen. The Journal of Cell Biology 1988;107:1893-900.

[37] Jennewein C, Tran N, Paulus P, Ellinghaus P, Eble JA, Zacharowski K. Novel aspects of fibrin(ogen) fragments during inflammation. Molecular Medicine (Cambridge, Mass) 2011;17:568-73.

[38] Luyendyk JP, Schoenecker JG, Flick MJ. The multifaceted role of fibrinogen in tissue injury and inflammation. Blood 2019;133:511-20.

[39] Ryu JK, Petersen MA, Murray SG, Baeten KM, Meyer-Franke A, Chan JP, et al. Blood coagulation protein fibrinogen promotes autoimmunity and demyelination via chemokine release and antigen presentation. Nature Communications 2015;6.

[40] Kopec AK, Abrahams SR, Thornton S, Palumbo JS, Mullins ES, Divanovic S, et al. Thrombin promotes diet-induced obesity through fibrin-driven inflammation. The Journal of Clinical Investigation 2017;127:3152-66.

[41] Flick MJ, Du X, Witte DP, Jirousková M, Soloviev DA, Busuttil SJ, et al. Leukocyte engagement of fibrin(ogen) via the integrin receptor alphaMbeta2/Mac-1 is critical for host inflammatory response in vivo. The Journal of Clinical Investigation 2004;113:1596-606.

[42] Perez RL, Roman J. Fibrin Enhances the Expression of Il-1-Beta by Human Peripheral-Blood Mononuclear-Cells - Implications in Pulmonary Inflammation. Journal of Immunology 1995;154:1879-87.

[43] Flick MJ, LaJeunesse CM, Talmage KE, Witte DP, Palumbo JS, Pinkerton MD, et al. Fibrin(ogen) exacerbates inflammatory joint disease through a mechanism linked to the integrin alphaMbeta2 binding motif. The Journal of Clinical Investigation 2007;117:3224-35.

[44] Duong H, Wu B, Tawil B. Modulation of 3D Fibrin Matrix Stiffness by Intrinsic Fibrinogen-Thrombin Compositions and by Extrinsic Cellular Activity. Tissue Engineering Part A 2009;15:1865-76.

[45] Tseng T-C, Wong C-W, Hsieh F-Y, Hsu S-h. Biomaterial Substrate-Mediated Multicellular Spheroid Formation and Their Applications in Tissue Engineering. Biotechnology Journal 2017;12.

[46] Cui X, Dini S, Dai S, Bi J, Binder BJ, Green JEF, et al. A mechanistic study on tumour spheroid formation in thermosensitive hydrogels: experiments and mathematical modelling. Rsc Advances 2016;6:73282-91.

[47] Collet JP, Park D, Lesty C, Soria J, Soria C, Montalescot G, et al. Influence of fibrin network conformation and fibrin fiber diameter on fibrinolysis speed - Dynamic and structural approaches by confocal microscopy. Arteriosclerosis, Thrombosis, and Vascular Biology 2000;20:1354-61.

[48] Berrier AL, Yamada KM. Cell–matrix adhesion. Journal of Cellular Physiology 2007;213:565-73.

[49] Murphy KC, Fang SY, Leach JK. Human mesenchymal stem cell spheroids in fibrin hydrogels exhibit improved cell survival and potential for bone healing. Cell and Tissue Research 2014;357:91-9.

[50] Edmondson R, Broglie JJ, Adcock AF, Yang LJ. Three-Dimensional Cell Culture Systems and Their Applications in Drug Discovery and Cell-Based Biosensors. Assay and Drug Development Technologies 2014;12:207-18.

[51] Hildebrandt C, Büth H, Thielecke H. A scaffold-free in vitro model for osteogenesis of human mesenchymal stem cells. Tissue and Cell 2011;43:91-100.

[52] Mayor R, Etienne-Manneville S. The front and rear of collective cell migration. Nature Reviews Molecular Cell Biology 2016;17:97-109.

[53] Van Winkle AP, Gates ID, Kallos MS. Mass Transfer Limitations in Embryoid Bodies during Human Embryonic Stem Cell Differentiation. Cells Tissues Organs 2012;196:34-47.

[54] Lee H-H, Chang C-C, Shieh M-J, Wang J-P, Chen Y-T, Young T-H, et al. Hypoxia Enhances Chondrogenesis and Prevents Terminal Differentiation through PI3K/Akt/FoxO Dependent Anti-Apoptotic Effect. Scientific Reports 2013;3:2683.

[55] Öztürk E, Hobiger S, Despot-Slade E, Pichler M, Zenobi-Wong M. Hypoxia regulates RhoA and Wnt/β-catenin signaling in a context-dependent way to control re-differentiation of chondrocytes. Scientific Reports 2017;7:9032.

[56] Collins DH, Ghadially FN, Meachim G. Intra-Cellular Lipids of Cartilage. Annals of The Rheumatic Diseases 1965;24:123-135.

[57] Villalvilla A, Gomez R, Largo R, Herrero-Beaumont G. Lipid Transport and Metabolism in Healthy and Osteoarthritic Cartilage. International Journal of Molecular Sciences 2013;14:20793-808.

[58] Bhang SH, Cho SW, La WG, Lee TJ, Yang HS, Sun AY, et al. Angiogenesis in ischemic tissue produced by spheroid grafting of human adipose-derived stromal cells. Biomaterials 2011;32:2734-47.

[59] Amos PJ, Kapur SK, Stapor PC, Shang HL, Bekiranov S, Khurgel M, et al. Human Adipose-Derived Stromal Cells Accelerate Diabetic Wound Healing: Impact of Cell Formulation and Delivery. Tissue Engineering Part A 2010;16:1595-606.

[60] Wang CC, Chen CH, Hwang SM, Lin WW, Huang CH, Lee WY, et al. Spherically Symmetric Mesenchymal Stromal Cell Bodies Inherent with Endogenous Extracellular Matrices for Cellular Cardiomyoplasty. Stem cells (Dayton, Ohio) 2009;27:724-32.

[61] Shi Y, Wang Y, Li Q, Liu K, Hou J, Shao C, et al. Immunoregulatory mechanisms of mesenchymal stem and stromal cells in inflammatory diseases. Nature Reviews Nephrology 2018;14:493-507.

[62] Quarto RMD, Mastrogiacomo MP, Cancedda RMD, Kutepov SMMD, Mukhachev VMD, Lavroukov AMD, et al. Repair of Large Bone Defects with the Use of Autologous Bone Marrow Stromal Cells. The New England Journal of Medicine 2001;344:385-6.

[63] Hu X, Wang Y, Tan Y, Wang J, Liu H, Wang Y, et al. A Difunctional Regeneration Scaffold for Knee Repair based on Aptamer-Directed Cell Recruitment. Advanced Materials 2017;29:1605235.

[64] Richardson SM, Hoyland JA, Mobasheri R, Csaki C, Shakibaei M, Mobasheri A. Mesenchymal Stem Cells in Regenerative Medicine: Opportunities and Challenges for Articular Cartilage and Intervertebral Disc Tissue Engineering. Journal of Cellular Physiology 2010;222:23-32.

[65] Cui XL, Tang JN, Hartanto Y, Zhang JB, Bi JX, Dai S, et al. NIPAM-based Microgel Microenvironment Regulates the Therapeutic Function of Cardiac Stromal Cells. ACS Applied Materials & Interfaces 2018;10:37783-96.

[66] Lee CH, Cook JL, Mendelson A, Moioli EK, Yao H, Mao JJ. Regeneration of the articular surface of the rabbit synovial joint by cell homing: a proof of concept study. Lancet 2010;376:440-8.

[67] Lee JM, Ryu JH, Kim EA, Jo S, Kim BS, Lee H, et al. Adhesive barrier/directional controlled release for cartilage repair by endogenous progenitor cell recruitment. Biomaterials 2015;39:173-81.

[68] Narcisi R, Cleary MA, Brama PAJ, Hoogduijn MJ, Tuysuz N, ten Berge D, et al. Long-Term Expansion, Enhanced Chondrogenic Potential, and Suppression of Endochondral Ossification of Adult Human MSCs via WNT Signaling Modulation. Stem Cell Reports 2015;4:459-72.

[69] Fischer L, Boland G, Tuan RS. Wnt-3A enhances bone morphogenetic protein-2-mediated chondrogenesis of murine C3H10T1/2 mesenchymal cells. The Journal of Biological Chemistry 2002;277:30870-8.

[70] Lenas P, Moos M, Luyten FP. Developmental Engineering: A New Paradigm for the Design and Manufacturing of Cell-Based Products. Part I: From Three-Dimensional Cell Growth to Biomimetics of In Vivo Development. Tissue Engineering Part B-Review 2009;15:381-94.

[71] Kronenberg HM. Developmental regulation of the growth plate. Nature 2003;423:332-6.

[72] Santos MI, Reis RL. Vascularization in Bone Tissue Engineering: Physiology, Current Strategies, Major Hurdles and Future Challenges. Macromolecular Bioscience 2010;10:12-27.

[73] Farrell E, Both SK, Odorfer KI, Koevoet W, Kops N, O'Brien FJ, et al. In-vivo generation of bone via endochondral ossification by in-vitro chondrogenic priming of adult human and rat mesenchymal stem cells. BMC Musculoskeletal Disorders 2011;12.

[74] Ficat RP, Ficat C, Gedeon P, Toussaint JB. Spongialization: A New Treatment for Diseased Patellae. Clinical Orthopaedics and Related Research 1979:74-83.

[75] Radhakrishnan J, Manigandan A, Chinnaswamy P, Subramanian A, Sethuraman S. Gradient nano-engineered in situ forming composite hydrogel for osteochondral regeneration. Biomaterials 2018;162:82-98.

[76] Pereira DR, Canadas RF, Silva-Correia J, Morais AD, Oliveira MB, Dias IR, et al. Injectable gellan-gum/hydroxyapatite-based bilayered hydrogel composites for osteochondral tissue regeneration. Appllied Materials Today 2018;12:309-21.

[77] Zhou FF, Hong Y, Zhang XZ, Yang L, Li J, Jiang DM, et al. Tough hydrogel with enhanced tissue integration and in situ forming capability for osteochondral defect repair. Appllied Materials Today 2018;13:32-44.

[78] Cheng RY, Yan YF, Liu H, Chen H, Pan GQ, Deng LF, et al. Mechanically enhanced lipo-hydrogel with controlled release of multi-type drugs for bone regeneration. Appllied Materials Today 2018;12:294-308.

Supplementary information

Allogeneic Primary Mesenchymal Stem/Stromal Cell Aggregates within Poly(*N*-Isopropylacrylamide-co-Acrylic Acid) Hydrogel for Osteochondral Regeneration

Jiabin Zhang [a], Ming Zhang [c], Rongcai Lin [c], Seonho Yun [a], Yuguang Du [e], Liming Wang [c], Qingqiang Yao [c,], Andrew Zannettino [b,]*, Hu Zhang [a, d,]**

[a] School of Chemical Engineering, The University of Adelaide, Adelaide, SA 5005, Australia

[b] Adelaide Medical School, The University of Adelaide, Adelaide, SA 5001, Australia

[c] Department of Orthopaedic Surgery, Institute of Digital Medicine, Nanjing First Hospital, Nanjing Medical University, Nanjing, 210006, China

[d] Henry E. Riggs School of Applied Life Sciences, Keck Graduate Institute, California, CA 91711, USA

[e] Institute of Process Engineering, Chinese Academy of Sciences, Beijing, 100190, China

*Corresponding Authors: Dr Q Yao (yaoqingqiang@njmu.edu.cn), Prof. A Zannettino (andrew.zannettino@adelaide.edu.au), and Prof. H Zhang (hu_zhang@kgi.edu)

Published: Applied Materials Today 2019, 100487, DOI: 10.1016/j.apmt.2019.100487.

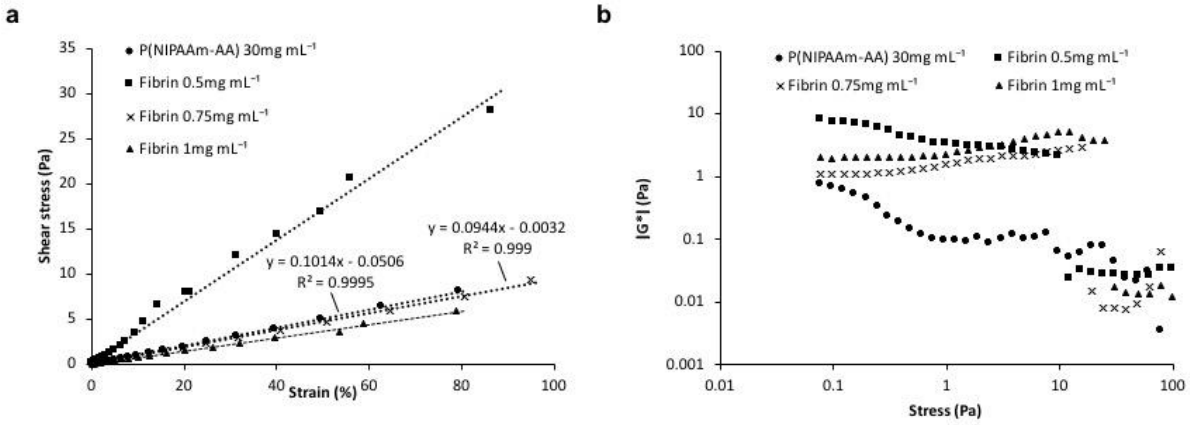

Figure S4.1 (a) Shear stress of p(NIPAAm-AA) and fibrin hydrogels under different strains. (b) Absolute complex moduli (|G*|) of p(NIPAAm-AA) and fibrin hydrogels under different stresses.

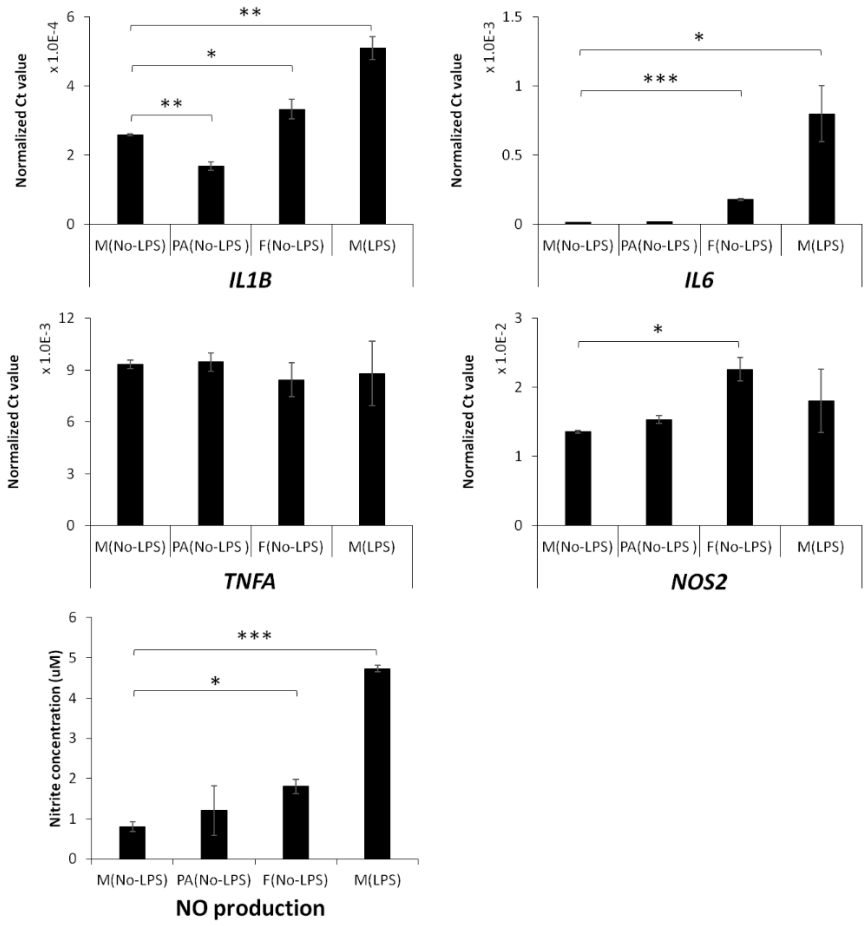

Figure S4.2 mRNA expression of pro-inflammatory-related genes (*IL1B*, *IL6*, *TNFA*, *NOS2*) and nitric oxide (NO) production from mouse macrophage cultured in the medium without stimulation of lipopolysaccharide (LPS) in the medium (M (No-LPS)), in the P(NIPAAm-AA) hydrogel-containing medium (PA (No-LPS)), or in the fibrin hydrogel-containing medium (F (No-LPS)) for 24 h. The mouse macrophage pre-activated by 200 ng/mL of LPS and cultured in the medium for 24 h (M (LPS)) as a positive control. Data were presented as mean ± standard error (SE), *n*=3. "*" for $\rho < 0.05$; "**" for $\rho < 0.01$; "not significant (n.s.)" for $\rho > 0.05$.

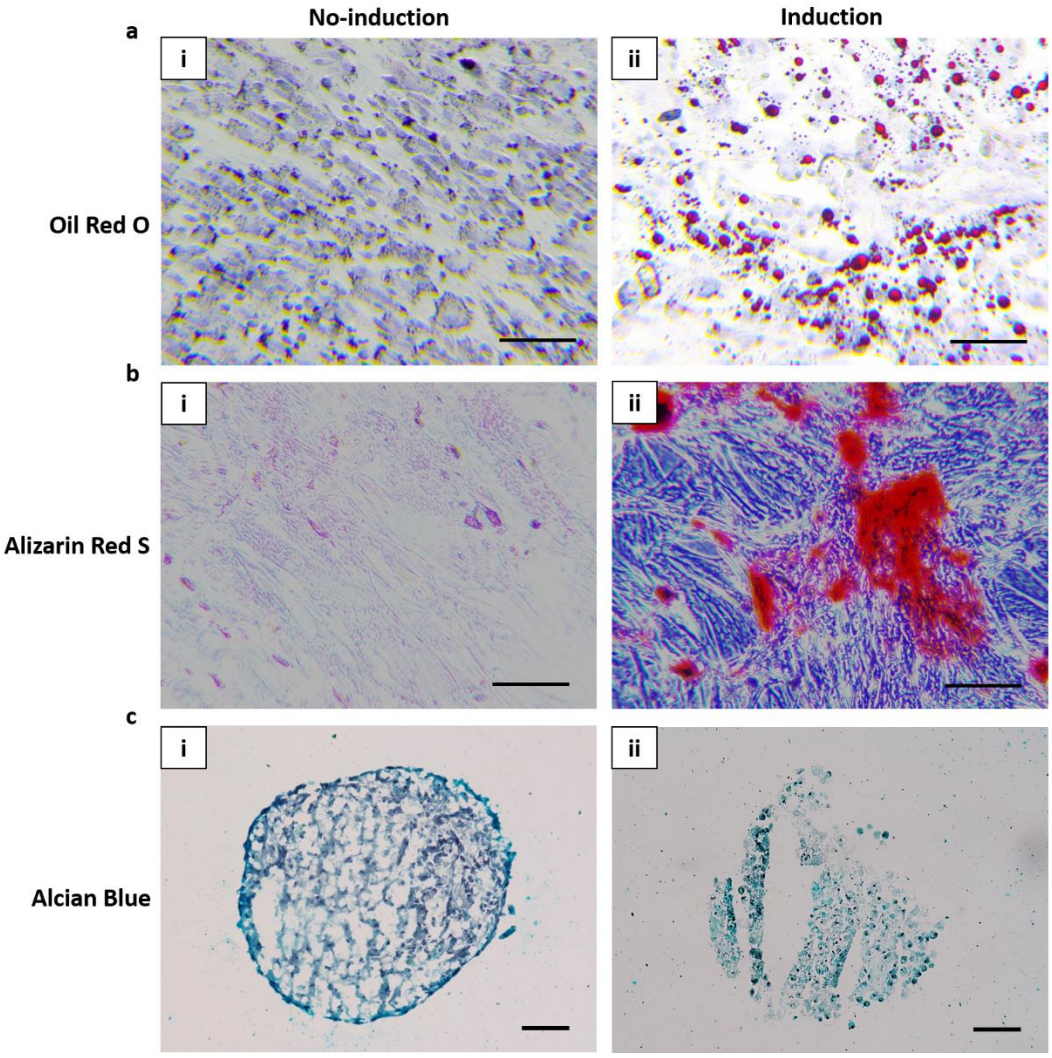

Figure S4.3 Multi-pluripotency of rabbit primary bone marrow-derived mesenchymal stromal/stem cells. (a) Oil Red O staining images of the cells cultured in the (i) complete medium or (ii) adipogenic induction medium for 3 weeks. Blue: cell nuclei; Red: lipids. Scale bar: 100 µm. (b) Alizarin Red S staining images of the cells cultured in the (i) complete medium or (ii) osteogenic induction medium for 6 weeks. Red: mineral calcium. Scale bar: 100 µm. (c) Alcian Blue staining images of the cells cultured in the (i) complete medium or (ii) chondrogenic induction medium for 3 weeks. Black: cell nuclei; Blue: sulfated GAGs. Scale bar: 100 µm.

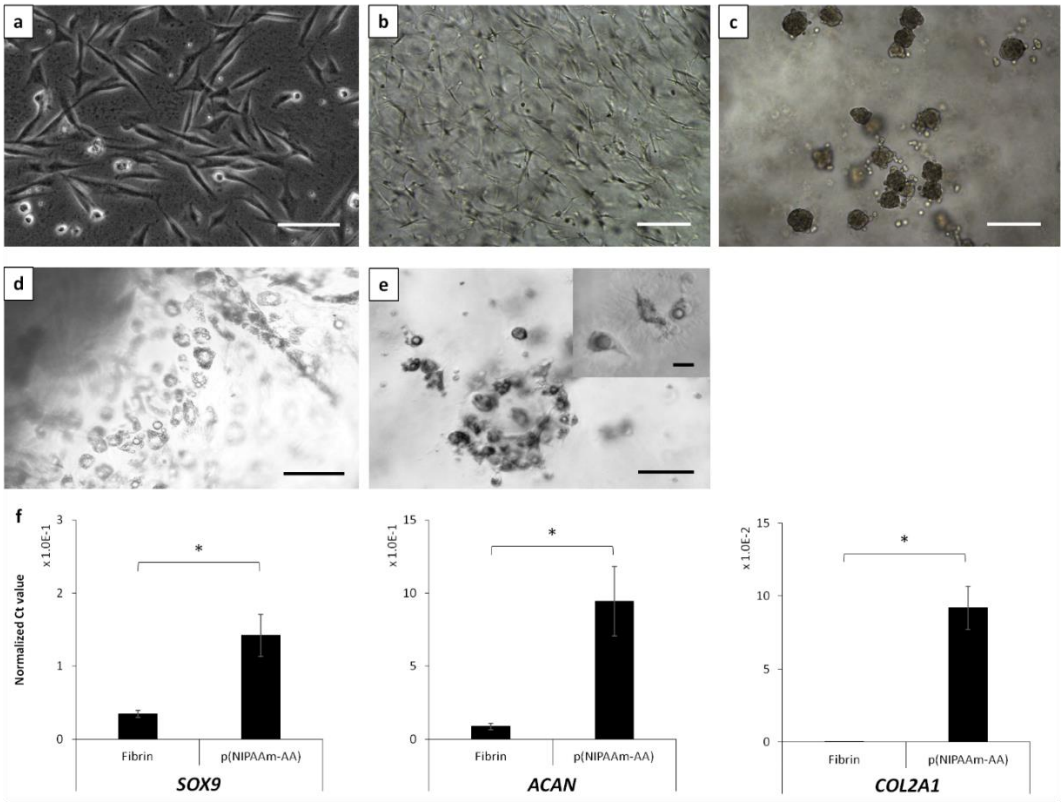

Figure S4.4 Optical images of primary rabbit bone marrow-derived mesenchymal stromal/stem cells (BMSCs) cultured (a) on a two-dimensional (2D) tissue culture plate (scale bar: 50 μm), (b) in fibrin hydrogel (scale bar: 200 μm), or (c) in p(NIPAAm-AA) hydrogel (scale bar: 200 μm) with complete cell culture medium after overnight. (d) An optical image of chondrogenesis-induced rabbit BMSCs cultured in the fibrin hydrogel for 4 weeks (scale bar: 100 μm). (e) Optical images of chondrogenesis-induced rabbit BMSCs cultured in the p(NIPAAm-AA) hydrogel for 4 weeks at a lower magnification (scale bar: 100 μm) and a higher magnification (inset scale bar: 10 μm).

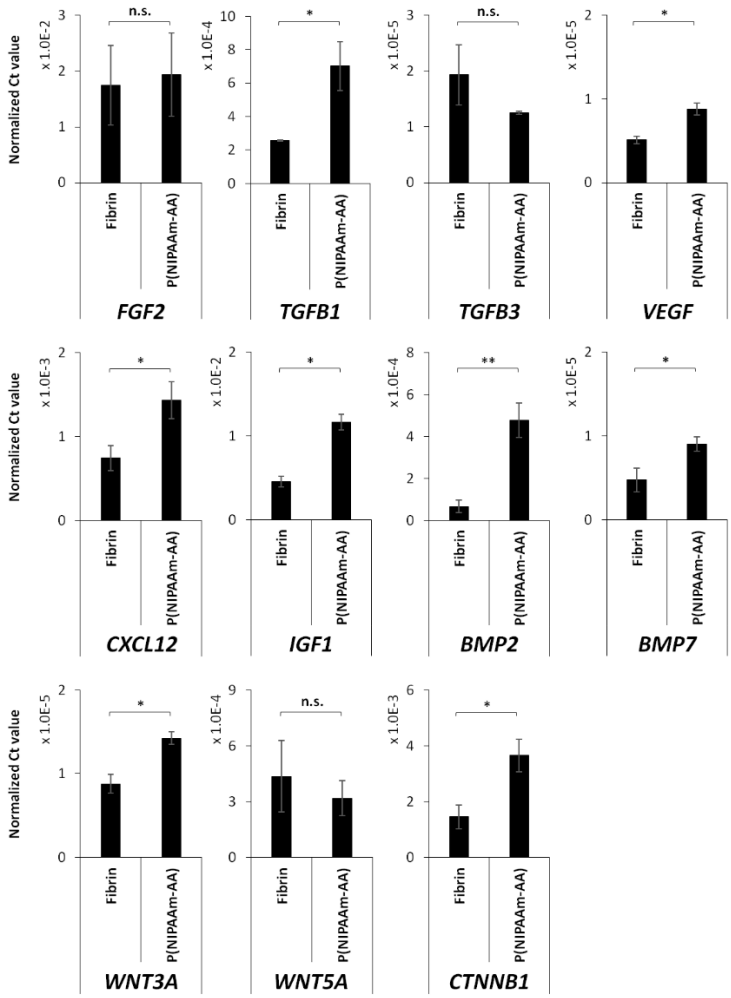

Figure S4.5 mRNA expression of paracrine signalling-related genes (*FGF2*, *TGFB1*, *TGFB3*, *VEGF*, *CXCL12*, *IGF1*, *BMP2*, *BMP7*, *WNT3A*, *WNT5A*, *CTNNB1*) for primary rabbit bone marrow-derived mesenchymal stem/stromal cells cultured in the fibrin or p(NIPAAm-AA) hydrogels overnight. Data were presented as mean ± standard error (SE), n=3. "*" for $\rho < 0.05$; "**" for $\rho < 0.01$; "not significant (n.s.)" for $\rho > 0.05$.

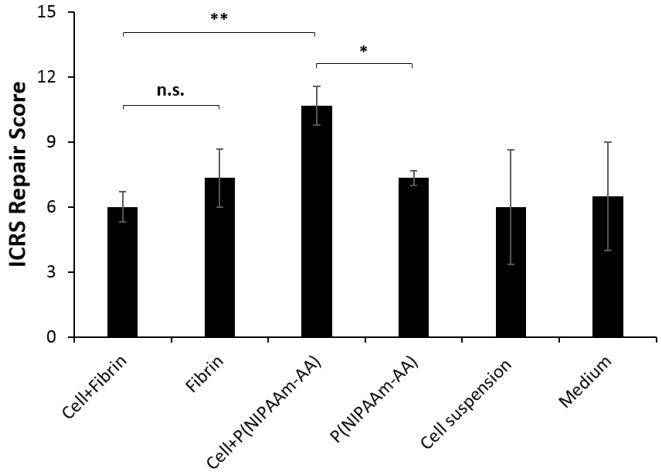

Figure S4.6 ICRS score of regenerated cartilage three months after implantation of medium only (Medium), cell suspensions (Cell suspension), fibrin hydrogel (Fibrin), cell and fibrin hydrogel hybrid (Cell+Fibrin), p(NIPAAm-AA) hydrogel (P(NIPAAm-AA)), or cell and p(NIPAAm-AA) hydrogel hybrid (Cell+P(NIPAAm-AA)). Data were presented as mean ± standard error (SE), n=3. "*" for $\rho < 0.05$; "**" for $\rho < 0.01$; "not significant (n.s.)" for $\rho > 0.05$.

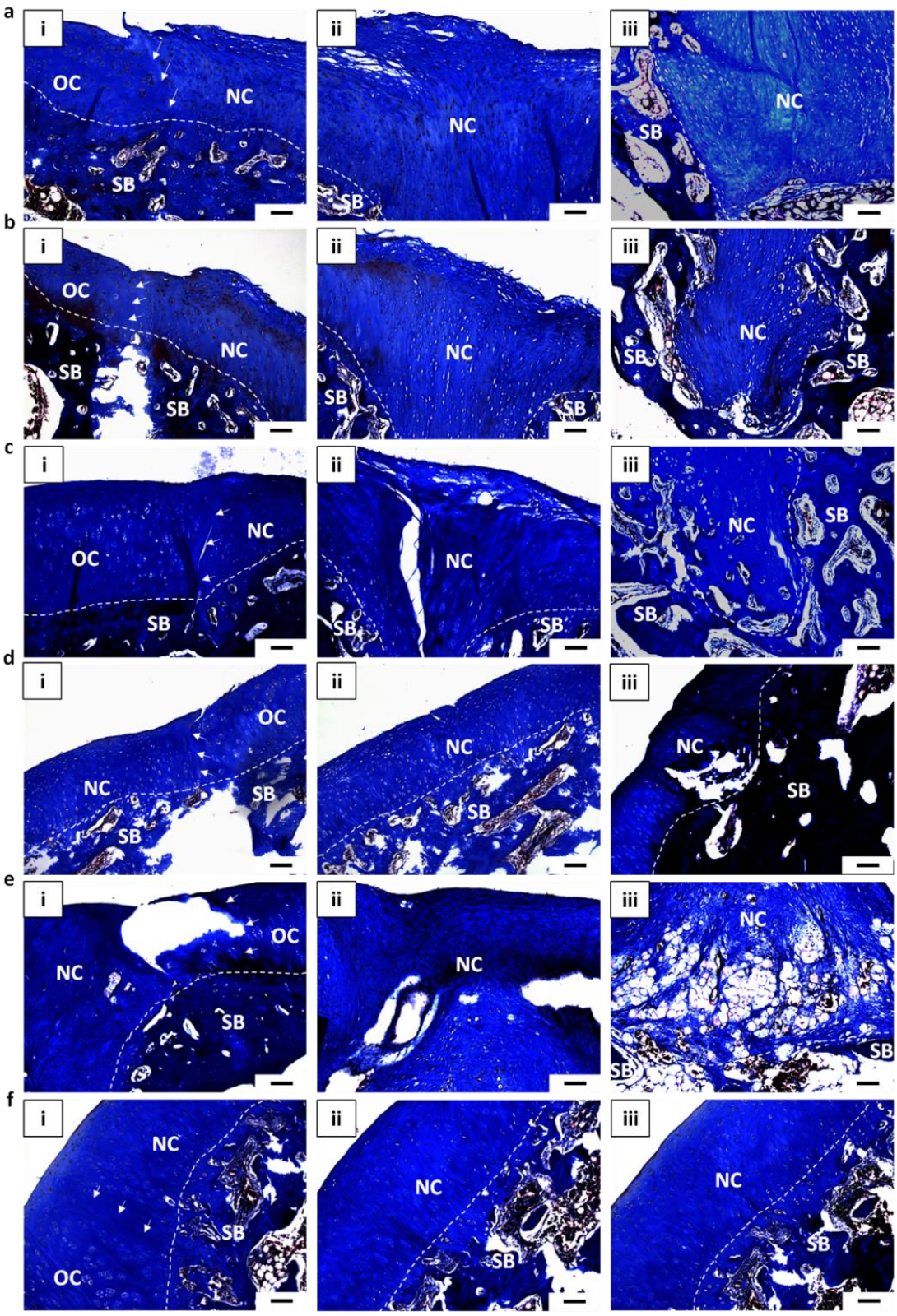

Figure S4.7 Masson's Trichrome staining images of the regenerative osteochondral tissues three months after the implantation of (a) medium only, (b) cell suspensions, (c) fibrin hydrogel, (d) cell and fibrin hydrogel, (e) p(NIPAAm-AA) hydrogel, (f) cell and p(NIPAAm-AA) hydrogel at (i) the border of the osteochondral defect, (ii) the center of the osteochondral defect, and (iii) the bottom of the osteochondral defect. Black dots: cell nuclei; Blue: collagen; Red: cytoplasm. NC: new cartilage; OC: old cartilage; SB: subchondral bone. White dashed lines separate the cartilage from the subchondral bone. White arrows point to the interface between new cartilage and old cartilage. (Scale bar: 100 μm)

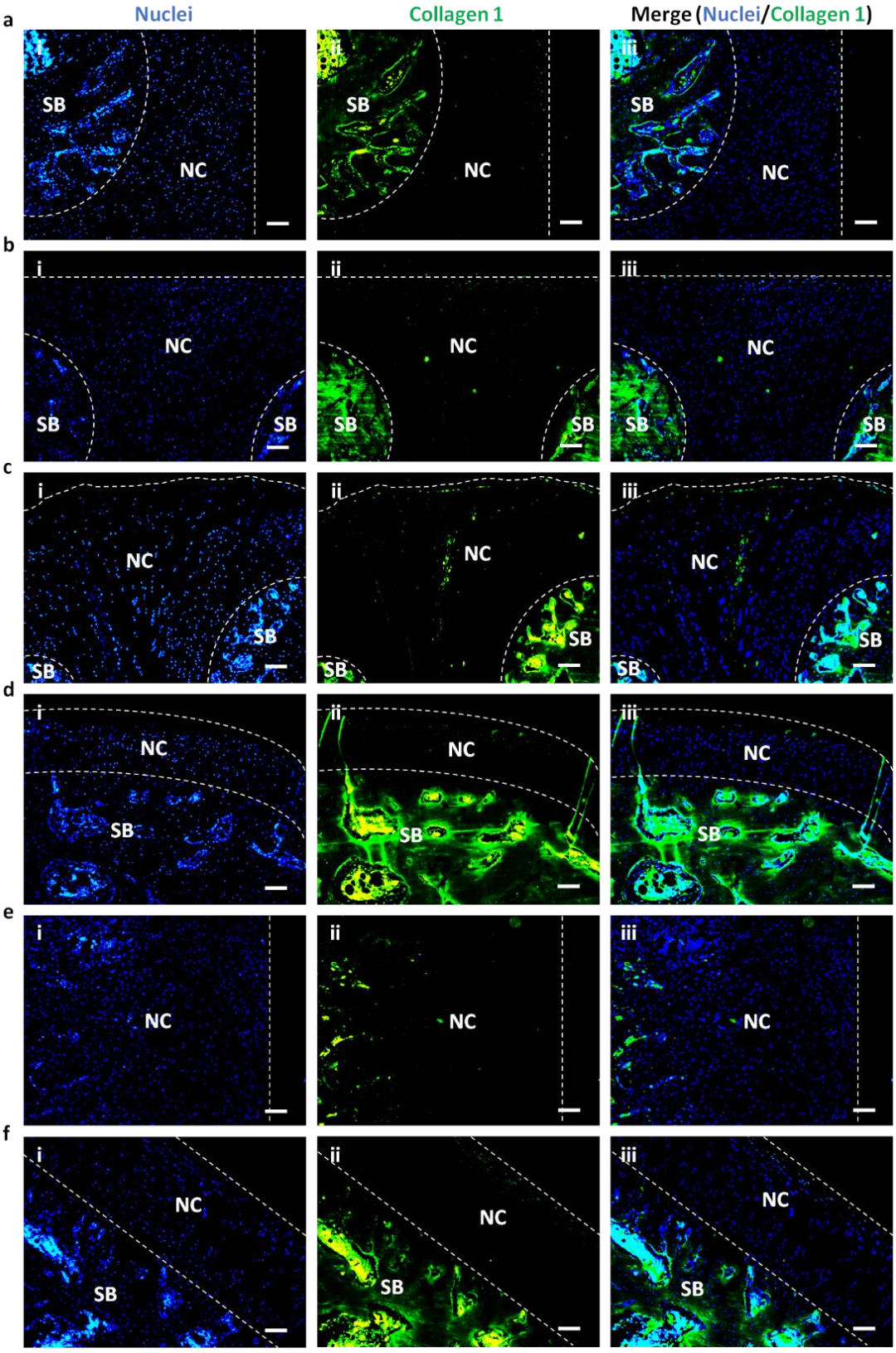

Figure S4.8 Immunofluorescent staining images of the regenerative osteochondral tissues three months after the implantation of (a) medium only, (b) cell suspensions, (c) fibrin hydrogel, (d) cell and fibrin hydrogel, (e) p(NIPAAm-AA) hydrogel, (f) cell and p(NIPAAm-AA) hydrogel. (i) Hoechst 33342-staining images, (ii) Alexa Fluor 488-staining images, (iii) Merged images with Hoechst 33342 and Alexa Fluor 488 staining. Blue: cell nuclei; Green: type 1 collagen. NC: new cartilage; SB: subchondral bone. White dashed lines separate the new cartilage from the subchondral bone. (Scale bar: 100 μm)

Table S4.1 The sequences of specific human genes.

Primers		Sequence (5'➔3')
Human	*SOX9*	Forward: AGGTGCTCAAAGGCTACGAC
		Reverse: GCTTCTCGCTCTCGTTCAGA
	ACAN	Forward: CTGCTTCCGAGGCATTTC
		Reverse: GCTCGGTGGTGAACTCTAGC
	COL2A1	Forward: ATCACAGGCTTCCATTGACC
		Reverse: CTCCACAGCATCGATGTCAC
	COL10A1	Forward: AATGCCCACAGGCATAAAAG
		Reverse: AGGACTTCCGTAGCCTGGTT
	ACTB	Forward: GATCATTGCTCCTCCTGAGC
		Reverse: GTCATAGTCCGCCTAGAAGCAT

Table S4.2 The sequences of specific mouse genes.

Primers		Sequence (5'➔3')
Mouse	*IL1B*	Forward: CGACAAAATACCTGTGGCCT
		Reverse: TTCTTTGGGTATTGCTTGGG
	IL6	Forward: GAAACCGCTATGAAGTTCCTCTCTG
		Reverse: TGTTGGGAGTGGTATCCTCTGTGA
	TNFA	Forward: AGGGTCTGGGCCATAGAACT
		Reverse: CCACCACGCTCTTCTGTCTAC
	NOS2	Forward: GGCAGCCTGTGAGACCTTTG
		Reverse: TGAAGCGTTTCGGGATCTG
	ACTB	Forward: AGGTGACAGCATTGCTTCTG
		Reverse: GCTGCCTCAACACCTCAAC

Table S4.3 The sequences of specific rabbit genes.

Primers		Sequence (5'➔3')
Rabbit	*SOX9*	Forward: GGTGCTCAAGGGCTACGACT
		Reverse: GGGTGGTCTTTCTTGTGCTG
	ACAN	Forward: AGGTCGTGGTGAAAGGTGTTG
		Reverse: GTAGGTTCTCACGCCAGGGA
	COL2A1	Forward: AACACTGCCAACGTCCGAT
		Reverse: CTGCAGCACGGTATAGGGA
	FGF2	Forward: TACAACTTCAAGCAGAAGAG
		Reverse: CAGCTCTTAGCAGACATTGG
	TGFB1	Forward: TGCGGCAGCTGTACATTGAC
		Reverse: GGCAGAAGTTGGCGTGGTA
	TGFB3	Forward: TGGCTGTTGAGAAGAGAGTCC
		Reverse: TGCTTCAGGGTTCAGAGTGTT
	VEGF	Forward: GCGGCGTTCTCAGTGGTGTT
		Reverse: TGGGTGCTGGCTTGTTCCTC
	CXCL12	Forward: AAACCCGTCAGCCTGAGCTACAGA
		Reverse: TCTTGAGATGCTTGACGTTGGCTC
	IGF1	Forward: TGGTGGATGCTCTCAGTTCGTGT
		Reverse: GCTGATACTTCTGAGTCTTGGGCA
	BMP2	Forward: CGCCTCAAATCCAGCTGTAAG
		Reverse: GGGCCACAATCCAGTCGTT
	BMP7	Forward: TGGAGACGCTGGATGG
		Reverse: CTGCGGAAGTGGACCT
	WNT3A	Forward: AGGACATCGAGTTTGGTGGG
		Reverse: CTCGTTGTTGTGGCGGTTCA
	WNT5A	Forward: AGCCAATTCTTGGTGGTCCC
		Reverse: CTTGAGAAAGTCCCGCCAGT
	CTNNB1	Forward: CCAATCATGCACCATTGCGT
		Reverse: ACTCCCTCCACAAACTGCTG
	GAPDH	Forward: TCACCATCTTCCAGGAGCGA
		Reverse: CACAATGCCGAAGTGGTCGT

CHAPTER V

FABRICATION OF A NEO-CARTILAGE PATCH BY FUSING CELL AGGREGATES GENERATED IN A THERMOSENSITIVE HYDROGEL ONTO ELECTROSPUN FILM

Statement of Authorship

Title of Paper	Fabrication of a neo-cartilage patch by fusing cell aggregates generated in a thermosensitive hydrogel onto electrospun film.
Publication Status	☐ Published ☐ Accepted for Publication ☐ Submitted for Publication ☑ Unpublished and Unsubmitted work written in manuscript style
Publication Details	

Principal Author

Name of Principal Author (Candidate)	Jiabin Zhang
Contribution to the Paper	Performed experiments, analysed data, writing manuscript.
Overall percentage (%)	80%
Certification:	This paper reports on original research I conducted during the period of my Higher Degree by Research candidature and is not subject to any obligations or contractual agreements with a third party that would constrain its inclusion in this thesis. I am the primary author of this paper.
Signature	Date 26/07/2019

Co-Author Contributions

By signing the Statement of Authorship, each author certifies that:

i. the candidate's stated contribution to the publication is accurate (as detailed above);

ii. permission is granted for the candidate in include the publication in the thesis; and

iii. the sum of all co-author contributions is equal to 100% less the candidate's stated contribution.

Name of Co-Author	Seonho Yun
Contribution to the Paper	Experiment design and evaluation of data.
Signature	Date 16/07/2019

Name of Co-Author	Yuguang Du
Contribution to the Paper	Proof read the manuscript and evaluation.
Signature	Date 2019. 7. 15

Name of Co-Author	Andrew Zannettino		
Contribution to the Paper	Proof read the manuscript, experiment design, and evaluation of data.		
Signature		Date	16 July 2019

Name of Co-Author	Hu Zhang		
Contribution to the Paper	Proof read the manuscript, experiment design, and evaluation of data.		
Signature		Date	15-07-2019

Please cut and paste additional co-author panels here as required.

Fabrication of A Neo-Cartilage Patch by Fusing Cell Aggregates Generated in A Thermosensitive Hydrogel onto Electrospun Film

Jiabin Zhang [a], *Seonho Yun* [a], *Yuguang Du* [d], *Andrew C.W. Zannettino* [b, *], *Hu Zhang* [a, c, *]

[a] School of Chemical Engineering, The University of Adelaide, Adelaide, SA 5005, Australia

[b] Adelaide Medical School, The University of Adelaide, Adelaide, SA 5001, Australia

[c] Henry E. Riggs School of Applied Life Sciences, Keck Graduate Institute, California, CA 91711, USA

[d] Institute of Process Engineering, Chinese Academy of Sciences, Beijing, 100190, China

*Corresponding Authors: Prof. H Zhang (hu_zhang@kgi.edu) and Prof. A Zannettino (andrew.zannettino@adelaide.edu.au)

Prepared in publication format

5.1 Graphical abstract

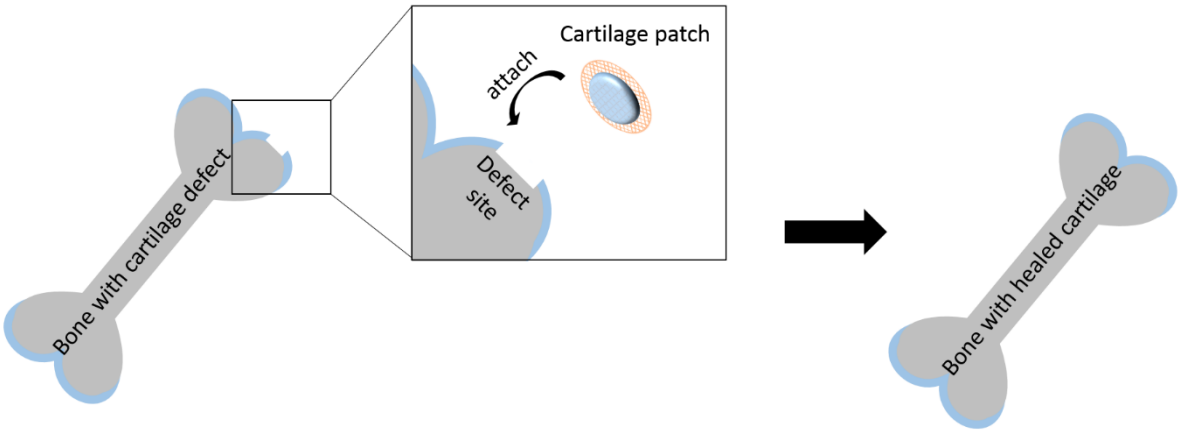

A human neo-cartilage patch was generated with the collaboration of poly (*N*-isopropylacrylamide)-based hydrogel and electrospun gelatin film for potential cartilage tissue engineering.

5.2 Abstract

Irregular defects at sites of degenerative cartilage often accompany osteoarthritis (OA). The development of novel cells/biomaterials-based cartilage tissue engineering methods to address these defects may provide a durable approach to limit the development of OA. In the present study, we fabricated a neo-cartilage patch by fusing cell aggregates onto a biodegradable nanofiber film for degenerative cartilage repair. Human mesenchymal stem/stromal cell (MSC) aggregates were prepared and induced chondrogenesis in a thermosensitive hydrogel, poly (*N*-isopropylacrylamide-co-acrylic acid) (p(NIPAAm-AA)). Chondrogenic differentiation was confirmed by examination of chondrogenesis-related gene expression and the deposition of sulfated GAGs and collagen 2A1. The formation of cell aggregates was due to cell migration in response to a gradient of the chemoattractant. After ECMs were produced from these cell aggregates, small aggregates were found to be bridged by differentiated MSC-derived ECM proteins, which led to the creation of cell-dense hollow shell structures. These differentiated MSC aggregates were harvested by diluting the hydrogel in the cold phosphate buffer and transferred onto an electrospun film for fabricating a neo-cartilage patch by mechanical force and spatial confinement. While future work is required, these fabricated neo-cartilage patches may be able to integrate into the irregular defects under compressive stresses and achieve cartilage regeneration *in vivo*.

KEYWORDS: hydrogel, chondrogenesis, human mesenchymal stem/stromal cell, electrospinning, cell aggregates, cartilage regeneration

5.3 Introduction

Osteoarthritis (OA) is a chronic joint disease that is nearly always accompanied by irregular defects on the articular hyaline cartilage surface. These defects are often difficult to heal owing to the avascular nature of the tissue and the limited number of chondrogenic progenitor cells in the defect area. [1] Tissue engineering, utilizing biomaterials and/or cells, represents a potential approach to promote cartilage regeneration. [2] However, due to the irregular structure of the

damaged cartilage, it is challenging to retain the implanted biomaterials and/or cells *in situ*. While injectable hydrogels can deliver cells *in vivo*, in a minimal invasive manner to fill deep irregular defects, the poor mechanical properties of the hydrogels, represents a key constraint for their use at the degenerative cartilage surface. [3, 4]

Mesenchymal stem/stromal cells (MSCs), are capable of differentiation into a number of mature cell lineages, including chondrocytes, osteocytes and adipocytes. [5] In the context of tissue engineering strategies, cell aggregates are believed to be superior to individual cells, due to their functional enhancement in secretion of endogenous growth factors and deposition of extracellular matrices (ECMs). [6, 7] The methods of generating cell aggregates can be divided principally into three groups: spontaneous cell aggregation-mediated fabrication of cell aggregates, such as hanging drop culture or culture on non-adhesion plates [8]; substrate-mediated fabrication of cell aggregates, such as culture on positive charged [9] or thermosensitive surfaces [10]; and technology-assisted fabrication of cell aggregates, such as magnetic levitation [11] and negative di-electrophoresis [12]. While hydrogels are widely used for three-dimensional (3D) stem cell culture, few have been used to stimulate the formation of cell aggregates *in situ* for specific applications. Further, the intrinsic mechanism of cell aggregates formation within hydrogels has not been reported. [13-19]

The thermosensitive hydrogel is one type of smart material that can reversibly gel in response to a change in the external temperature. [20] We have previously reported a thermosensitive hydrogel, p(NIPAAm-AA), that could facilitate multi-lineage differentiation of human MSCs by the formation of cell aggregates *in situ*. [21] In this study, we examined the mechanism by cell aggregates formation occurred within the p(NIPAAm-AA). To this end, we found that the hydrogel promoted cell migration, leading to the generation and fusion of cell aggregates in the p(NIPAAm-AA) hydrogel. Formation of small cell aggregates within the p(NIPAAm-AA) hydrogel led to a more efficient transportation of inductive biomolecules and a more significant up-regulation in expression of chondrogenesis-related genes and the production of ECM

proteins compared to cell pellets. The differentiated cells were harvested from the hydrogel at room temperature and transferred onto an electrospun film and fused into an integrated neo-cartilage due to spatial confinement and external mechanical compression. The fabricated neo-cartilage patch could be used for cartilage regeneration by simply attaching it to the degenerated cartilage with the assistance of a medical glue or suture and the cells within the neo-cartilage may be able to integrate into the irregular defects by remodeling the surrounding ECM proteins.

5.4 Materials and methods

5.4.1 Poly (*N*-isopropylacrylamide)-based anionic hydrogel synthesis

The poly (*N*-isopropylacrylamide-acrylic acid) (p(NIPAAm-AA)) anionic hydrogel was synthesized according to a previous study. [22] Briefly, *N*-isopropylacrylamide (NIPAAm, Tokyo Chemical Industry) was recrystallized from *n*-hexane and dried overnight. *N*, *N*'-methylenebisacrylamide (MBA, Sigma-Aldrich), sodium dodecyl sulfate (SDS, BDH Laboratory Supplies Poole), acrylic acid (AA, Acros Organics) and the NIPAAm dissolved in ultrapure water at a molar ratio of 2 : 1.2 : 1 : 99, after which the precursor solution was transferred into a 250 mL three-necked flask and degassed by supplying nitrogen gas for 45 min at 50 °C. 1 mM potassium persulfate (KPS, Chem-Supply) solution was injected into the precursor solution to initiate the free radical emulsion polymerization with continuous nitrogen gas supply after increasing the heating temperature to 70 °C. Poly (*N*-isopropylacrylamide) (p(NIPAAm)) was synthesized by following the same protocol of p(NIPAAm-AA) synthesis, but without the addition of acrylic acid. The synthesized hydrogel was transferred into a molecular porous membrane tube (Spectrum Labs, MW 12-14 kDa) and dialyzed against ultrapure water up to one week with daily change of water at room temperature. The dialyzed hydrogel was then concentrated to around 120 mg/mL by heating at 70 °C. The final concentration of the concentrated hydrogel was measured and calculated by weighing the dry weight of a 100 μL concentrated hydrogel.

5.4.2 Fourier-Transform Infrared Spectroscopy (FTIR)

The infrared spectra of the functional groups in the MBA, NIPAAm, and dried p(NIPAAm-AA) were detected by recording the transmittance from 4000 cm^{-1} to 400 cm^{-1} using a Nicolet 6700 Fourier-transform infrared spectrometer (Thermo Fisher).

5.4.3 Reversible gelation

The concentrated p(NIPAAm-AA) hydrogel was first diluted into 50 mg/mL with 1 × PBS (Sigma-Aldrich). The diluted p(NIPAAm-AA) hydrogel was then mixed with 1 × PBS containing magnesium chloride ($MgCl_2$, Chem-Supply) at various concentrations and complete cell culture medium (α-minimal essential medium (MEM, Sigma-Aldrich) + 10% (v/v) fetal calf serum (FCS, Sigma-Aldrich) + additives (ADDs, 50 U/mL- 50 μg/mL penicillin-streptomycin (CSL), 2 mM L-glutamine (JRH), 1 mM sodium pyruvate (Sigma-Aldrich), 15 mM HEPES (Life Technologies))) at a volumetric ratio of 3 : 1 : 1 to a final concentration of p(NIPAAm-AA) at 30 mg/mL and Mg^{2+} at 0, 0.01 M, 0.025 M, 0.05 M, 0.075 M, and 0.1 M for gelation studies. 500 μL of the prepared hydrogels, with various ionic strengths, was pipetted into a 1.5 mL Eppendorf tube and incubated at 37 °C for 30 min. Stability of the hydrogels at 37 °C was examined by inverting the Eppendorf tube, while liquification of the gelled p(NIPAAm-AA) hydrogels at room temperature was recorded at two time points (5 min and 30 min). The time-dependent gelation and liquification process were also monitored by measuring the transmittance of 30 mg/mL p(NIPAAm-AA) with 0.01 M $MgCl_2$ at 37 °C from 0 to 30 min and at 25 °C from 30 to 60 min using a VersaMax microplate reader (Molecular Devices) at a wavelength of 720 nm. Besides, the syneresis effect of p(NIPAAm-AA) and p(NIPAAm) hydrogels were also examined by preparing the hydrogels at the same polymer concentration (30 mg/mL) and ionic strength (0.01 M Mg^{2+}) and incubating at 37 °C for 30 min.

5.4.4 Electrospinning

8 % (w/v) of gelatin (Sigma-Aldrich) were dissolved in a co-solvent (1,1,1,3,3,3-Hexafluoro-2-propanol (Sigma-Aldrich) : H_2O at a volumetric ratio of 39:1). The gelatin solution was injected into a needle with a size of 23G (Terumo) by a syringe pump (Harvard apparatus) at

an injection ratio of 1.25 mL/h and charged with a high voltage of 15 kV using a high voltage supply (Glassman High Voltage). Electrospinning was operated at room temperature and a metal earth-grounded plate was placed under the needle at a distance of 8 cm to collect the electrospun nanofibers. After electrospinning, the films were left in the fume hood to eliminate the remaining organic solvent. The electrospun films were cut into a circle shape with a diameter of 10 mm and overlaid by compressing the films with a stainless-steel ring (inner diameter: 5 mm and outer diameter: 10 mm) on the top of the electrospun films, after which the electrospun films were heated in an oven for 2 h at 190 °C.

5.4.5 Cell viability assay

An immortalised human mesenchymal stem/stromal cell line, UE7T-13 (RIKEN BioResources Center, Ibaraki, Japan, http://en.brc.riken.jp), with a passage number of 44-45 was used in this study and their multi-lineage differentiation capacity was reported in a previous study. [21] 100 μL of UE7T-13 cell suspension in the complete cell culture medium at a density of 1×10^5 cells/mL was added into a well of a 96-well plate and cultured overnight in a humidified incubator containing 5% CO_2 at 37 °C. Following overnight incubation, the spent cell culture media were replaced with fresh media supplemented with various concentrations of $MgCl_2$ (0, 0.01 M, 0.025 M, 0.05 M, 0.075 M, and 0.1 M) and the cells were further incubated for 24 h. The media in each 96 well were then replaced with 100 μL of fresh complete cell culture medium and 10 μL of 5 mg/mL 3-(4,5-dimethylthiazol-2-yl)-2,5-diphenyltetrazolium bromide (MTT, Thermo Fisher). Following an additional 4 h incubation, the supernatant was discarded and 100 μL dimethyl sulfoxide (DMSO, Chem-Supply) was added into each well to dissolve the purple crystals within the cells. The absorbance was read at a wavelength of 595 nm with an iMark™ microplate reader (BIO-RAD). All data were normalized to the absorbance value of those cells cultured in the media prepared with ultrapure water, 1× PBS, and complete medium at a volumetric ratio of 3 : 1 : 1.

In addition, 250 μL of 30 mg/mL p(NIPAAm-AA) hydrogel with 0.01 M $MgCl_2$ was first coated onto each well of a 48-well plate and incubated at 37 °C for 1 h. Subsequently, an additional 250 μL of cell suspension, with 30 mg/mL p(NIPAAm-AA) hydrogel in the complete media, at a cell density of 1×10^6 cells/mL, was added into the p(NIPAAm-AA)-coated wells at 37 °C. The cell-gel hybrids were allowed to incubate in a humidified condition containing 5% CO_2 at 37 °C for 1 h before toping up 500 μL of complete cell culture medium. The cell culture media were changed every other day. On day 1 and 9, the cell morphology was imaged under a CKX41 microscope (Olympus) after the cell-gel hybrids were cooled down to room temperature and the liquid solution became transparent. 250 μL of the staining working solution (4 μM calcein AM and 2 μM ethidium homodimer-1 in 1× PBS) was added into each well after discarding the top medium. The cell-gel hybrids were kept in darkness at room temperature for 30 min, and cells were then imaged under a CKX41 fluorescent microscope. Live cells displayed a green color, while dead cells were stained with a red color.

The electrospun films were cut to fit the bottom of a 96-well plate. 40 μL of UE7T-13 cell solution, containing around1×10^4 cells, was then added onto tissue culture plates and the electrospun films, respectively, and the cells were pre-cultured for 4 h to allow attachment in a humidified incubator containing 5 % CO_2 at 37 °C. After another 160 μL of fresh complete medium was added to each well, the 96-well plate was incubated as above for an additional 24 h. The MTT assay was performed and the reading absorbance values were normalized to cells cultured on the 96-well plate without electrospun films.

5.4.6 Cell migration assay

100 μL cell-gel hybrids, with a cell seeding density of 1×10^6 cells/mL, were prepared and pre-incubated in the upper chamber of each well in a 24-well plate separating from the bottom well by a membrane with an average pore size of 3 μm (Thermo Fisher) at 37 °C for 1 h. The upper chambers for “Control” and “Top-10% FCS” groups were filled with 100 μL warm cell culture medium with 10 % FCS, while the chamber for the “Top-20% FCS” group was filled with 100

μL warm cell culture medium with 20% FCS, and 100 μL warm cell culture medium without FCS was added into the upper chamber for the "Down-10% FCS" group. On the contrary, 700 μL of warm cell culture medium containing 10 % FCS was gently added along the wall of each well into the lower chamber for both "Control" and "Down-10% FCS" groups, while the same volume of cell culture medium without FCS was added along the wall of each well into the lower chamber for "Top-10% FCS" and "Top-20% FCS" groups. The 24-well plate containing cell-gel hybrids in the inserts was gently transferred into a humidified incubator containing 5% CO_2 at 37 °C for 18 h, and the media and cell-gel hybrids were discarded. The inserts were gently washed twice with 1× PBS to remove any no-adherent cells. The attached cells on the bottom of the inserts were first fixed in a co-solvent (ethanol (Chem-Supply): acetic acid (Chem-Supply) at a volumetric ratio of 6 : 1) for 10 min at room temperature, and washed twice with 1× PBS. 1 μg/mL of DAPI staining solution prepared in methanol (Chem-Supply) was then added into the inserts to stain the cell nuclei for 3 min. The inserts were then washed in 1× PBS once and immersed in ultrapure water on a glass slide. Five images were randomly taken for each insert under a CKX41 fluorescent microscope and processed with image J to quantify the amount of cell nuclei on the inserts. The cells cultured in the culture medium with 10 % FCS were used in the "Control" group, while cells starved in cell culture medium without FCS overnight were used in the "Down-10% FCS", "Top-10% FCS", and "Top-20% FCS" groups. All data were normalized to the value of the "Control" group and presented as a percentage of normalized cell migration.

5.4.7 Scanning electron microscopy (SEM)

The cell-gel hybrids were incubated in the upper chamber of a 24-well plate with 10 % FCS as the chemoattractant in the lower chamber. After 18 h, the media were discarded and the cell-gel hybrids were rapidly frozen in liquid nitrogen and dried overnight using an Alpha 2-4 LD freeze dryer (Martin Christ). The freeze-dried cell-gel hybrid was then surface coated with a

thin layer of platinum and imaged under a XL30 scanning electron microscope (Philips) at an accelerating voltage of 10 kV.

The electrospun nanofibers were coated with a thin layer of platinum and 5 images were randomly captured at different areas of the electrospun film using a XL30 SEM. The SEM images were processed by image J to measure the inter-fiber pore size formed by adjacent nanofibers (Only the pores with an area larger than 0.5 μm² were measured) and the fiber diameter by randomly selecting 20 fibers per SEM image.

5.4.8 Chondrogenesis

The cell-gel hybrids were incubated in a humidified atmosphere containing 5% CO_2 at 37 °C for 9 days with a change of the cell culture medium every other day. After culturing in the complete medium for 9 days, chondrogenesis of the encapsulated cells was induced for a pre-defined period (4 weeks, 6 weeks, and 8 weeks) by replacing the complete cell culture medium with a chondrogenic induction medium (high glucose Dulbecco's Modified Eagle's Medium (DMEM-high, Sigma-Aldrich) supplemented with 50 U/mL- 50 μg/mL penicillin-streptomycin (CSL), 100 μM L-ascorbate-2-phosphate (WAKO), 2 mM L-glutamine, 0.1 μM DBL™ dexamethasone sodium phosphate (Hospira Australia), 1× ITS + (BD Biosciences), 10 ng/mL human transforming growth factor-beta 3 (TGF-β3, Chemicon International), and 0.125% bovine serum albumin (BSA, Sigma-Aldrich). A cell suspension containing 2.5×10^5 cells was centrifuged into a cell pellet in a 15 mL polypropylene tube at a rotating speed of 600 rcf for 5 min. The cell pellet was used as the control and was cultured as described for the p(NIPAAm-AA) hydrogel to induce chondrogenesis.

5.4.9 qRT-PCR

After inducing chondrogenesis for 4, 6 and 8 weeks, cells were harvested from the p(NIPAAm-AA) hydrogel by cooling and diluting the cell-gel hybrids in 1× PBS at 4 °C. Following centrifugation at 600 rcf, the supernatants were discarded and the cells were lysed in TRIzol (Life technologies). The supernatants were transferred into a new Eppendorf tube after adding

chloroform (Chem-Supply) and spinning at 12000 rcf and 4 °C for 15 min. Isopropanol (Chem-Supply) was added to the supernatant to precipitate the mRNA at 4 °C with glycogen (Roche Diagnostics) acting as a carrier. After spinning and washing in 75% cold ethanol (Chem-Supply), the precipitated mRNA was dissolved in RNase-free water and measured the concentration with a Nanodrop spectrophotometer (Therm Fisher). The mixtures of 1 μg of extracted mRNA, 0.1 ng of random primers (Geneworks), 10 nmol of dNTPs (Adelab Scientific), and nuclease free water (Invitrogen) with a final volume of 14 μL were incubated at 65 °C for 5 min and subsequently cooled at 4 °C for 1 min using a Veriti 96 well thermal cycler (Applied Biosystems). The mixtures were further mixed with 100 nmol of DTT (Thermo Fisher), 200 U of SuperScript^{TM} IV reverse transcriptase (Thermo Fisher), and 4 μL of 5x superscript IV reverse transcriptase buffer (Thermo Fisher). Reverse transcription was initiated at 55 °C for 60 min and 80 °C for another 10 min using a thermal cycler. Real-time polymerase chain reaction (PCR) was performed using a CFX Real-Time PCR Detection System (BIO-RAD) for a mixture of 2 μL diluted cDNA, 7.5 μL SYBR fluorescent probe (QIAGEN), 0.75 μL primer pairs (Table 1), and 4.75 μL RNase free water. The genes for all samples were performed in triplicate and the RNase free water was used as a control. All data were normalized to the value of the *ACTB* gene.

Table 5.1 The sequences of specific genes.

Primers	**Sequence (5'➔3')**
SOX9	Forward: AGGTGCTCAAAGGCTACGAC
	Reverse: GCTTCTCGCTCTCGTTCAGA
ACAN	Forward: CTGCTTCCGAGGCATTTC
	Reverse: GCTCGGTGGTGAACTCTAGC
COL 2A1	Forward: ATCACAGGCTTCCATTGACC
	Reverse: CTCCACAGCATCGATGTCAC
ACTB	Forward: GATCATTGCTCCTCCTGAGC
	Reverse: GTCATAGTCCGCCTAGAAGCAT

5.4.10 Fabrication of a neo-cartilage patch

The fabrication of a neo-cartilage patch is shown in Figure 5.1. Briefly, cells embedded inside the p(NIPAAm-AA) hydrogel were subjected to chondrogenic culture conditions as described above. Following 4 weeks of chondrogenic induction, the cells were harvested from the hydrogel by washing in 1× PBS and spinning at 383 rcf. The harvested cells from 16 wells of a 48-well plate were then transferred onto an overlaid electrospun film inside a stainless-steel ring that was pre-sterilized in ethanol and located in a well of a 24-well plate (inner diameter: 5 mm, outer diameter: 10 mm, height: 1 mm). A 3 g sterilized stainless-steel block was used to compress the cell-film hybrid from the top. 30 mg/mL p(NIPAAm-AA) hydrogel prepared by mixing 50 mg/mL p(NIPAAm-AA), 0.05 M $MgCl_2$ in 1× PBS, and inductive medium at a volumetric ratio of 3 : 1 : 1 was added into the well so that the whole stainless-steel mold was completely immersed in the liquid. The cells were further cultured in the inductive medium for an additional 2 weeks, and the p(NIPAAm-AA) hydrogel and the stainless-steel mold were subsequently removed and the cells were gently washed with 1× PBS twice. After cells were transferred onto the overlaid electrospun films, they were stained with 4 μM calcein AM and imaged using a CKX41 fluorescent microscope.

5.4.11 Histology and immunofluorescence staining

After inducing chondrogenesis at pre-determined periods, the cell-gel hybrids were diluted and washed in 1× PBS twice and centrifuged at 383 rcf for 5 min to separate cells from the hydrogel. The cells that had undergone chondrogenic induction and the fabricated neo-cartilage patch were, in turn, fixed in 4 % cold paraformaldehyde (Sigma-Aldrich) overnight, washed in 1× PBS twice, and embedded in the 30 % sucrose solution (Chem-Supply) overnight. In addition, the cells that had undergone chondrogenic induction together with the p(NIPAAm-AA) hydrogel were also directly frozen in liquid nitrogen without processing in paraformaldehyde and the sucrose solution. An OCT compound (Tissue-Tek) was used to embed the the cells and the fabricated neo-cartilage patch in a pre-labelled cryomold (Tissue-Tek). After keeping them

at room temperature for 10 min, the cryomolds were transferred to a dry ice box. The frozen cryomolds were rolled with aluminum foil and stored in a sealed bag at -80 °C. Before sectioning, the frozen cryomolds were warmed to -20 °C for 20 min. The frozen cells and the neo-cartilage patch were cut into sections at a thickness of 8 μm using a Cryostat Shandon Cryotome E (Thermo Fisher) and transferred onto the gelatin (Sigma-Aldrich)/chromium potassium sulfate dodecahydrate ($CrK(SO_4)_2 \bullet 12H_2O$, Sigma-Aldrich) coated glass slides (Livingstone). The samples were kept at room temperature for 1 h before storing in a sealed slide box at -80 °C. Before histologically or immunofluorescently staining, the frozen sections were dried in a fume hood at room temperature for 1 h.

5.4.11.1 Haematoxylin and Eosin (H&E)

The sections were, in turn, stained in Mayers haematoxylin (Sigma-Aldrich) for 10 min, washed in running tap water for 5 min, differentiated in 0.3 % acidic alcohol once, washed in running tap water once, washed in Scott's tap water once, stained in Eosin (Sigma-Aldrich) for 1 min, washed in tap water once, dehydrated and cleared in 90 % ethanol, 100 % ethanol, and xylene, respectively. After mounting in a CV mountant and covering with coverslips, the stained sections were imaged under a CKX41 microscope.

5.4.11.2 Alcian Blue

The sections were stained in 1% Alcian Blue solution (Sigma-Aldrich) for 30 min and counterstained with 0.1% nuclear fast red solution (Sigma-Aldrich) for 5 min. After staining, the sectioned slides were, in turn, rinsed with distilled water, 70% ethanol, 100% ethanol, and xylene. After drying in air, a CV mounting medium was added onto the stained sections and covered with coverslips. Finally, the stained tissues were imaged under a CKX41 microscope.

5.4.11.3 Masson's Trichrome

The sections were, in turn, stained in the Weigert's iron haematoxylin working solution (Sigma-Aldrich) for 10 min, washed in running warm tap water for 10 min, washed in distilled water once, stained in the Biebrich scarlet-acid fuchsin solution (Sigma-Aldrich) for 10 min, washed

in distilled water once, differentiated in the phosphomolybdic-phosphotungstic acid solution (Sigma-Aldrich) for 10 min, stained in an Aniline Blue solution (Sigma-Aldrich) for 10 min, washed in distilled water once, differentiated in 1 % acetic acid (Sigma-Aldrich) for 5 min, washed in distilled water once, dehydrated in 95 % ethanol and 100 % ethanol, and cleared in xylene. The stained sections were imaged under a CKX41 microscope after mounting in the CV mountant and covering with coverslips.

5.4.11.4 Collagen 2A1 immunofluorescence staining

The frozen tissue sections were, in turn, blocked with 5% normal goat serum solution (Thermo Fisher) for 1 h in a humidified box at room temperature, bound with a rabbit anti-collagen 2A1 primary antibody (Santa Cruz) at a dilution of 1 : 250 overnight in a humidified box at 4 °C, washed in 1× PBS three times, bound with fluorescein (FITC)-labeled goat-anti-rabbit secondary antibody (SouthernBiotech) at a dilution of 1 : 250 for 2 h in a shielded humidified box at room temperature. The sections were subsequently counterstained in 300 nM of the DAPI solution (Sigma-Aldrich) for 15 min and washed in 1× PBS three times (5 min each) at room temperature. After mounting in the ProLong Gold Antifade reagent (Invitrogen) and covering with coverslips, the stained sections were imaged under an IX53 fluorescent microscope (Olympus).

5.4.12 Statistical Analysis

All experiments were performed in triplicates and data were presented as mean ± standard error (SE). One-tailed student *t*-test was used to compare the difference of two mean values. $p < 0.05$ implied a significant difference between two mean values.

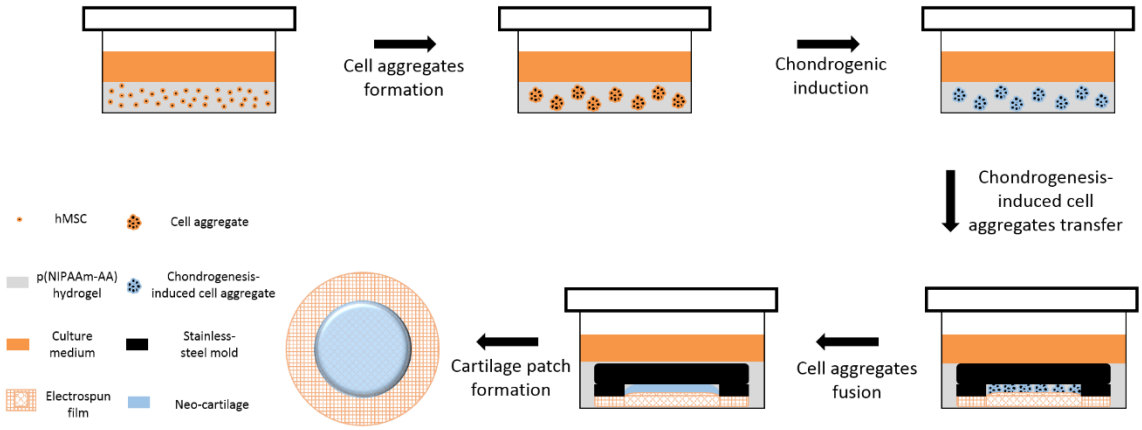

Figure 5.1 The procedure of in-vitro cartilage patch fabrication.

5.5 Results

5.5.1 Characterization of p(NIPAAm-AA) hydrogel

To confirm successful synthesis of p(NIPAAm-AA) hydrogel, Fourier-Transform Infrared Spectroscopy (FTIR) was used to determine the functional groups in the p(NIPAAm-AA). (Figure 5.2) It was shown that a peak of N-H was found at 3282.19 cm^{-1} in NIPAAm, at 3301.21 cm^{-1} in MBA and at 3292.69 cm^{-1} in p(NIPAAm-AA). The peak in p(NIPAAm-AA) was broader than that of NIPAAm and MBA due to merging of the peak of O-H in the O=C-OH group and N-H. (Figure 1) Moreover, the signal peak of O=C in the O=C-NH group was seen at 1621.25 cm^{-1} in NIPAAm, 1625.7 cm^{-1} in MBA, and 1628.31 cm^{-1} in p(NIPAAm-AA). The peak of O=C in p(NIPAAm-AA) was also merged with that of O=C in the O=C-OH group. The $CH(CH_3)_2$ group was identified in NIPAAm at 1452.77 cm^{-1} and in MBA at 1455.68 cm^{-1}. Double carbon bonds (C=C) were only seen in the FTIR spectra of NIPAAm at 960.29 cm^{-1} and MBA at 990.25 cm^{-1}, while they disappeared in p(NIPAAm-AA) due to polymerization.

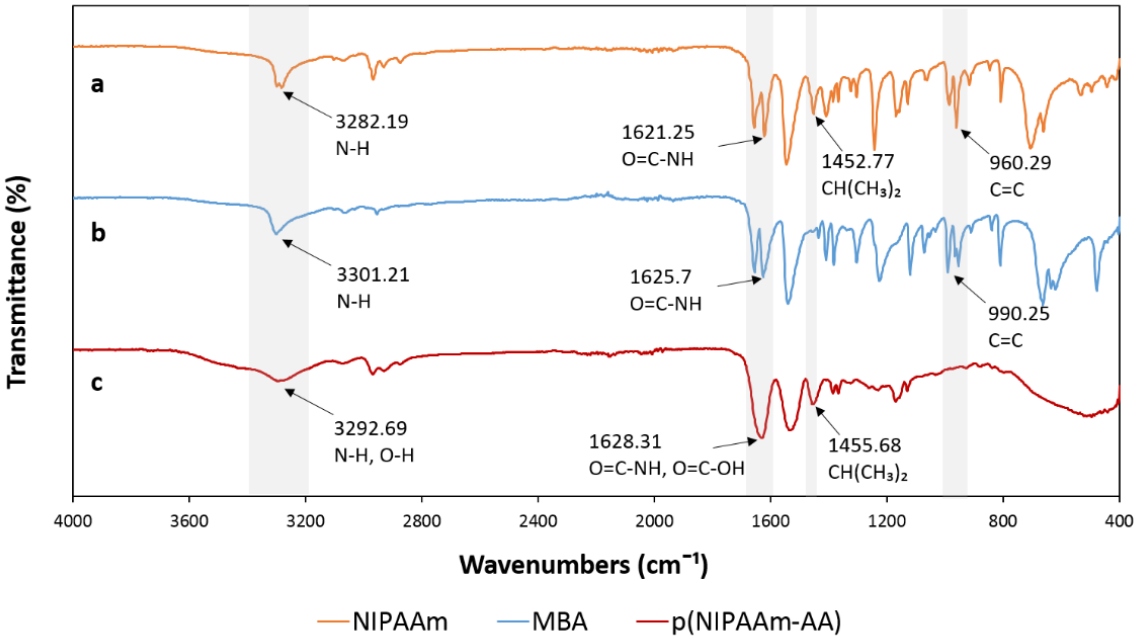

Figure 5.2 FTIR spectra of (a) *N*-isopropylacrylamide (NIPAAm), (b) *N*, *N*'-Methylenebisacrylamide (MBA), and (c) poly (*N*-isopropylacrylamide-co-acrylic acid) (p(NIPAAm-AA)).

5.5.2 Gelation and liquification of p(NIPAAm-AA) hydrogel

1× PBS with various concentrations of magnesium chloride was mixed with the p(NIPAAm-AA) hydrogel to facilitate gel formation. The p(NIPAAm-AA) solution mixed with 1× PBS at 37 °C for 30 min could not form a gel, (Figure 5.3 a) while p(NIPAAm-AA) hydrogels were successfully formed after incubation at 37 °C for 30 min at a concentration of $MgCl_2$ higher than 0.01 M. Liquefication of p(NIPAAm-AA) hydrogels was time- and Mg^{2+}- dependent at 25 °C. p(NIPAAm-AA) hydrogels with a Mg^{2+} concentration of 0.01 M and 0.025 M turned into liquid at 25 °C for 5 min, whereas all p(NIPAAm-AA) hydrogels at all Mg^{2+} concentrations were liquefied into a transparent solution at the same temperature for 30 min. To achieve rapid liquification of p(NIPAAm-AA) hydrogels at room temperature, Mg^{2+} may be controlled at a concentration lower than 0.05 M.

Moreover, the time-dependent gelation and liquefication profile of the p(NIPAAm-AA) hydrogel with 0.01 M Mg^{2+} were also established by measuring the transmittance of the hydrogel at 37 °C and 25 °C. It was shown that the transmittance of the hydrogel dramatically decreased when heating at 37 °C during the first 10 min and increased when cooling at 25 °C

between 30-40 min. The transmittance of the p(NIPAAm-AA) hydrogel remained stable after full gelation and liquification. (Figure 5.3 b)

Hydrogel syneresis was seen after incubation of p(NIPAAm) hydrogels at a concentration of 30 mg/mL in the presence of 0.01 M Mg^{2+} at 37 °C for 30 min, however, syneresis was not observed with p(NIPAAm-AA) hydrogels (Figure 5.3 c), which was in agreement with previous reports [22, 23].

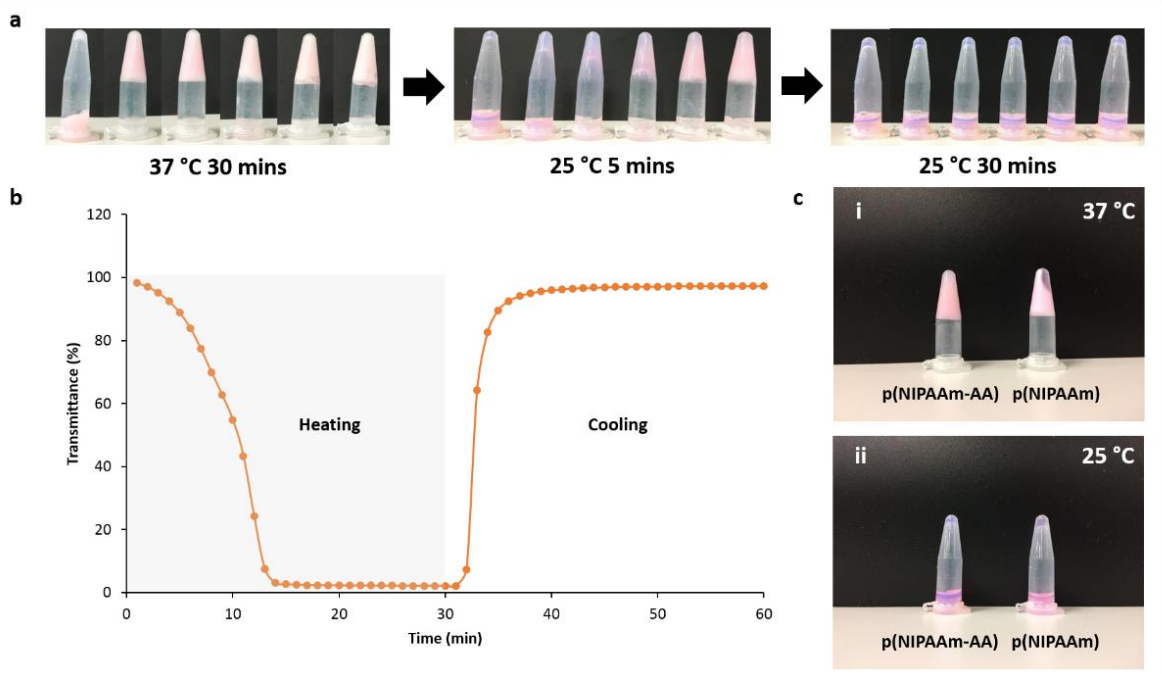

Figure 5.3 (a) Liquification of p(NIPAAm-AA) hydrogels prepared with different ionic strengths (left to right: 1× PBS, 0.01 M $MgCl_2$ in 1× PBS, 0.025 M $MgCl_2$ in 1× PBS, 0.05 M $MgCl_2$ in 1× PBS, 0.075 M $MgCl_2$ in 1× PBS, 0.1 M $MgCl_2$ in 1× PBS) at 25 °C. (b) Time-dependent gelation and liquification process of p(NIPAAm-AA) hydrogel prepared with 0.01 M $MgCl_2$ in 1× DPBS by measuring the transmittance at 37 °C from 0 to 30 min and 25 °C from 30 min to 60 min. (c) Macroscopy images of p(NIPAAm-AA) and p(NIPAAm) hydrogels revealing their thermosensitive behaviour. (i) Gelation of the hydrogels after heating at 37 °C for 30 min. Distinct syneresis was only seen in the p(NIPAAm) hydrogel; (ii) Liquification of the hydrogels after cooling at 25 °C for 30 min.

5.5.3 Cytotoxicity of p(NIPAAm-AA) hydrogels and $MgCl_2$

The viability of UE7T-13 cells cultured in different concentration of $MgCl_2$ for 24 h was measured by the MTT assay. The data presented in Figure 5.4a suggests that medium with 0.01 M $MgCl_2$ was not toxic to the UE7T-13 cells, while cells in the media with a concentration of $MgCl_2$ higher than 0.01 M had an extremely low cell viability, implying Mg^{2+} was detrimental to UE7T-13 cell viability at a concentration higher than 0.01 M. When cells were cultured

inside the p(NIPAAm-AA) hydrogel at a $MgCl_2$ concentration of 0.01 M on day 1 and day 9, the majority of cells displayed a green color, indicating excellent cell viability and the biocompatibility of the p(NIPAAm-AA) hydrogel at a $MgCl_2$ concentration of 0.01 M. (Figure 5.4 b) Interestingly, individual cells had a round shape on day 1, whilst cellular aggregates were presented in the p(NIPAAm-AA) hydrogel on day 9.

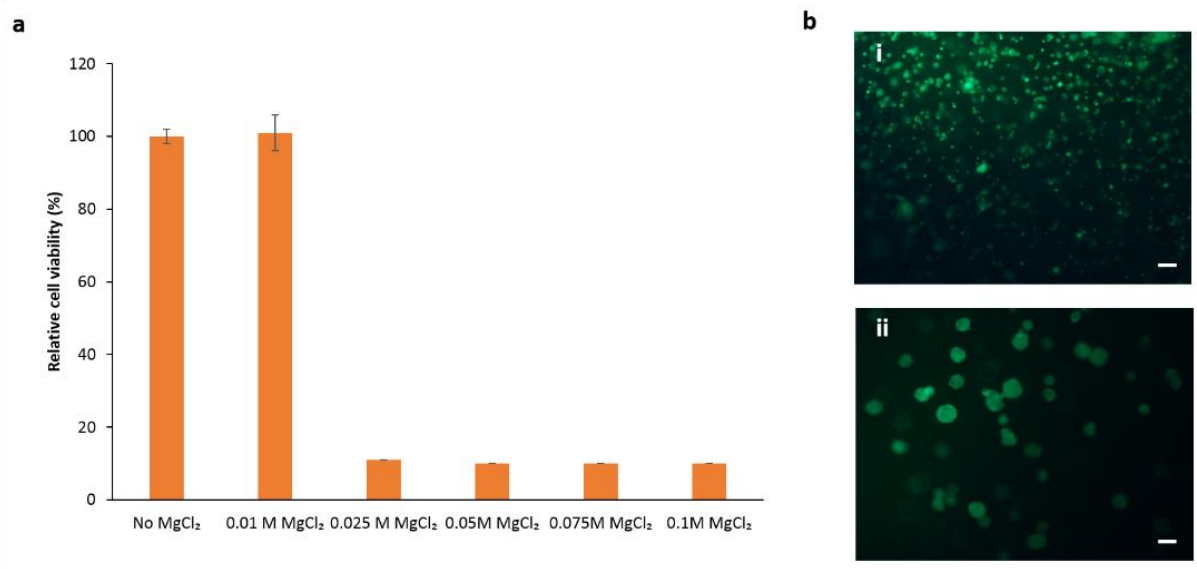

Figure 5.4 (a) UE7T-13 cell viability assay after 24 h by MTT; (b) Live and dead staining of UE7T-13 cells cultured in the p(NIPAAm-AA) hydrogel on (i) day 1 and (ii) day 9. Green: live cells; Red: dead cells. Scale bar: 100 µm.

5.5.4 Cell migration inside p(NIPAM-AA) hydrogel

The cell-gel hybrids were incubated on top of a porous transwell membrane in three different culture media supplemented with 10% FCS in the upper chamber and 10% FCS in the microwell below the membrane as a control; (Figure 5.5a control) 10% FCS only in the microwell below the membrane; (Figure 5.5a down-migration) and 10% FCS only in the upper chamber above the membrane. (Figure 5.5a up-migration) A chemoattractant (FCS) gradient was developed in the vertical direction owing to the concentration difference of FCS for both down-migration and up-migration. When the chemoattractant concentration decreased from the chamber below the membrane to the chamber above the membrane, cells migrated inside the p(NIPAM-AA) hydrogel to the membrane of the upper chamber, resulting in approximately 2-fold increase in cell number on the cell membrane, compared to the control. (Figure 5.5 b)

However, a greater than 50% decrease in the cell number attached onto the membrane of the upper chamber when the chemoattractant gradient decreased from the chamber above the membrane to the microwell below the membrane. There was no significant difference at two initial concentrations of the chemoattractant (20% vs 10%). The decrease in the cell number due to cell migration through the p(NIPAAm-AA) hydrogel was also evidenced from the fluorescent DAPI staining images of the porous membrane of the upper chamber. (Figure 5.5 c)

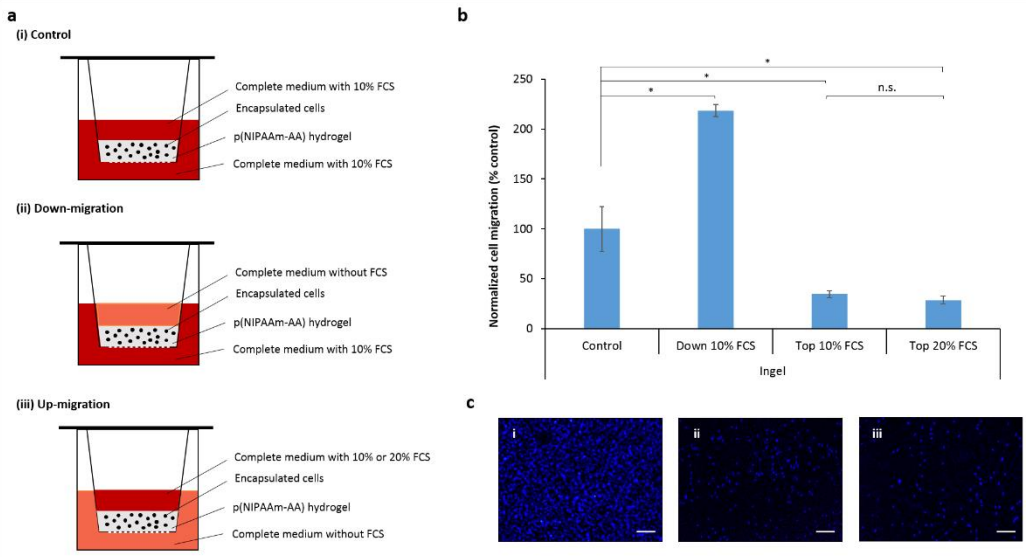

Figure 5.5 (a) Schematic of UE7T-13 single cell migration assay in the poly (*N*-isopropylacrylamide-acrylic acid) hydrogel for 18 h. (b) Migration of UE7T-13 cells, which were normalized to that of control. Control: cells were kept in the complete medium with 10% FCS at all time. Down-10% FCS, Top-10% FCS, and Top-20% FCS: the cells pre-starved in the medium without FCS overnight were further cultured inside p(NIPAAm-AA) hydrogel in the upper chamber and fed with either 10% of FCS as the chemoattractant in the lower chamber, or 10% of FCS as the chemoattractant in the upper chamber, or 20% of FCS as the chemoattractant in the upper chamber for 18 h. After 18 h, the upper chambers were gently washed with 1x DPBS twice and stained with DAPI for 10 minutes. 5 images were randomly captured per insert and measured with image J, $n = 3$ inserts per group, $^{**}p < 0.001$. (c) Fluorescent images of migrated UE7T-13 cells on the bottom of the inserts for (i) Down-10% FCS, (ii) Top-10% FCS, and (iii) Top-20% FCS by DAPI staining. Blue: cell nuclei. Scale bar: 100 µm.

The cell-hydrogel hybrids were also imaged by SEM. Single individual cells were found to locate inside the p(NIPAAm-AA) hydrogel without a chemoattractant gradient on day 1. The SEM images also revealed a porous structure of the freeze-dried p(NIPAAm-AA) hydrogel. (Figure 5.6 a) When a chemoattractant gradient was applied, a migrated cell aggregate was

shown at the bottom of the hydrogel which may migrate through the p(NIPAAm-AA) hydrogel. (Figure 5.6 b)

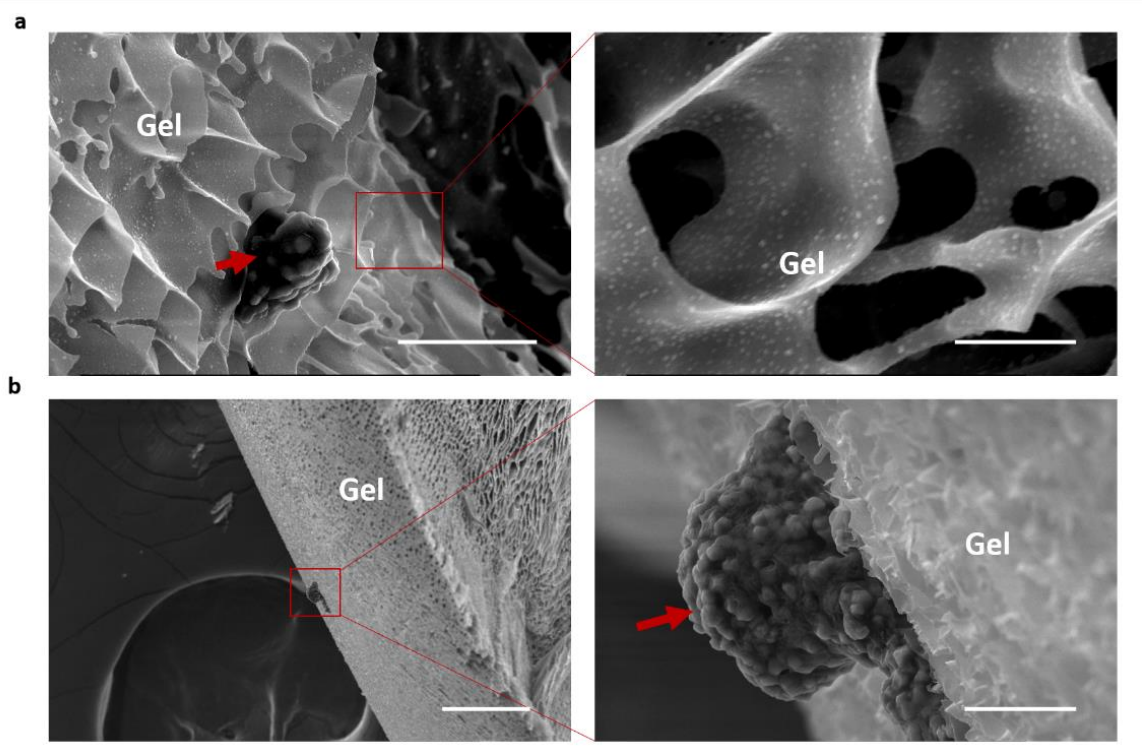

Figure 5.6 (a) SEM images of UE7T-13 cell cultured in the p(NIPAAm-AA) hydrogel on day 1 at lower magnification (scale bar: 10 µm) and higher magnification (scale bar: 2 µm); (b) SEM images of UE7T-13 the cell aggregate migrating through p(NIPAAm-AA) hydrogel to the bottom after 18 h with 10% FCS of bottom chemoattractant at lower magnification (scale bar: 100 µm) and higher magnification (scale bar: 10 µm). The arrow pointed to the cells.

UE7T-13 cells cultured inside the p(NIPAAm-AA) hydrogel behaved differently from those cultured as cell pellets in the polypropylene tubes. (Figure S5.1) When cells were embedded in the p(NIPAAm-AA) hydrogel, individual cells were initially well distributed in the hydrogel, which was evident from the images obtained from a CKX41 optical microscope. (Figure 5.7 a) Once cell aggregates were formed after 9 days, collagen, one of the major ECM proteins, was produced around the cell aggregates as shown by the Masson's Trichrome Blue staining. (Figure 5.7 b) After culture in inductive media for 8 weeks, the cell aggregates displayed an atypical structure with rich collagen depositing around the cell aggregates and connection between cell aggregates was established via rich collagen fibrils. (Figure 5.7 c) The p(NIPAAm-AA) hydrogel in the inductive medium contracted into a smaller size and large cell pellets were seen on the surface of the hydrogel after induction for 4 weeks. (Figure S5.2 c) At

the late-stage of chondrogenic induction, the p(NIPAAm-AA) hydrogel was further contracted and cells were found on the surface of the p(NIPAAm-AA) hydrogel with an adherent morphology surrounded with distinct blue-stained collagen. (Figure 5.7 d) Moreover, cell pellets with a larger size were also seen on the contracted hydrogel. In contrast, large cell pellets in the polypropylene tubes were generated after centrifugation on day 1. Cells were found to gradually detach from cell pellets from day 1 to week 4. As chondrogenic induction progressed, there were more cell aggregates with a small size in the polypropylene tubes. (Figure S5.2 a and b) Moreover, these cell aggregates were found to migrate upwards along the tube wall and merge with the large cell pellet into a single cell pellet after induction at week 8.

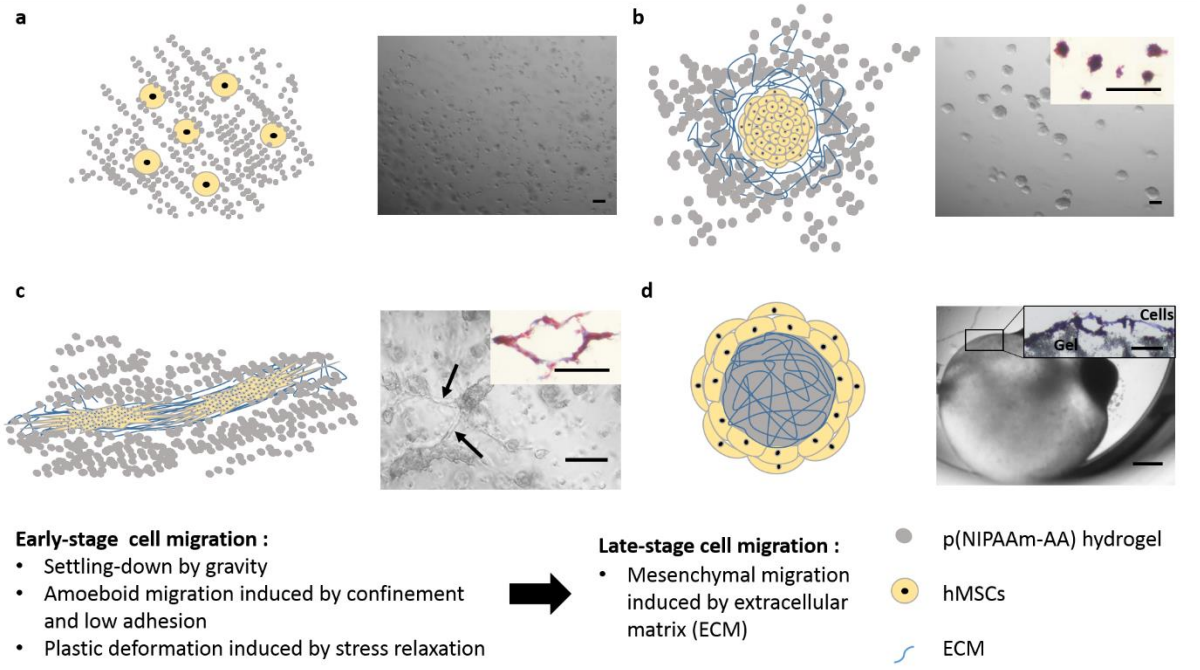

Figure 5.7 Mechanisms of human mesenchymal stem/stromal cells (hMSCs) migration within p(NIPAAm-AA) hydrogels. (a) The scheme (left) and optical microscopy image (right) of individual cells cultured within p(NIPAAm-AA) hydrogels on the day 1. Scale bar: 100 µm. (b) The scheme (left), optical microscopy image (right), and Masson's trichrome staining image (right-inset) of the cell aggregates within p(NIPAAm-AA) hydrogels on the day 9. Scale bar: 100 µm. (c) The scheme (left), optical image (right), and Masson's trichrome staining image (right-inset) of cell aggregate migration within p(NIPAAm-AA) hydrogels after inducing chondrogenesis for 8 weeks in chondrogenic media from the day 9 (Arrows point to the connection sites between the cell aggregates). Scale bar: 100 µm. (d)The scheme (left), optical image (right, scale bar: 1 mm), and Masson's trichrome staining image (right-inset, scale bar: 100 µm) of cell migration and spreading out of the ECM-rich contracted p(NIPAAm-AA) hydrogels after inducing chondrogenesis for 8 weeks in chondrogenic media from day 9. Dark red: cell nuclei; Pink: cell cytoplasm; Blue: collagen.

5.5.5 Chondrogenesis

After inducing chondrogenesis for 4, 6 and 8 weeks, the expression of chondrogenesis-related genes (*SOX9*, *ACAN*, and *COL 2A1*) in the cells cultured in polypropylene tubes and p(NIPAAm-AA) hydrogels was assessed. The mRNA expression of *SOX9*, *ACAN*, and *COL 2A1* in cells cultured inside p(NIPAAm-AA) hydrogels were significantly higher than that in cells cultured as cell pellets in the polypropylene (PP) tubes at week 4. (Figure 5.8 a) After 6 weeks, a significant difference was still seen for the mRNA expression of *SOX9* and *COL 2A1*, but no difference for *ACAN*. (Figure 5.8 b) After inducing chondrogenesis for 8 weeks, the mRNA expression of *ACAN* in cells cultured inside p(NIPAAm-AA) hydrogels was higher than that in cells cultured as cell pellets in polypropylene tubes, while no significant difference was seen in the mRNA expression of *SOX9* and *COL 2A1*. (Figure 5.8 c)

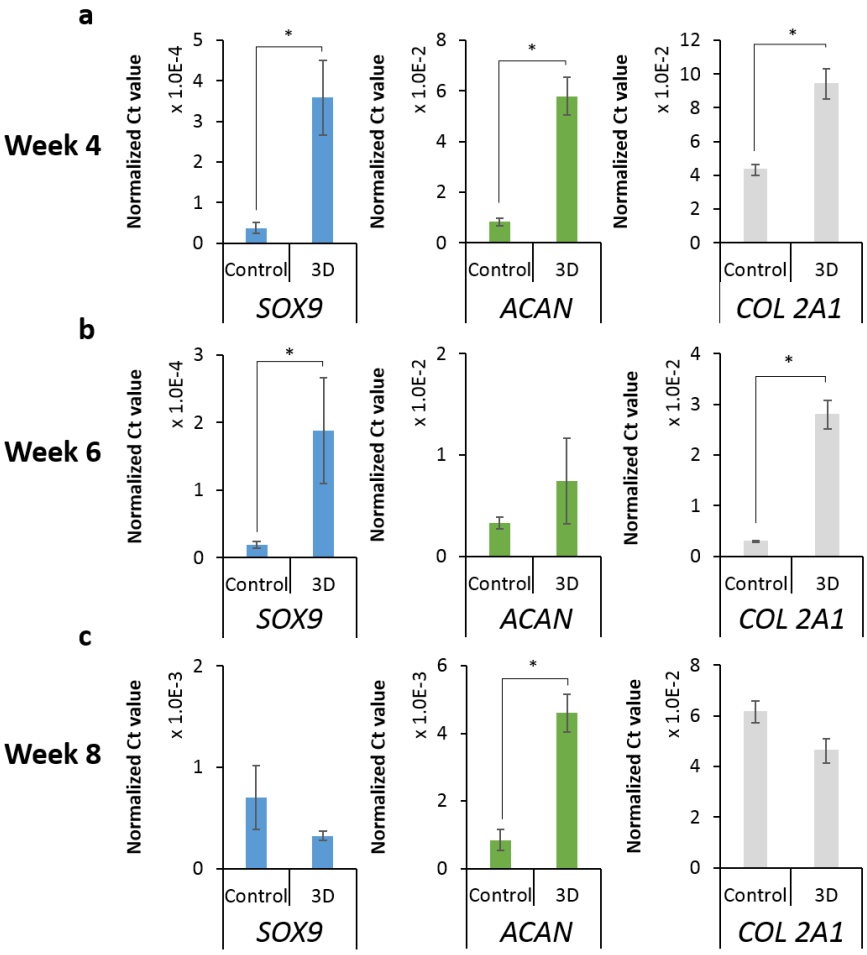

Figure 5.8 mRNA expression of chondrogenic genes (*SOX9*, *ACAN*, and *COL 2A1*) in UE7T-13 cells induced with chondrogenic inductive media for (a) 4 weeks, (b) 6 weeks, and (c) 8 weeks. Control: UE7T-13 cells spun into pellets and cultured in the polypropylene tubes; 3D: UE7T-13 cells incorporated in p(NIPAAm-AA) hydrogels. All data were normalized to that of *ACTB* and presented as the mean ± standard error ($n = 3$). *$p < 0.05$.

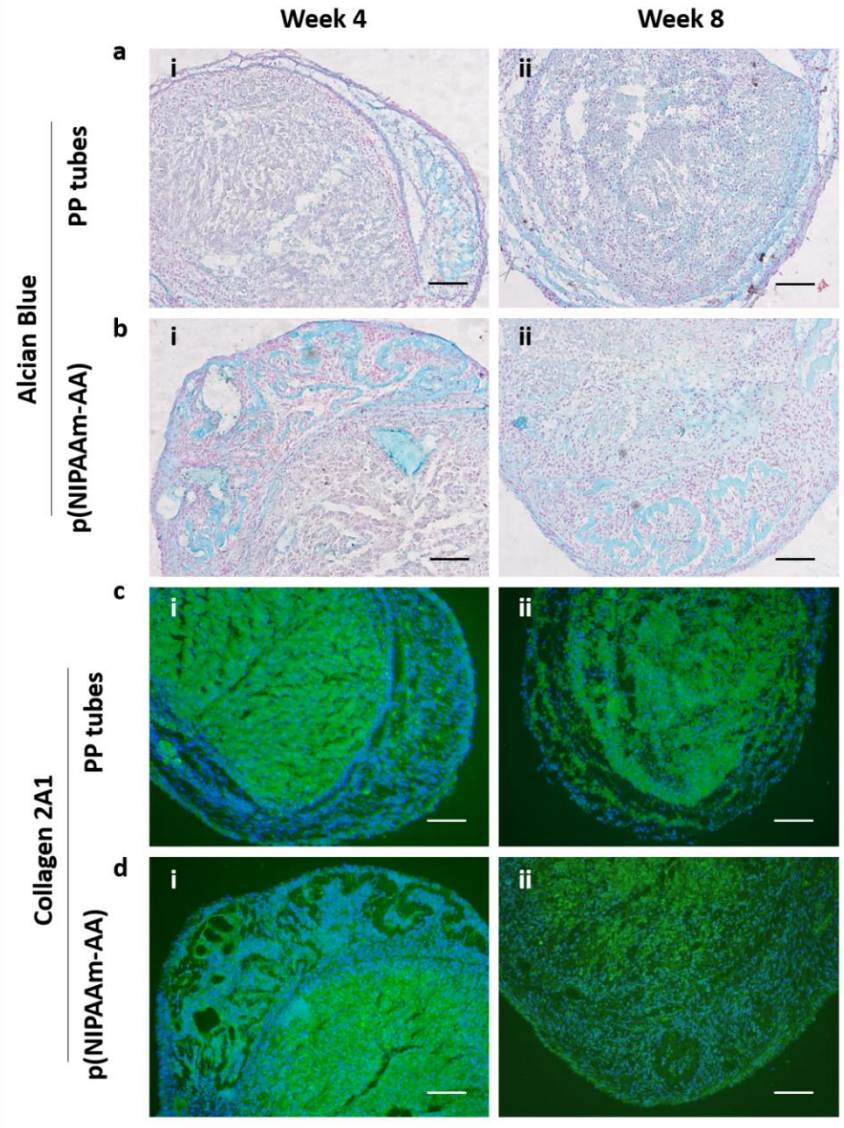

Figure 5.9 Alcian Blue staining images (Red: cell nuclei; Blue: sulfated GAGs) and immunofluorescent staining images (Blue: DAPI-labelled cell nuclei; Green: FITC-labelled collagen 2A1) of UE7T-13 cultured (a,c) as cell pellets in polypropylene (PP) tubes or (b,d) within p(NIPAAm-AA) hydrogels for (i) 4 weeks or (ii) 8 weeks. Scale bar: 100 µm.

Furthermore, histological and immunofluorescent staining also revealed deposition of sulfated glycosaminoglycans (GAGs) and collagen 2A1 within the neo-cartilage formed in polypropylene tubes and p(NIPAAm-AA) hydrogels. (Figure 5.9) The deposited sulfated GAGs were mainly distributed at the peripheral area of the neo-cartilages at week 4. However, sulfated GAGs produced in the neo-cartilage formed in the p(NIPAAm-AA) hydrogels were more distinct than those formed in the polypropylene tubes. In addition, it was seen that the cell pellets formed in the polypropylene tubes had a porous structure at week 4 and 8, however, the porous cell pellets formed in the p(NIPAAm-AA) hydrogels at week 4 possessed a more

compact structure and the internal spaces between cells were filled with sulfated GAGs at week 8. In contrast, collagen 2A1 was mainly distributed in the central area of the neo-cartilages in both systems at week 4. A similar distribution of collagen 2A1was still seen in the neo-cartilages in the polypropylene tubes after week 8, while the collagen 2A1 in the neo-cartilages embedded in the p(NIPAAm-AA) hydrogels was more uniformly distributed, which was in accordance with the distribution of sulfated GAGs.

5.5.6 Characterization of electrospun films

The morphology of the electrospun films characterized by SEM revealed no beads on each nanofiber. (Figure S5.3 a) Over 80% of inter-fiber pores were less than 5 μm^2, and fibers had an average diameter of 500 nm with a uniform size distribution. (Figure S5.3 b and c) The cytotoxicity of the electrospun films was measured by the MTT assay. After seeding on the electrospun films for 24 h, cells had a high cell viability, almost identical to the viability seen with cells on a conventional tissue culture plate. (Figure S5.3 d)

5.5.7 Fabrication of a neo-cartilage patch

After transferring chondrogenesis-induced cell aggregates onto the electrospun film, cells displayed an adherent fibroblast-like morphology. (Figure S5.4) Moreover, the cells were merged into a neo-cartilage with a size of 5 mm in diameter and 1 mm in height by the spatial confinement of the stainless-steel mold and block. (Figure 5.10 a) Furthermore, the histological staining revealed that the neo-cartilage was attached to the electrospun film. (Figure 5.10 b) Sulfated GAGs and collagen 2A1 within the neo-cartilage were stained with a blue color by the Alcian Blue staining and a green color by immunofluorescent staining, respectively. (Figure 5.10 c and d)

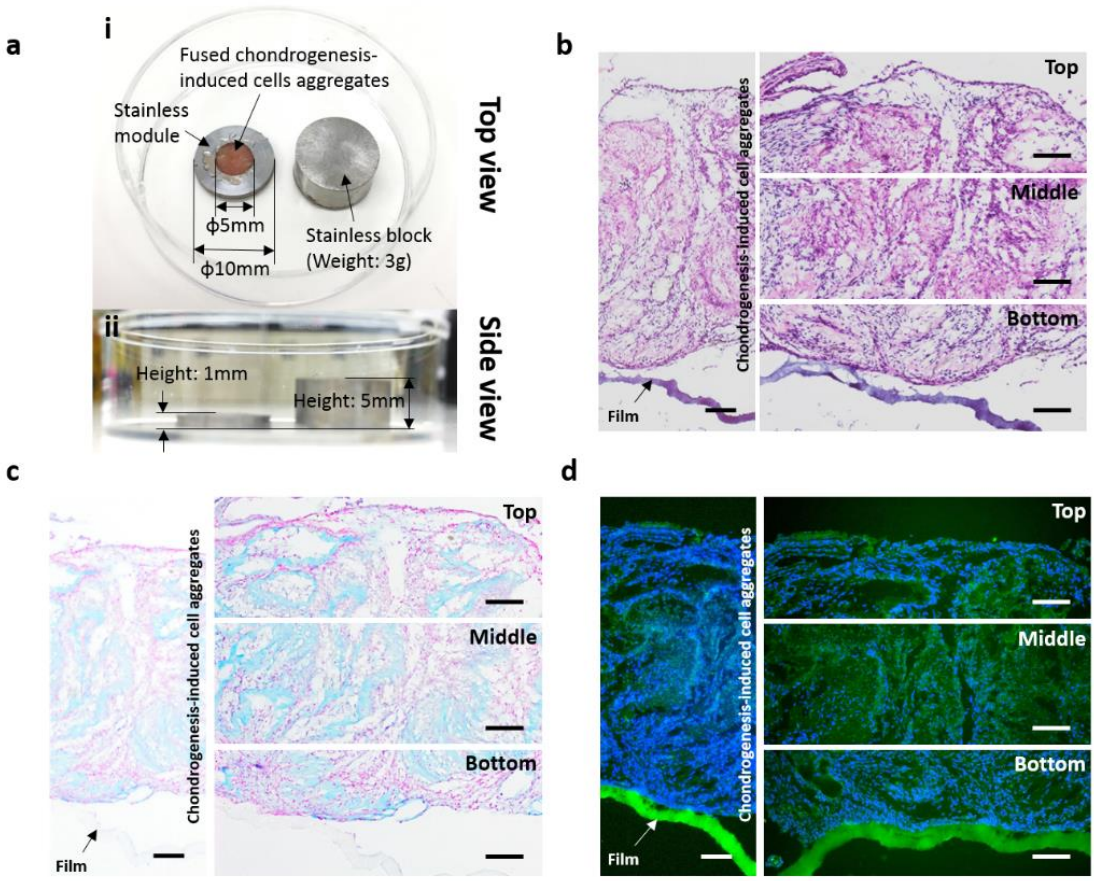

Figure 5.10 (a) Fusion of chondrogenesis-induced cell aggregates in a stainless module with a stainless block forcing on the top during cell culturing. Diameter and height of the generated cartilage are 5 mm and 1 mm, respectively. (b) Hematoxylin & Eosin staining images of the *in-vitro* fabricated cartilage patch at low magnification (left) and high magnification (right) (Blue: cell nuclei; Pink: cell cytoplasm). (c) Alcian Blue staining images of the in-vitro fabricated cartilage patch at low magnification (left) and high magnification (right) (Red: cell nuclei; Blue: sulfated GAGs). (d) Immunofluorescent staining images of the *in-vitro* fabricated cartilage patch at low magnification (left) and high magnification (right) (Green: FITC-labelled collagen 2A1; Blue: DAPI-labelled cell nuclei). Scale bar: 100 μm.

5.6 Discussion

To eliminate the syneresis of p(NIPAAm) at 37 °C, acrylic acid was copolymerized into p(NIPAAm) to increase its hydrophilicity, which was confirmed from the FTIR spectra of p(NIPAAm-AA) with a new peak of O=C-OH, rather than a peak of the C=C group in p(NIPAAm). (Figure 5.2) Due to the introduction of a hydrophilic moiety, p(NIPAAm-AA) did not form a gel without ionic crosslinking at 37 °C. In this study, magnesium cations were employed to facilitate crosslinking of the p(NIPAAm-AA) hydrogel for gelation. As the concentration of Mg^{2+} increased, the gel formed at 37°C became more stable, leading to a longer liquefication time. (Figure 5.3 a) However, a higher concentration of Mg^{2+} may affect the cell

membrane potential and interfere with the normal function of ion channels across the cell membrane. [24] From the cell viability assay, it was shown that Mg^{2+} at a low concentration (0.01 M) was non-toxic to cells, while Mg^{2+} at a concentration higher than 0.025 M was very detrimental to cell viability. (Figure 5.4) When cells were embedded within the p(NIPAAm-AA) hydrogel in the presence of 0.01 M Mg^{2+}, a high cell viability was obtained from the live-dead staining images, indicating excellent biocompatibility of p(NIPAAm-AA) at a minimal gelation concentration of 30 mg/mL. (Figure 5.4 b) Cell aggregates were present within the p(NIPAAm-AA) hydrogel on day 9, (Figure 5.4 b) while the mechanism of forming cell aggregates was unclear. We hypothesized that cell migration, inside the hydrogels, might contribute to formation of cellular aggregates. Mg^{2+}/COO^{-}-induced ionic crosslinking and hydrophobic interaction resulted in cavities with various sizes within the p(NIPAAm-AA) hydrogel. [25] (Figure 5.6) When individual cells were embedded inside the p(NIPAAm-AA) hydrogel at 37 °C, due to the absence of cellular binding sites in the p(NIPAAm-AA) polymeric structure, these cells initially homogeneously distributed inside the hydrogel. These cells may then migrate through the soft gel structure by their intrinsic gravity and cell-cell interactions leading to the formation of cell aggregates. This may provide an explanation for the observation that cells were attached on the membrane of the microwell insert even without a chemoattractant gradient. (Figure 5.5 b) When a 10 % of FCS gradient was applied from the well below the membrane to the chamber above the membrane, the embedded cells moved downwards through inter-fiber pores due to their intrinsic gravity and a chemoattractant gradient. Amoeboid-like migration of cells might be induced due to spatial confinement and the weak interaction forces between cells and supporting hydrogels. [26] Hence, adherent cells on the membrane of the upper chamber were significantly increased compared to the control without a chemoattractant gradient (Figure 5.5 b) and a cell aggregate was seen to migrate through the p(NIPAAm-AA) hydrogel network to the bottom. (Figure 5.6 b) When the chemoattractant gradient was generated by decreasing 10 % FCS from the chamber above the

membrane to the well below the membrane, upward amoeboid-like migration of the embedded cells might be realized through the polymeric network. Cell migration was not affected by the initial concentration of the chemoattractant, which might be due to the saturation of the FCS receptors on the cell membrane. [27, 28] A small number of adherent cells were still seen on the membrane even in the presence of a upward chemoattractant gradient, because these cells might retain in the bottom of the p(NIPAAm-AA) hydrogel, where the confinement for single cells was not sufficient to initiate amoeboid-like migration and overcome the cell gravity. (Figure 5.5 c) The embedded cells might also be able to temporarily liquefy the surrounding p(NIPAAm-AA) hydrogel by chemoattractant-induced stiffening on the cell membrane and disrupting the ionic crosslinking to induce stress relaxation of the hydrogel [29] because of the weak mechanical structure of the p(NIPAAm-AA) hydrogel [21].

It was widely reported that cell aggregates were capable of enhancing secretion of endogenous growth factors and deposition of extracellular matrix (ECM) proteins [6], both of which might promote chondrogenesis in the context of chondrogenic inducton. A higher expression of chondrogenesis-related genes (*SOX9*, *ACAN*, and *COL 2A1*) (Figure 5.8) and greater production of sulfated GAGs and collagen 2A1 (Figure 5.9 i), two major ECM components in cartilage [30], were found in the cells cultured inside the p(NIPAAm-AA) hydrogel at week 4 compared to cells cultured as cell pellets. The difference in cellular behavior in two culture systems might be due to developmental properties of cell aggregates. Because the p(NIPAAm-AA) hydrogel facilitated the formation of small cell aggregates at the early-stage, the surface-to-volume ratio of the cells cultured inside the p(NIPAAm-AA) hydrogel was substantially larger than that of cells cultured as cell pellets, resulting in more efficient transportation of both endogenous growth factors and exogenous inductive components present in the media for small cell aggregates compared to the large cell pellets. [31] The production of ECM proteins (Figure 5.7 b) was further enhanced around these small cell aggregates after incubating these aggregates in the chondrogenic medium. The accumulated ECM could interact with the p(NIPAAm-AA)

hydrogel to build "bridges" within the p(NIPAAm-AA) hydrogel for the embedded cell aggregates. (Figure 5.7 c) Cell aggregates could, therefore, migrate inside the p(NIPAAm-AA) hydrogel by binding to the deposited ECM proteins [32], which led to the contraction of the p(NIPAAm-AA) hydrogel and establishment of contacting communication between cell aggregates. In contrast, it was found that even though cells were forced into large cell pellets by centrifugation, some cells gradually detached from the cell pellets, leading to a decrease in the size of cell pellets when culturing in the complete culture medium without inductive biomolecules. (Figure S5.1) Those detached cells would reform cell aggregates within the polypropylene tubes and merge into a larger cell aggregate when cells were incubated in the inductive medium, which was quite similar to the development of cell aggregates inside the p(NIPAAm-AA) hydrogel. (Figure S5.1) Meanwhile, cell migration was also observed for cells cultured in polypropylene tubes due to the enhanced deposition of ECM by the cell aggregates on the tube wall. The mobility of small cell aggregates was better than that of large cell pellets, resulting in a longer migrated distance (Figure S5.2 a), which was more distinct for cells cultured in the chondrogenic induction medium in the polypropylene tubes. (Figure S5.2 b) However, the fusion of cell aggregates in the polypropylene tubes was not as efficient as that in the p(NIPAAm-AA) hydrogels since endogenous growth factors secreted from cell aggregates would rapidly diffuse into the medium, but could not form a gradient to initiate migration of cell aggregates. In contrast, due to the obstacle of the p(NIPAAm-AA) polymeric network, endogenous growth factors could be transiently retained around the cell aggregate, generating a chemoattractant gradient to initiate the migration of cell aggregates and fusion of cell aggregates. [27] Therefore, a relatively large neo-cartilage was formed within the p(NIPAAm-AA) hydrogel. (Figure 5.7 d and Figure S5.2 c) Although no significant difference was found in the mRNA expression of chondrogenesis-related genes *ACAN* (at week 6), *SOX9* and *COL 2A1* (week 8) (Figure 5.8 b and c) and the deposition of sulfated GAGs and collagen 2A1 at week 8 (Figure 5.9 ii) for cells cultured in the polypropylene tubes and the p(NIPAAm-

AA) hydrogel, more efficient transportation of biomolecules within small cell aggregates and the developmental difference of cell aggregates reinforced the p(NIPAAm-AA) hydrogel as a better platform for short-term chondrogenesis of mesenchymal stem/stromal cells.

Because of reversibility of the p(NIPAAm-AA) hydrogel (Figure 5.3), these chondrogenesis-induced cell aggregates were harvested from the hydrogel by simply diluting the hydrogels at room temperature and transferred onto the electrospun films (Figure S5.4). The mechanical loading of a stainless-steel block could, on the one hand, induce a compressive stress on the cell aggregates to enhance the chondrogenesis of cell aggregates [33] and accelerate the attachment of cell aggregates onto the electrospun film [34]. On the other hand, the stainless-steel block together with the stainless-steel ring also created a spatial confinement for the cell aggregates, which forced cell fusion into an integrated neo-cartilage. A neo-cartilage patch with a diameter of 5 mm and a height of 1 mm was successfully fabricated. (Figure 5.10) The neo-cartilage patch could be potentially used for treatment of an irregular degenerated cartilage by simply attaching it to the defect sites and initiating cartilage integration when bearing a compressive stress.

5.7 Conclusion

In this study, we synthesized a thermosensitive p(NIPAAm-AA) hydrogel that was capable of reversible gelation based on the external temperature and the absence of syneresis. With the assistance of magnesium ions at a biocompatible concentration, human mesenchymal stem/stromal cells were embedded in the p(NIPAAm-AA) hydrogels. Cells could form cell aggregates within the p(NIPAAm-AA) hydrogel at the early-stage by cell migration, initiated by the intrinsic cell gravity, confinement- and low adhesion- induced amoeboid-like migration, and the stress relaxation of the p(NIPAAm-AA) hydrogel. After inducing in the chondrogenic medium, the embedded cells could further migrate close to each other to form contacting connection by accumulatively produced extracellular matrices and the local gradient of endogenous growth factors, and thus develop into larger aggregates. Efficient transportation of

inductive biomolecules for smaller cell aggregates and gradual development into large aggregates led to significantly higher mRNA expression of chondrogenesis-related genes and more distinct production of sulfated GAGs and collagen 2A1 in the cells cultured in the p(NIPAAm-AA) hydrogel than those cultured as cell pellets in the polypropylene tubes. The chondrogenesis-induced cell aggregates were harvested from the p(NIPAAm-AA) hydrogel, transferred onto the electrospun film by a compressive stress, and fused together by spatial confinement. An integrated neo-cartilage patch was fabricated, which might be potentially used for the treatment of irregular degenerated cartilage by simply attaching to the defect sites and initiating cartilage integration when bearing a compressive stress.

ACKNOWLEDGEMENT

HZ would like to acknowledge the financial support from ARC Discovery Project (DP160104632) and The Medical Advancement Without Animal (MAWA) Trust. JBZ thanks the IPE-UoA Scholarship (BES).

DISCLOSURE

The authors report no declaration of interest.

SUPPLEMENTARY INFORMATION

For further details of (1) Developmental difference of multicellular structure in the p(NIPAAm-AA) hydrogel and polypropylene tubes (Figure S5.1); (2) Optical images of cells cultured in the p(NIPAAm-AA) hydrogel and polypropylene tubes for 4 weeks with/without chondrogenic inductive medium (Figure S5.2); (3) Characterization of electrospun scaffolds (Figure S5.3); (4) A fluorescent image of chondrogenesis-induced cell aggregates on an electrospun film (Figure S5.4), please refer to the “Supplementary information”.

5.8 Reference

[1] Camarero-Espinosa S, Rothen-Rutishauser B, Foster EJ, Weder C. Articular cartilage: from formation to tissue engineering. Biomaterials Science 2016;4:734-67.

[2] Rai V, Dilisio MF, Dietz NE, Agrawal DK. Recent strategies in cartilage repair: A systemic review of the scaffold development and tissue engineering. Journal of Biomedical Materials Research Part A 2017;105:2343-54.

[3] Sivashanmugam A, Arun Kumar R, Vishnu Priya M, Nair SV, Jayakumar R. An overview of injectable polymeric hydrogels for tissue engineering. European Polymer Journal 2015;72:543-65.

[4] Radhakrishnan J, Subramanian A, Krishnan UM, Sethuraman S. Injectable and 3D Bioprinted Polysaccharide Hydrogels: From Cartilage to Osteochondral Tissue Engineering. Biomacromolecules 2017;18:1-26.

[5] Richardson SM, Hoyland JA, Mobasheri R, Csaki C, Shakibaei M, Mobasheri A. Mesenchymal stem cells in regenerative medicine: Opportunities and challenges for articular cartilage and intervertebral disc tissue engineering. Journal of Cellular Physiology 2010;222:23-32.

[6] Sébastien S, Ang-Chen T, Yan L, Teng M. Three-Dimensional Aggregates of Mesenchymal Stem Cells: Cellular Mechanisms, Biological Properties, and Applications. Tissue Engineering Part B: Reviews 2014;20:365-80.

[7] Lee YB, Kim EM, Byun H, Chang H-k, Jeong K, Aman ZM, et al. Engineering spheroids potentiating cell-cell and cell-ECM interactions by self-assembly of stem cell microlayer. Biomaterials 2018;165:105-20.

[8] Hildebrandt C, Buth H, Thielecke H. A scaffold-free in vitro model for osteogenesis of human mesenchymal stem cells. Tissue Cell 2011;43:91-100.

[9] Cheng NC, Wang S, Young TH. The influence of spheroid formation of human adipose-derived stem cells on chitosan films on stemness and differentiation capabilities. Biomaterials 2012;33:1748-58.

[10] Kim J, Ma T. Endogenous Extracellular Matrices Enhance Human Mesenchymal Stem Cell Aggregate Formation and Survival. Biotechnology Progress 2013;29:441-51.

[11] Souza GR, Molina JR, Raphael RM, Ozawa MG, Stark DJ, Levin CS, et al. Three-dimensional Tissue Culture Based on Magnetic Cell Levitation. Nature nanotechnology 2010;5:291-6.

[12] Ahadian S, Yamada S, Ramon-Azcon J, Ino K, Shiku H, Khademhosseini A, et al. Rapid and high-throughput formation of 3D embryoid bodies in hydrogels using the dielectrophoresis technique. Lab on a Chip 2014;14:3690-4.

[13] Yang L, Xulin J, Ling L, Zhi-Nan C, Ge G, Rui Y, et al. 3D printing human induced pluripotent stem cells with novel hydroxypropyl chitin bioink: scalable expansion and uniform aggregation. Biofabrication 2018;10:044101.

[14] Wang Y-L, Lin S-P, Nelli SR, Zhan F-K, Cheng H, Lai T-S, et al. Self-Assembled Peptide-Based Hydrogels as Scaffolds for Proliferation and Multi-Differentiation of Mesenchymal Stem Cells. Macromolecular Bioscience 2017;17:1600192.

[15] Maia FR, Lourenço AH, Granja PL, Gonçalves RM, Barrias CC. Effect of Cell Density on Mesenchymal Stem Cells Aggregation in RGD-Alginate 3D Matrices under Osteoinductive Conditions. Macromolecular Bioscience 2014;14:759-71.

[16] Mellati A, Kiamahalleh MV, Madani SH, Dai S, Bi J, Jin B, et al. Poly(N-isopropylacrylamide) hydrogel/chitosan scaffold hybrid for three-dimensional stem cell culture and cartilage tissue engineering. Journal of Biomedical Materials Research Part A 2016;104:2764-74.

[17] Mellati A, Dai S, Bi J, Jin B, Zhang H. A biodegradable thermosensitive hydrogel with tuneable properties for mimicking three-dimensional microenvironments of stem cells. RSC Advances 2014;4:63951-61.

[18] Mellati A, Fan C-M, Tamayol A, Annabi N, Dai S, Bi J, et al. Microengineered 3D cell-laden thermoresponsive hydrogels for mimicking cell morphology and orientation in cartilage tissue engineering. Biotechnology and Bioengineering 2017;114:217-31.

[19] Bidarra SJ, Barrias CC, Granja PL. Injectable alginate hydrogels for cell delivery in tissue engineering. Acta Biomaterialia 2014;10:1646-62.

[20] Zhang J, Zhang H, Xu X. CHAPTER 17 Smart Materials to Regulate the Fate of Stem Cells. Smart Materials for Tissue Engineering: Applications: The Royal Society of Chemistry; 2017. p. 473-504.

[21] Zhang J, Yun S, Bi J, Dai S, Du Y, Zannettino ACW, et al. Enhanced multi-lineage differentiation of human mesenchymal stem/stromal cells within poly(N-isopropylacrylamide-acrylic acid) microgel-formed three-dimensional constructs. Journal of Materials Chemistry B 2018;6:1799-814.

[22] Shen Z, Bi J, Shi B, Nguyen D, Xian CJ, Zhang H, et al. Exploring thermal reversible hydrogels for stem cell expansion in three-dimensions. Soft Matter 2012;8:7250-7.

[23] Gan T, Guan Y, Zhang Y. Thermogelable PNIPAM microgel dispersion as 3D cell scaffold: effect of syneresis. Journal of Materials Chemistry 2010;20:5937-44.

[24] Bortner CD, Cidlowski JA. The role of apoptotic volume decrease and ionic homeostasis in the activation and repression of apoptosis. Pflügers Archiv: European Journal of Physiology 2004;448:313-8.

[25] Guan Y, Zhang Y. PNIPAM microgels for biomedical applications: from dispersed particles to 3D assemblies. Soft Matter 2011;7:6375-84.

[26] Liu Y-J, Le Berre M, Lautenschlaeger F, Maiuri P, Callan-Jones A, Heuzé M, et al. Confinement and Low Adhesion Induce Fast Amoeboid Migration of Slow Mesenchymal Cells. Cell 2015;160:659-72.

[27] S. VB-FW. In Situ Tissue Regeneration: Chemoattractants for Endogenous Stem Cell Recruitment. Tissue Engineering Part B: Reviews 2014;20:28-39.

[28] Laird DJ, von Andrian UH, Wagers AJ. Stem Cell Trafficking in Tissue Development, Growth, and Disease. Cell 2008;132:612-30.

[29] Chaudhuri O, Gu L, Klumpers D, Darnell M, Bencherif SA, Weaver JC, et al. Hydrogels with tunable stress relaxation regulate stem cell fate and activity. Nature Materials 2015;15:326.

[30] POOLE CA. Review. Articular cartilage chondrons: form, function and failure. Journal of Anatomy 1997;191:1-13.

[31] Rasheena E, Jenkins BJ, F. AA, Liju Y. Three-Dimensional Cell Culture Systems and Their Applications in Drug Discovery and Cell-Based Biosensors. ASSAY and Drug Development Technologies 2014;12:207-18.

[32] Friedl P, Gilmour D. Collective cell migration in morphogenesis, regeneration and cancer. Nature Reviews Molecular Cell Biology 2009;10:445.

[33] Fahy N, Alini M, Stoddart MJ. Mechanical stimulation of mesenchymal stem cells: Implications for cartilage tissue engineering. Journal of Orthopaedic Research 2018;36:52-63.

[34] Bhumiratana S, Eton RE, Oungoulian SR, Wan LQ, Ateshian GA, Vunjak-Novakovic G. Large, stratified, and mechanically functional human cartilage grown in vitro by mesenchymal condensation. Proceedings of the National Academy of Sciences 2014;111:6940-5.

Supplementary information

Fabrication of A Neo-Cartilage Patch by Fusing Cell Aggregates Generated in A Thermosensitive Hydrogel onto Electrospun Film

Jiabin Zhang [a], *Seonho Yun* [a], *Yuguang Du* [d], *Andrew Zannettino* [b, *], *Hu Zhang* [a, c, *]

[a] School of Chemical Engineering, The University of Adelaide, Adelaide, SA 5005, Australia

[b] Adelaide Medical School, The University of Adelaide, Adelaide, SA 5001, Australia

[c] Henry E. Riggs School of Applied Life Sciences, Keck Graduate Institute, California, CA 91711, USA

[d] Institute of Process Engineering, Chinese Academy of Sciences, Beijing, 100190, China

*Corresponding Authors: Prof. H Zhang (hu_zhang@kgi.edu) and Prof. A Zannettino (andrew.zannettino@adelaide.edu.au)

Prepared in Publication format

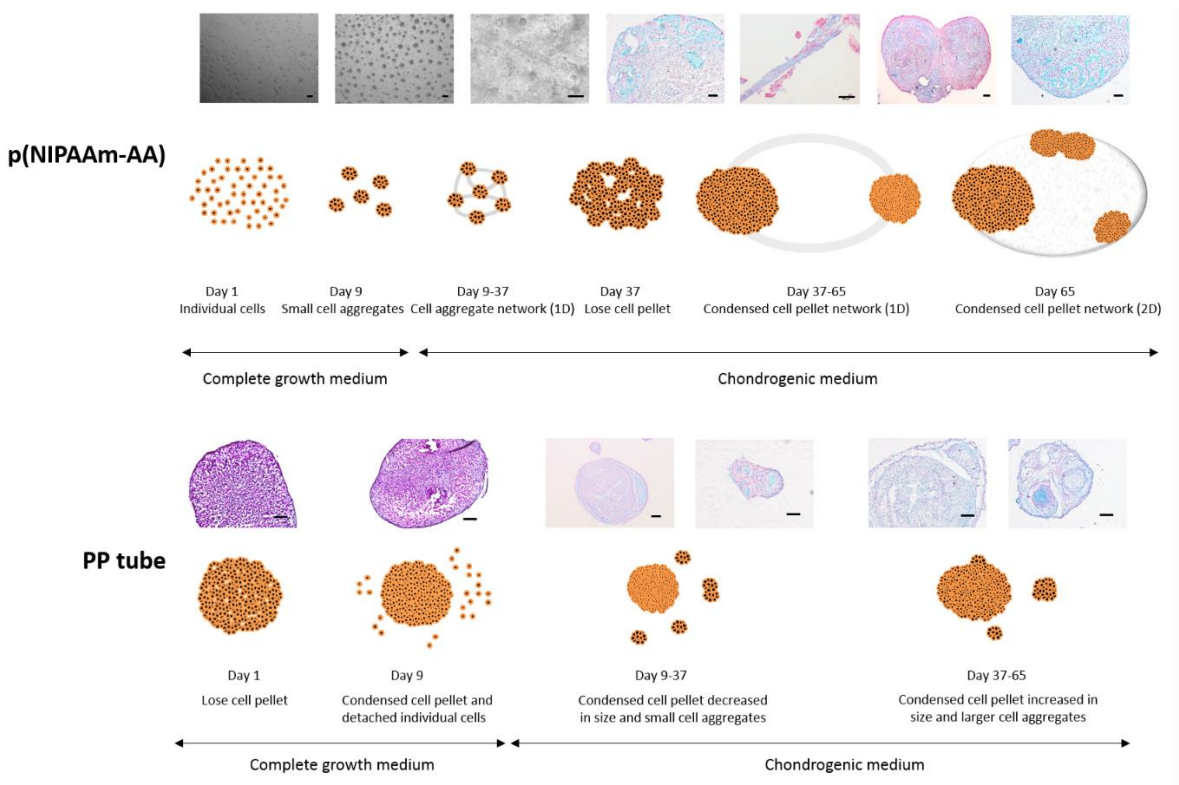

Figure S5.1 *In-vitro* chondrogenic progression of human mesenchymal stem/stromal cells within poly (*N*-isopropylacrylamide-acrylic acid) hydrogels and polypropylene (PP) tubes. Scale bar: 100 µm.

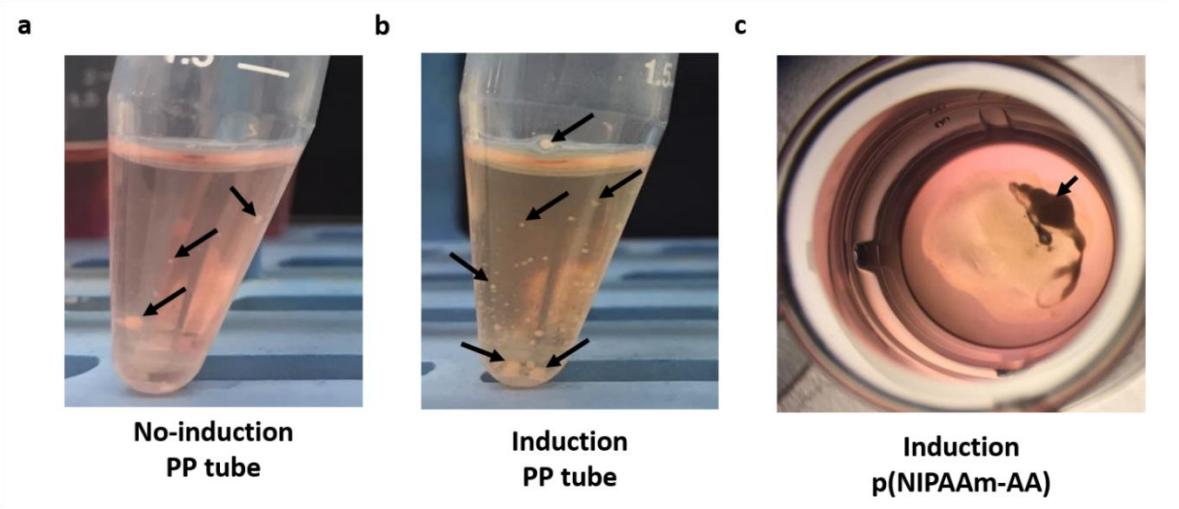

Figure S5.2 Optical images of UE7T-13 cells cultured in (a) polypropylene (PP) tubes without inductive media, (b) polypropylene (PP) tubes with chondrogenic inductive media, or (c) poly (*N*-isopropylacrylamide-acrylic acid) (p(NIPAAm-AA)) hydrogels with chondrogenic inductive media for 4 weeks *in vitro*. Scale bar: 100 µm. Arrows point to migrated cell aggregates and cell pellets.

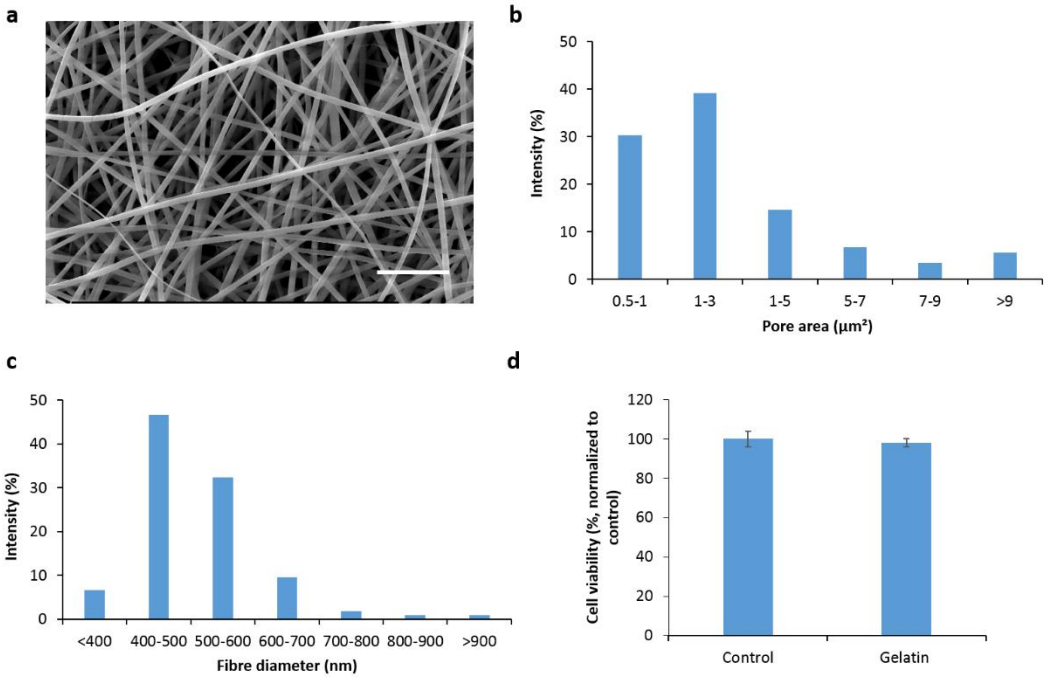

Figure S5.3 (a) SEM image of electrospun scaffolds. Scale bar: 5 μm. (b) Pore size distribution of electrospun scaffolds. (c) Fiber diameter distribution of electrospun scaffolds. (d) Cell viability study of UE7T-13 by MTT assay in 24 h. Control: cells were cultured on 96-well tissue culture plate; Gelatin: cells were cultured on electrospun gelatin scaffolds. Data were normalized to the control and presented as mean ± standard error. n = 3.

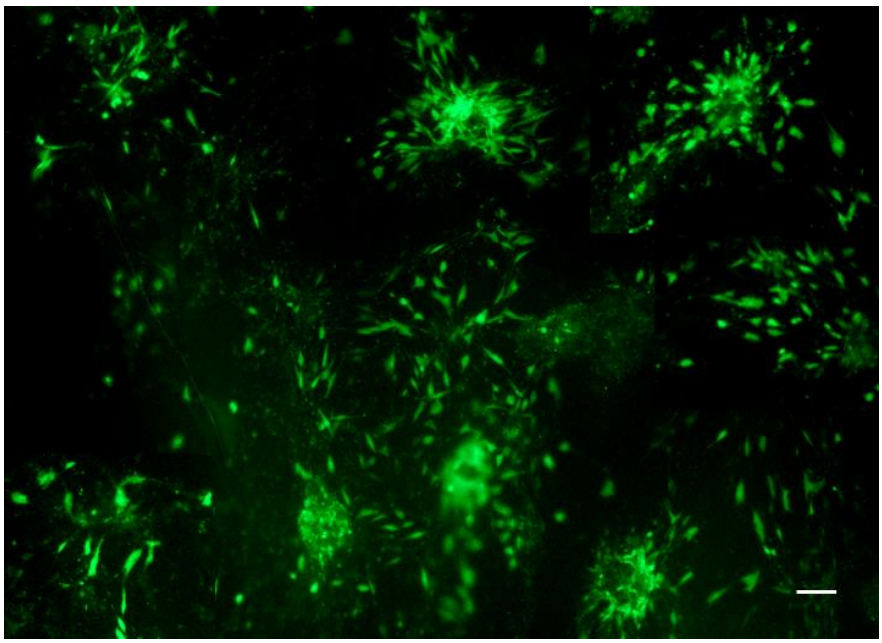

Figure S5.4 Fluorescent image of chondrogenesis-induced hMSCs attaching on an electrospun gelatin scaffold by calcein-AM staining. Green: cells. Scale bar: 100 μm.

CHAPTER VI

ENHANCED CHONDROGENESIS AND OSTEOGENESIS BY EMBEDDING HUMAN MESENCHYMAL STEM/STROMAL CELLS WITHIN A MAGNETIC-FIELD RESPONSIVE “DANCING” BALL

Statement of Authorship

Title of Paper	Enhanced Chondrogenesis and Osteogenesis by Embedding Human Mesenchymal Stem/Stromal Cells within A Magnetic-Field Responsive "Dancing" Ball.
Publication Status	☐ Published ☐ Accepted for Publication ☐ Submitted for Publication ☑ Unpublished and Unsubmitted work written in manuscript style
Publication Details	

Principal Author

Name of Principal Author (Candidate)	Jiabin Zhang
Contribution to the Paper	Performed experiments, analysed data, writing manuscript.
Overall percentage (%)	80%
Certification:	This paper reports on original research I conducted during the period of my Higher Degree by Research candidature and is not subject to any obligations or contractual agreements with a third party that would constrain its inclusion in this thesis. I am the primary author of this paper.
Signature	Date: 26/07/2019

Co-Author Contributions

By signing the Statement of Authorship, each author certifies that:

i. the candidate's stated contribution to the publication is accurate (as detailed above);

ii. permission is granted for the candidate in include the publication in the thesis; and

iii. the sum of all co-author contributions is equal to 100% less the candidate's stated contribution.

Name of Co-Author	Seonho Yun
Contribution to the Paper	Experiment design and evaluation of data.
Signature	Date: 16/07/2019

Name of Co-Author	Afshin Karami
Contribution to the Paper	Experiment design and evaluation of data.
Signature	Date: 16/7/19

Name of Co-Author	Yuguang Du		
Contribution to the Paper	Proof read the manuscript and evaluation.		
Signature		Date	2019.7.15

Name of Co-Author	Andrew Zannettino		
Contribution to the Paper	Proof read the manuscript, experiment design, and evaluation of data.		
Signature		Date	16 July 2019

Name of Co-Author	Hu Zhang		
Contribution to the Paper	Proof read the manuscript, experiment design, and evaluation of data.		
Signature		Date	15-07-2019

Please cut and paste additional co-author panels here as required.

Enhanced Chondrogenesis and Osteogenesis by Embedding Human Mesenchymal Stem/Stromal Cells within A Magnetic-Field Responsive "Dancing" Ball

Jiabin Zhang[1], *Seonho Yun*[1], *Afshin Karami*[1], *Yuguang Du*[4], *Andrew Zannettino*[2, *], *Hu Zhang*[1, 3, *]

[1]School of Chemical Engineering, The University of Adelaide, Adelaide, SA 5005, Australia

[2]Adelaide Medical School, The University of Adelaide, Adelaide, SA 5001, Australia

[3]Henry E. Riggs School of Applied Life Sciences, Keck Graduate Institute, California, CA 91711, USA

[4]Institute of Process Engineering, Chinese Academy of Sciences, Beijing, 100190, China

[*]Corresponding authors: Prof. A. Zannettino (andrew.zannettino@adelaide.edu.au) and Prof. H. Zhang (hu_zhang@kgi.edu)

Prepared in publication format

6.1 Graphical abstract

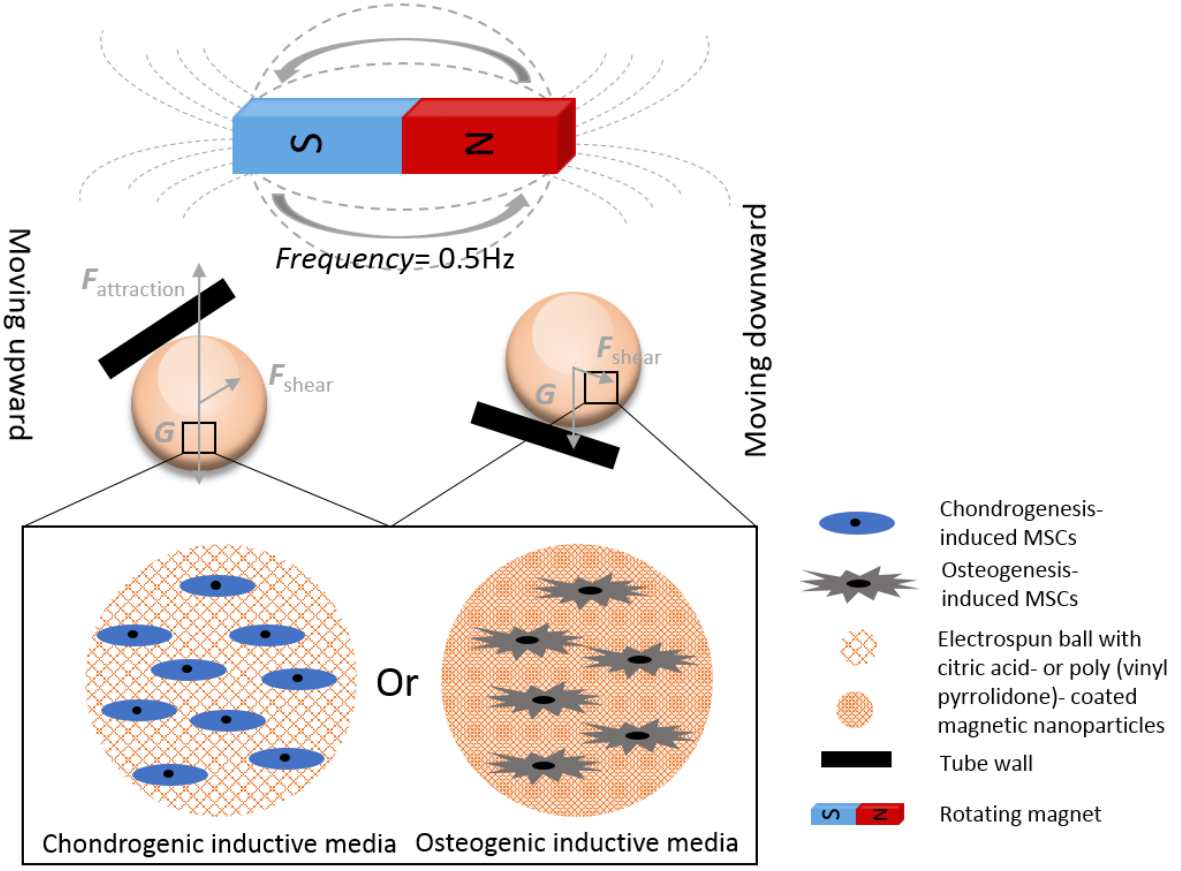

In this study, a magnetic field-responsive ball together with an in-house rotating magnet device were fabricated to study stem cell differentiation. As a result, chondrogenesis and osteogenesis of mesenchymal stromal/stem cells are significantly enhanced within the magnetic field-responsive balls by the synergic effect of dynamic magnetic field, mechanical stimulation, fiber topography, dynamic culture, gelatin polymer, and inductive biomolecules.

6.2 Abstract

Mesenchymal stromal/stem cells (MSCs) represent a novel cell therapy source to treat severe diseases, such as osteoarthritis. However, the therapeutic benefit of MSCs are highly dependent on their differentiation state and the intended clinical application. MSC differentiation is regulated by many factors, while traditional cell culture systems are limited in providing multiple stimuli. Here, a magnetic field-responsive ball is successfully fabricated by incorporating magnetic nanoparticles (MNPs) into the electrospun nanofibers. When positioning near a rotating magnet (f = 0.5 Hz), the electrospun film-derived balls, together with the MSCs, are driven upward/downward in the culture container and induced mechanical stimulation by spatial restriction and fluid flow. The extracellular matrix-mimicking scaffold and the dynamic magnetic field significantly enhance cell chondrogenesis instead of osteogenesis. Moreover, the difference in the fiber topography results in selective up-regulation of chondrogenesis-related genes (*COL 2A1* and *ACAN*) for the balls with citric acid-coated MNPs. In contrast, osteogenesis-related genes (*RUNX2* and *SPARC*) are selectively and significantly up-regulated for the balls with PVP-coated MNPs. Hence, the magnetic field-responsive scaffolds together with an in-house rotating magnet device can be a novel system for study influence of multiple stimuli on stem cell differentiation *in vitro*.

KEYWORDS: multi-lineage cell differentiation, mesenchymal stromal/stem cell, magnetic field, mechanical stimulation, magnetic nanoparticle-incorporated nanofibers

6.3 Introduction

Mesenchymal stromal/stem cells (MSCs), a multipotent mesodermal-tissue derived stem cell population, show great potential in cell-based therapy to treat several severe diseases [1, 2], including late-stage osteoarthritis (OA) [3-5]. The mechanisms which underlie their therapeutic function are thought to involve paracrine effect [6, 7] and/or their capacity to differentiate, amongst other cells, into cells of the osteochondral lineage cells [8]. Many factors in the stem cell niche can influence cell differentiation including physical [9-11] and biochemical stimuli

[12-14]. External magnetic field [15, 16] and mechanical force [17-19] are two physical stimuli that can regulate the fate of stem cells. Numerous studies have examined the impact of frequency [20] and magnetization [18] of a pulsed electromagnetic field [16] or a static magnetic field [21] on chondrogenesis and osteogenesis of MSCs. To this end, magnetic nanoparticles (MNPs) have been incorporated into scaffolds/hydrogels in order to regulate the fate of stem cells by their intrinsic magnetism. [22, 23] However, there are very few studies on examining the synergistic impact of an external alternating magnetic field and the MNPs on the fate of stem cells. In addition, dynamic strain at a certain frequency and intensity may also enhance chondrogenesis and osteogenesis of MSCs. [24-27] For example, in one study, mechanical stimulation was induced in a customized bioreactor in which compression on the cell-embedded scaffold was achieved by alternating the vertical movement of a ceramic ball and shear stress was induced on the cells by horizontal movement of the ball. [19] Although the frequency and the intensity of both mechanical stimulations was well controlled, the system was only able to apply the mechanical stimulations on one sample and was prone to contamination when the scaffold was directly and repetitively contacted with the ceramic ball in the culture medium.

Herein, we developed a cell culture system that allows us to apply an external alternating magnetic field and simultaneously induce mechanical stimulation on the cells embedded within an extracellular matrix (ECM)-mimicking 3D scaffold. The 3D scaffold was constructed in a ball-like shape from electrospun gelatin films with incorporation of two different MNPs. The magnetic field-responsive scaffolds were characterized by various methods to evidence the embedment of MNPs inside the electrospun nanofibers. Moreover, cytotoxicity of MNPs and electrospun films and cell proliferation in the electrospun film-derived balls were also measured by MTT assay. The magnetic field-responsive scaffolds were used to study influence of multiple stimuli on chondrogenesis and osteogenesis of hMSCs in the presence of an alternating magnetic field.

6.4 Materials and methods

6.4.1 Preparation of MNPs and fabrication of scaffolds

The details of magnetic nanoparticle preparation and scaffold fabrication were described in "Supporting Information". The process for preparing electrospun films and film-derived balls with/without MNPs incorporation was shown in Figure S6.1.

6.4.2 X-ray diffraction

The synthesized MNPs and the electrospun films with/without incorporation of MNPs were characterized by X-ray diffraction (XRD) using a Rigaku MiniFlex 600 X-ray diffractometer at a voltage of 40 kV and a current of 15 mA. The XRD patterns were recorded from 10° to 80° (2θ) at a speed of 10°/min and an interval of 0.02°.

6.4.3 Scanning electron microscopy and transmission electron microscopy

After electrospinning, a small piece of the electrospun film with/without incorporation of MNPs was coated with a thin layer of platinum and imaged by a XL30 FEGSEM (Philips) with an accelerating voltage of 10 kV.

Nanofibers with/without MNPs was also directly electrospun onto a copper grid for 5 sec and sandwiched with another copper grid for transmission electron microscopy using a CM 200 TEM (Philips). During TEM imaging, an energy dispersive X-ray spectrum (EDS) was also recorded to confirm the existence of MNPs within the electrospun nanofibers.

6.4.4 Thermogravimetric analysis

A ball with/without incorporation of MNPs (3 mg) was transferred to an alumina crucible and the thermostability was determined by a thermogravimetric analyzer (TGA)/ differential scanning calorimeter (DSC) 2 (Mettler Toledo). The sample was heated from 25 °C to 1550 °C at a heating rate of 10 °C/min and supplied with air as a purge gas at a continuous flowing rate of 50 mL/min.

6.4.5 Magnetic behavior study

Magnetic hysteresis loops of MNPs, gelatin balls, gelatin balls with citric acid coated MNPs, and gelatin balls with PVP coated MNPs were measured by a vibrating sample magnetometer (VSM, lakeshore 7407) at room temperature, respectively.

6.4.6 Swelling ratio measurement

The balls with/without incorporation of MNPs were weighted at a dried status (W_{dry}). After soaking in water for 30 min, excessive water was removed and the balls were weighted at a wet status (W_{wet}). The swelling ratio was calculated according to the following formula. All measurements were repeated in triplicates.

$$\text{Swelling ratio (fold)} = \frac{W_{\text{wet}}}{W_{\text{dry}}} \quad (1)$$

6.4.7 Biocompatibility assay

An immortalized human mesenchymal stromal/stem cell line (UE7T-13, RIKEN BioResources Center) at passage 45-47 was used for the biocompatibility assay of MNPs and electrospun films with/without MNPs. The multi-potency of hMSCs has been studied previously. [28-30] The biocompatibility study of magnetic nanoparticles was described in detail in "Supporting Information". All electrospun films were cut to fit the bottom of a 96-well plate. A hMSC solution (40 μL) containing around 1×10^4 cells was then added onto the electrospun films and the cells were cultured for 4 h in a humidified incubator containing 5 % CO_2 at 37 °C before addition of fresh complete medium (160 μL/well). The 96-well plate was placed in the incubator up to 24 h, after which the MTT assay was performed. The absorbance of the cells directly cultured on a 96-well plate without electrospun films was used as the control. All the absorbance values were normalized to the value of control and presented as cell viability.

6.4.8 Cell proliferation in the balls

The electrospun film-derived balls with/without MNPs were placed into individual 1.5 mL Eppendorf tubes with lids open for cell culture. Cell solution (20 μL) containing 1×10^4 cells was injected into each electrospun film-derived ball from multiple sites to allow homogeneous cell distribution within the scaffolds. Cells were incubated for 4 h to allow complete cell

attachment to the scaffolds prior to addition of fresh medium (180 µL). During cell culture, the Eppendorf tubes were placed inside the Falcon petri dishes with a dimension of 100 mm × 20 mm (Corning) under a humidified condition at 37 °C with 5 % CO_2 supply. The medium was changed every other day. On day 1 and 3, MTT assay was performed to determine cell growth. The cells cultured on a 96-well plate were used as the control. All data were normalized to the absorbance value of the control measured on day 1 and presented as fold increase in cell number.

6.4.9 Cell differentiation under an external alternating magnetic field

An in-house device, consisting of a reversible gearhead motor (Jaycar electronics) with a maximal torque of 2.1 kg cm fixed on the top of a clear plastic stage, a MP-3080 power supply (Jaytech) connected to the motor, a N52 magnet block with a dimension of 50 mm × 25 mm × 10 mm and a balanced block with the equivalent weight as the magnet block, both of which were fixed to a rotating bar driven by the attached motor. The distance from the balanced block or the magnet block to the rotating center and the height of the rotating bar were adjustable. During chondrogenic and osteogenic induction, the Eppendorf tubes containing cell-loaded balls were placed 2 cm below the rotating magnet block at a rotating frequency of 0.5 Hz. Following chondrogenic or osteogenic induction for three weeks, mRNA was extracted and detected for expression of specific genes by qRT-PCR. Primer sequences of targeting genes are shown in Table S1. All data were normalized to the value for the *ACTB* gene.

6.4.9.1 Chondrogenesis

The experimental set-up was similar to the above cell proliferation study. hMSCs were loaded into electrospun film-derived balls at a cell density of 2.5×10^5 per ball, and incubated in complete cell culture medium overnight. The culture medium was replaced with the same volume of chondrogenic induction medium as reported in a previous study [28]. For the control, a similar number of cells were centrifuged in a 12 mL polypropylene tube (SARSTEDT Australia) at 600 rcf for 5 min and cultured in the complete medium overnight to form a large cell pellet. The pellet was then transferred to a 1.5 mL of Eppendorf tube and cultured in the

same way as that for the cell-loaded balls. All cells submerged in the chondrogenic medium were exposed to an alternating magnetic field for three weeks with medium change three times per week. Cells cultured in the balls without MNPs or without exposure to the external magnetic field were used as the control groups.

6.4.9.2 Osteogenesis

The cell-loaded balls were subjected to the similar procedure as the chondrogenesis except that the medium was replaced with osteogenic medium as reported in a previous study [28]. The cells for the control were cultured on a 48-well plate with the same cell number per well with or without exposure to the external alternating magnetic field.

6.4.10 Histology and immunofluorescence staining

After three weeks of induction culture, cells and scaffolds were processed by cryosection for hematoxylin and eosin (H&E) staining to visualize cell distribution in the scaffolds, Alcian Blue staining to evidence production of sulfated glycosaminoglycans (GAGs), Alizarin Red S staining to evidence deposition of calcium, immunofluorescence staining for collagen 2A1, aggrecan, and osteocalcin. All stained sections were imaged with an IX53 fluorescence microscope (Olympus).

6.4.11 Statistical analysis

All experiments were performed in triplicates and data were presented as mean ± standard error. One-tailed student t-test was used to evaluate the statistical significance. * $0.01 < p < 0.05$ and ** $0.001 < p < 0.01$ were considered as a significant difference and a very significant difference, respectively, while *** $p < 0.001$ was considered as a highly significant difference.

6.5 Results and discussion

6.5.1 Evidence of MNPs in magnetic field-responsive scaffolds

The characterization of magnetic nanoparticles (MNPs) (Figure S6.2 and Figure S6.3), the optimization of electrospinning parameters (Figure S6.4), and the characterization of

electrospun nanofibers with/without MNPs (Figure S6.5) were described in the "Supporting Information".

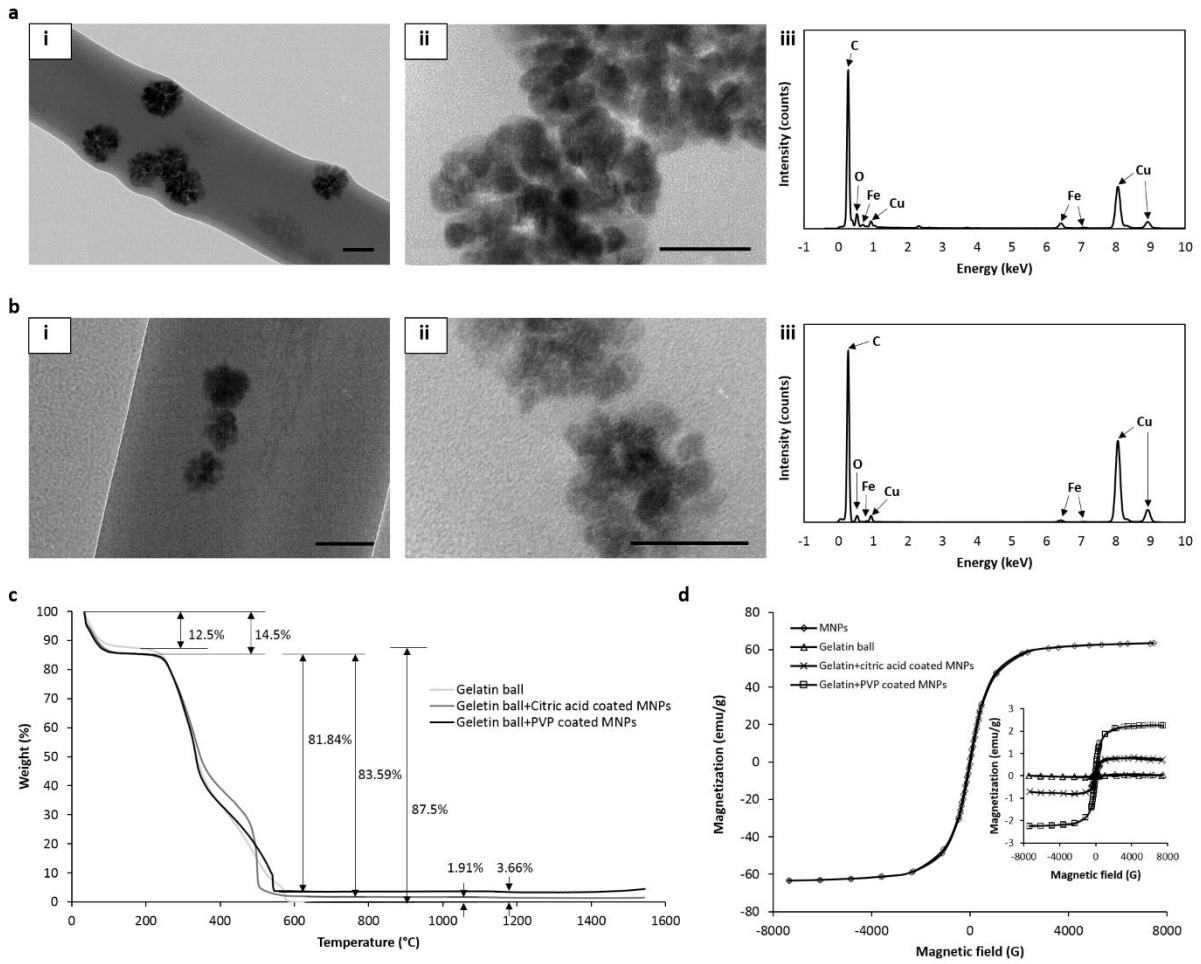

Figure 6.1 Transmission electron microscopy images of the electrospun films with (a) citric acid-coated MNPs or (b) PVP-coated MNPs at (i) a lower magnification (scale bar: 100 nm) and (ii) a higher magnification (scale bar: 50 nm) and (iii) energy dispersive X-ray spectrum for both electrospun films. (c) Thermogravimetric analysis of balls with/without MNPs with a thermal heating from 25 to 1550 °C in presence of air flow at 50 mL/min. (d) Hysteresis loops of magnetic nanoparticles (MNPs), electrospun gelatin ball (Gelatin ball), electrospun gelatin ball with citric acid coated MNPs (Gelatin+citric acid coated MNPs), and electrospun gelatin ball with PVP coated MNPs (Gelatin+PVP coated MNPs).

As TEM images indicated, the MNPs located inside the electrospun nanofibers induced protrusion at the edge of the electrospun nanofibers (Figure 6.1i), which confirmed that MNPs were successfully embedded inside the electrospun nanofibers. Besides, the synthesized magnetic nanoparticles maintained a spheroid-like structure with many smaller particles (Figure 6.1ii), which was unaffected by electrospinning and consistent with a previously published study [31]. Furthermore, the chemical components of the particles were further

confirmed to be the iron element detected by EDS (Figure 6.1iii). It was worth noting that metal copper signals were also observed in the energy dispersive X-ray spectra, which came from the coppery grids used in TEM imaging. XRD peaks of the electrospun film with incorporation of citric acid or PVP-coated MNPs were shifted to a lower angle because of the planar compressive stress-induced strain [32]. (Figure S6.6) However, the overall XRD pattern was still similar to the standard one of Fe_3O_4 in JCPDS card No.19-629 [31], which also indicated that the MNPs were successfully incorporated into the electrospun films.

Thermogravimetric analysis revealed that the ball without MNPs incorporation was completely combusted at around 610 °C, while there was 1.91% residue in the ball with incorporation of citric acid-coated MNPs and 3.66% residue in the ball with PVP-coated MNPs due to high thermo-stability of Fe_3O_4 (Figure 6.1c). Furthermore, incorporation of citric acid coated MNPs or PVP coated MNPs enabled gelatin ball responsive to a dynamic magnetic field. (Figure 6.1d) It was showed that saturation magnetic moment of gelatin balls with PVP-coated MNPs was also higher than that of gelatin ball with citric acid coated MNPs, 2.2 emu/g and 0.8 emu/g, respectively, which was consistent with TGA results. (Figure 6.1d)

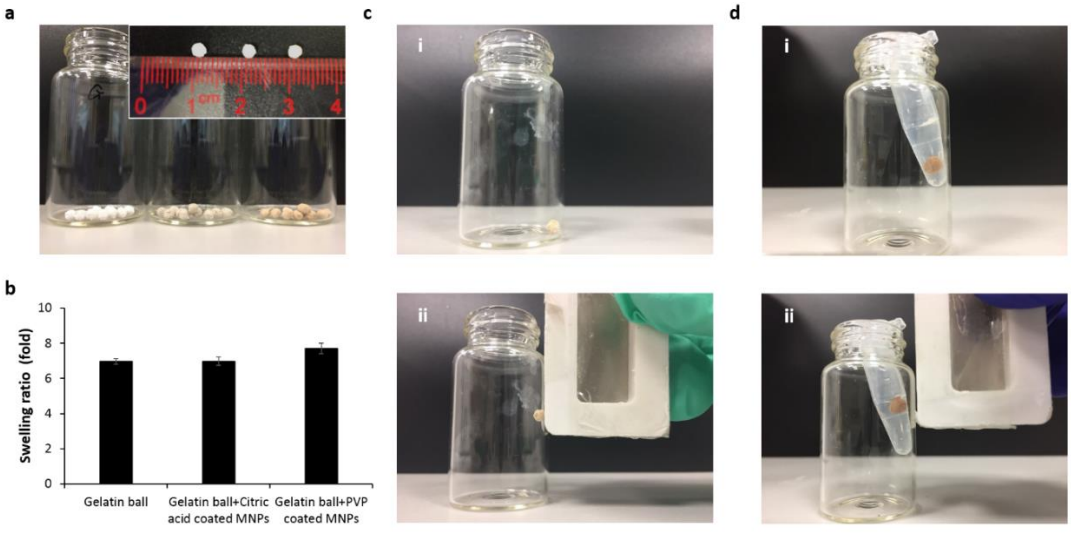

Figure 6.2 (a) Distinct color for different electrospun film-derived balls and their size measurement (inset). Left: balls without MNPs; Middle: balls with citric acid-coated MNPs; Right: balls with PVP-coated MNPs. (b) Swelling ratio of the electrospun film-derived balls with/without MNPs. Data were presented as mean ± standard error, n = 3. (c) Magnetic field responding behavior of a ball with MNPs at a dry status: (i) settling down with no magnet and (ii) suspending with a magnet. (d) Magnetic field responding behavior of a ball with MNPs in water: (i) settling down with no magnet and (ii) suspending with a magnet.

The average size of electrospun film-derived balls with/without MNPs was approximately 3 mm in diameter. (Figure 6.2a) Due to incorporation of MNPs, the fabricated balls displayed a distinct color: the balls without MNPs incorporation appeared bright white, while the balls with incorporation of PVP-coated MNPs had a darker brown color compared to those with incorporation of citric acid-coated MNPs. (Figure 6.2a) The swelling ratio of the balls with/without incorporation of MNPs was also measured and calculated according to the Eq. 1. Since the total weight of the MNPs was negligible compared to the total weight of the balls, there was no significant difference in the swelling ratio among three types of balls with an approximately 7-fold increase, indicating an excellent capacity of water retention. (Figure 6.2b) To avoid cytotoxicity of chemical residue [33], a physical crosslinking method was used in this study by heating the fabricated balls at 190 °C for 2 h [34]. After crosslinking, the balls maintained their ball-like structures in water due to the formation of the amide bonds. The magnetic ball in air (Figure 6.2c) or water (Figure 6.2d) settled down when no magnet was present, while it moved along the wall of the container and remained suspended in the presence of a magnetic field.

6.5.2 Cell viability and cell proliferation

It was found that cells cultured on electrospun film-derived balls with or without MNPs had a relatively high cell viability, over 90%, and no significant difference was seen among all groups. (Figure 6.3a) However, cell number of balls with/without MNPs was significantly higher than that of the tissue culture plate, particularly on day 1. ($p < 0.001$ for balls without MNPs on day 1, $0.001 < p < 0.01$ for balls without MNPs on day 3 and balls with MNPs on day 1 and 3 compared to the control group on the tissue plate) (Figure 6.3b) There was no significant difference in cell proliferation among the balls with or without MNPs. The high surface area might contribute to the cell proliferation in the gelatin electrospun film-derived balls, while the presence of MNPs did not have an impact on cell proliferation. In addition, the porous structure

of electrospun film-derived balls (Figure S6.4f) also facilitated cell penetration and migration and enhanced nutrients and gases exchange.

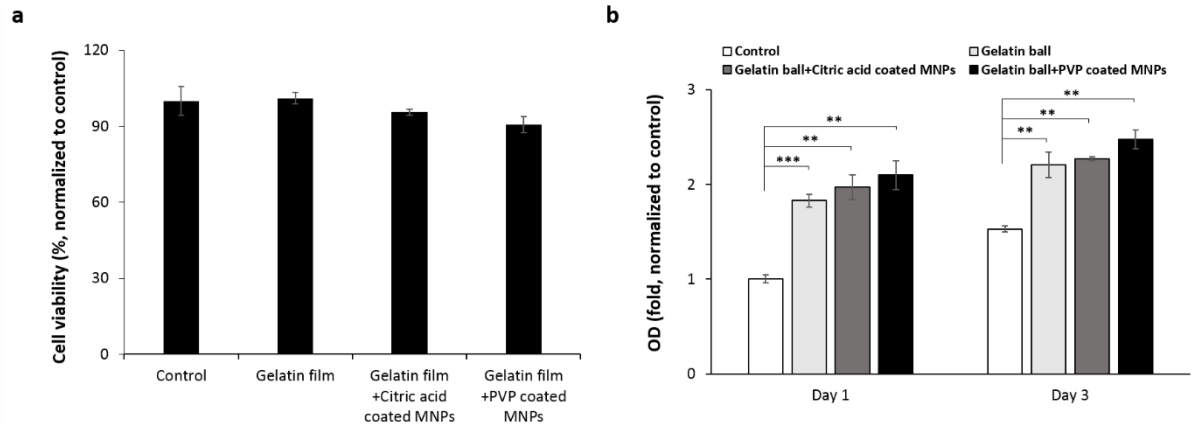

Figure 6.3 (a) Cell viability measurement by MTT after 24 h. Control: hMSCs were cultured on a 96-well tissue culture plates; Gelatin film, Gelatin film + Citric acid-coated MNPs, Gelatin film + PVP coated MNPs on the x-axis: hMSCs were cultured on the electrospun gelatin films without MNPs incorporation, with incorporation of citric acid-coated MNPs, and with incorporation of PVP-coated MNPs, respectively. All data were normalized to the absorbance value of the control and presented as the mean ± standard error (n = 3). (b) Cell proliferation measurement by MTT. Control: hMSCs on a 96-well tissue culture plate; Gelatin ball, ball+Citric acid-coated MNPs, Gelatin ball+PVP-coated MNPs: hMSCs in the balls without MNPs incorporation; with incorporation of citric acid-coated MNPs, and with incorporation of PVP-coated MNPs, respectively. All data were normalized to the absorbance value of the control measured on day 1 and presented as mean ± standard error (n = 3). *, **, *** indicated $0.01 < p < 0.05$, $0.001 < p < 0.01$, and $p < 0.001$, respectively.

6.5.3 Regulation of cell differentiation using alternating magnetic field and mechanical stimulation

During cell induction, hMSCs, on the one hand, were exposed to an external alternating magnetic field, which were reported to play an important role on osteogenesis [35] and chondrogenesis [16] of stem cells. On the other hand, for cells cultured inside the electrospun film-derived balls, they were stimulated with mechanical force and dynamic magnetic field. When a magnet block approached above the top of magnetic balls, the seeded cells and their carrier balls were attracted to roll upward by a magnetic attraction ($F_{\text{attraction}}$). Otherwise, the balls settled down due to the intrinsic gravity (G) when the magnet block moved away the balls. The movement of electrospun film-derived balls was restricted along the walls of the Eppendorf tube due to the space limitation and the balls were forced to rotate anti-clockwise upward/downward paralleling to the contacted walls of the tube. Rolling movement of the soft

balls may generate stretching or compressing stimulations on cells. Moreover, ball movement-induced fluid flow generated a shear force (F_{shear}) on the ball and the seeded cells. The shear force was applied to cells in an alternating direction at the same frequency as the rotational magnetic block. (Figure 6.4) The synergetic impact of an alternating magnetic field, mechanical stimulation, ECM mimicking polymeric surface, fiber topography, dynamic culture, and inductive biomolecules on the cell differentiation was shown in Table S2.

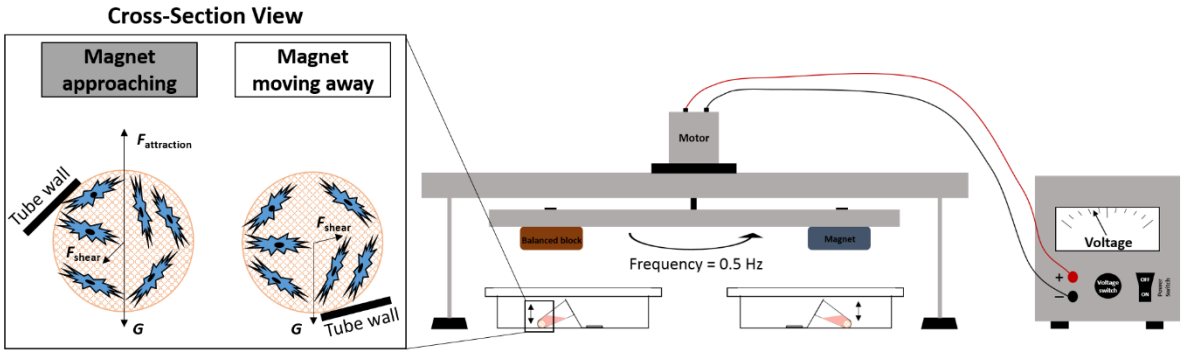

Figure 6.4 A schematic illustration of dual-stimulation induced by alternating magnetic force and mechanical force on hMSCs cultured inside electrospun film-derived balls with/without MNPs.

6.5.3.1 Chondrogenesis of hMSCs

It was shown that the mRNA expression of *COL 2A1* gene ($0.001 < p < 0.01$) and *ACAN* ($p < 0.001$) for hMSCs inside the electrospun film-derived balls without MNPs after inducing chondrogenesis for three weeks in comparison with the cell pellets under the same magnetic field (Figure 6.5), which was in consistent with other published studies regarding the promotion of gelatin on chondrogenesis of MSCs. [36-39]. It was believed that extracellular matrix (ECM) plays an important role in regulation of stem cell differentiation [40], therefore, cells inside the ECM-mimicking scaffolds without MNPs behaved differently from those condensed cell pellets when both exposing to an alternating magnetic field. Gelatin used in our study was extracted from the bovine skin (Sigma-Aldrich) by the base method. Hence, the material is a mixture of different denatured collagens, including type 2 collagen. [41] Despite the 3D structure of collagen being denatured by heating, the functional peptides, which were detectable by immunofluorescence (Figure S6.7), were capable of engaging with the appropriate integrin

adhesion molecules on the cells. [42, 43] A similar significant increase in mRNA expression of *ACAN* and *COL 2A1* genes was also observed for hMSCs cultured inside balls with incorporation of citric acid-coated MNPs compared to the cell pellets ($p < 0.001$) and balls with incorporation of PVP-coated MNPs ($0.001 < p < 0.01$ for *ACAN gene* and $0.01 < p < 0.05$ for *COL 2A1* gene) compared to cell pellets. (Figure 6.5) Besides, a highly significant increase in the mRNA expression of *COL 2A1* gene was found for hMSCs exposed to an external alternating magnetic field, which was in consistent with the conclusions of other previous studies [16, 20, 44]. (Figure 6.5) The enhanced chondrogenesis may be explained by the fact that the dynamic magnetic field at such a low frequency (0.5 Hz) may initiate the Ca^{2+} influx across the plasma membrane and trigger the relevant intracellular signaling pathways, such as the Wnt signaling pathway. [16, 44-46] The dynamic magnetic field also significantly up-regulated the mRNA expression of *COL1A1* gene ($0.01 < p < 0.05$), a gene mainly expresses in a fibrocartilage but none in a hyaline cartilage [47], for hMSCs cultured inside the electrospun film-derived balls without MNPs. (Figure 6.5) However, with the same stimulation of a dynamic magnetic filed, the mRNA expression of *COL1A1* gene for cells cultured in the both magnetic field-responsive scaffolds was significantly lower than that for cell pellets ($0.01 < p < 0.05$). (Figure 6.5) When normalizing the mRNA expression value of *COL2A1* gene to that of *COL1A1* gene, a similar result as the mRNA expression of *COL2A1* gene was seen, which revealed that the impact of dynamic magnetic field mainly induced chondrogenesis of cell pellets towards a fibrocartilage, while chondrogenesis of cells cultured in electrospun film-derived balls with incorporation of citric acid-coated MNPs was directed to an hyaline cartilage.

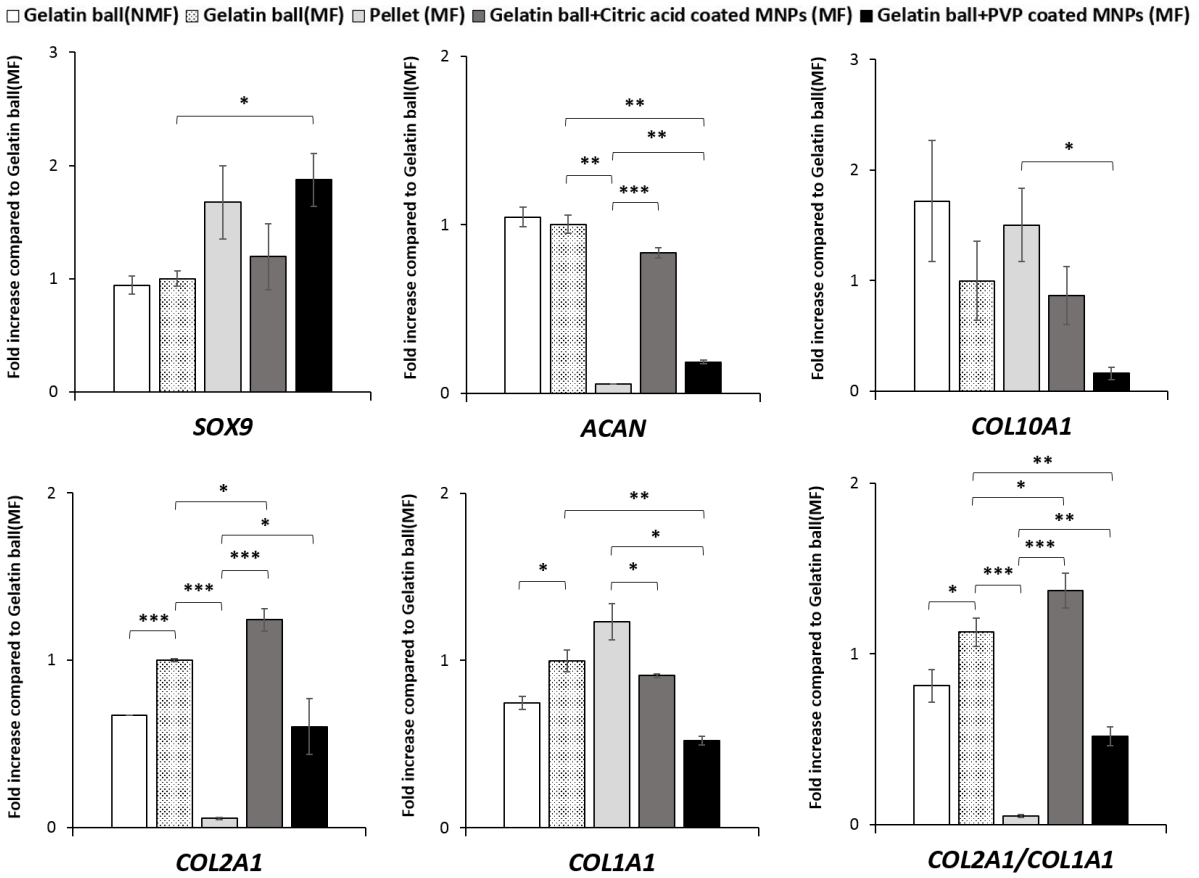

Figure 6.5 mRNA expression of chondrogenesis-related genes (*SOX9, ACAN, COL 2A1, COL1A1,* and *COL 10A1*) in hMSCs after induced chondrogenesis for three weeks. Gelatin ball (NMF), Gelatin ball (MF), Gelatin ball+Citric acid coated MNPs (MF), Gelatin ball+PVP coated MNPs (MF): induced chondrogenesis for cells seeded in the gelatin balls without MNPs without a magnetic field; without MNPs in a magnetic field; with citric acid-coated MNPs in a magnetic field; and with PVP-coated MNPs in a magnetic field, respectively. Pellet (MF): induced chondrogenesis for cells centrifuged into pellets in a magnetic field. mRNA expression of all genes was normalized to the value of *ACTB* gene and showed as fold increase in Ct value compared to Gelatin ball (MF). Data were presented as mean ± standard error (n = 3). *, **, *** indicated $0.01 < p < 0.05$, $0.001 < p < 0.01$, and $p < 0.001$, respectively.

The role of mechanical stimulation in induced chondrogenesis was revealed by comparing hMSCs cultured inside the balls with MNPs to those inside the balls without MNPs. A significantly increased level of the mRNA expression of *COL 2A1* gene was found for those cells cultured inside the balls with citric acid-coated MNPs ($0.01 < p < 0.05$). (Figure 6.5) Because the incorporated amount of citric acid-coated MNPs embedded inside the electrospun nanofibers was quite small, approximately 1.91% of a ball (Figure 6.1c), and the structure of balls was still maintained even immersing in medium for three weeks, citric acid-coated MNPs might neither be able to stimulate the cells by the intrinsic magnetism of the citric acid-coated MNPs nor be up-taken inside the cells to mediate the chondrogenesis-related signaling

pathways. Hence, the main contributor for the increased mRNA expression of *COL 2A1* gene might be due to the mechanical stimulation [48-50] and promoted mass transfer of chondrogenic biomolecules by dynamic movement [51]. On the contrary, a significantly lower level of the mRNA expression of *COL 10A1* gene ($0.01 < p < 0.05$), a specific gene of the hypertrophic chondrocytes, and a significantly higher level in the mRNA expression of *SOX9* ($0.001 < p < 0.01$), an early chondrogenesis-related gene, in hMSCs cultured inside the balls with PVP-coated MNPs revealed that the chondrogenic enhancement presented a much delayed manner in balls with PVP-coated MNPs. (Figure 6.5) The non-uniform electrospun nanofibers of electrospun film-derived balls with PVP-coated MNPs (Figure 6.1c) promoted spreading of the cell with a stretched nucleus, while hMSCs cultured inside the balls with citric acid-coated MNPs displayed a chondrocyte-like shape with a round nucleus (Figure S6.8), which might, therefore, enhanced chondrogenesis of hMSCs. [52-55]

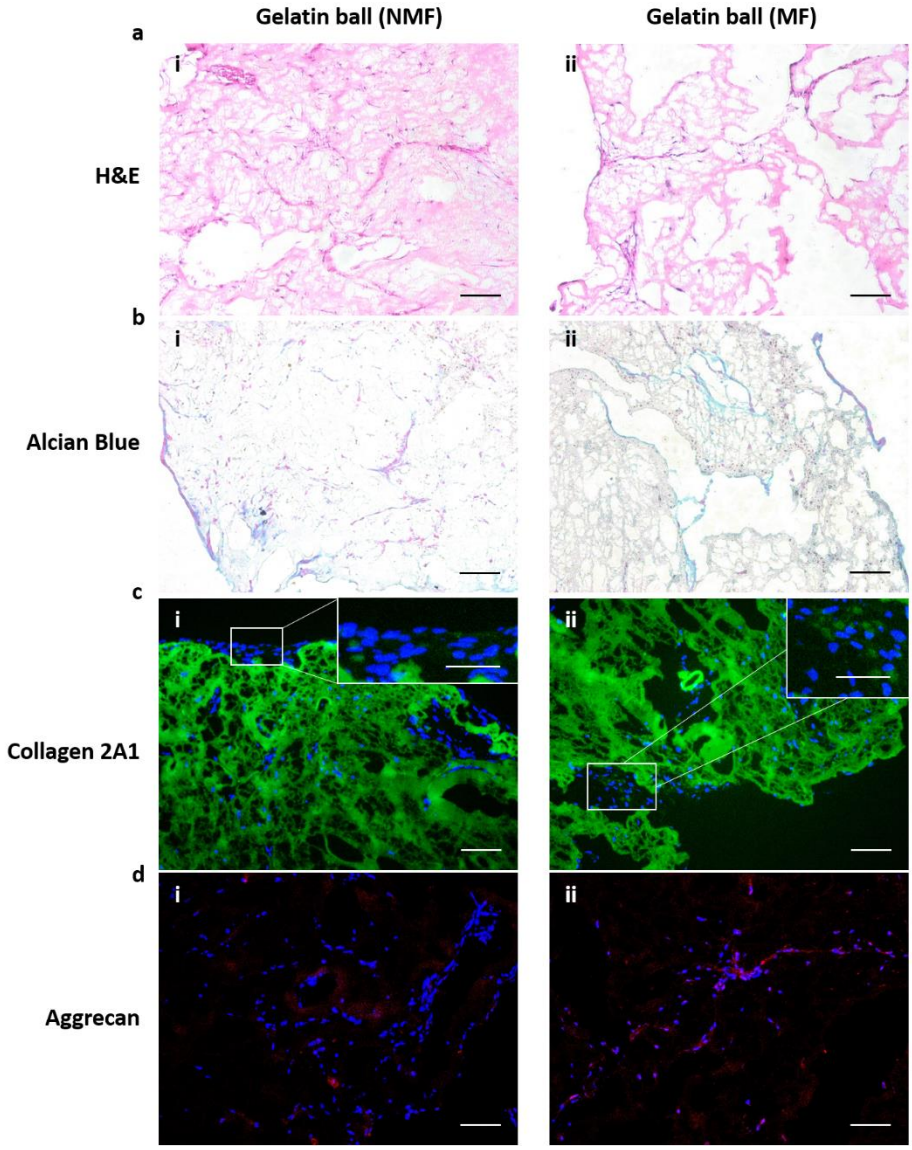

Figure 6.6 Histology and immunofluorescence images of hMSCs after induced chondrogenesis in the gelatin balls (i) without an magnetic field or (ii) in a magnetic field for three weeks. (a) Hematoxylin and eosin (H&E) staining images. Blue: cell nuclei; Red: cytoplasm; Pink: collagen and gelatin nanofibers. Scale bar: 100 μm. (b) Alcian Blue staining images. Blue: sulfated glycosaminoglycans (GAGs); Red: cell nuclei. Scale bar: 100 μm. (c) Collagen 2A1 immunofluorescence staining images. Green: collagen 2A1; Blue: cell nuclei. Scale bar of a lower magnification: 100 μm (i); Scale bar of a higher magnification: 50 μm (ii). (d) Aggrecan immunofluorescence staining images. Red: aggrecan; Blue: cell nuclei. Scale bar: 100 μm. Gelatin ball (NMF) and Gelatin ball (MF): cells in the gelatin balls without a magnetic field and in a magnetic field respectively.

The H&E staining images revealed a highly porous structure of the balls and homogeneous distribution of cells. (Figure 6.6a and Figure 6.7a) Sulfated glycosaminoglycans (GAGs), one of the main components of cartilage, were also evident and stained as a blue color in the all groups, however, no significant difference between them was seen. (Figure 6.6b and Figure 6.7b) Even though the electrospun films were also stained as a green color (Figure S6.7), more

evident collagen 2A1 staining was observed in the cells after stimulation in the alternating magnetic field than that without stimulation (Figure 6.6c), which was consistent with the difference in the mRNA expression of *COL 2A1* gene. However, no significant difference of stained collagen 2A1 was seen between cell pellets, balls with citric acid-coated MNPs, and balls with PVP-coated MNPs. (Figure 6.7c) Aggrecan was stained in a red color for both cells cultured with/without an external magnetic field, while no significant difference between them was noticed. (Figure 6.6d) No significant difference in aggrecan protein expression was seen between in the cell pellets and in the balls with PVP-coated MNPs. However, more positively stained aggrecan was shown in the balls with citric acid-coated MNPs compared to that in the cell pellets, which was in accordance with the difference shown in the mRNA expression of *ACAN* gene. (Figure 6.5 and Figure 6.7d)

The synergistic contribution from the magnetic field, mechanical stimulation, and ECM-mimicking scaffolds revealed that electrospun film-derived balls with citric acid-coated MNPs held great potential for enhancing chondrogenesis of hMSCs in an alternating magnetic field and a dynamic culture environment. (Table S2)

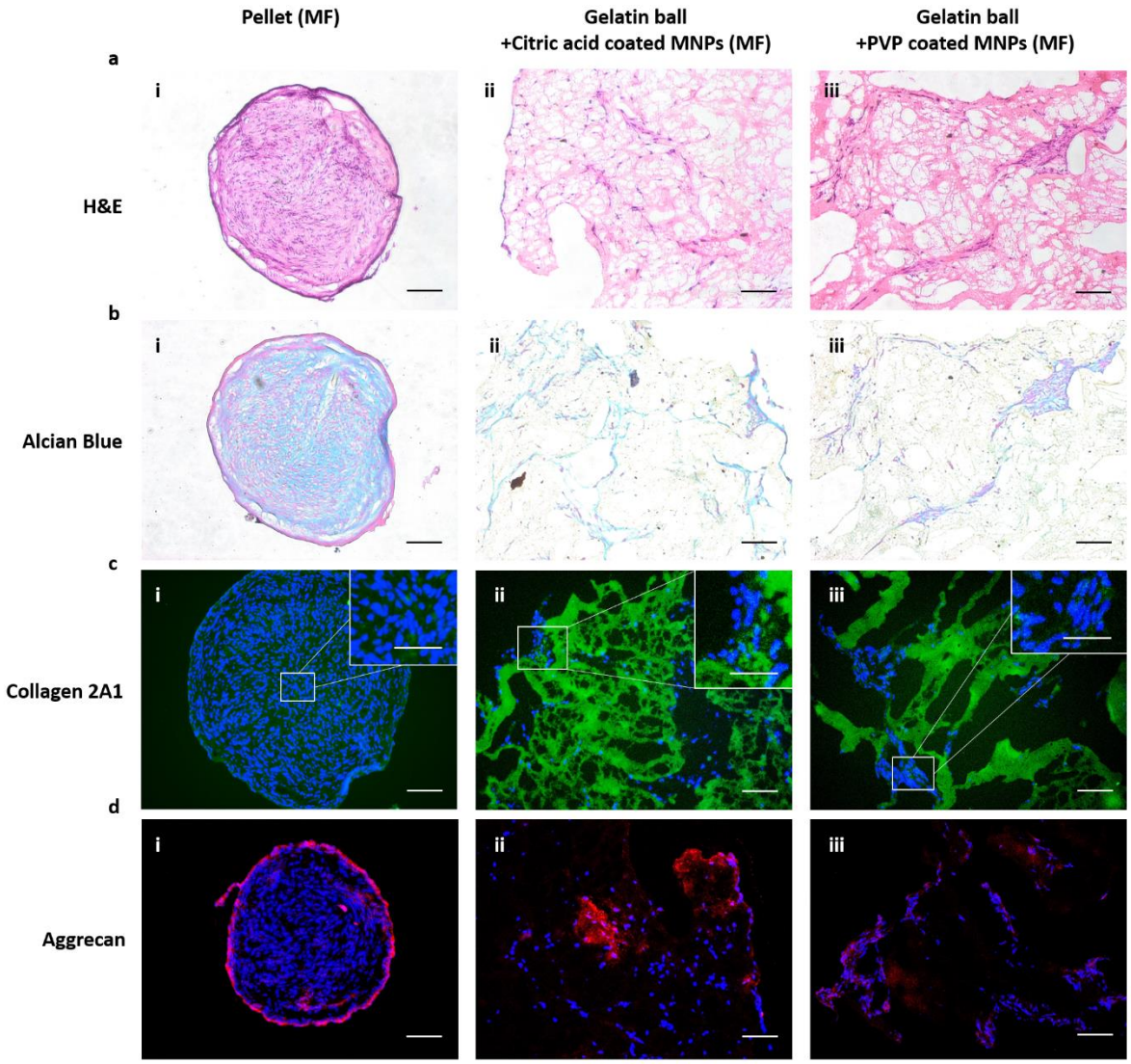

Figure 6.7 Histology and immunofluorescence images of hMSCs in an external magnetic field after induced chondrogenesis for three weeks (i) in cell pellets, or (ii) in balls with citric acid-coated MNPs, or (iii) in balls with PVP-coated MNPs. (a) Hematoxylin and eosin (H&E) staining images. Blue: cell nuclei; Red: cytoplasm; Pink: collagen and gelatin nanofibers. Scale bar: 100 μm. (b) Alcian Blue staining images. Blue: sulfated glycosaminoglycans (GAGs); Red: cell nuclei. Scale bar: 100 μm. (c) Collagen 2A1 immunofluorescence staining images. Green: FITC-labelled collagen 2A1; Blue: DAPI-labelled cell nuclei. Scale bar of a lower magnification: 100 μm; Scale bar of a higher magnification: 50 μm. (d) Aggrecan immunofluorescence staining images. Red: PE-labelled aggrecan; Blue: DAPI-labelled cell nuclei. Scale bar: 100 μm. Pellet (MF), Gelatin ball+Citric acid coated MNPs (MF), and Gelatin ball+PVP coated MNPs (MF): cells were centrifuged into pellets, and seeded in the balls with incorporation of citric acid-coated MNPs and PVP-coated MNPs in the presence of a magnetic field, respectively.

6.5.3.2 Osteogenesis of hMSCs

When the 2D cell culture with or without an alternating magnetic field was used to study the effect of magnetic field on cell osteogenesis, no significant difference was seen in the mRNA expression of osteogenesis-related genes (*RUNX2*, *SPARC*, *SP7*, and *BGLAP*), which

demonstrated that the alternating magnetic field at such a frequency and a magnetization level did not influence the osteogenesis of hMSCs. Moreover, the cells cultured inside the balls without MNPs expressed a similar level of osteogenesis-related genes (*RUNX2*, *SPARC*, *SP7*, and *BGLAP*) as the cells cultured on the 2D tissue culture plates, which indicated that gelatin and the 3D structure of the balls did not affect the osteogenesis of hMSCs. (Figure 6.8)

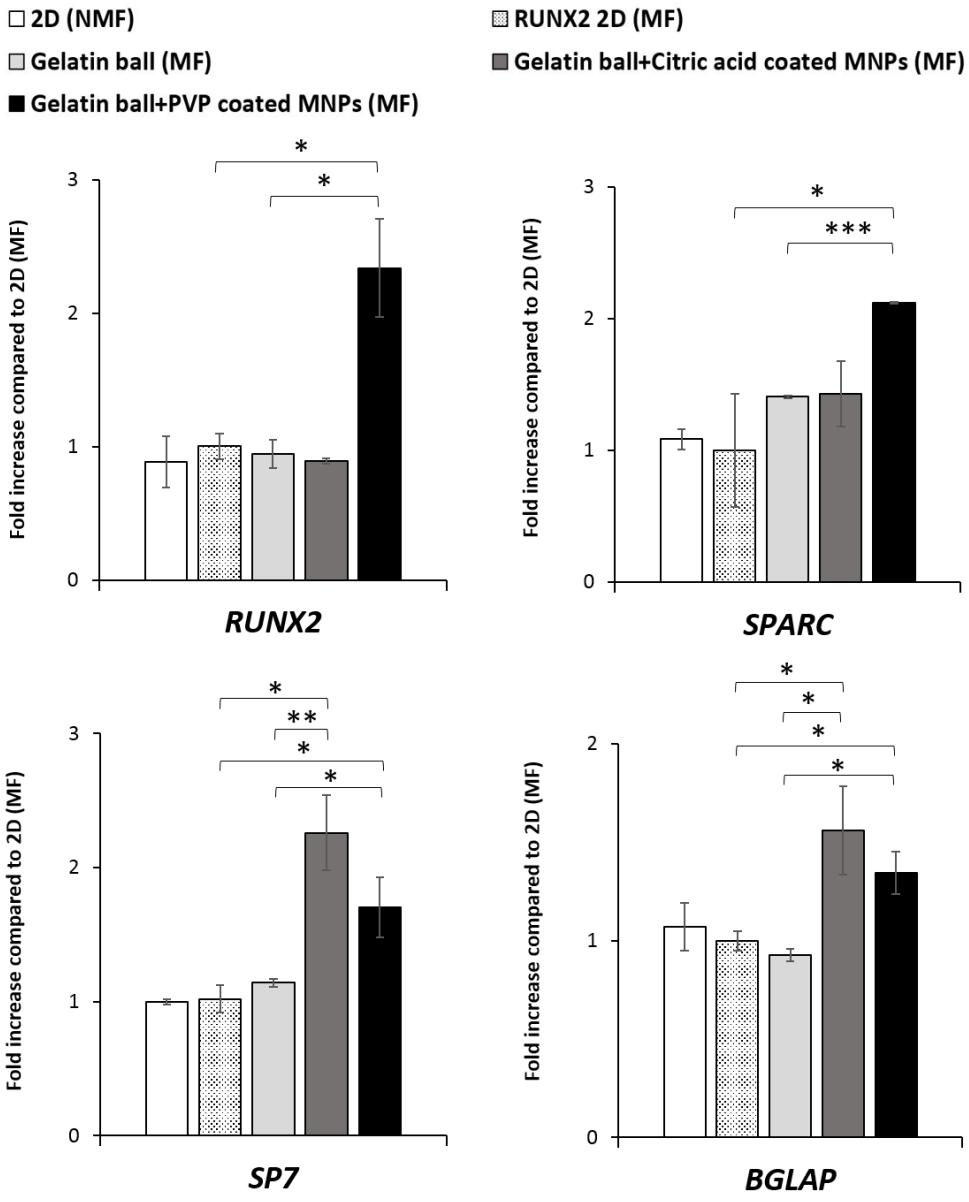

Figure 6.8 mRNA expression of osteogenesis-related genes (*RUNX2, SPARC, SP7,* and *BGLAP*) in hMSCs after induced osteogenesis for three weeks. 2D (NMF), 2D (MF): Cells were incubated in a 48-well plate without and with a magnetic field, respectively; Gelatin ball (MF), Gelatin ball+Citric acid coated MNPs (MF), Gelatin ball+PVP coated MNPs (MF): cells were incubated in the gelatin balls in a magnetic field without MNPs, with citric acid-coated MNPs, and with PVP-coated MNPs, respectively. mRNA expression of all genes was normalized to the value of *ACTB* gene and showed as fold increase in Ct value compared to 2D (MF). Data were presented as mean ± standard error (n = 3). *, **, *** indicated $0.01 < p < 0.05$, $0.001 < p < 0.01$, and $p < 0.001$ respectively.

However, the mRNA expression of *RUNX2* gene was significantly enhanced in cells cultured inside the balls with PVP-coated MNPs compared to that cultured on 2D plates and inside balls without MNPs ($0.01 < p < 0.05$). Similarly, significant enhancement in the mRNA expression of *SPARC* gene was observed in cells cultured inside the balls with PVP-coated MNPs compared to those cultured on 2D plates ($0.01 < p < 0.05$) and inside the balls without MNPs ($p < 0.001$). The exclusive up-regulation of *RUNX2* and *SPARC* genes for hMSCs cultured inside the balls with PVP-coated MNPs might be due to the different amount of MNPs incorporation in the balls. There was more PVP-coated MNPs inside the balls, 3.66% of a ball, than citric acid-coated MNPs (1.91%), which resulted in a slightly stronger mechanical stimulation from the balls with PVP-coated MNPs. (Figure 6.1c) The expression of *RUNX2* gene, a central control gene, was mainly regulated by chemical signals and the mechanical stress. [56] Hence, although the cells in all groups were cultured in the same osteogenesis-inductive medium, a stronger mechanical stimulation applied to the cells cultured inside the balls with PVP-coated MNPs facilitates up-regulation of a higher level of the mRNA expression of *RUNX2* gene. [18] Moreover, *SPARC* gene, an osteoblast specific downstream gene, was regulated by *RUNX2* gene [56], therefore, its expression was in accordance with that of *RUNX2* gene, namely exclusively promoted for the cells cultured inside the balls with PVP-coated MNPs. (Figure 6.8) In addition, the impact of nanofiber topography on stem cell differentiation might also account for the different expression of osteogenesis-related genes in the cell-seeded balls with citric acid- or PVP- coated MNPs. Since non-uniform size distribution of electrospun nanofibers with PVP-coated MNPs facilitated spreading of the attached hMSCs (Figure S6.8iii) [57], osteogenesis of hMSCs were accordingly enhanced [50, 58] with the synergetic impact of osteogenesis-inductive medium, mechanical stimulation [50, 59, 60], and enhanced supply of inductive biomolecules during dynamic movement [61].

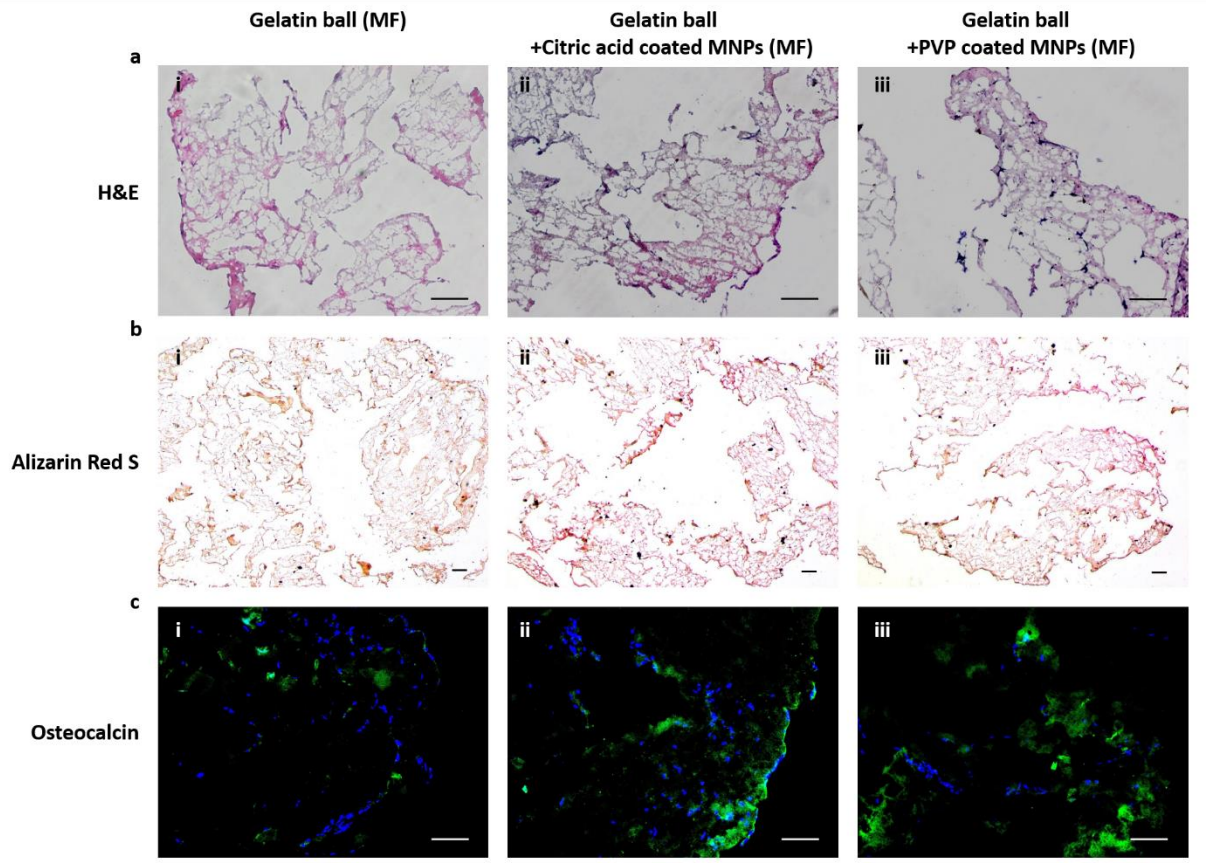

Figure 6.9 Histology and immunofluorescence images of hMSCs after induced osteogenesis for three weeks in the gelatin balls (i) without MNPs, or (ii) with citric acid-coated MNPs, or (iii) with PVP-coated MNPs, in the presence of an external magnetic field. (a) Hematoxylin and eosin (H&E) staining images. Blue: cell nuclei; Red: cytoplasm; Pink: collagen. (b) Alizarin Red S staining images. Orange: deposited calcium. (c) Osteocalcin immunofluorescence staining images. Green: FITC-labelled Osteocalcin; Blue: DAPI-labelled cell nuclei. Scale bar: 100 μm. Gelatin ball (MF), Gelatin ball+Citric acid coated MNPs (MF), Gelatin ball+PVP coated MNPs (MF): cells were incubated in the gelatin balls without MNPs, with citric acid-coated MNPs, and with PVP-coated MNPs in the presence of a magnetic field.

The mRNA expression of *SP7* gene and *BGLAP* gene were significantly enhanced in the cells cultured inside the balls with citric acid-coated MNPs and PVP-coated MNPs ($0.001 < p < 0.01$ for *SP7* gene expression between cells inside the balls with citric acid-coated MNPs and inside the balls without MNPs; $0.01 < p < 0.05$ for other comparisons). Since function of *SP7* gene, one important osteoblast-specific gene, was independent of *RUNX2* gene [56], the regulated signaling pathway of *SP7* gene might be also different from that of *RUNX2* gene when hMSCs were exposed to chemical and mechanical stimulations. Hence, the significantly enhanced mRNA expression of *SP7* gene was both seen in balls with citric acid- or PVP- coated MNPs. Furthermore, the expression of *BGLAP* gene, an osteoblast-specific downstream gene

whose protein expression was the second most abundant protein in bones, was regulated by *RUNX2* and *SP7* genes, therefore, its mRNA expression was consistent with that of *RUNX2* and *SP7* genes. [56] (Figure 6.8) The enhancement in osteogenesis for cells cultured inside the balls with citric acid- or PVP- coated MNPs was also confirmed with distinct red-stained calcium deposition and more FITC-labelled osteocalcin compared to that inside the balls without MNPs (Figure 6.9), which was in consistence with the difference shown in the mRNA expression of *BGLAP* gene (Figure 6.8).

Mechanical stimulation, scaffold surface topology, and chemical signals have been found to play a synergistic effect on enhancing osteogenesis of hMSCs, which was the case of electrospun film-derived balls with PVP-coated MNPs in the presence of an alternating magnetic field. (Table S2)

6.6 Conclusion

In this study, we have demonstrated that a 3D porous electrospun film-derived ball with incorporation of MNPs was biocompatible and could facilitate cell growth. It could be driven upward/downward along the wall of the container by an external alternating magnetic field. The synergetic effect of nanofiber topography, mechanical stimulation, dynamic culture, and inductive media enhanced the chondrogenesis of hMSCs cultured inside the electrospun film-derived balls with citric acid-coated MNPs and osteogenesis of hMSCs cultured inside the electrospun film-derived balls with PVP-coated MNPs. Hence, the magnetic field-responsive scaffolds together with an in-house rotating magnet device can be a novel system for study influence of multiple stimuli on stem cell differentiation *in vitro*.

SUPPLEMENTARY INFORMATION

Supplementary data please refer to “Supplementary information”.

ACKNOWLEDGEMENTS

HZ would like to acknowledge the financial support from ARC Discovery Project (DP160104632) and The Medical Advancement Without Animal (MAWA) Trust. JBZ thanks the IPE-UoA Scholarship (BES).

CONFLICT OF INTEREST

The authors declare no conflict of interest.

6.7 Reference

[1] Sensebé L, Krampera M, Schrezenmeier H, Bourin P, Giordano R. Mesenchymal stem cells for clinical application. Vox Sanguinis 2010;98:93-107.

[2] Squillaro T, Peluso G, Galderisi U. Clinical Trials with Mesenchymal Stem Cells: An Update. Cell Transplantation 2016;25:829-48.

[3] Filardo G, Madry H, Jelic M, Roffi A, Cucchiarini M, Kon E. Mesenchymal stem cells for the treatment of cartilage lesions: from preclinical findings to clinical application in orthopaedics. Knee Surgery, Sports Traumatology, Arthroscopy 2013;21:1717-29.

[4] McGonagle D, Baboolal TG, Jones E. Native joint-resident mesenchymal stem cells for cartilage repair in osteoarthritis. Nature Reviews Rheumatology 2017;13:719.

[5] Ondresik M, Maia FRA, Morais AD, Gertrudes AC, Bacelar AHD, Correia C, et al. Management of knee osteoarthritis. Current status and future trends. Biotechnology and Bioengineering 2017;114:717-39.

[6] Madrigal M, Rao KS, Riordan NH. A review of therapeutic effects of mesenchymal stem cell secretions and induction of secretory modification by different culture methods. Journal of Translational Medicine 2014;12:260.

[7] Shi Y, Wang Y, Li Q, Liu K, Hou J, Shao C, et al. Immunoregulatory mechanisms of mesenchymal stem and stromal cells in inflammatory diseases. Nature Reviews Nephrology 2018;14:493-507.

[8] Quarto RMD, Mastrogiacomo MP, Cancedda RMD, Kutepov SMMD, Mukhachev VMD, Lavroukov AMD, et al. Repair of Large Bone Defects with the Use of Autologous Bone Marrow Stromal Cells. The New England Journal of Medicine 2001;344:385-6.

[9] Yang C, Tibbitt MW, Basta L, Anseth KS. Mechanical memory and dosing influence stem cell fate. Nature Materials 2014;13:645.

[10] Higuchi A, Ling Q-D, Chang Y, Hsu S-T, Umezawa A. Physical Cues of Biomaterials Guide Stem Cell Differentiation Fate. Chemical Reviews 2013;113:3297-328.

[11] Gelmi A, Zhang J, Cieslar-Pobuda A, Ljunngren MK, Los MJ, Rafat M, et al. Electroactive 3D materials for cardiac tissue engineering. 2015. p. 94301T-T-7.

[12] Watt FM, Huck WTS. Role of the extracellular matrix in regulating stem cell fate. Nature Reviews Molecular Cell Biology 2013;14:467.

[13] Zhang J, Zhang H, Xu X. CHAPTER 17 Smart Materials to Regulate the Fate of Stem Cells. Smart Materials for Tissue Engineering: Applications: The Royal Society of Chemistry; 2017. p. 473-504.

[14] Ding S, Kingshott P, Thissen H, Pera M, Wang PY. Modulation of human mesenchymal and pluripotent stem cell behavior using biophysical and biochemical cues: A review. Biotechnology and Bioengineering 2017;114:260-80.

[15] Boda SK, Thrivikraman G, Basu B. Magnetic field assisted stem cell differentiation–role of substrate magnetization in osteogenesis. Journal of Materials Chemistry B 2015;3:3150-68.

[16] Parate D, Franco-Obregón A, Fröhlich J, Beyer C, Abbas AA, Kamarul T, et al. Enhancement of mesenchymal stem cell chondrogenesis with short-term low intensity pulsed electromagnetic fields. Scientific Reports 2017;7:9421.

[17] Choi JR, Yong KW, Choi JY. Effects of mechanical loading on human mesenchymal stem cells for cartilage tissue engineering. Journal of Cellular Physiology 2017;233:1913-28.

[18] Horner CB, Hirota K, Liu J, Maldonado M, Hyle Park B, Nam J. Magnitude-dependent and inversely-related osteogenic/chondrogenic differentiation of human mesenchymal stem

cells under dynamic compressive strain. Journal of Tissue Engineering and Regenerative Medicine 2018;12:e637-e47.

[19] Cochis A, Grad S, Stoddart MJ, Farè S, Altomare L, Azzimonti B, et al. Bioreactor mechanically guided 3D mesenchymal stem cell chondrogenesis using a biocompatible novel thermo-reversible methylcellulose-based hydrogel. Scientific Reports 2017;7:45018.

[20] Yi HG, Kang KS, Hong JM, Jang J, Park MN, Jeong YH, et al. Effects of electromagnetic field frequencies on chondrocytes in 3D cell-printed composite constructs. Journal of Biomedical Materials Research Part A 2016;104:1797-804.

[21] Amin HD, Brady MA, St-Pierre JP, Stevens MM, Overby DR, Ethier CR. Stimulation of Chondrogenic Differentiation of Adult Human Bone Marrow-Derived Stromal Cells by a Moderate-Strength Static Magnetic Field. Tissue Engineering Part A 2014;20:1612-20.

[22] Singh RK, Patel KD, Lee JH, Lee E-J, Kim J-H, Kim T-H, et al. Potential of Magnetic Nanofiber Scaffolds with Mechanical and Biological Properties Applicable for Bone Regeneration. PLOS ONE 2014;9:1-16.

[23] Chen H, Sun J, Wang Z, Zhou Y, Lou Z, Chen B, et al. Magnetic Cell–Scaffold Interface Constructed by Superparamagnetic IONP Enhanced Osteogenesis of Adipose-Derived Stem Cells. ACS Applied Materials & Interfaces 2018;10:44279-89.

[24] Meinert C, Schrobback K, Levett PA, Lutton C, Sah RL, Klein TJ. Tailoring hydrogel surface properties to modulate cellular response to shear loading. Acta Biomaterialia 2017;52:105-17.

[25] Steinmetz NJ, Aisenbrey EA, Westbrook KK, Qi HJ, Bryant SJ. Mechanical loading regulates human MSC differentiation in a multi-layer hydrogel for osteochondral tissue engineering. Acta Biomaterialia 2015;21:142-53.

[26] Mack JJ, Corrin AA, Lucato SLDE, Dunn JCY, Wu BW, Cox BN. Enhanced cell viability via strain stimulus and fluid flow in magnetically actuated scaffolds. Biotechnology and Bioengineering 2013;110:936-46.

[27] Shahin K, Doran PM. Tissue engineering of cartilage using a mechanobioreactor exerting simultaneous mechanical shear and compression to simulate the rolling action of articular joints. Biotechnology and Bioengineering 2012;109:1060-73.

[28] Zhang J, Yun S, Bi J, Dai S, Du Y, Zannettino ACW, et al. Enhanced multi-lineage differentiation of human mesenchymal stem/stromal cells within poly(N-isopropylacrylamide-acrylic acid) microgel-formed three-dimensional constructs. Journal of Materials Chemistry B 2018;6:1799-814.

[29] Aomatsu E, Takahashi N, Sawada S, Okubo N, Hasegawa T, Taira M, et al. Novel SCRG1/BST1 axis regulates self-renewal, migration, and osteogenic differentiation potential in mesenchymal stem cells. Scientific Reports 2014;4:3652.

[30] Fitter S, Gronthos S, Ooi SS, Zannettino ACW. The Mesenchymal Precursor Cell Marker Antibody STRO-1 Binds to Cell Surface Heat Shock Cognate 70. Stem Cells 2017;35:940-51.

[31] Lin M, Huang H, Liu Z, Liu Y, Ge J, Fang Y. Growth–Dissolution–Regrowth Transitions of Fe3O4 Nanoparticles as Building Blocks for 3D Magnetic Nanoparticle Clusters under Hydrothermal Conditions. Langmuir 2013;29:15433-41.

[32] Cullity BD. Elements of x-ray diffraction. 2d ed. Reading, Mass.: Addison-Wesley Pub. Co.; 1978.

[33] Panzavolta S, Gioffrè M, Focarete ML, Gualandi C, Foroni L, Bigi A. Electrospun gelatin nanofibers: Optimization of genipin cross-linking to preserve fiber morphology after exposure to water. Acta Biomaterialia 2011;7:1702-9.

[34] Chen W, Chen S, Morsi Y, El-Hamshary H, El-Newhy M, Fan C, et al. Superabsorbent 3D Scaffold Based on Electrospun Nanofibers for Cartilage Tissue Engineering. ACS Applied Materials & Interfaces 2016;8:24415-25.

[35] Boda SK, Thrivikraman G, Basu B. Magnetic field assisted stem cell differentiation – role of substrate magnetization in osteogenesis. Journal of Materials Chemistry B 2015;3:3150-68.

[36] Aixin C, A. CS, Pinyuan T, K. BA, Paweena U, M. KC, et al. Recombinant Extracellular Matrix Protein Fragments Support Human Embryonic Stem Cell Chondrogenesis. Tissue Engineering Part A 2018;24:968-78.

[37] Bosnakovski D, Mizuno M, Kim G, Takagi S, Okumura M, Fujinaga T. Chondrogenic differentiation of bovine bone marrow mesenchymal stem cells (MSCs) in different hydrogels: Influence of collagen type II extracellular matrix on MSC chondrogenesis. Biotechnology and Bioengineering 2006;93:1152-63.

[38] Rutgers M, Saris DB, Vonk LA, Rijen MHv, Akrum V, Langeveld D, et al. Effect of Collagen Type I or Type II on Chondrogenesis by Cultured Human Articular Chondrocytes. Tissue Engineering Part A 2013;19:59-65.

[39] Sawatjui N, Limpaiboon T, Schrobback K, Klein T. Biomimetic scaffolds and dynamic compression enhance the properties of chondrocyte- and MSC-based tissue-engineered cartilage. Journal of Tissue Engineering and Regenerative Medicine 2018;12:1220-9.

[40] Theocharis AD, Skandalis SS, Gialeli C, Karamanos NK. Extracellular matrix structure. Advanced Drug Delivery Reviews 2016;97:4-27.

[41] Kozlov PV, Burdygina GI. The Structure and Properties of Solid Gelatin and the Principles of Their Modification. Polymer 1983;24:651-66.

[42] Aldana AA, Abraham GA. Current advances in electrospun gelatin-based scaffolds for tissue engineering applications. International Journal of Pharmaceutics 2017;523:441-53.

[43] Chou S-F, Luo L-J, Lai J-Y, Ma DH-K. Role of solvent-mediated carbodiimide cross-linking in fabrication of electrospun gelatin nanofibrous membranes as ophthalmic biomaterials. Materials Science and Engineering: C 2017;71:1145-55.

[44] Ross CL, Siriwardane M, Almeida-Porada G, Porada CD, Brink P, Christ GJ, et al. The effect of low-frequency electromagnetic field on human bone marrow stem/progenitor cell differentiation. Stem Cell Research 2015;15:96-108.

[45] Green JD, Tollemar V, Dougherty M, Yan Z, Yin L, Ye J, et al. Multifaceted signaling regulators of chondrogenesis: Implications in cartilage regeneration and tissue engineering. Genes & Diseases 2015;2:307-27.

[46] Vining KH, Mooney DJ. Mechanical forces direct stem cell behaviour in development and regeneration. Nature Reviews Molecular Cell Biology 2017;18:728.

[47] Camarero-Espinosa S, Rothen-Rutishauser B, Foster EJ, Weder C. Articular cartilage: from formation to tissue engineering. Biomaterials Science 2016;4:734-67.

[48] Fahy N, Alini M, Stoddart MJ. Mechanical stimulation of mesenchymal stem cells: Implications for cartilage tissue engineering. Journal of Orthopaedic Research 2018;36:52-63.

[49] Kennedy KM, Bhaw-Luximon A, Jhurry D. Cell-matrix mechanical interaction in electrospun polymeric scaffolds for tissue engineering: Implications for scaffold design and performance. Acta Biomaterialia 2017;50:41-55.

[50] Guilak F, Cohen DM, Estes BT, Gimble JM, Liedtke W, Chen CS. Control of Stem Cell Fate by Physical Interactions with the Extracellular Matrix. Cell Stem Cell 2009;5:17-26.

[51] Luciani N, Du V, Gazeau F, Richert A, Letourneur D, Le Visage C, et al. Successful chondrogenesis within scaffolds, using magnetic stem cell confinement and bioreactor maturation. Acta Biomaterialia 2016;37:101-10.

[52] Rai V, Dilisio MF, Dietz NE, Agrawal DK. Recent strategies in cartilage repair: A systemic review of the scaffold development and tissue engineering. Journal of Biomedical Materials Research Part A 2017;105:2343-54.

[53] Zhang T, Gong T, Xie J, Lin SY, Liu Y, Zhou TF, et al. Softening Substrates Promote Chondrocytes Phenotype via RhoA/ROCK Pathway. ACS Applied Materials & Interfaces 2016;8:22884-91.

[54] Wimpenny I, Ashammakhi N, Yang Y. Chondrogenic potential of electrospun nanofibres for cartilage tissue engineering. Journal of Tissue Engineering and Regenerative Medicine 2012;6:536-49.

[55] Bhattacharjee A, Katti DS. Pore Alignment in Gelatin Scaffolds Enhances Chondrogenic Differentiation of Infrapatellar Fat Pad Derived Mesenchymal Stromal Cells. ACS Biomaterials Science & Engineering 2019;5:114-25.

[56] Kirkham G, Cartmell S. CHAPTER 13 Genes and Proteins Involved in the Regulation of Osteogenesis. Topics in Tissue Engineering; 2007;3.

[57] Shalumon KT, Binulal NS, Deepthy M, Jayakumar R, Manzoor K, Nair SV. Preparation, Characterization and Cell Attachment Studies of Electrospun Multi-scale Poly(caprolactone) Fibrous Scaffolds for Tissue Engineering. Journal of Macromolecular Science, Part A 2010;48:21-30.

[58] Baik KY, Park SY, Heo K, Lee K-B, Hong S. Carbon Nanotube Monolayer Cues for Osteogenesis of Mesenchymal Stem Cells. Small (Weinheim an der Bergstrasse, Germany) 2011;7:741-5.

[59] Park S-H, Sim WY, Min B-H, Yang SS, Khademhosseini A, Kaplan DL. Chip-Based Comparison of the Osteogenesis of Human Bone Marrow- and Adipose Tissue-Derived Mesenchymal Stem Cells under Mechanical Stimulation. PLOS ONE 2012;7:e46689.

[60] Henstock JR, Rotherham M, Rashidi H, Shakesheff KM, El Haj AJ. Remotely Activated Mechanotransduction via Magnetic Nanoparticles Promotes Mineralization Synergistically With Bone Morphogenetic Protein 2: Applications for Injectable Cell Therapy. Stem Cells Translational Medicine 2014;3:1363-74.

[61] Stiehler M, Bünger C, Baatrup A, Lind M, Kassem M, Mygind T. Effect of dynamic 3-D culture on proliferation, distribution, and osteogenic differentiation of human mesenchymal stem cells. Journal of Biomedical Materials Research Part A 2009;89A:96-107.

[62] Jin R, Lin B, Li D, Ai H. Superparamagnetic iron oxide nanoparticles for MR imaging and therapy: design considerations and clinical applications. Current Opinion in Pharmacology 2014;18:18-27.

[63] Lu X, Niu M, Qiao R, Gao M. Superdispersible PVP-Coated Fe3O4 Nanocrystals Prepared by a "One-Pot" Reaction. The Journal of Physical Chemistry B 2008;112:14390-4.

[64] Zhang N, Lock J, Sallee A, Liu H. Magnetic Nanocomposite Hydrogel for Potential Cartilage Tissue Engineering: Synthesis, Characterization, and Cytocompatibility with Bone Marrow Derived Mesenchymal Stem Cells. ACS Applied Materials & Interfaces 2015;7:20987-98.

[65] Wilhelm C, Gazeau F, Roger J, Pons JN, Bacri JC. Interaction of Anionic Superparamagnetic Nanoparticles with Cells: Kinetic Analyses of Membrane Adsorption and Subsequent Internalization. Langmuir 2002;18:8148-55.

[66] Huang X, Zhang F, Wang Y, Sun X, Choi KY, Liu D, et al. Design Considerations of Iron-Based Nanoclusters for Noninvasive Tracking of Mesenchymal Stem Cell Homing. ACS Nano 2014;8:4403-14.

[67] Huang D-M, Hsiao J-K, Chen Y-C, Chien L-Y, Yao M, Chen Y-K, et al. The promotion of human mesenchymal stem cell proliferation by superparamagnetic iron oxide nanoparticles. Biomaterials 2009;30:3645-51.

[68] Tsaroom A, Matyjaszewski K, Silverstein MS. Spontaneous core-sheath formation in electrospun nanofibers. Polymer 2011;52:2869-76.

Supplementary information

Enhanced Chondrogenesis and Osteogenesis by Embedding Human Mesenchymal Stem/Stromal Cells within A Magnetic-Field Responsive "Dancing" Ball

Jiabin Zhang[1], *Seonho Yun*[1], *Afshin Karami*[1], *Yuguang Du*[4], *Andrew Zannettino*[2, *], *Hu Zhang*[1, 3, *]

[1]School of Chemical Engineering, The University of Adelaide, Adelaide, SA 5005, Australia

[2]Adelaide Medical School, The University of Adelaide, Adelaide, SA 5001, Australia

[3]Henry E. Riggs School of Applied Life Sciences, Keck Graduate Institute, California, CA 91711, USA

[4]Institute of Process Engineering, Chinese Academy of Sciences, Beijing, 100190, China

*Corresponding authors: Prof. A. Zannettino (andrew.zannettino@adelaide.edu.au) and Prof. H. Zhang (hu_zhang@kgi.edu)

Prepared in publication format

6.1 Materials and methods

6.1.1 Magnetic nanoparticle synthesis

Magnetic nanoparticles (MNPs) were synthesized as described in a previous study. [1] Briefly, iron (III) chloride hexahydrate ($FeCl_3 \bullet 6H_2O$, 1.36 g, Sigma-Aldrich), sodium acetate anhydrous (NaAc, 1.2 g, Sigma-Aldrich), ethylenediaminetetraacetic acid disodium salt (EDTA-2Na, 0.068g, Ajax Finechem) were dissolved in ethylene glycol (40 mL, Sigma-Aldrich) and sonicated in an ultrasonic bath (Grant XUBA1) for 2 h. The homogenous mixture was transferred to a 50 mL hydrothermal autoclave reactor and heated at 200 ℃ overnight. After the synthesis, the precipitates were centrifuged and harvested in a 50 mL tube at 800 rcf for 15 min. The synthesized MNPs were then in turn washed with water and ethanol three times each and dried overnight at 50 ℃.

6.1.2 Surface coating

The synthesized MNPs were immersed either in poly (vinyl pyrrolidone) (PVP, 5 mg/mL, Sigma-Aldrich) aqueous solution or in citric acid (0.05 $_M$, Chem-supply) aqueous solution (pH = 5.5, adjusted by addition of ammonia solution (10%)) and sonicated for 5 min. After incubation for another 4 h, the MNPs were centrifuged at 800 rcf for 15 min. The supernatant was discarded and the coated MNPs were dried at 50 ℃ overnight.

6.1.3 Particle size measurement

The MNPs, citric acid coated MNPs, and PVP coated MNPs were homogenously dissolved in water at 0.5 mg/mL with the aid of sonication for 30 min, respectively. The particle size distribution was measured by dynamic light scattering (DLS) with a detected angle of 90° at 25 ℃ using a Zetasizer Nano ZS (Malvern).

6.1.4 Fabrication of scaffolds

Briefly, 8 (w/v) % of the electrospinning solution was prepared by dissolving gelatin (0.12 g, Sigma-Aldrich) in the co-solvent (1.5 mL, 1,1,1,3,3,3-Hexafluoro-2-propanol (HFIP, Sigma-Aldrich) : H_2O at a volumetric ratio of 39:1) at 40 ℃ for 2 h. Citric acid coated MNPs or PVP

coated MNPs were mixed well with the electrospinning solution by sonication treatment for 1 h. The electrospinning solution was left static for a few min to precipitate the excessive MNPs, after which an electrospinning solution with a saturated concentration of MNPs was obtained. The electrospinning solution with/without MNPs was then drawn into a 5 mL of plastic syringe (BD) and connected to a plastic pipeline equipped with a needle (Terumo) at a size of 23G. The electrospinning solution was driven down by a PHD ULTRA syringe pump (Harvard apparatus) towards a metal panel grounded to the earth. The distance between the metal panel and the needle tip was kept at 8 cm, while the injection rate was varied from 0.75 mL/h to 1.25 mL/h. The needle tip and the metal panel were separately connected with the positive and negative poles of a high voltage supplier (Glassman High Voltage). The electrospinning was performed at a high voltage supply ranging from 15 kV to 20 kV at room temperature. During the electrospinning, a glass slide was mounted on the metal panel to collect the electrospun nanofibers. The electrospun nanofibers were then imaged under an optical microscope to determine the optimal electrospinning parameters.

After electrospinning, the electrospun films were kept in a fume hood overnight to remove any remaining HFIP residue. Secondary large pores between the electrospun films were created by rolling a dermal roller equipped with 540 micro-needles on the film. Electrospun scaffold (3 mg) and ethanol (20 µL) were added into a 1.5 mL Eppendorf tube, and the scaffolds were spun to form a ball-like morphology. The balls were then dried at 50 °C overnight to remove ethanol and transferred to a glass bottle. Physical crosslinking of balls was performed by heating the dried balls at 190 °C for 2 h. Each gelatin ball was transferred back to a 1.5 mL Eppendorf tube for further crosslinking by immersing the ball in water for 20 min and the ball was freeze-dried in an Alpha 2-4 LD plus lyophilizer (Martin Christ) overnight. The crosslinked balls were then washed and sterilized in ethanol and dried at 50 °C overnight. The size of the balls was measured by a ruler and imaged to reveal the difference in the morphology among the balls

with/without incorporation of MNPs. In addition, magnetic force-driven movement of the balls with MNPs incorporation were examined at a dried condition or in water by an external magnet.

6.1.5 Fiber diameter and pore size measurement

20 nanofibers and 60 pores created among the neighboring nanofibers were randomly selected from each SEM image and 5 SEM images were processed with image J to measure the nanofiber diameter and the pore area. In addition, the secondary pores were imaged with an Axio Vert. A1 inverted microscope (Zeiss) and the averaged diameter was calculated by randomly processing 60 pores with image J.

6.1.6 Biocompatibility of magnetic nanoparticles

Approximately 1×10^4 of hMSCs were seeded onto each well of a 96-well plate and cultured with complete cell culture medium (200 μL, α-modified minimum essential medium (MEM, Sigma-Aldrich) with Gibco fetal bovine serum (FBS, 10 (v/v)%, Thermo Fisher) and 1× additive's (ADDs) (L-glutamine (2×10^{-3} M, JRH), penicillin-streptomycin (50 U/mL- 50 μg/mL, CSL), HEPES (1.5×10^{-2} M, Life Technologies), sodium pyruvate (1×10^{-3} M, Sigma-Aldrich)) at 37 °C in a humidified incubator containing 5 % of CO_2. After incubation overnight, half of the medium was replaced by fresh complete medium containing MNPs, citric acid- coated MNPs, or PVP- coated MNPs with a final particle concentration ranging from 0 to 10 μg/mL. The cells were further cultured for an additional 24 h, and imaged with a CKX41 fluorescent microscope (Olympus). In addition, cells in the 96-well plate were further incubated for another 4 h after gently washing with 1× Dulbecco's phosphate-buffered saline (DPBS, Sigma-Aldrich) before adding complete culture medium (100 μL) and 3-(4,5-Dimethylthiazol-2-yl)-2,5-diphenyltetrazolium bromide (MTT, 10 μL, 5 mg/mL, Thermo Fisher) into each well. The medium in each well of the 96-well plate was replaced with dimethyl sulfoxide (DMSO, 100 μL, Chem-Supply) to dissolve the formed purple crystals within cells. The absorbance of the solution in the 96-well plate was then read by an iMarkTM microplate reader (BIO-RAD)

at a wavelength of 595 nm. The absorbance values were normalized to that without the addition of MNPs and presented as the cell viability.

6.2 Results and discussion

6.2.1 Characterization of magnetic nanoparticles

To confirm successful synthesis of magnetic nanoparticles (MNPs), X-ray diffraction (XRD) was performed. From the XRD data, it was observed that the peaks occurred at 2θ = 30.06 °, 35.52 °, 43.06 °, 53.8 °, 57.06 °, 62.76 °, and 74.18 ° (Figure S6.2a), consistent with the standard XRD pattern of Fe_3O_4 in JCPDS card No.19-629 [1]. To keep the magnetic nanoparticles stable in the organic solvent, citric acid [2] and poly (vinyl pyrrolidone) (PVP) [3] are two common surfactants for coating MNPs prior to electrospinning. However, the mechanism of stabilization of MNPs by citric acid was different from that by PVP. Citric acid facilitates stabilization of citric acid-coated MNPs in both polar and non-polar solvents due to free carboxylate groups (COO^-). The MNPs with free carboxylate groups has a negative charge, which induces sufficient electrostatic repulsion among citric acid-coated MNPs to overcome the attraction generated by the intrinsic magnetism of MNPs. [2] In contrast, the amphiphilicity of PVP helps stabilizing the PVP-coated MNPs distributed in both polar and non-polar solvents instead of electrostatic repulsion due to a neutral property of PVP. [4] Dynamic light scattering was then used as an indirect method to confirm coating of citric acid or PVP on the surface of MNPs. An increase in the average particle size of citric acid-coated MNPs (140.8 nm) and PVP-coated MNPs (237.7 nm) compared to that without coating (119.7nm) confirmed successful coating of citric acid or PVP onto the MNPs (Figure S6.2b). Moreover, the narrowest particle distribution of the citric acid-coated MNPs indicated that the citric acid-coated MNPs had the most uniform size and was very stable in water. However, the widest particle size distribution of PVP-coated MNPs may be ascribed to different length of polymer chains of PVP, due to various degrees of polymerization in producing PVP. Since the polymer chains of PVP on the surface of MNPs may interact with each other to induce aggregation of MNPs at a high concentration, a peak

corresponding to a large particle size was observed for PVP-coated MNPs. (Figure S6.2b) The aggregation of PVP-coated MNPs was less severe than that of MNPs without any coating. (Figure S6.2b)

6.2.2 Endocytosis and cell viability

After incubation with MNPs at different concentrations for 24 h, hMSCs exhibited a normal fibroblast-like morphology, similar to those cultured in the complete medium without MNPs. However, red particles were seen within the cells cultured with MNPs, citric acid-coated MNPs, and PVP-coated MNPs at a concentration of 10 μg/mL, indicating that MNPs were uptaken by hMSCs through the endocytosis [5-7] with the endocytosed Fe_3O_4 nanoparticles oxidized into Fe_2O_3 [8]. (Figure S6.3a) Moreover, the MTT results indicated excellent biocompatibility of MNPs at various concentration for hMSCs. (Figure S6.3b)

6.2.3 Optimization of electrospinning parameters

The process for preparing electrospun films and film-derived balls with/without MNPs incorporation was shown in Figure S6.1. Since MNPs might become unstable and precipitate at a high voltage, the electrospinning operation was executed in a short time. No significant difference was observed when electrospinning the gelatin/citric acid-coated MNPs hybrid with an injection rate increasing from 0.75 mL/h to 1.25 mL/h at a fixed voltage supply of 15 kV and a fixed collective distance of 8 cm (Figure S6.4a-c). A precipitation was clearly seen in Figure S6.4 d and e when increasing the applied voltage from 15 kV up to 20 kV and keeping the injection rate at 1 mL/h and the collective distance at 8 cm. As the voltage supply increased, the MNPs became unstable due to relatively high electrostatic interactions. (Figure S6.4) Hence, to rapidly electrospin continuous nanofibers without beads and avoid precipitation of citric acid or PVP-coated MNPs, an injection rate of 1.25 mL/h and a high voltage of 15 kV were determined as the optimal parameters and applied for all electrospinning processes.

6.2.4 Characterization of electrospun nanofibers with/without MNPs

The SEM images at a lower magnification revealed the successful electrospinning of nanofiber in the absence of beads. (Figure S6.5i) At a higher magnification, the surface of the nanofibers without MNPs was smooth, while citric acid-coated MNPs or PVP-coated MNPs were clearly seen within the nanofibers. (Figure S6.5ii)

When the needle outer surface was connected to the positive pole of a high voltage supply, the gelatin polymer in the solution within the needle was repelled into the center due to its positive charge, while the citric acid-coated MNPs with an overall negative surface charge were distributed adjacent to the needle surface because of the electrostatic attraction. [9] Meanwhile, negatively charged citric acid-coated MNPs can interact with positively charged gelatin polymer, allowing them to be successfully embedded inside the electrospun nanofibers with a slight increase in the electrospun nanofiber diameter. (Figure S6.5b and Figure S6.5d) On the contrary, overall charge of PVP-coated MNPs was positive since PVP was neutral. Hence, PVP-coated MNPs were pushed into the center due to electrostatic repulsion induced by the positive pole of the high voltage supply and the positively charged gelatin macromolecules. However, PVP-coated MNPs moved further into the center than gelatin polymers due to their small molecular weight compared to gelatin macromolecules. This made the PVP-coated MNPs more easily aggregate and initiate precipitation, which may block the nozzle and narrow the inner diameter of the electrospinning needle, accordingly leading to a decrease in the diameter of the electrospun nanofibers. When PVP-coated MNPs aggregates were accumulated to a high level near the nozzle, the PVP coated-MNPs were sprayed onto the electrospun films, and a normal electrospinning resumed. Since this process was continuously repeated during electrospinning the gelatin and PVP-coated MNPs hybrid, the diameter of the electrospun nanofibers in the electrospun films with PVP-coated MNPs had a wide distribution. (Figure S6.5c and Figure S6.5d)

Although majority of the pores created among neighboring electrospun nanofibers inside the electrospun films with/without MNPs were less than 5 μm^2 (Figure S6.5e), with the aid of a

dermal roller equipped with 540 micro-needles, the secondary pores generated among the electrospun films were approximately 65.5 μm in diameter (Figure S6.4f), which allowed better cell penetration and migration inside the electrospun films-derived balls.

6.3 Reference

[1] Lin M, Huang H, Liu Z, Liu Y, Ge J, Fang Y. Growth–Dissolution–Regrowth Transitions of Fe3O4 Nanoparticles as Building Blocks for 3D Magnetic Nanoparticle Clusters under Hydrothermal Conditions. Langmuir 2013;29:15433-41.

[2] Singh RK, Patel KD, Lee JH, Lee E-J, Kim J-H, Kim T-H, et al. Potential of Magnetic Nanofiber Scaffolds with Mechanical and Biological Properties Applicable for Bone Regeneration. PLOS ONE 2014;9:1-16.

[3] Jin R, Lin B, Li D, Ai H. Superparamagnetic iron oxide nanoparticles for MR imaging and therapy: design considerations and clinical applications. Current Opinion in Pharmacology 2014;18:18-27.

[4] Lu X, Niu M, Qiao R, Gao M. Superdispersible PVP-Coated Fe3O4 Nanocrystals Prepared by a "One-Pot" Reaction. The Journal of Physical Chemistry B 2008;112:14390-4.

[5] Zhang N, Lock J, Sallee A, Liu H. Magnetic Nanocomposite Hydrogel for Potential Cartilage Tissue Engineering: Synthesis, Characterization, and Cytocompatibility with Bone Marrow Derived Mesenchymal Stem Cells. ACS Applied Materials & Interfaces 2015;7:20987-98.

[6] Wilhelm C, Gazeau F, Roger J, Pons JN, Bacri JC. Interaction of Anionic Superparamagnetic Nanoparticles with Cells: Kinetic Analyses of Membrane Adsorption and Subsequent Internalization. Langmuir 2002;18:8148-55.

[7] Huang X, Zhang F, Wang Y, Sun X, Choi KY, Liu D, et al. Design Considerations of Iron-Based Nanoclusters for Noninvasive Tracking of Mesenchymal Stem Cell Homing. ACS Nano 2014;8:4403-14.

[8] Huang D-M, Hsiao J-K, Chen Y-C, Chien L-Y, Yao M, Chen Y-K, et al. The promotion of human mesenchymal stem cell proliferation by superparamagnetic iron oxide nanoparticles. Biomaterials 2009;30:3645-51.

[9] Tsaroom A, Matyjaszewski K, Silverstein MS. Spontaneous core-sheath formation in electrospun nanofibers. Polymer 2011;52:2869-76.

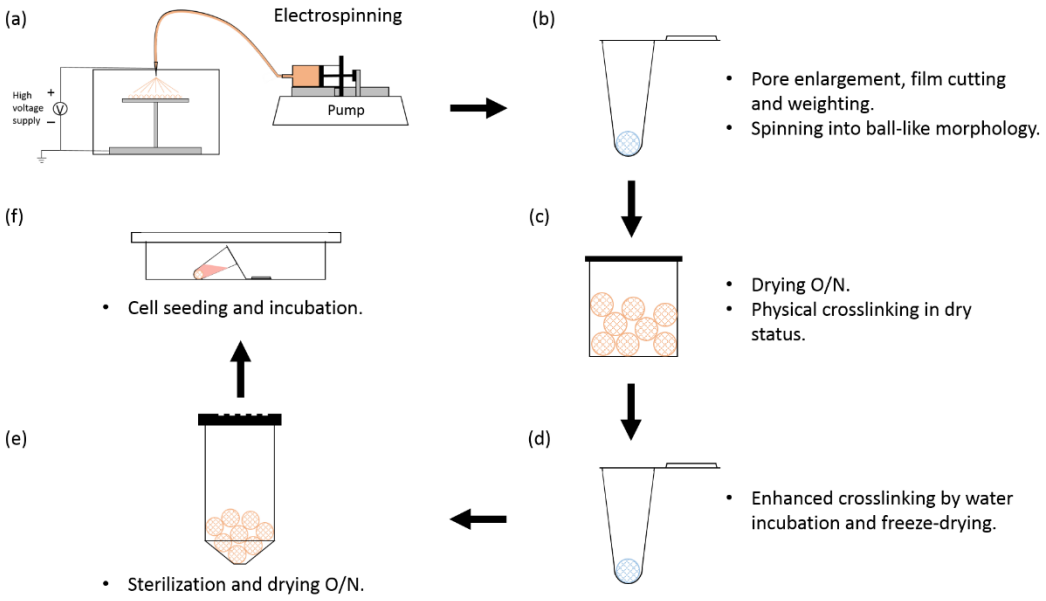

Figure S6.1 Fabrication of electrospun gelatin films-derived balls for embedding cells. (a) Electrospinning a gelatin solution with/without MNPs to produce electrospun films. (b) Rolling the electrospun films into a ball-like morphology. (c) Physical crosslinking electrospun film-derived balls. (d) Enhancing the crosslinking of electrospun film-derived balls. (e) Sterilizing the balls before seeding cells. (f) Seeding cells into the balls and incubating them in the cell culture media.

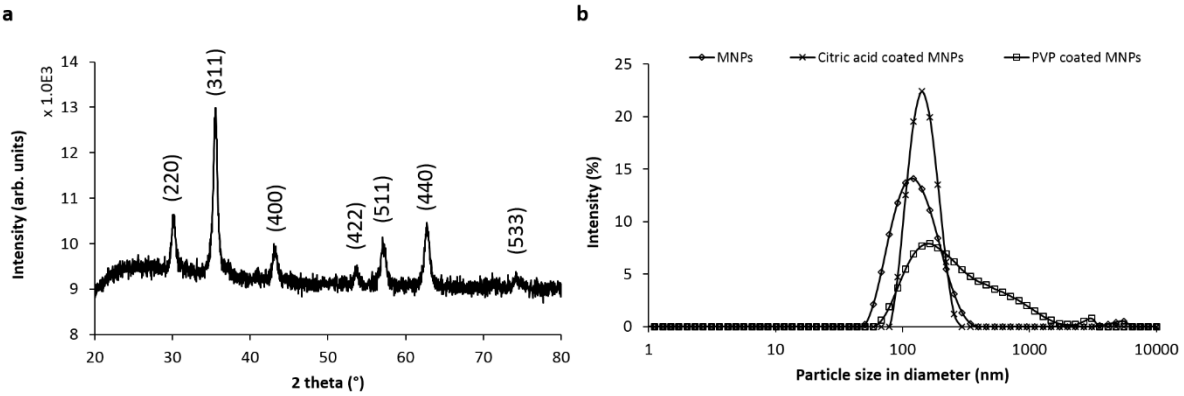

Figure S6.2 (a) XRD pattern of Fe_3O_4. (b) Particle size distribution of MNPs by DLS measurement.

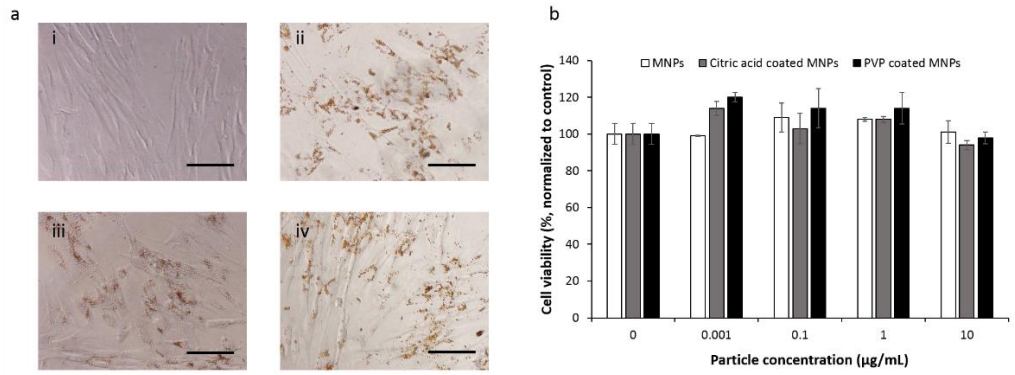

Figure S6.3 (a) Optical images of hMSCs cultured in the complete medium after 24 h (i) without MNPs, or with 10 μg/mL (ii) MNPs, (iii) citric acid-coated MNPs, and (iv) PVP-coated MNPs. Scale bar: 100 μm. (b) Cell viability of hMSCs cultured with MNPs at various concentrations. Cells cultured in the complete medium without MNPs were used as the control. All data were normalized to the absorbance value of the control and presented as mean ± standard error, $n = 3$.

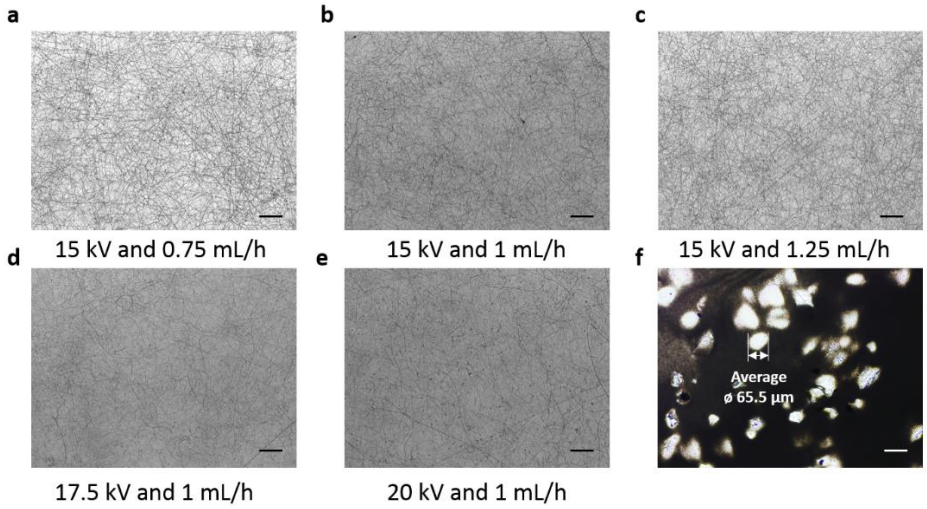

Figure S6.4 Optical microscopy images of electrospun films generated by electrospinning gelatin and citric acid coated MNPs hybrid at varying voltage ((a-c) 15 kV; (d) 17.5 kV; (e) 20 kV) and injection rate ((a) 0.75 mL/h; (b,d-e) 1 mL/h; (c) 1.25 mL/h). The electrospinning was performed with 23G needle and 8 cm of collective distance at room temperature. (f) Generation of the secondary pores by rolling a dermal roller equipped with 540 microneedles on the electrospun films. The average diameter of the secondary pores was around 65.5 μm, which was calculated by random measurement of 60 pores with image J. Scale bar: 100 μm.

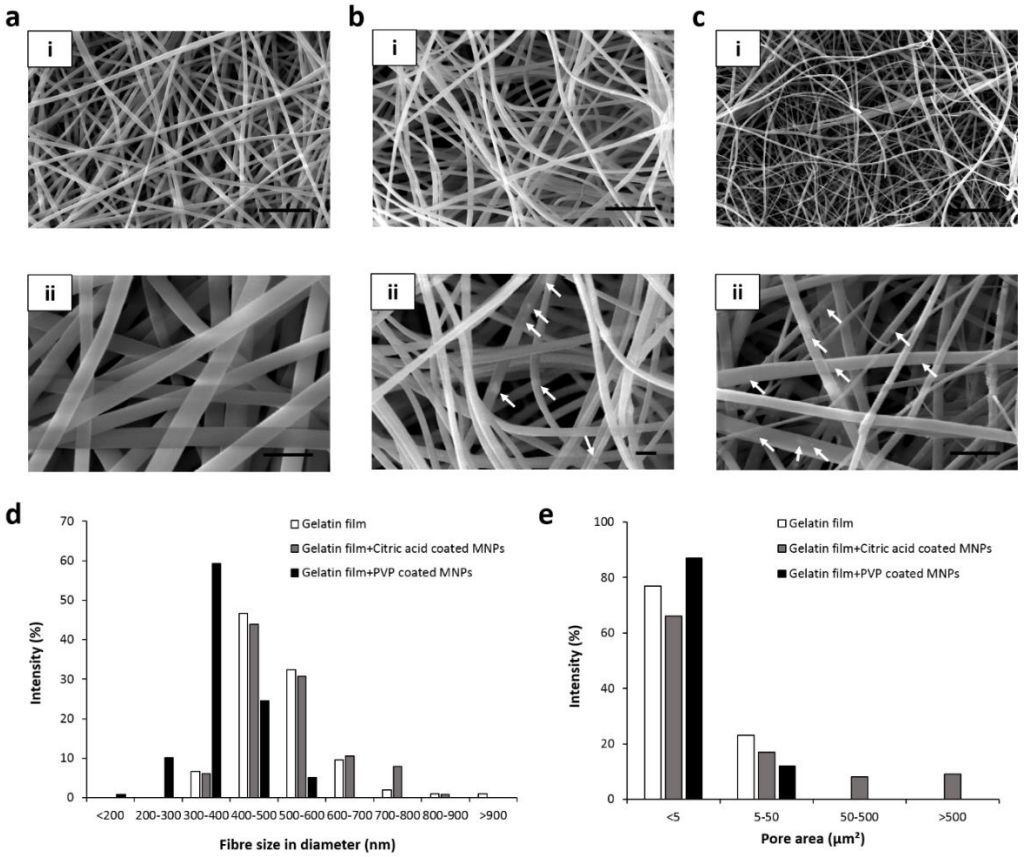

Figure S6.5 SEM images of electrospun films fabricated (a) without magnetic nanoparticles (MNPs) incorporation, (b) with incorporation of citric acid-coated MNPs, (c) with incorporation of PVP-coated MNPs at 15kV voltage, 1.25 mL/h injection rate with (i) a lower magnification (scale bar: 5 µm) and (ii) a higher magnification (scale bar: 1 µm). Red arrows point to the MNPs. (d) Size distribution of nanofibers and (e) pore size distribution of the electrospun gelatin films with or without MNPs.

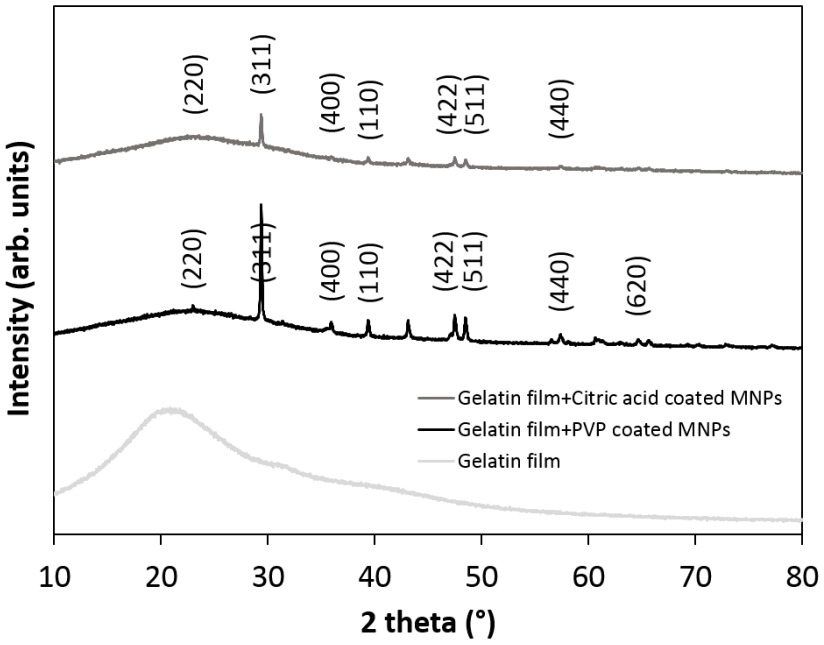

Figure S6.6 XRD pattern of electrospun gelatin films without MNPs incorporation, electrospun gelatin films with the incorporation of citric acid coated MNPs, and electrospun gelatin films with the incorporation of PVP coated MNPs.

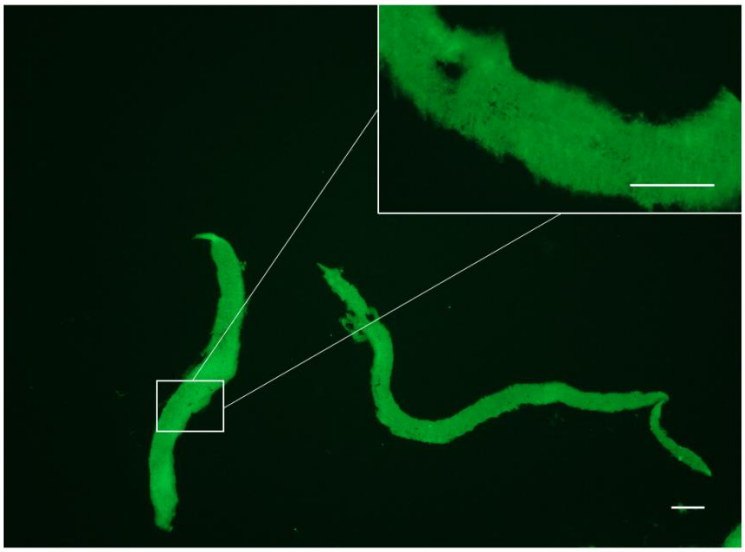

Figure S6.7 Collagen 2A1 immunofluorescence staining images of cross-sectioned electrospun films without cells at the lower magnification and the higher magnification (the up-right inset). The porous structure could be seen across the electrospun scaffolds. Green: FITC-labelled collagen 2A1. Scale bar: 100 µm.

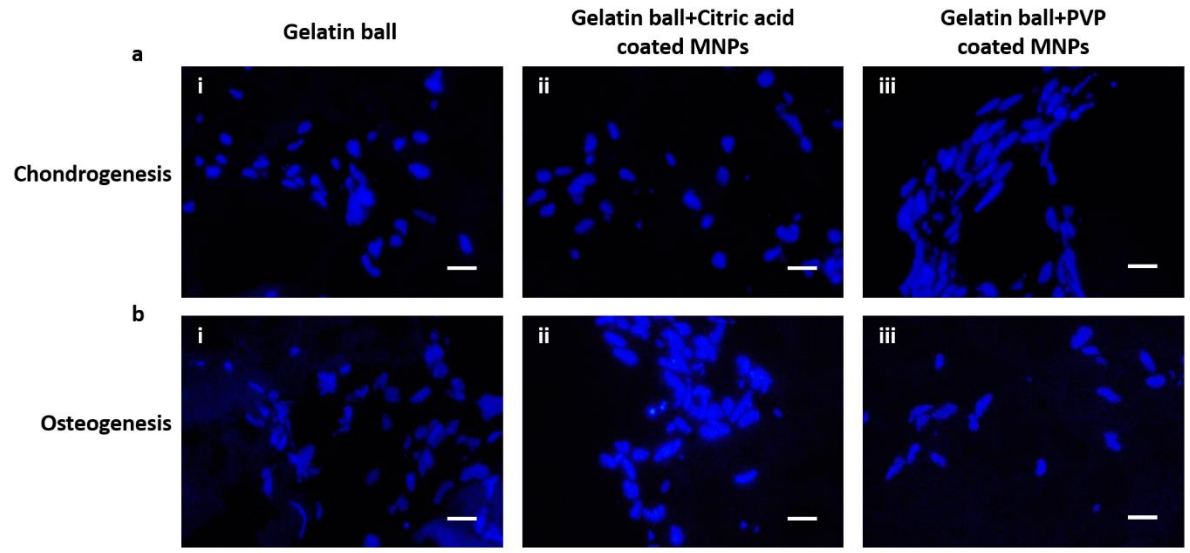

Figure S6.8 Nuclei morphology of cells induced (a) chondrogenesis or (b) osteogenesis inside the electrospun film-derived balls (i) without MNPs, or (ii) with citric acid-coated MNPs, or (iii) with PVP coated MNPs. Blue: DAPI-stained cell nuclei. Scale bar: 20 µm

Table S6.1 Specific primers for Real-Time PCR.

Genes	**Primer sequence (5'→3')**
ACTB	Forward: GATCATTGCTCCTCCTGAGC Reverse: GTCATAGTCCGCCTAGAAGCAT
SOX9	Forward: AGGTGCTCAAAGGCTACGAC Reverse: GCTTCTCGCTCTCGTTCAGA
ACAN	Forward: CTGCTTCCGAGGCATTTC Reverse: GCTCGGTGGTGAACTCTAGC
COL 2A1	Forward: ATCACAGGCTTCCATTGACC Reverse: CTCCACAGCATCGATGTCAC
COL 10A1	Forward: AATGCCCACAGGCATAAAAG Reverse: AGGACTTCCGTAGCCTGGTT
RUNX2	Forward: GTGGACGAGGCAAGAGTTTCA Reverse: CATCAAGCTTCTGTCTGTGCC
BGLAP	Forward: ATGAGAGCCCTCACACTCCTCG Reverse: GTCAGCCAACTCGTCACAGTCC
SP7	Forward: CTGCGGGACTCAACAACTCT Reverse: GAGCCATAGGGGTGTGTCAT
SPARC	Forward: ATGTGCATCAGTCGCAAGAA Reverse: AAGTCTCTGGTTTGCCATCG

Table S6.2 Synergetic effect of physical and biochemical stimuli on the cell differentiation of mesenchymal stromal/stem cells cultured in different systems.

System type	Induction type	Inductive biomolecules	Fiber topography	Materials	Magnetic field	Mechanical stimulation	Dynamic culture
Electrospun film-derived ball	Chondrogenesis	+[1]	+	+	+	N/A[2]	N/A
	Osteogenesis	+	N/A	N/A	N/A	N/A	N/A
Electrospun film-derived ball with citric acid-coated MNPs	Chondrogenesis	+	+	+	+	+	+
	Osteogenesis	+	N/A	N/A	N/A	+	+
Electrospun film-derived ball with PVP-coated MNPs	Chondrogenesis	+	–[3]	+	+	+	+
	Osteogenesis	+	+	N/A	N/A	+	+
Cell pellet	Chondrogenesis	+	N/A	N/A	+	N/A	N/A
2D tissue culture plate	Osteogenesis	+	N/A	N/A	N/A	N/A	N/A

[1] Positive influence
[2] Not applicable or no influence
[3] Negative influence

CHAPTER VII

CONCLUSIONS AND FUTURE DIRECTIONS

7.1 Conclusions

The distinct physiological structure of cartilage and bone makes it challenging to achieve promising osteochondral regeneration with current single therapeutic strategies for treatment of OA. Smart materials as ECM-mimicking scaffolds/hydrogels that can actively regulate the fate of stem cells according to external stimuli in addition to conventional structural support have inspired researchers to explore their potential application in stem cell therapy for OA treatment. In this thesis, two smart materials, a thermo-responsive hydrogel and a magnetic field-responsive scaffold, were fabricated either as an *in-vitro* platform for stem cell differentiation or as a vehicle for *in-vivo* delivery of stem cells for cartilage and bone tissue regeneration.

In contrast to conventional methods of fabrication of cell aggregates, uniform-sized cell aggregates without a necrotic centre were generated by 3D hydrogel-mediated cell aggregation inside the thermo-responsive p(NIPAAm-AA) hydrogel. As an *in-vitro* platform for stem cell differentiation (Chapter 3), MSCs cultured in the hydrogel were induced to form cell aggregates *in situ* with enhanced multi-lineage differentiation avoiding extra procedures for harvest and embedment of cell aggregates into new supporting systems.

Although a variety of thermo-responsive hydrogels were fabricated and studied, very few of such soft hydrogels are reported to apply in cartilage and bone tissue engineering due to their soft mechanical strength. In our study (Chapter 4), by contrast, a thermo-responsive ultra-soft p(NIPAAm-AA) hydrogel was used as a delivery vehicle for injection of cell aggregates into an osteochondral defect site. In addition to synergy of enhanced paracrine effects and cell differentiation, such soft hydrogels benefited to osteochondral regeneration by facilitating penetration of endogenous stem/progenitor cells into the hydrogels and remodeling of ECMs.

Cell migration inside the thermo-responsive 3D hydrogel was evidenced over an extended period, revealing its involvement in cell aggregation. The resultant MSC-derived chondrocytes were harvested and used as building blocks for fabrication of a neo-cartilage patch *in vitro* by mechanical forcing- and spatial confinement- mediated cell fusion. Integration of such an *in-*

vitro engineered living neo-cartilage patch into the irregular defects by cell fusion may be a novel strategy for superficial cartilage regeneration *in vivo*. (Chapter 5)

By coupling magnetic field-responsive scaffolds with an alternating magnetic field (Chapter 6), a series of external stimuli can be introduced to stem cells, therefore, whose fate was able to be regulated. With such an *in-vitro* smart platform, influence of various factors on differentiation of stem cells can be systematically studied. Moreover, enhanced chondrogenesis and osteogenesis of MSCs in a magnetic field-responsive scaffold upon exposure of an alternating magnetic field might also hold potential promise in *in-vivo* cartilage and bone regeneration.

7.2 Future directions

Despite of promising osteochondral regeneration *in vivo* (Chapter 4), non-biodegradability of p(NIPAAm-AA) might be a potential issue. It was notable that there was no visible p(NIPAAm-AA) hydrogel remaining in the regenerated cartilage and bone. Therefore, a further study systematically tracking distribution of injected p(NIPAAm-AA) *in vivo* might be necessary before clinical trials. In addition, the *in-vivo* expression of chondrogenesis-related and osteogenesis-related genes might also need to be evaluated in the further study.

Even though theoretical integration of an *in-vitro* engineering neo-cartilage patch into superficial defects of cartilage by mechanical forcing-mediated cell fusion might be applicable, the complex *in-vivo* environment still makes it challenging. (Chapter 5) Therefore, when considering *in-vivo* application for cartilage regeneration, a series of potential issues need to be addressed. For example, retention of such a neo-cartilage patch *in situ* might require the assistance of a medical glue [1, 2] or suture [3].

As Chapter 2 indicates, in addition to the potential application of a magnetic field in targeting delivery, regulation of stem cell fate by a magnetic field was also previously reported. However, a systematic study of influences of the magnetic field on fate of stem cells using a consistent system is still necessary. When considering the synergy of other factors, requirements of such a system become demanding. Since the magnet and its distance to cells and the rotating

frequency are all controllable in our platform (Chapter 6), the influence of the magnetic field including intensity and frequency on chondrogenesis and osteogenesis of MSCs can be further studied *in vitro* using the magnetic field-responsive scaffolds and the in-house rotating magnet device. It is known that pre-conditioned MSCs are capable of achieving a higher cell survival rate and enhance biological functions after implanting *in vivo*. [4] Hence, with synergy of a series of external stimuli, the pre-chondrogenesis induced MSCs may advance in restoration of an osteochondral defect by cartilage regeneration and endochondral ossification. [5, 6] However, an *in-vitro* study on pro-inflammation and degradation of magnetic field-responsive scaffolds should be performed prior to implantation of chondrogenesis-induced MSCs and magnetic field-responsive scaffolds *in vivo*.

7.3 Reference

[1] Wang DA, Varghese S, Sharma B, Strehin I, Fermanian S, Gorham J, et al. Multifunctional chondroitin sulphate for cartilage tissue-biomaterial integration. Nature Materials 2007;6:385-92.

[2] Sharma B, Fermanian S, Gibson M, Unterman S, Herzka DA, Cascio B, et al. Human Cartilage Repair with a Photoreactive Adhesive-Hydrogel Composite. Science Translational Medicine 2013;5:167ra6.

[3] Gomoll AH, Probst C, Farr J, Cole BJ, Minas T. Use of a Type I/III Bilayer Collagen Membrane Decreases Reoperation Rates for Symptomatic Hypertrophy After Autologous Chondrocyte Implantation. The American Journal of Sports Medicine 2009;37:20S-23S.

[4] Richardson SM, Hoyland JA, Mobasheri R, Csaki C, Shakibaei M, Mobasheri A. Mesenchymal Stem Cells in Regenerative Medicine: Opportunities and Challenges for Articular Cartilage and Intervertebral Disc Tissue Engineering. Journal of Cellular Physiology 2010;222:23-32.

[5] Fahy N, Alini M, Stoddart MJ. Mechanical stimulation of mesenchymal stem cells: Implications for cartilage tissue engineering. Journal of Orthopaedic Research 2018;36:52-63.

[6] Camarero-Espinosa S, Rothen-Rutishauser B, Foster EJ, Weder C. Articular cartilage: from formation to tissue engineering. Biomaterials Science 2016;4:734-67.

APPENDICES

Statement of Authorship

Title of Paper	CHAPTER 17 Smart Materials to Regulate the Fate of Stem Cells.
Publication Status	☑ Published ☐ Accepted for Publication ☐ Submitted for Publication ☐ Unpublished and Unsubmitted work written in manuscript style
Publication Details	Zhang, J.; Zhang, H.; Xu, X., In Smart Materials for Tissue Engineering: Applications. The Royal Society of Chemistry: 2017, pp 473-504. doi: 10.1039/9781788010542-00473.

Principal Author

Name of Principal Author (Candidate)	Jiabin Zhang
Contribution to the Paper	Literature review and book chapter writing.
Overall percentage (%)	80%
Certification:	This paper reports on original research I conducted during the period of my Higher Degree by Research candidature and is not subject to any obligations or contractual agreements with a third party that would constrain its inclusion in this thesis. I am the primary author of this paper.
Signature	Date 26/07/2019

Co-Author Contributions

By signing the Statement of Authorship, each author certifies that:

i. the candidate's stated contribution to the publication is accurate (as detailed above);

ii. permission is granted for the candidate in include the publication in the thesis; and

iii. the sum of all co-author contributions is equal to 100% less the candidate's stated contribution.

Name of Co-Author	Hu Zhang
Contribution to the Paper	Proof read the manuscript, experiment design, and evaluation of data.
Signature	Date 15-07-2019

Name of Co-Author	Xia Xu
Contribution to the Paper	Proof read the manuscript and evaluation.
Signature	Date 26-July-2019

Please cut and paste additional co-author panels here as required.

Downloaded by Institute of Process Engineering, Chinese Academy of Sciences on 1/3/2019 5:15:03 AM.
Published on 03 May 2017 on https://pubs.rsc.org | doi:10.1039/9781788010542-00473

CHAPTER 17

Smart Materials to Regulate the Fate of Stem Cells

JIABIN ZHANG[a], HU ZHANG*[a] AND XIA XU[b]

[a]School of Chemical Engineering, The University of Adelaide, Adelaide, SA 5005, Australia; [b]Institute of Process Engineering, Chinese Academy of Sciences, Beijing, 100190, China
*E-mail: hu.zhang@adelaide.edu.au

17.1 Introduction

Many serious diseases, such as Parkinson's disease (PD), acute myocardial infarction (MI), and acute low back pain (LBP), are caused by either tissue/organ degeneration or accident damage and they interrupt the normal daily activities of patients.[1–3] Stem cell therapy, as a potential treatment for these diseases, is currently being intensively explored by many researchers.[4] Stem cells, such as embryonic stem cells (ESCs) or adult stem cells, together with biocompatible support materials are injected into the defect or damaged site, allowing stem cells to proliferate and then differentiate into target cells *in situ*. In the last decades, more and more researchers have focused on the applicability of the implanted materials for stem cell cultivation.[5] Scaffolds or hydrogels generated from various materials are modified to mimic the properties of the extracellular matrix (ECM),[6] which is an essential component of the surrounding environment of cells to provide mechanical supports for stem cells and facilitate signal communications between cells or cells–ECM. However, most of the reported materials provide passive supports for the stem cells,[7] while only a few have functions of active regulation in the proper differentiation of stem cells.[8]

Smart Materials No. 25
Smart Materials for Tissue Engineering: Applications
Edited by Qun Wang
© The Royal Society of Chemistry 2017
Published by the Royal Society of Chemistry, www.rsc.org

View Online

Downloaded by Institute of Process Engineering, Chinese Academy of Sciences on 1/3/2019 5:15:03 AM.
Published on 03 May 2017 on https://pubs.rsc.org | doi:10.1039/9781788010542-00473

Smart materials, just like traditional normal biomaterials, can provide ECM-like topography for stem cells. More importantly, smart materials can be physically or chemically modified by actively responding to external stimuli, such as temperature, electricity, pH, shear stress, light and ions.[9,10] Smart materials with finely tuned properties can be utilised to accurately and directly regulate differentiation of the encapsulated stem cells (Figure 17.1) because stem cell differentiation, to a great extent, depends on the mechanical/chemical properties of the surrounding microenvironment.[11,12]

Smart materials are divided into groups according to external stimuli, such as thermosensitive (temperature), thixotropic (shear stress), conductive/electroactive (electricity), photo-responsive (light), pH-responsive (pH) and others. They are widely reported to be used as injectable materials in the liquid form of hydrogels containing stem cells, which can turn into the gel form and encapsulate stem cells inside the hydrogels in response to temperature, light, shear stress, or pH after injection.[13,14] These hydrogels further recruit internal chemical growth factors or signal factors, or receive physical simulations *in situ*[9] so that the encapsulated stem cells are differentiated into cell types in the damaged site for effective repair and regeneration.[1] Stem cell differentiation

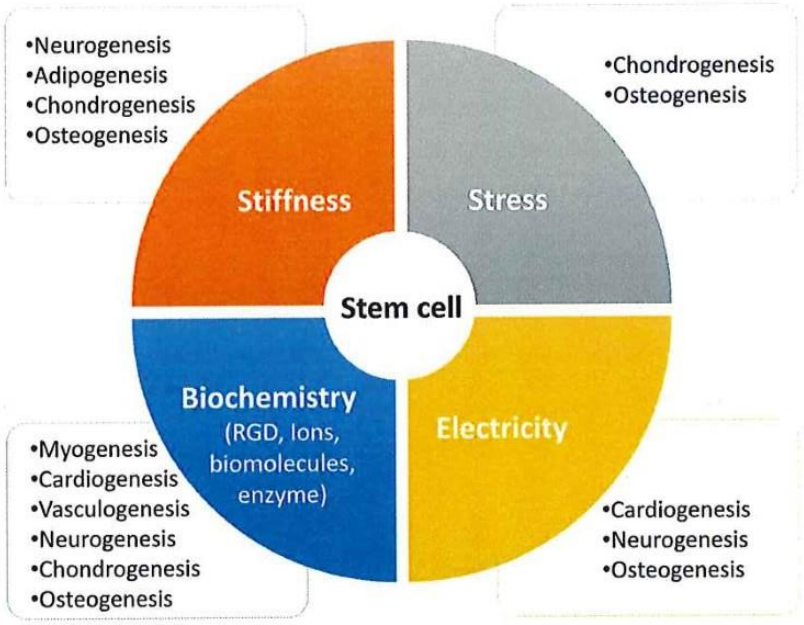

Figure 17.1 Differentiation of stem cells in response to external stimuli. Chemical stimuli, such as RGDs, ionic strength, growth factors and enzymes, facilitate directing the differentiation of stem cells into a wide range of cell types,[14] while neurogenesis, cardiogenesis and osteogenesis are enhanced through electrical stimulus[20] and mechanical stimulus of the supported materials.[15] Moreover, shear stress is often utilised to induce bone and cartilage formation.[10]

View Online

Downloaded by Institute of Process Engineering, Chinese Academy of Sciences on 1/3/2019 5:15:03 AM.
Published on 03 May 2017 on https://pubs.rsc.org | doi:10.1039/9781788010542-00473

can also be regulated by either the property changes or inherent stiffness and topography of the smart materials.[15] Conductive/electroactive materials that have bulk property changes in response to electrical stimuli have been widely applied in osteogenesis and neural differentiation for bone and neural regeneration, respectively.[16,17] Light-responsive and pH-responsive hydrogels allow control of the concentration and distribution of incorporated biomolecules in the gel, which play a role in guiding the differentiation of stem cells.[14] Each type of smart material can even respond to more than one single stimulus[18] and a combination of two or more smart materials is used to achieve spatial and temporal control over stem cell differentiation.[19]

There have been excellent reviews on smart materials. A few reviews address the application of smart materials in drug/gene delivery for cancer treatment[14,21,22] and some of them focus on the modelling of physical cues and elucidation of the mechanisms that influence cell behaviours,[12,23] such as cell attachment, spreading and proliferation. However, very few of them cover the details in the differentiation of stem cells.[10,11] Among a very few of them, piezoelectric materials are comprehensively reviewed in regulating stem cell fate.[20] Therefore, the present review focuses mainly on the application of smart materials, including scaffolds and hydrogels, in guiding stem cell differentiation in response to external stimuli, such as temperature, electricity, pH, shear stress, light and ions.

17.2 Thermosensitive Materials

Thermosensitive materials, usually in the form of hydrogels for applications in tissue engineering and regenerative medicines, not only have a hydrophilic property but also allow a sol–gel transition by a simple increase or decrease of the surrounding temperature (Figure 17.2). The gelation can be initiated

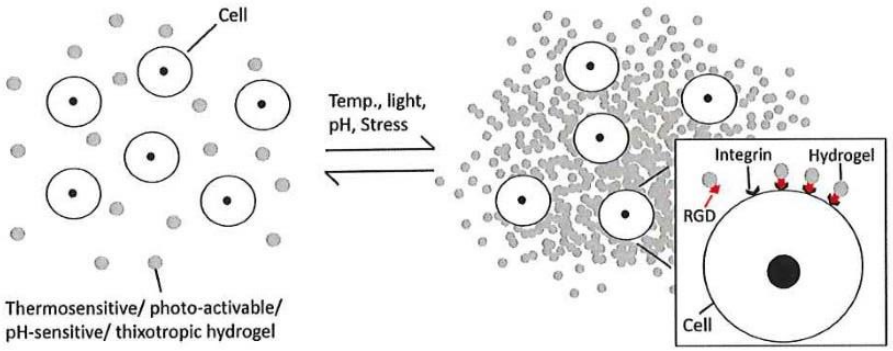

Figure 17.2 Schematic of encapsulation of stem cells in thermosensitive, photoactive, pH-sensitive or thixotropic hydrogels due to external stimuli. The incorporated biomolecules or the conjugated RGDs interact with the integrin of the encapsulated stem cells and direct differentiation of stem cells into defined cells.[14] Adapted from ref. 25 with permission from the Royal Society of Chemistry.

View Online

Downloaded by Institute of Process Engineering, Chinese Academy of Sciences on 1/3/2019 5:15:03 AM.
Published on 03 May 2017 on https://pubs.rsc.org | doi:10.1039/9781788010542-00473

above the lower critical solution temperature (LCST) or below the upper critical solution temperature (UCST). LCST thermosensitive hydrogels, such as polyethylene glycol (PEG)-based copolymers, polyethylene oxide-polypropylene oxide-polyethylene triblock copolymers (PEO–PPO–PEO)[24] and poly(*N*-isopropylacrylamide) (PNIPAAm),[25,26] are more popularly utilised since the LCST is close to body temperature (Table 17.1). In addition, the inherent properties of LCST thermosensitive hydrogels, including stiffness, biocompatibility and gelation temperature, can be adjusted by copolymerizing with other biocompatible components. Conjugation of RGD peptides/proteins with the hydrogels facilitates cell binding to the receptors of cells for better adhesion or guided differentiation.[27]

17.2.1 Facilitating Cell Differentiation by *in vivo* Gelation

Because of the adjustability of the gelation temperature for thermosensitive materials, LCST thermosensitive hydrogels are often employed as injectable carriers for stem cells, which can not only supply *in situ* gel formation to localize stem cells in the damaged/degenerative site, but also provide assistive functions for guiding stem cell differentiation. After implantation, the hydrogels turn into a three-dimensional (3D) gel-like network structure to retain the encapsulated stem cells, avoiding stem cell migration into other sites or circulation in the blood vessels. Physiological stimuli produced by the host are received by cells through the thermosensitive hydrogels, and these localized stimuli can guide differentiation of stem cells into specific lineage cells in the injection site. For instance, Gao *et al.* directly injected rat adipose-derived mesenchymal stem cells (ASCs), which were encapsulated in a chitosan-based thermosensitive hydrogel (chitosan chloride and β-glycerophosphate (β-GP)), into the ischemia-induced acute kidney injury site.[28] Four weeks after the transplantation, pre-labelled rat ASCs were found to hold a positive epithelial cell marker (Anti-pan-CK antibody) and vascular endothelial cell marker (anti-CD31 antibody), which indicated that the encapsulated stem cells were induced for differentiation into renal epithelial cells and vascular endothelial cells. Through analysing the concentration level of creatinine and blood urea nitrogen (BUN), it was shown that the concentration of both components continuously decreased from a significant value to a relatively normal level during the implantation period, which meant that the function of the injured kidneys was repaired and improved by the thermosensitive hydrogel–ASCs hybrid. Another *in vivo* study of the impact of thermosensitive hydrogels upon the differentiation of stem cells was reported by Li *et al.*, who injected Dil-labelled brown ASCs and a single-wall carbon nanotube-modified poly(*N*-isopropylacrylamide) (PNIPAAm) mixture into myocardial infarction (MI) lesion sites.[29] The improvement in the left ventricular shortening fraction (LVSF) and the left ventricular ejection fraction (LVEF) was observed by echocardiography in four weeks. In addition, the MI area and the thickness of the ventricular wall at the MI lesion site was significantly

View Online

Downloaded by Institute of Process Engineering, Chinese Academy of Sciences on 1/3/2019 5:15:03 AM.
Published on 03 May 2017 on https://pubs.rsc.org | doi:10.1039/9781788010542-00473

decreased and prominently increased, respectively. The immunofluorescent images of the cardiac section also indicated that the implanted ASCs differentiated towards cardiac lineage cells with expression of cardiac proteins, such as cTnT and α-SA.

17.2.2 Determining Cell Differentiation by Gel Modification

Thermosensitive hydrogels can also induce differentiation of stem cells through changes of their hydrogel properties.[5] It was reported that over 76% of bone-marrow-derived MSCs cultured in the stiffer thermosensitive hydrogel (NIPAAm/AAc/NAS/HEMA-PTMC) at a Young's modulus of 45 kPa and 65 kPa for fourteen days were detected to proceed with cardiac differentiation by expressing specific genes and proteins (cTnI and MEF2C).[30] Moreover, incorporation of biomolecules inside the thermosensitive hydrogel and conjugation of proteins/peptides with the thermosensitive polymers are both effective methods to regulate the fate of stem cells (Figure 17.2). L-Alanine was copolymerized with ethylene glycol to form a thermosensitive polymer poly(ethylene glycol)-*block*-poly(L-alanine) (PEG-L-PA) by Yeon *et al.*[31] The ASCs encapsulated in the thermosensitive hydrogel expressed a high level of collagen II *in vitro* and generated sulfated glycosaminoglycan *in vivo*, which indicated chondrogenic differentiation of ASCs within the hydrogels. Chun *et al.* also conjugated the GRGDS peptide, a cell-binding ligand, into poly(organophosphazene) and investigated expression of genes and proteins for rabbit MSCs encapsulated in the poly(organophosphazene)–RGD hydrogel.[32] Four weeks after transplantation of the MSCs–hydrogel hybrid in mice, it was observed that osteocalcin (OCN) and collagen I were significantly expressed in addition to calcium deposition. This illustrated that the thermosensitive hydrogel poly(organophosphazene)–RGD can be utilised to direct osteogenesis of stem cells. Apart from peptide/protein conjugation, bioactive molecules can also be incorporated into the hydrogel and regulate differentiation of the encapsulated stem cells. By co-encapsulating TGF-β3 and human-bone-marrow-derived MSCs (hBMSCs) into the thermosensitive hydrogel, the hBMSCs were directed to osteogenesis with the evidence of collagen II and glycosaminoglycan (GAG) expression.[33] In addition, it was reported that the encapsulated bFGF inside the thermosensitive hydrogel, NIPAAm/AAc/NAS/HEMA-PTMC, improved survival of MSCs and their differentiation towards cardiomyocyte-like cells, which could be potentially applied in the treatment of myocardial infarction.[34] Researchers also attempted to incorporate other small components inside the thermosensitive hydrogels to achieve fate regulation of stem cells. For instance, nanohydroxyapatite (nHAp) was shown not only to enhance the properties of the thermosensitive hydrogel, such as swelling and protein adsorption, but also to promote expression of osteogenic genes and proteins, such as Runx2, ALP, COL-I and OCN, as well as calcium deposition for the encapsulated mouse MSCs inside the chitosan-based hydrogel.[35]

Downloaded by Institute of Process Engineering, Chinese Ac
Published on 03 May 2017 on https://pubs.rsc.org | doi:1

Table 17.1 Thermosensitive materials and their regulation for the fate of stem cells.

Material	Crosslink method	Biodegradability	Phase change temperature range	Responded property change	Dimension (2D/3D)	Encapsulated cell type	Differentiation type	Differentiation evidence	Application	References
PNIPAAm/SWCNTs (single-wall carbon nanotubes)	—	No	32 °C	Phase change: sol under 32 °C and gel above 32 °C	3D	ASCs	Cardiac differentiation	*In vivo* test; protein: cTnT, α-SA	Injectable gel formation for myocardial repair	29 and 71
Poly (NIPAAm/AAc/NAS/HEMA-PTMC) molar 85:6:5:4 (adjust stiffness by bFGF)	Ionic cross-linking (DPBS, pH 7.4)	Degradable (thermal transition temperature of degraded hydrogel elevated to 49.4 °C)	23.8 ± 0.6 °C	Phase change at 23.8 ± 0.6 °C; rapid gelation at 37 °C <7 s	3D	BMSCs	76% Cardiomyocyte-like cells	mRNA: MEF2C, CACNA1c; protein: cTnI	Injectable *in situ* gel formation for infarcted hearts	30 and 72
Poly(NIPAM-*co*-HEMA-*co*-DBA)-*b*-PCL-poly-(NIPAM-*co*-HEMA-*co*-DBA) (adjust stiffness by collagen I)	Ionic cross-linking (DPBS, pH 7.4)	Degradable (LCST of degraded hydrogel is 47.5 °C)	17.7–22.4 °C	Rapid gelation at 37 °C <5 s	3D	Cardiosphere-derived cells (CDCs)	Mature cardiomyocyte lineage	Cardiac markers: cTnT, MYH6; pre-mature cardiac marker: GATA4; protein: cTnI	Injectable *in situ* gel formation for infarcted hearts	73
Aminated hyaluronic acid-*g*-poly(*N*-isopropylacrylamide) (AHA-*g*-PNIPAAm)	—	Partially	30 °C	Phase change: sol under 30 °C and gel above 30 °C	3D	hASCs	—	*In vivo* test	Adipose tissue engineering	74

Downloaded by Institute of Process Engineering, Chinese Ac
Published on 03 May 2017 on https://pubs.rsc.org | doi:1

PNIPAAm-AA-HEMA-macromers (oligoLA/oligoHB/oligoTMC)	—	Degradable (LCST of degrade production poly(NIPAAm-*co*-AAc-*co*-HEMA) is 44 °C)	14.6–23.7 °C	Phase change: sol at 4 °C and gel at 37 °C within 7 s	3D	mBMSCs	Myogenic differentiation	Myosin heavy chain (MHC), myogenin, MyoD1, MEF2 in 14 days 20 kPa elastic expansion moduli	Skeletal muscle regeneration	75
PNIPAAm-*co*-AAc with TGF- β3	—	No	—	—	3D	hBMSCs	Chondrogenesis	*In vivo* test; collagen II; glycosaminoglycan (GAG) for ECM	Chondrogenic engineering	33
PNIPAAm–PAA	—	No	—	Phase change: sol under 37 °C and gel above 37 °C	3D	mASCs	Adipocyte	*In vivo* test	Depressed defects	76
PNIPAAm-MAA-mPEGMA-MDO-TA (PN-TA)	—	Degradable	39–31 °C	Phase change: sol at25 °C and gel at 37 °C	3D	Rat cardiac myoblast H9c2	—	*In vivo* test inflammatory responses, enhance the intracellular calcium level and induce a large intracellular calcium transient	Myocardial infarction therapy	77

(*continued*)

Downloaded by Institute of Process Engineering, Chinese Ac
Published on 03 May 2017 on https://pubs.rsc.org | doi:1

Table 17.1 (*continued*)

Material	Crosslink method	Biodegradability	Phase change temperature range	Responded property change	Dimension (2D/3D)	Encapsulated cell type	Differentiation type	Differentiation evidence	Application	References
Chitosan-*g*-PNIPAAm	Ionic cross-linking (PBS, pH 7.4)	No	25–37 °C	Phase change: sol under 37 °C and gel above 37 °C	3D	Mouse embryonic mesenchymal progenitor cells C3H/10T1/2	—	—	Regenerative medicine	78
Chitosan/nanohydroxyapatite/collagen	Ionic cross-linking (β-glycerophosphate , β-GP)	No	31 °C	Phase change: sol under 31 °C and gel above 31 °C	3D	Rat BMSCs	—	*In vivo* test	Cell delivery	79
2.5 wt% Chitosan and 1 wt% gelatin + Sr	Ionic cross-linking (β-GP)	Degradable	36 °C	Phase change: sol under 36 °C and gel above 36 °C	3D	Human exfoliated deciduous teeth (SHEDs) MSCs	Osteoblast	ALP; mRNA: Collagen I, Runx2, OP, ON; protein: BMP-2; calcium deposit	Bone formation	71
Zinc-doped chitosan/nanohydroxyapatite/beta-glycerophosphate (Zn-CS/nHAp/ β-GP)	Ionic cross-linking (β-GP)	Degradable	37 °C	Phase change: sol at 4 °C and gel at 37 °C	3D	mMSCs	Osteoblasts	*In vivo*; mRNA: Runx2, ALP, COL-I, OCN; protein: Runx2; calcium deposition	Bone regeneration	35

Downloaded by Institute of Process Engineering, Chinese Ac
Published on 03 May 2017 on https://pubs.rsc.org | doi:1

Chitosan chloride	Ionic cross-linking (β-GP)	Degradable	37 °C	Phase change: sol under 37 °C and gel above 37 °C	3D	mASCs	Renal tubular epithelial-like and vascular endothelial-like cells	*In vivo* test Pan-CK for epithelial cells and CD31 for vascular endothelial cells	Acute kidney injury	28
Poly(ethylene glycol)-*b*-poly(L-alanine) (PEG-L-PA)	—	Degradable	The sol-to-gel transition temperatures decreased from 47 to 20 °C, from 34 to 14 °C, and from 18 to 6 °C as the concentrations were increased from 8.0 to 17.0 wt%, from 2.0 to 6.0 wt%, and from 1.0 to 2.0 wt% for P50–06, P50–11, and P50–25, respectively		3D	ASCs	Chondrogenesis	Collagen II *in vitro*; sulfated glycosaminoglycan *in vivo*	Injectable tissue engineering	31
Tetronic–tyramine with FN or RGD	—	No	37 °C	Phase change: sol at 4 °C and gel at 37 °C	2D	hMSCs	—	*In vivo* test	Cell patch	80
Poly(organophosphazene)-RGD	—	Degradable	37 °C	Phase change: sol under 37 °C and gel above 37 °C	3D	Rabbit MSCs	Osteoblast	*In vivo* test; mRNA: OCN; calcium deposition; protein: collagen I	Bone tissue engineering	32

Downloaded by Institute of Process Engineering, Chinese Ac
Published on 03 May 2017 on https://pubs.rsc.org | doi:1

Table 17.2 Electroactive materials and their regulation for the fate of stem cells.

Material	Stimuli	Dimension (2D/3D)	Culture medium	Encapsulated cell type	Differentiation type	Differentiation evidence	Application	Reference
Laminin-coated PPy-DBS	±0.25 mA cm^{-2} biphasic waveform of 100 μs pulses with 20 μs interphase open circuit potential and a 3.78 ms short circuit (250 Hz) 8 h day^{-1} for 3 days	2D	Differentiation media	hNSCs	Neurons and glial cells	β-III tubulin (TUJ1) for neurons and glial fibrillary acidic protein (GFAP) for glial cells	*In vitro* modelling, translational drug discovery and regeneration medicine	43
PPy	Direct current field (DCF), 0.035, 0.35, 3.5 V cm^{-1} for 2, 4, 12 h	2D	Differentiation medium	Rat bone marrow stromal cells (rBMSCs)	Osteoblasts	Up-regulated mRNA: core binding factor 1 (Cbfa1), osteocalcin (OCN); earlier expressed alkaline phosphatase activity (ALP); improved calcium deposition and mineralization	Coating on the medical devices with a transparent appearance	44
(Fibronectin/pyrrole/2-hydroxy-5-sulfonic aniline)-coated PVDF	3 d without stimulation, 6 d with stimulation at 100 mV mm^{-1} for 4 h day^{-1}, no stimulation thereafter	3D	Differentiation medium	hBMSCs	Osteoblasts	Improved ALP express, calcium and collagen deposition, mineralization	Formation of calcified extracellular matrix associated with bone	17

Downloaded by Institute of Process Engineering, Chinese Ac
Published on 03 May 2017 on https://pubs.rsc.org | doi:1

(Collagen I alone or with sulfated hyaluronan)-coated PANI (PANI/Col I/sHya)	Pulsed electric field (PEF) 7 ms rectangular pulses 3.6 mV cm^{-1} 10 Hz	2D	Differentiation medium	Primary hMSCs	Osteoblasts	Up-regulated ALP and OCN, calcium deposition	Regulate stem cell behaviour with controlled physicochemical cues and optimal stimulation modalities	40
(Laminin/poly-L-ornithine)-coated PEDOT:PSS	Pulsed stimulation potential 100 Hz 24 h during the first 4 days' culture with EGF, FGF-2 and B27 on crosslinked PEDOT:PSS and 12 h during differentiation time (following 8 days)	2D	Differentiation medium	Human neural progenitor cell line (ReNcell VM)	Neuronal and glial lineages	Tuj1 for neurons	Neuronal engineering	41
HCl doped PANI	10 days of 100 mV cm^{-1} electrical field stimuli in cycle of 10 min day^{-1}	2D	Standard cell culture medium	hMSCs	Neural-like cells	Decreased expression in nestin and higher expression of β-III tubulin	Integrating substrate conductivity and external electric stimuli to manipulate the cell functionality *in vitro*	42

View Online

Downloaded by Institute of Process Engineering, Chinese Academy of Sciences on 1/3/2019 5:15:03 AM.
Published on 03 May 2017 on https://pubs.rsc.org | doi:10.1039/9781788010542-00473

17.3 Electroactive/Conductive Materials

Electroactive materials are conductive and they change their bulk properties in response to different frequencies of applied electricity. Electrochemistry and inverse piezoelectricity are the two main contributing factors for bulk change when applying alternating electricity. Electrochemistry utilises the ionic exchange between the electroactive materials and the electrolytes to achieve swelling and contraction,[36] while inverse piezoelectricity induces deformation due to the inherent inverse piezoelectric property of the electroactive materials in an applied electrical field.[20] Hence, electroactive materials can be divided into two categories: (a) electrochemical materials, such as polypyrrole (PPy) and PPy-coated films/scaffolds, polyaniline (PANI) and PANI-coated films/scaffolds, poly(3,4-ethylenedioxythiophene) (PEDOT) and PEDOT-coated films/scaffolds, and (b) piezoelectric materials, such as polyvinylidene fluoride (PVDF), PVDF-*co*-polymers, and collagen (Table 17.2). Moreover, piezoelectric materials can also generate electricity due to mechanical deformation, which is called piezoelectricity.

17.3.1 Electrochemical Materials

Firstly, the effect of electroactive materials on differentiation of stem cells can be merely based on the inherent conductivity and stiffness. It was reported that polylactide with chondroitin sulfate-doped PPy (PLA–PPy) slightly improved expression of alkaline phosphatase (ALP), an osteogenic marker, while this enhancement was considered as a typical impact of 3D scaffolds on the hASCs supplied with the standard cell culture medium.[37] The effect of electrical stimulation on the early osteogenic differentiation of hASCs was not observed, however, electrical stimulation-induced differentiation into fibroblastic and vasculogenic cells was detected in another study by Tandon *et al.* in the standard cell culture medium.[38] Furthermore, when supplying hASCs with the osteogenic medium in a two-dimensional (2D) system, mineralization and expression of osteogenic genes and proteins were observed.[39] Compared to direct chemical stimulation, electrical stimulation showed less influence on the early osteogenesis of hASCs, because electrical stimulation helps in improving osteogenic induction of the osteogenic medium on hASCs but not osteogenic initiation. In addition, the source of stem cells may also play a role in the tendency of cell differentiation, which could explain why hASCs showed fibroblastic and vasculogenic behaviour rather than osteogenesis in response to electrical stimulation in the standard cell culture medium.

Secondly, when appropriately combining electrical and chemical stimulation, differentiation of stem cells can be well controlled (Figure 17.3(A)). Electrical stimulation in the osteogenic or neurobasal medium induced osteogenesis[17,40] or neural differentiation,[41] respectively. Even without the neurobasal medium, hMSCs were found to differentiate into neuron-like cells on a HCl-doped PANI film charged with a cycled electrical field.[42] Stewart

View Online

Downloaded by Institute of Process Engineering, Chinese Academy of Sciences on 1/3/2019 5:15:03 AM.
Published on 03 May 2017 on https://pubs.rsc.org | doi:10.1039/9781788010542-00473

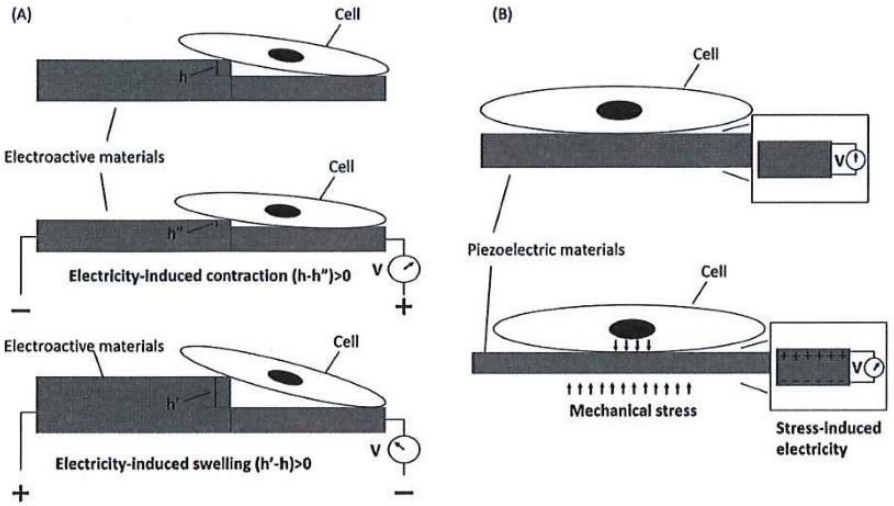

Figure 17.3 Schematic of electroactive materials regulating the fate of stem cells. Swelling and contraction of the electroactive scaffolds due to external electricity are shown in (A). When an altered electrical field is applied to the electroactive scaffolds, the scaffolds contract and swell due to the ion exchange between the scaffold and the electrolyte[36] or the inverse piezoelectricity.[20] Hence, the attached stem cells are stimulated by mechanical stress to induce specific cell differentiation. The electricity produced by piezoelectric materials is shown in (B). When the scaffolds are stressed or attached stem cells contract, the piezoelectric materials produce electricity on the surface, which is in turn utilised as an electrical stimulus to differentiate the stem cells, such as neurogenesis or osteogenesis.[45] Adapted with permission from *Journal of Biomedical Materials Research A*, **136**, Ribeiro, C., Sencadas, V., Correia, D. M., Lanceros-Mendez, S. Piezoelectric polymers as biomaterials for tissue engineering applications, 46–55, copyright (2015) with permission from Elsevier.

et al. reported that human neural stem cells (hNSCs) were predominantly differentiated into neurons, while fewer glial cells were detected, seven days after they were cultured on a dodecylbenzenesulfonate-doped polypyrrole (PPy-DBS) film in the neurobasal medium and exposed to an alternating electrical field.[43] In addition, accelerated osteogenesis was also reported when rat bone marrow stromal cells (rBMSCs) were cultured on the PPy film in the osteogenic medium in a direct current field.[44]

17.3.2 Piezoelectric Materials

Piezoelectric materials can be utilised to direct differentiation of stem cells by piezoelectricity or inverse piezoelectricity (Figure 17.3(B)). Piezoelectricity was applied to direct hASCs towards osteogenic differentiation.[45] The hASCs dynamically cultured on the β-poly(vinylidene fluoride) (β-PVDF) film coating with fibronectin in a standard cell culture medium expressed much

View Online

Downloaded by Institute of Process Engineering, Chinese Academy of Sciences on 1/3/2019 5:15:03 AM.
Published on 03 May 2017 on https://pubs.rsc.org | doi:10.1039/9781788010542-00473

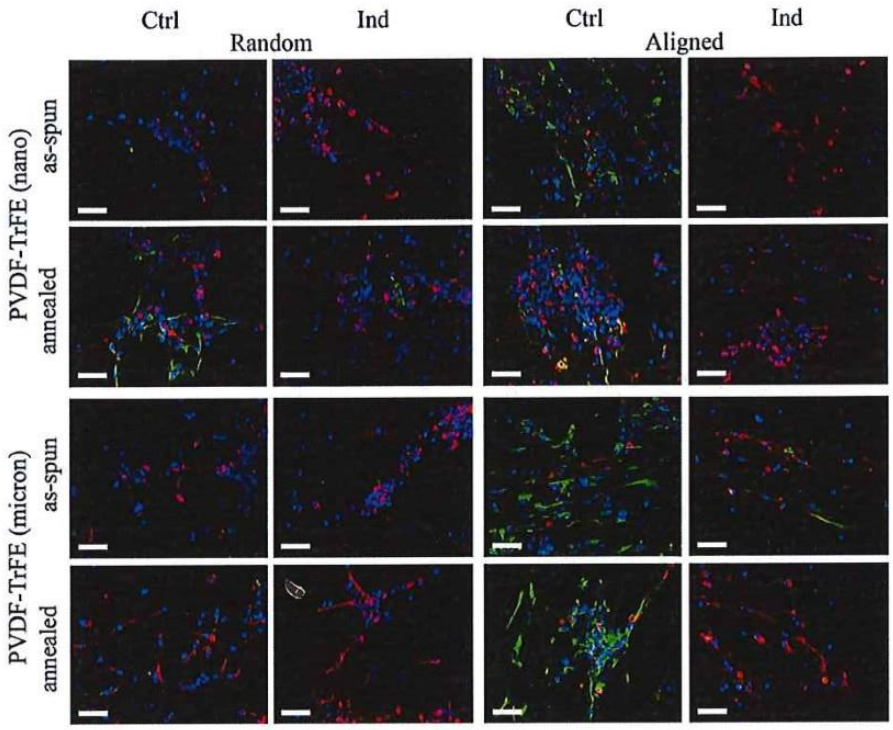

Figure 17.4 Immunofluorescent staining of hNPCs cultured on piezoelectric micro- and nano-sized PVDF-TrFE as-spun (without annealing), annealed (enhanced piezoelectricity), random and aligned scaffolds in control and induced medium at day nine.[16] Green: nestin; red: β-III tubulin; blue: GFAP and DAPI. (Scale bar = 50 μm). Reproduced with permission from Lee Y. S., *et al.*, *Tissue Eng Part A*, **18**, 2063, 2012. Copyright 2012: Mary Ann Liebert, Inc.

higher ALP than those statically cultured. Furthermore, Lee *et al.* successfully directed human neural progenitors (hNPCs) into mature neural cells on a piezoelectric scaffold, which was generated by electrospinning poly(vinylidene fluoride trifluoroethylene) (PVDF-TrFE, 65/35), even without a cell differentiation medium. PVDF-TrFE produced electricity, due to a cell-induced minute bulk change, and enhanced expression of the neuronal cell marker (β-III tubulin) (Figure 17.4).[16] In addition, a longer neurite was observed on the enhanced piezoelectric, micro-, and aligned PVDF-TrFE scaffolds.

17.4 Photo-Responsive Materials

Photo-responsive materials respond to certain wavelengths of light and change their properties, for instance, photo-polymerization induced by photo-initiators and gelation of acrylated monomers or biopolymers, such as

View Online

Downloaded by Institute of Process Engineering, Chinese Academy of Sciences on 1/3/2019 5:15:03 AM.
Published on 03 May 2017 on https://pubs.rsc.org | doi:10.1039/9781788010542-00473

acrylamide, acrylic acid, hydroxyethyl acrylate, NIPAAm, and PEG-monoacrylate.[13] In addition, photo-responsive materials may be activated to release electrons to induce electricity,[19] or activate reactive oxygen species (ROS) inside the cells.[46] Moreover, photo-responsive polymers can perform photolysis[47,48] or reversible isomerization[10] in response to a certain wavelength of light.

According to the reversibility of the responsive behaviour, photo-responsive materials can be divided into two categories: (a) photo-activatable/photo-cleavable materials, such as TiO_2, 5-aminolevulinic acid (5-ALA), polymers containing *o*-nitrobenzyl (*o*NB) moieties, 2-(2-nitrophenyl) propyl 2-(2-(2-(2-azidoethoxy)ethoxy)ethoxy)ethoxycarbamate (N3-TEG-ONH-NP-POC), 3-(4,5-dimethoxy-2-nitrophenyl)-2-butyl (DMNPB), and (b) reversible isomers, such as azobenzene groups or spiropyran groups containing polymers (Table 17.3).

17.4.1 Photo-Activatable Materials

When exposed to a certain wavelength of light, photo-initiated polymerization and gelation of a hydrogel (Figure 17.2) can provide mechanical support for the encapsulated stem cells to form a 3D *in-vivo*-ECM-mimicking environment, where the inherent stiffness of the hydrogel and the incorporated biomolecules can play a synergistic role in the differentiation of stem cells. Shell *et al.* successfully initiated the gelation of bis(acrylamide) and PEG-diacrylate with a vitamin B12 derivative, alkyl-cob(III)alamins Cy5-labeled ethyl-Cbl at a wavelength of 660 nm.[13] Due to the biocompatibility and biodegradability of PEG and the vitamin B12 derivative, stem cells were mixed with the photo-responsive materials and the PEG-diacrylate monomers, and the hybrids were implanted into the damaged cartilage. *In situ* gel formation was initiated under irradiation at 660 nm, which falls within the "optical window of tissue" (600–900 nm), a range of light wavelengths that allow maximal tissue penetration.[13] After gelation, stem cells were retained inside the hydrogel and further differentiated into chondrocytes for regeneration of the damaged cartilage by responding to the internal stimuli generated by the host.

Apart from polymerization and gelation for *in situ* regulation of stem cells, photo-responsive materials can also generate ROS under irradiation.[46] A high level of ROS is toxic to cells, but ROS at a certain dosage range can regulate intracellular signalling, and therefore, change the final cell lineage of stem cells.[49] Kushibiki *et al.* exposed the photo-responsive material, 5-aminolevulinic acid (5-ALA), to weak illumination to generate a low level of ROS inside primary rat MSCs.[46] The generated ROS promoted osteogenesis of MSCs by regulating the activator protein-1 (AP-1)-mediated signalling pathway. In addition, the excited photo-responsive materials generate electricity on the conductive substrate by accumulating released electrons (Figure 17.5(A)) and the minute electricity stimulated hNSCs to differentiate into mature neurons rather than glial cells.[19]

Downloaded by Institute of Process Engineering, Chinese Ac
Published on 03 May 2017 on https://pubs.rsc.org | doi:1

Table 17.3 Photo-responsive materials and their regulation for the fate of stem cells.

Material	Stimuli	Responded property change	Dimension (2D/3D)	Status (hydrogel/scaffold)	Culture medium	Encapsulated cell type	Differentiation type	Differentiation evidence	Application	Reference
Reduced graphene oxide (rGO)/TiO_2 heterojunction	Repeated pulse duration of 4 s and frequency of 1 Hz (4 flashes s^{-1} with xenon lamp) with intervals of 60 s for a total time of 30 min at each 12 h	Excited electrons transported from TiO_2 to cells on rGO through Ti–C and Ti–O–C bond	2D	Film	Extracellular medium: 140 mM NaCl, 5.0 mM KCl, 2.0 mM $CaCl_2$, 1.5 mM $MgCl_2$, 15.0 mM ascorbic acid (under the optimum conditions of this work), 10 mM 4-(2-hydroxyethyl)-1-piperazineethanesulfonic acid (HEPES), 10 mM glucose at pH 6.4	Human neural stem cells	Neurons (23-fold increase in the neuronal to glial cell ratio)	Neuron-specific β-III tubulin (TUJ1), glial fibrillary acidic protein (GFAP)	As nanostructure scaffold in neural regeneration and repair	19
5-ALA	Irradiation at 635 nm 30 mW cm^{-2} for 0, 24, 67, 102 sec (0, 1, 2, 3 J cm^{-2})	Intracellular reactive oxygen species (ROS) formation (CellROX reagent became fluorescent red)	2D	Film	Differentiation medium (complete medium + 10 nM dexamethasone + 10 mM β-glycerophosphate + 50 ug mL^{-1} ascorbic acid)	Rat BMSCs	Osteogenic differentiation	Calcium deposition with Alizarin red staining; ALP (early osteogenic marker) and osteocalcin (late osteogenic marker) expression	Bone engineering	46

Downloaded by Institute of Process Engineering, Chinese Ac
Published on 03 May 2017 on https://pubs.rsc.org | doi:1

Vitamin B12 derivative alkyl-cob(III) alamins (unlabeled and Cy5-labeled ethyl-Cbl)	Certain wavelength illumination 520 nm for unlabeled and Cy5-labeled ethyl-Cbl, and 660 nm for Cy5-labeled ethyl-Cbl	Photohomolysis of unlabeled or Cy5-labeled ethyl-Cbl at 520 nm or 660 nm, respectively, induces polymerization or gelation of acrylated monomers or biopolymers (by the ethyl radical)	3D	Hydrogel	—	—	—	—	Light-induced injectable hydrogel for tissue regeneration (phototherapeutics)	13
Heparin photogel contains thiolated heparin molecules and PEG molecules with bifunctional acryl terminated photolabile *o*-nitrobenzyl moieties	365 nm 600 W UV light exposure for 10 s	Heparin photogel degraded	2D	Hydrogel (FGF2 inside)	Differentiation medium contains IMDM + 1% FBS + 2% penicillin/streptomycin + 0.001 M nonessential amino acids + 0.5 U mL^{-1} insulin + 14 ng mL^{-1} glucagon + 100 × 10^{-9} M dexamethasone for 4 d and 1% FBS replaced with 1% B27 after 4 d	mESCs	Endoderm (encapsulated FGF2 induce differentiation)	Sox17 and FOXA2	Stem cell culture and study	81

(*continued*)

Downloaded by Institute of Process Engineering, Chinese Ac
Published on 03 May 2017 on https://pubs.rsc.org | doi:1

Table 17.3 (*continued*)

Material	Stimuli	Responded property change	Dimension (2D/3D)	Status (hydrogel/scaffold)	Culture medium	Encapsulated cell type	Differentiation type	Differentiation evidence	Application	Reference
SPAAC-based gel (PEG, 10 wt%), NPPOC-(photo-caged) for vitronectin-*o*NB to anchor (cells attach)	Collimated UV light (wavelength 365 nm, 5–20 mW cm^{-2}, 0–600 s) with a patterned chrome photomask or pulsed laser light for 3D photomediated protein ligation or photorelease	UV exposure to photolyze NPPOC and then immobilize VTN-CHO onto the gel and same light exposure to induce photoremoval of VTN-CHO	3D	Hydrogel	stemXVivo human osteogenic inductive medium + 1% penicillin/streptomycin	hBMSCs	Osteogenic differentiation (differentiation media induced together with cell attaching and spreading because of vitronectins)	OCN and ALP	Tissue engineering	50
Cyclic RGD peptide (cyclo-[RGDfK])-&cyclo[RGD-(DMNPB)] fK]-tethered SAMs of alkanethiols	Irradiation at 355 nm 3.5 mW cm^{-2} for 3 min	Decaged RGD and phototriggered cell attachment	2D	Monolayer	DMEM + 1% penicillin-streptomycin + 1% insulin-transferrin-selenium-X (ITS)	Murine C2C12 myoblast	Myogenic differentiation	Sarcomeric myosin positive	Biomedical devices	47
PEG5000 containing *o*-NB caged PFSST-KTC peptide (SAM)	UV exposure for 5 min	Detachment of PEG shell and enhancement of cell attachment	2D	Monolayer	DMEM + 10% FBS + 1% penicillin-streptomycin	Rat BMSCs	Osteogenesis	Calcium deposition and OPN expression	Regeneration medicine	48

Downloaded by Institute of Process Engineering, Chinese Ac
Published on 03 May 2017 on https://pubs.rsc.org | doi:1

Dynamic photo-responsive zwitterionic hydrogel consists of static zwitterionic monomer carboxybetaine acrylamide (CBAA), cyclic-RGD (cRGD)-functionalized CBAA and photo-switchable monomer spiropyran methacrylate (SPMA), cross-linked with zwitterionic carboxybetaine dimethacrylate (CBDMA)	Illumination at near-infrared light (NIR, 800 nm, 50 mW); NG-1 (50 mW NIR + 10 mW visible green light); NG-2 (50 mW NIR + 30 mW visible green light); visible green light (560 nm, 50 mW) for continuous 14 days	NIR transfers closed-ring hydrophobic form isomer (spiropyran, SP) to zwitterionic hydrophilic form isomer (merocyanine, MC) by two-photon excitation (TPE); visible green light transfers MC to SP by SPE	2D and 3D	Hydrogel	Bipotential (osteogenic and adipogenic) differentiation media	hMSCs	Osteogenesis and adipogenic differentiation	Adipogenic surface antigens (PPARG and FABP4) and neutral lipids; osteogenic surface antigens (Runx2 and OPN) and ALP	Regenerative medicine	82

View Online

Downloaded by Institute of Process Engineering, Chinese Academy of Sciences on 1/3/2019 5:15:03 AM.
Published on 03 May 2017 on https://pubs.rsc.org | doi:10.1039/9781788010542-00473

17.4.2 Photo-Cleavable Materials

Some photo-responsive materials provide specific binding sites for stem cells by conjugating the materials with RGD peptides/proteins or a cage to prevent such specific binding (Figure 17.5(C) and (D)). When irradiated at a certain wavelength, the covalent bonds between the photo-responsive materials and the RGD peptides/proteins are broken by photolysis. The released RGD peptides/proteins either are detached from the main structure of the polymer backbone or become available for cell binding after opening the caged components. Both approaches can be employed to control the duration and intensity of binding by adjusting the concentration of RGD binding ligands in the hydrogels. Based on this concept, Weis *et al.* caged cyclo[RGDfk]-tethered self-assembled monolayers (SAMs) with DMNPB and successfully achieved a controllable concentration of the RGD for cell binding on the SAMs by sequential irradiation.[47] The seeded myoblasts on the substrate were guided towards myogenic differentiation and achieved the maximal myogenesis when RGD was exposed to cells under illumination for six hours. Polymers are also modified to control caging and uncaging of RGD peptides under illumination. For instance, PEG with a photo-sensitive

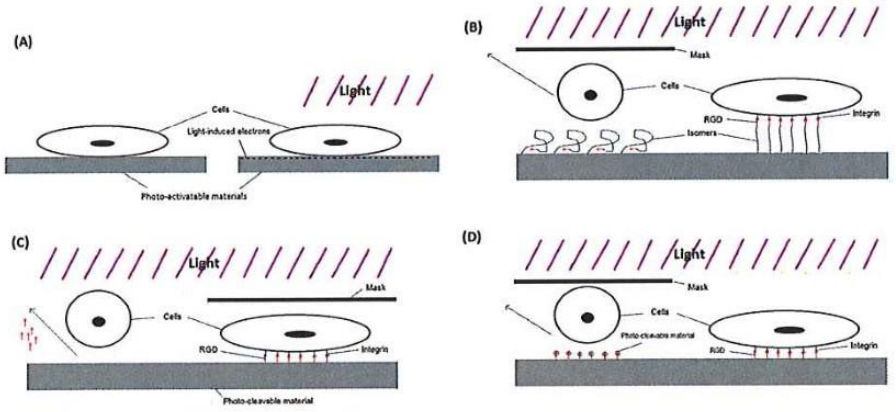

Figure 17.5 Schematic of photo-responsive materials regulating the fate of stem cells. (A) When a certain wavelength of light is applied to the photo-activatable materials, the excited electrons are released and play a role in stem cell differentiation.[19] (B) When illuminated by a certain wavelength of light, the RGDs conjugated to the isomers are reversibly exposed to the stem cells by light-induced isomerization and the differentiation of stem cells is regulated by the concentration of RGDs.[10] (C) The RGDs are pre-conjugated to the photo-cleavable materials and released upon illumination from the surface of scaffolds/hydrogels, which leads to stem cell detachment from the surface. (D) The RGDs mounted on the scaffolds/hydrogels are caged by the photo-cleavable materials, but released and exposed to the stem cells after illumination. In both ways, the concentration and the exposure time of RGDs in the scaffolds/hydrogels can be manually controlled for defined regulation of stem cell differentiation.[10]

View Online

Downloaded by Institute of Process Engineering, Chinese Academy of Sciences on 1/3/2019 5:15:03 AM.
Published on 03 May 2017 on https://pubs.rsc.org | doi:10.1039/9781788010542-00473

o-nitrobenzyl group was utilised to control the concentration of the peptides exposed to rat BMSCs. It was shown that the uncaged PFSSTKTC (Pro–Phe–Ser–Ser–Thr–Lys–Thr–Cys) peptide improved cell attachment[5] and directed rat BMSCs towards osteogenic differentiation in the standard cell culture medium.[48] Moreover, DeForest *et al.* reported the use of photocleavable materials to achieve defined distribution of proteins within a hydrogel.[50] Briefly, the first protein, bovine serum albumin (BSA_{488}) modified with 2,5-dioxopyrrolidin-1-yl 4-(4-(1-((4-(4-formylbenzamido)butanoyl)oxy) ethyl)-2-methoxy-5-nitrophenoxy)butanoate (NHS-*o*NB-CHO), was combined with PEG hydrogel.[50] On the other hand, the alkoxyamine groups of the PEG hydrogel were caged by NPPOC and these groups were activated upon illumination to anchor the second protein. Hence, when irradiation was applied to the PEG hydrogel, BSA_{488}-*o*BN-CHO was first photo-cleaved from the hydrogel by photolysis of *o*BN; at the same time, the cage by NPPOC was open to release the alkoxyamine groups to form the second protein complex BSA_{594}-*o*BN-CHO. Based on the concept, it was able to achieve controlled anchor or removal of vitronectins from the PEG hydrogel. By controlling concentration and spatial distribution of vitronectins exposed to hBMSCs, the stem cells were significantly promoted to express the early osteogenic marker ALP at day 4. After removal of vitronectins from the PEG hydrogel, expression of ALP in hBMSCs dropped back to the initial level at day 10.

17.4.3 Reversible Isomers

Photo-induced isomerization of spiropyran- or azobenzene-polymers can help to regulate differentiation by balancing specific and non-specific cell adhesion (Figure 17.5(B)). *Cis*-transition of azobenzene-polymers is triggered upon illumination of UV/visible light, which results in a complete change in the electronic structure, shape and polarity of the polymer. Through the transition, specific binding between the conjugated RGD sequences and stem cell integrin receptors can be manipulated and therefore the stem cell fate can be regulated. PEG is often incorporated inside the hydrogels to minimize non-specific binding.[8] On the contrary, spiropyran-polymers perform reversible transition between the hydrophilic zwitterionic form (merocyanine, MC) and the hydrophobic closed-ring form (spiropyran, SP), which has been used to demonstrate the effect of non-specific binding on stem cell differentiation. When near-infrared (NIR) light was applied to the photo-responsive hydrogel, the spiropyran moieties were transformed to the merocyanine moieties, and this transformation was inversed when a visible green light illuminated on the hydrogel. Exposure to green light resulted in an increase in the spiropyran form, thus an increase in non-specific cell–substrate interactions.[10] It was demonstrated that hMSCs hardly performed differentiation under the pure NIR light (in the zwitterionic form), while osteogenesis was preferred under the green light and adipogenesis was predominant after illumination under the NG-1 light (50 mW NIR and 10 mW green) (Figure 17.6). It was also noticed that differentiation of hMSCs was suspended after switching from the green light back to NIR.[51]

View Online

Downloaded by Institute of Process Engineering, Chinese Academy of Sciences on 1/3/2019 5:15:03 AM.
Published on 03 May 2017 on https://pubs.rsc.org | doi:10.1039/9781788010542-00473

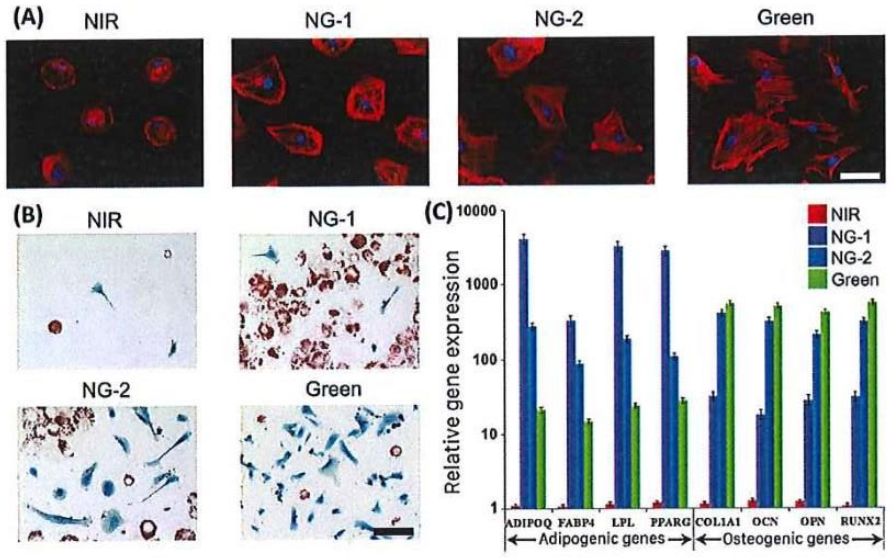

Figure 17.6 (A) Immunofluorescent staining of hMSCs cultured on the photo-responsive hydrogel in the osteogenic and adipogenic differentiation media under different illumination (NIR (800 nm): 50 mW; NG-1: 50 mW NIR + 10 mW green; NG-2: 50 mW NIR + 30 mW green; green (560 nm): 50 mW at day 14). Red: TRITC-phalloidin; blue: DAPI. (Scale bar = 15 μm). (B) Histological staining of adipogenic and osteogenic hMSCs by Oil Red O and Fast Blue salt, respectively, in the osteogenic and adipogenic differentiation media under different illumination at day 14. Red: neutral lipids; blue: alkaline phosphatase. (Scale bar = 100 μm). (C) Adipogenesis and osteogenesis level under various illumination ($p < 0.05$).[51] Adapted from ref. 51 with permission from the Royal Society of Chemistry.

17.5 Thixotropic Materials

Thixotropic materials change their properties in response to an applied shear stress. The viscoelasticity of thixotropic materials allows them to reversibly change their status between gel and sol at different shear stress levels. When being stressed or pipetted, the viscous property is over the elastic one, namely the loss modulus G″ is higher than the storage modulus G′, and the thixotropic hydrogel becomes sol.[14] Under stressed conditions, molecular interactions inside the thixotropic material, such as hydrogen bonding and hydrophobic and/or electrostatic interactions, become weak, which results in mechanical deformation of the hydrogel to form the sol status. After the stress is removed, the internal interactions are reconstructed and the mechanical gel structure is reformed. The recovery process from the sol back to the gel status is dependent on time as well as the interactions in the hydrogels,[14] and the process can be selectively manipulated by temperature,[14,52] pH,[53] or ionic components.[18]

View Online

Downloaded by Institute of Process Engineering, Chinese Academy of Sciences on 1/3/2019 5:15:03 AM.
Published on 03 May 2017 on https://pubs.rsc.org | doi:10.1039/9781788010542-00473

Thixotropic materials used in regeneration medicines are divided into two categories: (a) polymeric hydrogels formed by covalent crosslinking, such as a blend of silk fibroin (SF) and hydroxypropylcellulose (HPC), a blend of hyaluronic acid (HA) and methylcellulose, polyethylene glycol–silica (PEG–silica), nanofibrillar cellulose (NFC), and (b) supra-molecular hydrogels formed by non-covalent self-assembly, such as naphthalene-oligopeptide, the Max family (MAX1 and MAX8), tryptophan (W)-rich oligopeptides (CC 43 and Nedd 4.3), amyloids, and SF protein (Table 17.4).

17.5.1 Stiffness-Induced Cell Differentiation

Stem cells are homogeneously dispersed into thixotropic hydrogels in the form of a sol. The cell–sol hybrid is directly injected into the lesion site, and under stressed conditions, the hybrid is in the form of a sol so the solution can exactly fit into the *in vivo* damaged tissue (Figure 17.2). In the lesion site after removal of the applied stress, the hybrid turns back into a gel to retain stem cells in the damaged tissue. The injected hydrogel also plays a role in directing the fate of the incorporated stem cells by the stiffness of the hydrogel and *in vivo* electrical, mechanical, and chemical stimulation under physiological conditions. Pek *et al.* cultured hBMSCs in a 3D PEG-silica-based thixotropic hydrogel and demonstrated that various stiffnesses of the injectable hydrogel, which were measured by the minimal liquefaction stress (τ_y) required to transform gel to sol, promoted differentiation of the encapsulated stem cells towards different lineages: neural differentiation, myogenesis and osteogenesis at τ_y of 7 Pa, 25 Pa and 75 Pa, respectively.[54] In addition, when cell-binding RGD peptides were conjugated to the PEG-silica hydrogel, osteogenesis at a τ_y of 75 Pa was markedly enhanced with 13% higher expression of Runx2 and OCN, because the specific binding between the immobilized RGD ligands and the cellular membrane integrin at a stiffer hydrogel was tighter, and the tighter binding induced osteogenic differentiation.[54] Jacob *et al.* adjusted the inherent stiffness of an amyloid hydrogel by changing the concentrations of amyloid and ions, at which the encapsulated hBMSCs were detected to differentiate into the neural lineage.[55] The peptide Nap-GFFYGG-KOGEOGKOGSO in the supra-molecular-peptide/protein-formed thixotropic hydrogels was reported to work as a stimulus and selectively improved differentiation of mouse ESCs into vascular progenitor cells with a significantly high expression of the *Flk 1* gene.[56]

17.5.2 Stress Stiffening/Relaxation-Induced Cell Differentiation

Most hydrogels generated from filamentous biopolymers, such as collagen, F-actin and fibrin, become stiffer when the applied stress is above their critical stress (σ_c) level, which is called stress stiffening. It was recently reported that stress stiffening also plays an important role in regulation of stem cell fate

Downloaded by Institute of Process Engineering, Chinese Ac
Published on 03 May 2017 on https://pubs.rsc.org | doi:1

Table 17.4 Thixotropic materials and their regulation for the fate of stem cells.

Material	Dimension (2D/3D)	Culture medium	Encapsulated cell type	Differentiation type	Differentiation efficiency	Differentiation evidence	Application	Reference
RGD-conjugated PEG-silica gel (with varied liquefaction stress and RGD concentration)	3D	Culture media	hBMSCs	Neural differentiation for 7 Pa; myogenic differentiation for 25 Pa; osteogenesis for 75 Pa	RGD promoted proliferation and differentiation of hMSCs for stiffer gels with liquefaction stress >75 Pa	Neural (*ENO 2*), myogenic (*MYOG*). Osteogenic (*Runx2*, *OCN*) transcription factors	Tissue engineering	54
Amyloid hydrogel (Fmoc-conjugate peptides (Aβ42)), varying stiffness by changing peptide and salt concentration	2D	Knockout DMEM + 10% FBS + 2 mM glutamax + 0.25% penicillin and streptomycin	hBMSCs	Neuronal lineage for softest gel P5 6 mg mL^{-1}	—	Maximal spreading and elongation, β-III tubulin ENO2, GRIA3	Tissue engineering	55
Nap-GFFYGGKO-GEOGKOGSO	2D	Differentiation media	mESCs	Vascular progenitors	—	Mesoderm marker (*Flk 1*)	Vascular formation in regeneration medicine	56

Downloaded by Institute of Process Engineering, Chinese Ac
Published on 03 May 2017 on https://pubs.rsc.org | doi:1

RGD-PICs; modify the critical stress by changing the polymer length	3D	1 : 1 v/v osteogenic and adipogenic media	hMSCs	Adipocyte lowest critical stress ~9.4 Pa; predominant osteogenesis over adipogenesis with increasing critical stress	—	Rsterix stain and *Runx2* RT-PCR for osteogenesis; neural lipid and *PPAR-γ* for adipogenesis	Tissue engineering	57
Alginate (crosslinked with calcium and covalently coupled with RGD); modify stress relaxation time by changing the molecular weight polymers and the crosslinking densities of calcium	3D	DMEM + 10% FBS + 1% PS + 50 mg mL^{-1} L-ascorbic acid + 10 mM β-glycerophosphate + 0.1 μM dexamethasone	mBMSCs	Adipocyte at ~9 kPa and osteoblast at ~17 kPa	Adipogenesis differentiation decrease in rapidly relaxing gels ~1 minute; osteogenic differentiation significantly enhanced with faster stress relaxation	Neural lipid for adipogenesis and ALP for osteogenesis	Bone regeneration	58

View Online

Downloaded by Institute of Process Engineering, Chinese Academy of Sciences on 1/3/2019 5:15:03 AM.
Published on 03 May 2017 on https://pubs.rsc.org | doi:10.1039/9781788010542-00473

besides the inherent stiffness of the hydrogel.[57] By simply changing the polymer length of RGD-conjugated helical oligo(ethylene) glycol polyisocyanopeptides (RGD-PICs), the σ_C was accordingly adjusted without any influence on the stiffness and the density of RGD peptides. When hMSCs were encapsulated in the hydrogel, hMSCs were attached to the RGD ligand through specific interactions between RGD and cellular integrin (Figure 17.2), during which cells applied traction stress on the surrounding gel and the traction triggered stress stiffening of the hydrogel. The stress stiffening in turn affected differentiation of the stem cells.[57] It was shown that adipogenic differentiation was predominantly performed at a lower σ_C (~9.4 Pa), while osteogenesis was preferred at a higher σ_C (14.6–19.3 Pa).[57] Furthermore, it was reported that the stress relaxation time of the RGD-alginate hydrogel also influenced the differentiation of mouse mBMSCs.[58] Decreased adipogenesis at a stiffness of ~9 kPa and significantly enhanced osteogenesis at a stiffness of ~17 kPa in the faster relaxing gel (~1 minute) were observed, because the relaxation time of the hydrogel influenced the interaction between RGD and the cell integrin, and accordingly played a role in cell adhesion and differentiation.[58]

17.6 pH-Sensitive Materials

pH-Sensitive materials usually have certain pendant groups or bonds, which can be ionized or broken when the external pH is higher or lower than their acid dissociation constants (pK_a).[14] Ionization increases the osmotic pressure inside the hydrogel, which leads to water absorption and hydrogel swelling. In addition, electrostatic repulsion generated by the ionized anionic or cationic pendant components further enhances the ionization impact. Opposite to swelling, the hydrogel may also contract by simply inhibiting ionization of pendant groups and electrostatic repulsion.[14] pH-Sensitive materials include zwitterionic amino acid/peptide amphiphiles (H_2N-peptide/oligopeptide-COOH)[59] or polymers that consist of an amino group ($-NH_2$), or carboxyl group (–COOH),[60] or catechol ($C_6H_4(OH)_2$),[61] or a hydrogen bond (–NH–CO–),[62,63] or an ionic bond ($-NH_4^+\cdots OSO_3^-$–),[64] or an imine bond (–N=CH–).[65]

Most pH-sensitive materials are reported as carriers for drug/gene delivery, because the bonds in the drug-immobilized pH-sensitive materials are ionized in the abnormal pH condition of the tumour, and then the drug is released to achieve target treatment.[14,66,67] Based on this concept, bone morphogenetic protein 2 (BMP-2) was immobilized to pH-sensitive chitosan-functionalized mesoporous silica nanoparticles through hydrogen bond formation and the protein was selectively released to rat BMSCs, to control differentiation towards osteogenesis with the evidence of enhanced expression of ALP, Runx2, OPN and Col I.[62]

Furthermore, chondrogenic differentiation, adipogenesis, and osteogenesis of hASCs were all demonstrated when the stem cells were encapsulated inside a pH-sensitive chitosan-poly (acrylic acid) (chi-PAA) hydrogel, which might be due to the contraction and swelling properties of the chi-PAA

View Online

Downloaded by Institute of Process Engineering, Chinese Academy of Sciences on 1/3/2019 5:15:03 AM.
Published on 03 May 2017 on https://pubs.rsc.org | doi:10.1039/9781788010542-00473

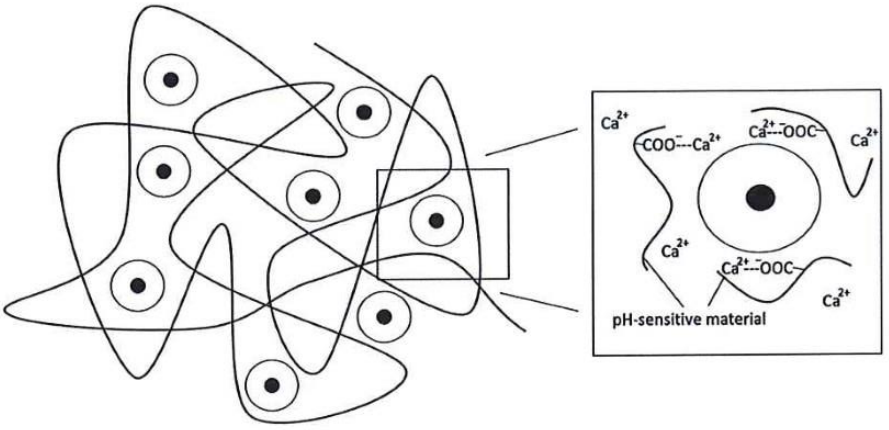

Figure 17.7 Schematic of pH-sensitive materials regulating the fate of stem cells. The carboxyl groups of PNIPAAm–AA were ionized as the anions when the pH was higher than their pK_a, which could attract cations, such as Ca^{2+}. As a result, the encapsulated stem cells were surrounded by the rich Ca^{2+} hydrogel and enhanced osteogenesis.[25,60]

hydrogel.[63] In addition, ionization and bond dissociation always improve the hydrophilicity of the hydrogels. Hence, pH-sensitive materials are easily transformed between sol and gel by simply varying the pH value (Figure 17.2), and they can be potentially applied as injectable hydrogels to provide an *in vivo* ECM-mimicking environment for encapsulated stem cells at physiological pH. Growth factors and RGD peptides/proteins are also incorporated or conjugated into the pH-sensitive hydrogels for regulation of stem cell fate (Figure 17.2). Dai *et al.* achieved selective improvement in expression of ALP and calcium deposition by encapsulating mBMSCs in a thermosensitive and pH-sensitive hydrogel (PNIPAAm–AA).[60] The ionized carboxyl groups of PNIPAAm–AA may play an important role in the capture of calcium, which is an osteogenic stimulus and further promotes osteogenesis of stem cells (Figure 17.7).[60]

17.7 Smart Materials in Clinical Applications

Currently, most cell culturing systems made of smart materials for stem cell therapy are still at the *in vitro* or *in vivo* animal research stage.[24] They were mainly designed to maximally mimic the properties of the extracellular matrix (ECM) so as to facilitate functioning of implanted stem cells similar to host cells *via in vivo* physiological stimulation. Thus, the stem cells can be induced to transform to the required cell types. One of the few successful applications of smart materials in the clinical trails of stem cell therapy was reported by Menasché *et al.* in 2015.[68,69] A hybrid of enzyme-sensitive fibrinogen and hESCs-derived cardiac progenitor cells was induced to form a thin layer of a 3D fibrin gel by thrombin, which was then implanted onto the

View Online

Downloaded by Institute of Process Engineering, Chinese Academy of Sciences on 1/3/2019 5:15:03 AM.
Published on 03 May 2017 on https://pubs.rsc.org | doi:10.1039/9781788010542-00473

infarcted area of a patient suffering from MI. Three months after the implantation, an improved left ventricular ejection fraction (LVEF) from 26% to 36% and contractility in the infarcted area were found. In addition, no adverse complications were shown. Even though it was hard to say that the improvement of cardiac function was due to the differentiation of the implanted hESCs-derived cardiac progenitor cells since vascular bypass surgery in a no-infarcted area was performed at the same time, the smart material utilised in this trial showed a good example for their future clinical applications. In addition, a monolayer of autologous oral mucosal epithelium was generated from the temperature-sensitive material PNIPAAm and implanted into a patient suffering total bilateral corneal limbal epithelial stem cell deficiency, which showed another possible clinical application of smart materials.[70] However, before full regulation of stem cells in clinical applications, the complicated mechanism of cell differentiation should be completely and clearly understood. Then the fate of stem cells can be controlled well either *in vivo* or *in vitro* by physical or chemical modification of the smart materials.[24]

17.8 Conclusions and Perspectives

Compared to traditional materials, smart materials are better alternatives for advancing stem cell therapy because they allow remote control of regulating the fate of the encapsulated stem cells both *in vitro* and *in vivo*. Most smart materials are easily modified for injectable stem cell carriers for implantation, and they not only facilitate delivery of stem cells into the lesion site but also provide an *in situ* ECM-mimicking environment for the stem cells.

Smart materials are also employed to direct the differentiation of stem cells through a variety of physical/chemical cues, including inherent stiffness, controlled release of encapsulated biomolecules, hydrophobic or electrostatic interactions, generated electricity or reactive oxygen species, and others, when they change their properties in response to external stimuli, such as temperature, pH, stress, or light.

However, how these physical/chemical cues created by the smart materials in response to external stimuli switch the gene expression of stem cells to another remains to be clarified. More importantly, precise control of interactions between these physical/chemical cues and stem cells are mandatory for spatially and temporarily regulating stem cell differentiation, which requires the development of novel "smarter" biomaterials. These biomaterials are able to make the cues available for stem cells by external stimuli when requested by cellular differentiation.

Acknowledgements

HZ would like to acknowledge financial support from the ARC Discovery Project (DP160104632) and The Medical Advancement Without Animal (MAWA) Trust. JBZ thanks the IPE-UoA Scholarship (BES).

View Online

Downloaded by Institute of Process Engineering, Chinese Academy of Sciences on 1/3/2019 5:15:03 AM.
Published on 03 May 2017 on https://pubs.rsc.org | doi:10.1039/9781788010542-00473

References

1. X. Li, E. Katsanevakis, X. Liu, N. Zhang and X. Wen, *Prog. Polym. Sci.*, 2012, **37**, 1105–1129.
2. J. Hou, L. Wang, J. Jiang, C. Zhou, T. Guo, S. Zheng and T. Wang, *Stem Cell Rev.*, 2013, **9**, 326–338.
3. T. Goldschlager, D. Oehme, P. Ghosh, A. Zannettino, J. V. Rosenfeld and G. Jenkin, *Curr. Stem Cell Res. Ther.*, 2013, **8**, 381–393.
4. S. Kriks, J.-W. Shim, J. Piao, Y. M. Ganat, D. R. Wakeman, Z. Xie, L. Carrillo-Reid, G. Auyeung, C. Antonacci, A. Buch, L. Yang, M. F. Beal, D. J. Surmeier, J. H. Kordower, V. Tabar and L. Studer, *Nature*, 2011, **480**, 547–551.
5. W. L. Murphy, T. C. McDevitt and A. J. Engler, *Nat. Mater.*, 2014, **13**, 547–557.
6. T. P. Kraehenbuehl, R. Langer and L. S. Ferreira, *Nat. Methods*, 2011, **8**, 731–736.
7. M. G.-F. Sandra Hofmann, in *Regenerative Medicine and Tissue Engineering: Cells and Biomaterials*, ed. D. Eberli, InTech, 2011, ch. 18, DOI: 10.5772/22061.
8. R. Ravichandran, S. Sundarrajan, J. R. Venugopal, S. Mukherjee and S. Ramakrishna, *Macromol. Biosci.*, 2012, **12**, 286–311.
9. A. Chan, R. P. Orme, R. A. Fricker and P. Roach, *Adv. Drug Delivery Rev.*, 2013, **65**, 497–514.
10. A. Higuchi, Q.-D. Ling, S. S. Kumar, Y. Chang, T.-C. Kao, M. A. Munusamy, A. A. Alarfaj, S.-T. Hsu and A. Umezawa, *Prog. Polym. Sci.*, 2014, **39**, 1585–1613.
11. A. Higuchi, Q.-D. Ling, Y. Chang, S.-T. Hsu and A. Umezawa, *Chem. Rev.*, 2013, **113**, 3297–3328.
12. H. Zhang, S. Dai, J. Bi and K.-K. Liu, *Interface Focus*, 2011, **1**, 792–803.
13. T. A. Shell and D. S. Lawrence, *Acc. Chem. Res.*, 2015, **48**, 2866–2874.
14. M. C. Koetting, J. T. Peters, S. D. Steichen and N. A. Peppas, *Mater. Sci. Eng., R*, 2015, **93**, 1–49.
15. A. Higuchi, Q.-D. Ling, S. S. Kumar, Y. Chang, A. A. Alarfaj, M. A. Munusamy, K. Murugan, S.-T. Hsu and A. Umezawa, *J. Mater. Chem. B*, 2015, **3**, 8032–8058.
16. Y. S. Lee and T. L. Arinzeh, *Tissue Eng., Part A*, 2012, **18**, 2063–2072.
17. J. G. Hardy, S. A. Geissler, D. Aguilar Jr, M. K. Villancio-Wolter, D. J. Mouser, R. C. Sukhavasi, R. C. Cornelison, L. W. Tien, R. C. Preda, R. S. Hayden, J. K. Chow, L. Nguy, D. L. Kaplan and C. E. Schmidt, *Macromol. Biosci.*, 2015, **15**, 1490–1496.
18. J. Mierczynska, J. Cybulska, B. Solowiej and A. Zdunek, *Carbohydr. Polym.*, 2015, **133**, 547–555.
19. O. Akhavan and E. Ghaderi, *Nanoscale*, 2013, **5**, 10316–10326.
20. C. Ribeiro, V. Sencadas, D. M. Correia and S. Lanceros-Méndez, *Colloids Surf., B*, 2015, **136**, 46–55.
21. B. Shi, H. Zhang, S. Z. Qiao, J. Bi and S. Dai, *Adv. Healthcare Mater.*, 2014, **3**, 1839–1848.

View Online

Downloaded by Institute of Process Engineering, Chinese Academy of Sciences on 1/3/2019 5:15:03 AM.
Published on 03 May 2017 on https://pubs.rsc.org | doi:10.1039/9781788010542-00473

22. Z. Shen, B. Shi, H. Zhang, J. Bi and S. Dai, *Soft Matter*, 2012, **8**, 1385–1394.
23. Z. Shen, A. Mellati, J. Bi, H. Zhang and S. Dai, *RSC Adv.*, 2014, **4**, 29146–29156.
24. D. Y. Kim, D. Y. Kwon, J. S. Kwon, J. H. Kim, B. H. Min and M. S. Kim, *Polym. Rev.*, 2015, **55**, 407–452.
25. Z. Shen, J. Bi, B. Shi, D. Nguyen, C. J. Xian, H. Zhang and S. Dai, *Soft Matter*, 2012, **8**, 7250–7257.
26. A. Mellati, M. Valizadeh Kiamahalleh, S. Dai, J. Bi, B. Jin and H. Zhang, *Mater. Sci. Eng., C*, 2016, **59**, 509–513.
27. S. A. Fisher, R. Y. Tam and M. S. Shoichet, *Tissue Eng., Part A*, 2014, **20**, 895–898.
28. J. Gao, R. Liu, J. Wu, Z. Liu, J. Li, J. Zhou, T. Hao, Y. Wang, Z. Du, C. Duan and C. Wang, *Biomaterials*, 2012, **33**, 3673–3681.
29. X. Li, J. Zhou, Z. Liu, J. Chen, S. Lü, H. Sun, J. Li, Q. Lin, B. Yang, C. Duan, M. Xing and C. Wang, *Biomaterials*, 2014, **35**, 5679–5688.
30. Z. Li, X. Guo, A. F. Palmer, H. Das and J. Guan, *Acta Biomater.*, 2012, **8**, 3586–3595.
31. B. Yeon, M. H. Park, H. J. Moon, S.-J. Kim, Y. W. Cheon and B. Jeong, *Biomacromolecules*, 2013, **14**, 3256–3266.
32. C. Chun, H. J. Lim, K. Y. Hong, K. H. Park and S. C. Song, *Biomaterials*, 2009, **30**, 6295–6308.
33. J. S. Park, D. G. Woo, H. N. Yang, H. J. Lim, K. M. Park, K. Na and K. H. Park, *J. Biomed. Mater. Res., Part A*, 2010, **92**, 988–996.
34. Z. Li, X. Guo and J. Guan, *Biomacromolecules*, 2012, **13**, 1956–1964.
35. S. Dhivya, S. Saravanan, T. P. Sastry and N. Selvamurugan, *J. Nanobiotechnol.*, 2015, **13**, 40.
36. A. Gelmi, J. Zhang, A. Cieslar-Pobuda, M. K. Ljunngren, M. J. Los, M. Rafat and E. W. H. Jager, *Proc. SPIE, Electroactive Polymer Actuators and Devices (EAPAD)*, 2015, **9430**, 94301T.
37. J. Pelto, M. Bjorninen, A. Palli, E. Talvitie, J. Hyttinen, B. Mannerstrom, R. Suuronen Seppanen, M. Kellomaki, S. Miettinen and S. Haimi, *Tissue Eng., Part A*, 2013, **19**, 882–892.
38. N. Tandon, B. Goh, A. Marsano, P.-H. G. Chao, C. Montouri-Sorrentino, J. Gimble and G. Vunjak-Novakovic, *Conf. Proc. IEEE Eng. Med. Biol. Soc.*, 2009, **1**, 6517–6521.
39. S. D. McCullen, J. P. McQuilling, R. M. Grossfeld, J. L. Lubischer, L. I. Clarke and E. G. Loboa, *Tissue Eng., Part C*, 2010, **16**, 1377–1386.
40. G. Thrivikraman, P. S. Lee, R. Hess, V. Haenchen, B. Basu and D. Scharnweber, *ACS Appl. Mater. Interfaces*, 2015, **7**, 23015–23028.
41. F. Pires, Q. Ferreira, C. A. V. Rodrigues, J. Morgado and F. C. Ferreira, *Biochim. Biophys. Acta, Gen. Subj.*, 2015, **1850**, 1158–1168.
42. G. Thrivikraman, G. Madras and B. Basu, *Biomaterials*, 2014, **35**, 6219–6235.
43. E. Stewart, N. R. Kobayashi, M. J. Higgins, A. F. Quigley, S. Jamali, S. E. Moulton, R. M. Kapsa, G. G. Wallace and J. M. Crook, *Tissue Eng., Part C*, 2015, **21**, 385–393.

View Online

Downloaded by Institute of Process Engineering, Chinese Academy of Sciences on 1/3/2019 5:15:03 AM.
Published on 03 May 2017 on https://pubs.rsc.org | doi:10.1039/9781788010542-00473

44. W. W. Hu, Y. T. Hsu, Y. C. Cheng, C. Li, R. C. Ruaan, C. C. Chien, C. A. Chung and C. W. Tsao, *Mater. Sci. Eng., C*, 2014, **37**, 28–36.
45. C. Ribeiro, J. Parssinen, V. Sencadas, V. Correia, S. Miettinen, V. P. Hytonen and S. Lanceros-Mendez, *J. Biomed. Mater. Res., Part A*, 2015, **103**, 2172–2175.
46. T. Kushibiki, Y. Tu, A. O. Abu-Yousif and T. Hasan, *Sci. Rep.*, 2015, **5**, 13114.
47. S. Weis, T. T. Lee, A. del Campo and A. J. Garcia, *Acta Biomater.*, 2013, **9**, 8059–8066.
48. K. Han, W. N. Yin, J. X. Fan, F. Y. Cao and X. Z. Zhang, *ACS Appl. Mater. Interfaces*, 2015, **7**, 23679–23684.
49. K. M. Holmstrom and T. Finkel, *Nat. Rev. Mol. Cell Biol.*, 2014, **15**, 411–421.
50. C. A. DeForest and D. A. Tirrell, *Nat. Mater.*, 2015, **14**, 523–531.
51. T. Bai, A. Sinclair, F. Sun, P. Jain, H.-C. Hung, P. Zhang, J.-R. Ella-Menye, W. Liu and S. Jiang, *Chem. Sci.*, 2016, **7**, 333–338.
52. X. Jia, Y. Chen, C. Shi, Y. Ye, M. Abid, S. Jabbar, P. Wang, X. Zeng and T. Wu, *Food Hydrocolloids*, 2014, **39**, 27–33.
53. S. M. Reddy, G. Shanmugam, N. Duraipandy, M. S. Kiran and A. B. Mandal, *Soft Matter*, 2015, **11**, 8126–8140.
54. Y. S. Pek, A. C. Wan and J. Y. Ying, *Biomaterials*, 2010, **31**, 385–391.
55. R. S. Jacob, D. Ghosh, P. K. Singh, S. K. Basu, N. N. Jha, S. Das, P. K. Sukul, S. Patil, S. Sathaye, A. Kumar, A. Chowdhury, S. Malik, S. Sen and S. K. Maji, *Biomaterials*, 2015, **54**, 97–105.
56. H. Liu, Y. Hu, H. Wang, J. Wang, D. Kong, L. Wang, L. Chen and Z. Yang, *Soft Matter*, 2011, **7**, 5430–5436.
57. R. K. Das, V. Gocheva, R. Hammink, O. F. Zouani and A. E. Rowan, *Nat. Mater.*, 2016, **15**, 318–325.
58. O. Chaudhuri, L. Gu, D. Klumpers, M. Darnell, S. A. Bencherif, J. C. Weaver, N. Huebsch, H.-p. Lee, E. Lippens, G. N. Duda and D. J. Mooney, *Nat. Mater.*, 2016, **15**, 326–334.
59. B. F. Lin, K. A. Megley, N. Viswanathan, D. V. Krogstad, L. B. Drews, M. J. Kade, Y. Qian and M. V. Tirrell, *J. Mater. Chem.*, 2012, **22**, 19447–19454.
60. Z. Dai, Y. Shu, C. Wan and C. Wu, *J. Biomater. Appl.*, 2015, **29**, 1272–1283.
61. S. Hong, K. Yang, B. Kang, C. Lee, I. T. Song, E. Byun, K. I. Park, S.-W. Cho and H. Lee, *Adv. Funct. Mater.*, 2013, **23**, 1856.
62. Q. Gan, J. Zhu, Y. Yuan, H. Liu, J. Qian, Y. Li and C. Liu, *J. Mater. Chem. B*, 2015, **3**, 2056–2066.
63. T. Debnath, S. Ghosh, U. S. Potlapuvu, L. Kona, S. R. Kamaraju, S. Sarkar, S. Gaddam and L. K. Chelluri, *PLoS One*, 2015, **10**, e0120803.
64. J. V. Araujo, N. Davidenko, M. Danner, R. E. Cameron and S. M. Best, *J. Biomed. Mater. Res., Part A*, 2014, **102**, 4415–4426.
65. K. Raghupathi, L. Li, J. Ventura, M. Jennings and S. Thayumanavan, *Polym. Chem.*, 2014, **5**, 1737–1742.
66. B. Shi, H. Zhang, J. Bi and S. Dai, *Colloids Surf., B*, 2014, **119**, 55–65.
67. B. Shi, H. Zhang, S. Dai, X. Du, J. Bi and S. Z. Qiao, *Small*, 2014, **10**, 871–877.
68. P. Menasché, V. Vanneaux, A. Hagege, A. Bel, B. Cholley, I. Cacciapuoti, A. Parouchev, N. Benhamouda, G. Tachdjian, L. Tosca, J. H. Trouvin, J. R.

View Online

Fabreguettes, V. Bellamy, R. Guillemain, C. Suberbielle Boissel, E. Tartour, M. Desnos and J. Larghero, *Eur. Heart J.*, 2015, **36**, 2011–2017.
69. P. Menasche, V. Vanneaux, J. R. Fabreguettes, A. Bel, L. Tosca, S. Garcia, V. Bellamy, Y. Farouz, J. Pouly, O. Damour, M. C. Perier, M. Desnos, A. Hagege, O. Agbulut, P. Bruneval, G. Tachdjian, J. H. Trouvin and J. Larghero, *Eur. Heart J.*, 2015, **36**, 743–750.
70. C. Burillon, L. Huot, V. Justin, S. Nataf, F. Chapuis, E. Decullier and O. Damour, *Invest. Ophthalmol. Visual Sci.*, 2012, **53**, 1325–1331.
71. W.-T. Su, W.-L. Chou and C.-M. Chou, *Mater. Sci. Eng. C*, 2015, **52**, 46–53.
72. Z. Li, X. Guo and J. Guan, *Biomacromolecules*, 2012, **13**, 1956–1964.
73. Z. Li, X. Guo, S. Matsushita and J. Guan, *Biomaterials*, 2011, **32**, 3220–3232.
74. H. Tan, C. M. Ramirez, N. Miljkovic, H. Li, J. P. Rubin and K. G. Marra, *Biomaterials*, 2009, **30**, 6844–6853.
75. Y. Rui, L. Xu, R. Chen, T. Zhang, S. Lin, Y. Hou, Y. Liu, F. Meng, Z. Liu, M. Ni, K. Sze Tsang, F. Yang, C. Wang, H. Chang Chan, X. Jiang and G. Li, *Sci. Rep.*, 2015, **5**, 11056.
76. X. Xiao, L. Yu, Z. Dong, R. Mbelek, K. Xu, C. Lei, W. Zhong, F. Lu and M. Xing, *J. Mater. Chem. B*, 2015, **3**, 5635–5644.
77. H. Cui, Y. Liu, Y. Cheng, Z. Zhang, P. Zhang, X. Chen and Y. Wei, *Biomacromolecules*, 2014, **15**, 1115–1123.
78. A. Mellati, S. Dai, J. Bi, B. Jin and H. Zhang, *RSC Adv.*, 2014, **4**, 63951–63961.
79. Z. Huang, B. Yu, Q. Feng, S. Li, Y. Chen and L. Luo, *Carbohydr. Polym.*, 2011, **85**, 261–267.
80. I. Jun, Y. B. Lee, Y. S. Choi, A. J. Engler, H. Park and H. Shin, *Biomaterials*, 2015, **54**, 44–54.
81. J. You, A. Haque, D.-S. Shin, K. J. Son, C. Siltanen and A. Revzin, *Adv. Funct. Mater.*, 2015, **25**, 4650–4656.
82. C. M. Kirschner and K. S. Anseth, *Small*, 2013, **9**, 578–584.

Downloaded by Institute of Process Engineering, Chinese Academy of Sciences on 1/3/2019 5:15:03 AM.
Published on 03 May 2017 on https://pubs.rsc.org | doi:10.1039/9781788010542-00473